TAMPEREEN TEKNILLINEN YLIOPISTO
TAMPERE UNIVERSITY OF TECHNOLOGY
Julkaisu 635 • Publication 635

Matei Rusu

Frequency Conversion Using Ultrafast Fiber Lasers

Tampere 2006

Tampereen teknillinen yliopisto. Julkaisu 635
Tampere University of Technology. Publication 635

Matei Rusu

Frequency Conversion Using Ultrafast Fiber Lasers

Thesis for the degree of Doctor of Technology to be presented with due permission for public examination and criticism in Tietotalo Building, Auditorium TB104, at Tampere University of Technology, on the 24th of November 2006, at 12 noon.

Tampereen teknillinen yliopisto - Tampere University of Technology
Tampere 2006

ISBN 952-15-1683-6 (printed)
ISBN 952-15-1716-6 (PDF)
ISSN 1459-2045

Preface

"The important thing in science is not so much to obtain new facts as to discover new ways of thinking about them."

Sir William Bragg (1862–1942)

Ultrashort laser pulses wrote an important chapter in the history of science. Delivering timing accuracy and optical power at unprecedented levels, ultrashort pulses available at wavelengths from mid infrared to UV brought progress in virtually all fields of science. Despite the ever increasing need for ultrashort pulses, a pulsed laser source offering compactness, tunability, and low price is still an unfulfilled promise.

Building a compact and efficient source of visible and UV pulses is a challenging task. Fiber technology offers a rich supply of compact and maintenance-free lasers delivering ultrashort pulses in a broad wavelength range. However, ultrashort pulses in the visible and UV domains are difficult to obtain directly from fiber lasers. The approach taken in this thesis relies on using mode-locked fiber lasers as pump sources for frequency conversion stages and broadband (supercontinuum) generation in nonlinear waveguides. The thesis work aims at optimizing the entire optical chain leading to visible and UV light, from the mode-locked fiber laser to the frequency conversion stage. Compact mode-locked lasers with repetition rate stabilization are assembled using all-fiber cavity components. Various designs of power amplifiers are investigated and solutions optimized for frequency conversion and supercontinuum generation are suggested. Frequency doubling and tripling by periodically-poled crystals is demonstrated in both waveguided and bulk device configurations. Finally, supercontinuum generation in customized nonlinear waveguides is demonstrated as a reliable source of tunable ultrashort pulses.

It is the author's sincere hope that the work embedded between the covers of this thesis constitutes a step in the long staircase towards compact and affordable ultrafast fiber laser sources and, in the good spirit of optics, shines some light on the problems and achievements of this amazing field of laser science.

Abstract

This thesis investigates novel methods of generating ultrashort optical pulses in the visible and ultraviolet wavelength ranges by frequency conversion and supercontinuum generation using mode-locked fiber lasers. Optimization of mode-locked fiber lasers by intracavity dispersion compensation and repetition rate stabilization is described.

An Nd mode-locked fiber laser is introduced as a way to obtain picosecond pulses in the near infrared (~900 nm). The fiber gain medium allows for efficient pumping of the 900 nm transition of the Nd and suppression of the parasitic 1060 nm oscillation.

High quality picosecond pulse operation of an Yb-doped fiber laser is obtained by employing intracavity dispersion compensation in all-fiber format. The required negative dispersion is obtained from a single-mode fiber taper. Owing to the all-fiber format, the laser cavity is more compact than the traditional setups using bulk elements for dispersion compensation.

Temporal synchronization between two mode-locked fiber lasers is obtained by cross phase modulation in a single-mode optical fiber. Using a special cavity design, all-optical clocking of a mode-locked fiber laser has been obtained. The clock source is an inexpensive telecom-grade laser diode. Exploiting the dissimilar gain spectra of Er and Yb-doped active fibers, a two-color mode-locked source has been constructed. The source emits two trains of pulses at 1550 nm and 1060 nm, synchronized by cross-phase modulation.

Visible and ultraviolet light pulses are obtained from a high power Yb-doped fiber laser by frequency conversion in a waveguided KTP crystal. The mechanisms permitting simultaneous generation of second and third harmonic light are discussed.

An all-fiber laser source optimized for pumping periodically-poled crystals is proposed. The source relies on interplay between frequency chirp and nonlinearity to prevent spectral broadening of a laser pulse inside the fiber amplifier.

The intimate mechanisms of supercontinuum generation in photonic crystal fibers are investigated by spectrally-sensitive autocorrelations. Soliton fission is shown to play a key role in the early stages of spectral broadening.

Using a frequency-doubled Yb-doped fiber laser, all-visible supercontinuum radiation is generated in a fiber taper. This novel broadband source covers the entire visible spectrum and, unlike traditional supercontinuum generators, does not produce any residual infrared radiation.

Acknowledgements

This thesis is the result of four long (and very interesting) years of research spent at the Optoelectronics Research Centre (ORC) of Tampere University of Technology. I really enjoyed my time here and this is in no small part due to my supervisor, Prof. Oleg Okhotnikov, whom I thank for guidance and support. His undivided enthusiasm, broad perspective, and constant encouraging really kept things going. Being his student was (and will probably be) an unforgettable experience.

My deepest gratitude goes to Prof. Markus Pessa, head of ORC, for being the driving force behind all research I have taken part in. Without him, much of what I achieved would not have been possible. Two thumbs up and a deep bow to Anne Viherkoski for her wonderful skills in sorting out the day-to-day administrative issues. For me, she was the "human interface" to the intricate management of research projects.

I gratefully acknowledge the financial support of Nokia Foundation, the Academy of Finland, and European Union.

To my friends and colleagues, a big "thank you". Much of my accomplishments I owe to Mircea Guina, whose support and friendship got me through the most difficult moments. I thank Antti Isomäki for being the best office mate one could ask for. I am indebted to Robert Herda for his valuable help with numerical simulations and experimental issues. I do remember the long hours we spent at trying to get the setups to work. This thesis is the solid proof that we managed. Many thanks to Samuli Kivistö for acting as my second right hand in the lab. His work with passive components is most appreciated. Antti Härkönen and Lasse Orsila were more than just colleagues; they were friends I could count on. Thanks for that. I am grateful to Tommi and Esa for all the help and soothing presence. Luis and Dionisio, you guys really made a difference. Special thanks to Kaj Torrkulla for being out there when most needed. Our "techie" meetings kept me sane. And to all people at ORC, my deepest gratitude for the wonderful research environment you created. It has been a pleasure and an honor working with you.

I am grateful to those people and companies who made my work possible. I thank Dr. Anatoly Grudinin from Fianium Ltd. (UK) for his valuable advice on many issues and for supplying the high power fiber lasers used in some experiments. I also thank Dr. Corin Gawith from Stratophase (UK) for his great "tips and tricks" on frequency conversion, as well as his customized PPLNs. To Dr. Edik Rafailov from Dundee University (UK), whose unparalleled enthusiasm and belief in what we were doing literally dragged me through, a great thank you. From way back in my past, I thank Prof. Dan Cojoc for his wonderful introduction to optics and Prof. Adrian Manea for guiding my first steps into the magnificent world of electronics. Virgil and Adina will always have a special place in my heart.

I thank my thesis reviewers, Dr. Kalle Ylä-Jarkko from Corelase Oy (Finland) and Prof. Andrei Fotiadi from Faculte Polytechnique de Mons (Belgium) for their outstanding contributions to improving the quality of this thesis.

To my family, especially my sister, you're too good for words.

My wife, Miruna, was my homing beacon. Thanks for putting up with me. Love you.

Tampere, 2006.

Contents

List of publications

[P1] M. Rusu, J. Konttinen, M. Guina, A. B. Grudinin, and O. G. Okhotnikov, "Femtosecond neodymium-doped fiber laser operating in the 894–909 nm spectral range," *IEEE Photon. Technol. Lett.* **16**, 1029–1031 (2004).

[P2] M. Rusu, R. Herda, S. Kivistö, and O. G. Okhotnikov, "Fiber taper for dispersion management in a mode-locked ytterbium fiber laser," *Opt. Lett.* **31**, 2257–2259 (2006).

[P3] M. Rusu, R. Herda and O. G. Okhotnikov, "Passively synchronized two-color mode-locked fiber system based on master-slave lasers geometry," *Opt. Express* **12**, 4719–4724 (2004).

[P4] M. Rusu, R. Herda and O. G. Okhotnikov, "1.05-um mode-locked Ytterbium fiber laser stabilized with the pulse train from a 1.54-um laser diode," *Opt. Express* **12**, 5258–5262 (2004).

[P5] M. Rusu, R. Herda and O. G. Okhotnikov, "Passively synchronized erbium (1550-nm) and ytterbium (1040-nm) mode-locked fiber lasers sharing a cavity," *Opt. Lett.* **29**, 2246–2248 (2004).

[P6] M. Rusu, E. U. Rafailov, R. Herda, O. G. Okhotnikov, S. M. Saltiel, P. Battle, S. McNeil, A. B. Grudinin, and W. Sibbett, "Efficient generation of green and UV light in a single PP-KTP waveguide pumped by a compact all-fiber system," *Appl. Phys. Lett.* **88**, 121105 (1–3) (2006).

[P7] M. Rusu and O. G. Okhotnikov, "All-fiber picosecond laser source based on nonlinear spectral compression," *Appl. Phys. Lett.* **89**, 091118 (1–3) (2006).

[P8] M. Rusu, A. B. Grudinin, and O. G. Okhotnikov, "Slicing the supercontinuum radiation generated in photonic crystal fiber using an all-fiber chirped-pulse amplification system," *Opt. Express* **13**, 6390–6400 (2005).

[P9] M. Rusu, S. Kivistö, C. B. E. Gawith, and O. G. Okhotnikov, "Red-green-blue (RGB) light generator using tapered fiber pumped with a frequency-doubled Yb-fiber laser," *Opt. Express* **13**, 8547–8554 (2005).

Supplemental publications

These publications are mentioned but not included in the thesis.

[SP1] M. Rusu, A. B. Grudinin, and O. G. Okhotnikov, "63-nJ, 2.5 ps pulse generation from a mode-locked fiber source with semiconductor saturable absorber and subsequent compression in photonic bandgap fiber," *International symposium on nonlinear optics ISOPL 04*, Dingle, Ireland (2006).

[SP2] A. M. Vainionpää, M. Rusu, and O. G. Okhotnikov, "Passively Mode-Locked Erbium Fiber Laser Synchronized to Clock using Vertical-Cavity Semiconductor Modulator Driven Optically with the 1.54um Laser Diode", oral presentation at *LEOS 2005*, Sydney, Australia, (2005).

Author's contribution to the included papers

This thesis is based on nine original journal articles published in international peer-reviewed press and provided as appendices to the thesis. Several sections of the thesis (especially chapters 4 and 5) include a number of currently unpublished results which may be considered for publication at a later time.
For all work reported, the author designed the experimental setup and performed most of the investigative work. Some of the experiments benefited from the contribution of the author's co-workers, especially in theoretical modeling and component manufacturing. The author's contribution to the experimental work and elaborating the manuscripts is listed in the Table below.

Paper number	*Author's contribution to experimental work*	*Author's contribution to writing the paper*
[P1]	50%	First author (30%)
[P2]	30%	First author (90%)
[P3]	50%	First author (80%)
[P4]	50%	First author (80%)
[P5]	40%	First author (60%)
[P6]	50%	First author (80%)
[P7]	90%	First author (90%)
[P8]	90%	First author (90%)
[P9]	70%	First author (90%)

List of acronyms used

a. u.	Arbitrary unit
TIR	Total internal refraction
CW	Continuous wave
MCVD	Modified chemical vapor deposition
ZBLAN	(ZrF – BaF – LaF – AlF – NaF) fluoride glass
UV	Ultraviolet
FWHM	Full-width-at-half-maximum
AM	Amplitude modulation
FM	Frequency modulation
NOLM	Nonlinear loop mirror
NALM	Nonlinear amplifying loop mirror
F8L	Figure of eight laser
SPM	Self phase modulation
XPM	Cross phase modulation
MBE	Molecular beam epitaxy
SESAM	Semiconductor saturable absorber mirror
DBR	Distributed Bragg reflector
MQW	Multiple quantum well
FPSA	Fabry-Perot saturable absorber
R-FPSA	Resonant Fabry-Perot saturable absorber
A-FPSA	Anti-resonant Fabry-Perot saturable absorber
LMA	Large mode-area
MOPA	Master-oscillator power-amplifier
CPA	Chirped-pulse amplification
RGB	Red-Green-Blue
WDM	Wavelength division multiplexer
RF	Radio frequency
GTI	Gires-Tournois interferometer
PLL	Phase-locked loop
SSFT	Split-step Fourier transform
FFT	Fast Fourier transform
SEMM	Semiconductor modulating mirror
LN	Lithium niobate
KTP	Potassium Titanium Oxide Phosphate
QPM	Quasi-phase matching
PPLN	Periodically-poled lithium niobate
TE	Thermoelectric
TPA	Two-photon absorption
PBGF	Photonic-bandgap fibers
DWDM	Dense wavelength division multiplexing
ZDW	Zero-dispersion wavelength
SSFS	Soliton self-frequency shifting

1 Introduction

1.1 Ultrashort pulses in a broad wavelength range

The key tool of the work described in this thesis is the *ultrashort optical pulse*, understood as an electromagnetic pulse whose temporal width lies in the range of several picoseconds to few hundreds of femtoseconds. Ultrashort optical pulses have unique features that render them superior to continuous wave laser beams in applications requiring short interaction time or high peak power. The narrow temporal width limits the interaction time between ultrashort pulses and the target medium and thus ultrashort pulses can be used as *fast sampling signals* with *reduced target damaging risk*. In addition, the energy confined within the narrow optical pulse gives rise to large optical powers and thus ultrashort pulses constitute ideal means for *pumping of nonlinear optical phenomena* and *precision machining of inorganic and organic materials.*

Various scientific applications specify the requirements of their ideal ultrashort pulse in terms of pulsewidth, central wavelength, and peak power [1]. The pulsewidth is particularly important in applications involving time-dependent phenomena. For a better illustration of the temporal resolution required by different fields of science, Fig. 1.1 shows, in logarithmic scale, a classification of several natural phenomena by their significant time duration (Δt) defined as the time interval required for a specific process to occur [2].

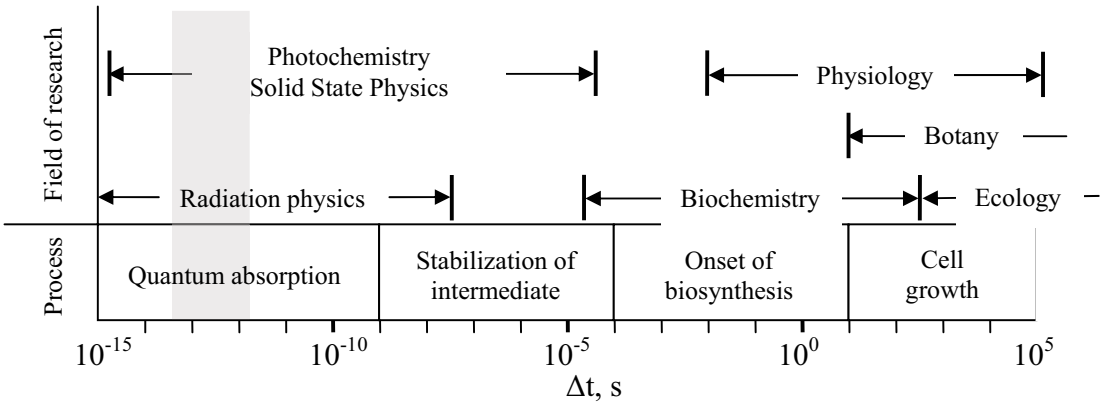

Fig. 1.1. Physical, chemical, and biological processes as a function of significant time duration (adapted from [2–4]). Δt is the time interval for a process to occur. The shaded area is the operating domain of mode-locked lasers.

The bottom section of the figure shows fundamental processes, whereas fields of endeavor are depicted in the top section. The shaded area delineates the operating range of mode-locked lasers. Spanning from several picoseconds to few tens of femtoseconds, mode-locked lasers cover an extensive part of the "fast" phenomena range. Notably, the timing precision achievable with mode-locked lasers is suitable for several "hot" topics of modern science such as quantum phenomena and photochemistry. Mode-locked lasers are thus highly-valued scientific tools, offering subpicosecond-scale temporal resolution with adjustable peak power and operating wavelength.

Tables 1.1 and 1.2 provide a quick glance at the applications of ultrashort optical pulses in modern research fields. Table 1.1 concentrates on short and intense optical pulses, whereas Table 1.2 reveals the applications of broadband supercontinuum radiation (originating from the interaction between an intense optical pulse with a nonlinear medium).

Table 1.1. Applications of ultrashort pulses.

Parameter of interest	*Application*	*Wavelength range (nm)*	*Pulse duration (fs)*	*Pulse peak power (kW)*	*Ref.*
Temporal resolution	Study of energy transfer between carotenoids and chlorophylls in photosynthesis	500–685	160	31	[5]
	Ultrafast time-gated and nonlinear microscopy	800–1064	9	388	[6] [7]
	Ultrafast optical sampling	850	100	0.01	[8]
Peak power	Simultaneous trapping (optical tweezers) and induced two-photon fluorescence of microparticles	800–1100	100	0.6	[9]
	High resolution imaging of live cells by second-harmonic generation	880	100	6.5	[10]
	Real-time investigation of biological tissue cross section by sum-frequency generation	800–1064	40	10^7	[11]
	Red light generation by frequency multiplication	1332–1338	~1000	270 mW average	[12] [13]
	Green light generation by frequency multiplication	1064 & 1338	~1000	200 mW average	[13] [14]
	Blue light generation by frequency multiplication	1338	~1000	16 mW average	[13]
	Surgery	630–1053	80–2000	38–50	[15] [16]
	Micropatterning and ablation of hard materials	780–800	100	$83–2.5 \cdot 10^6$	[17] [18]
	High field laser physics (laser plasma generated X rays)	780	50	$36 \cdot 10^6$	[19]

As shown in Table 1.1, picosecond and sub-picosecond pulses covering the vast wavelength range from blue (400 nm) to mid infrared (1600 nm) are employed in a wide selection of applications, from ultrafast biology to material processing. These applications rely upon different features of ultrashort pulses (large peak power, ultrashort time span or wavelength tuneability) and require peak powers from tens of W to several GW.

Numerous fields of science benefit from ultra-broadband radiation exhibiting limited coherence. By virtue of their high peak power, ultrashort pulses are ideal pump sources for the strong nonlinear phenomena leading to ultra-broadband radiation. Combined with properly designed nonlinear waveguides, mode-locked lasers constitute practical and reliable sources of broadband light. Several applications of wide spectrum optical radiation are presented in Table 1.2.

Table 1.2. Applications of broadband radiation consisting of bundled ultrashort pulses.

Parameter of interest	*Application*	*Wavelength range (nm)*	*Pump pulse energy (nJ)*	*Spectral brightness (mW/nm)*	*Ref.*
Spectral width	Raman spectroscopy	400–650	8	0.16	[20]
	Ultra-high numerical aperture optical coherence tomography	700–950	4.4	0.4	[21]
	UV light generation in silica waveguides	300–1600	10	0.002	[22]
	Frequency comb generation for metrological applications	300–700	>3000	>0.008	[23]

1.2 Incentives

Ultrashort pulses in a wavelength range spanning from UV to mid infrared are probably the tools of the future for many fields of activity. Research towards practical generators of such pulses is thus meaningful and important. A mere decade ago, aligning and maintaining a mode-locked laser required a wizard. A wizard with time to spare. In some cases, the costs incurred by the experiment were small compared to the costs of running the laser source. With the continuously decreasing physical size and maintenance requirements of mode-locked lasers, more and more scientific applications gain access to reliable sources of ultrashort optical pulses [24]. From this perspective, a quest for building a compact and reliable source of ultrashort pulses is all the more meaningful. Recently, *fiber lasers* emerged as promising candidates for ultrashort pulse generation [25]. Owing to the special characteristics of the all-fiber cavity as well as the lack of bulk optical components, fiber lasers offer compactness and reliability at unprecedented levels. The goal of this thesis is to investigate the design and manufacturing of fiber lasers suitable for producing ultrashort pulses in the near infrared and visible ranges. Several approaches are explored, such as the use of novel gain media, nonlinear frequency conversion, and wide spectral broadening in nonlinear fibers (supercontinuum generation).

The thesis is structured as a review of the author's work in the field, supported by brief theoretical considerations and previous research results. Chapter 2 provides an introduction to the field of fiber lasers, detailing the basic concepts of mode-locking and output power scaling. Chapter 3 elaborates on the optimization of mode-locked fiber lasers as ultrashort pulse generators. Results concerning chromatic dispersion compensation in all-fiber format and laser synchronization to external clock sources are presented. Visible light generation by frequency multiplication is discussed in chapter 4

along with the design of highly-efficient periodically-poled crystals for harmonic frequency generation. A novel fiber source delivering high power transform-limited pulses suitable for efficient frequency conversion is reported. Generation of broadband radiation (routinely referred to as *supercontinuum*) is detailed in chapter 5, followed by the introduction of a multistage system producing all-visible supercontinuum. Concluding remarks form the body of chapter 6.

2 Mode-locked fiber lasers

2.1 Brief history of fiber lasers

In strict terms, a fiber laser is an optical oscillator whose gain medium and cavity components are exclusively made of optical fiber. In selected cases, an extension of the concept is permitted in that the fiber laser cavity may contain certain bulk optical devices (such as gratings or prisms). The gain medium, however, is always fiber-based. Benefiting largely from the guided propagation of light in the fiber cavity, fiber lasers exhibit novel and attractive features which are inexistent or difficult to achieve in bulk solid state systems.

Optical gain experiments in Nd-doped glass fibers were conducted as early as 1964 [26–27]. Consisting of a fiber with 10 μm core and 1.5 mm cladding coiled around a flash lamp pump, the world's first fiber amplifier was considered a scientific curiosity rather than an application of real interest. However, several appealing features of the fiber gain media such as good optical field confinement, long interaction length, and small footprint had readily been identified as great potential for laser development [28]. The early decades of laser science witnessed the coexistence of rare-earth doped strands of crystalline materials used as waveguiding gain media [28–30] and multilayered glass fibers providing optical guiding by total internal refraction (TIR) at the interface between core and cladding [26, 31]. The latter approach prevailed, as the structure allowed for better waveguiding properties and interfacing with standard telecom fibers. Powered by advanced semiconductor pump laser modules, fiber amplifiers became increasingly efficient being able to provide large optical gain in simple end-pumped configurations [32]. In 1976, a breakthrough multimode fiber laser pumped by a semiconductor pump module was demonstrated [33]. The appealing continuous-wave (CW) operation of this laser at room temperature was ascribed to the excellent heat dissipation properties of the gain fiber medium.

In a seminal paper, researchers at Bell Labs reported the use of fused silica (SiO_2) as host matrix for rare-earth dopants in a core-cladding fiber structure [34]. Such gain fibers drew a large benefit from the mature low-loss silica fiber technology and allowed for large gain amplifiers to be manufactured. Despite significant improvement in pump and fiber technology, operation of fiber lasers at room temperature was only possible in pulsed or multimode regimes.

In 1985, Poole, Payne, and Fermann [35] developed an MCVD-based technology for fabricating doped silica fibers with accurate rare-earth doping level control. The method was repeatable and versatile, being readily adaptable to a wide range of rare-earth halides with high melting points (Nd, Er, and Yb, for instance). Simultaneously, the researchers reported on silica gain fibers embedding neodymium (Nd) and erbium (Er) ions, thus marking the starting point of modern fiber lasers. The controllable low dopant level permitted the use of long spans of gain fiber benefiting from stronger pump-signal interaction in the core and superior heat dissipation. High optical gain and single-mode operation (owing to the small core diameter) were amongst the predicted improvements of the novel MCVD technology. The work in [35] was followed by an account on the first truly CW, single-mode fiber laser based on a low-dopant level Nd gain fiber [36]. The laser proved superior to all previous systems in that it allowed for flexible pumping

strategies while maintaining low threshold values. The true single-mode operation of the laser enabled fused fiber components to be used in the cavity, resulting in a robust cavity configuration. Fused fiber components can act as pump/signal combiners or as output couplers. These low loss components can be fusion spliced to the laser cavity fiber and do not cause the diffraction or back reflection losses present in bulk laser optics. Characterization setups and procedures for the novel silica gain fibers with low doping levels emerged in the following years [37–38]. Based on the broad gain range of active silica fibers, widely tunable single-mode Nd and Er fiber lasers were reported [39].
Backed by the work of Kao and Hockham discussing, in premiere, the potential of cylindrical optical waveguides for telecommunications [40], the novel gain fibers set the stage for an unprecedented evolution in laser science. Improving at a nearly unmatched pace, fiber lasers grew to be the tool of choice for a large spectrum of applications.

2.2 Rare-earth elements for optical gain

The progress in fiber lasers is intimately coupled with the evolution of doped gain fibers. The following sections constitute a brief review of optical gain materials with particular emphasis on laser-active ions hosted in amorphous silica glass, which constitutes the key technology of modern doped optical fibers.

2.2.1 General considerations

Optical gain in dielectric media is provided by a group of elements known as *lanthanides (rare-earths)*. Despite their name, rare earths are not that rare. Cerium (Ce), the first element in the rare earths series, is present in the earth crust in a notable proportion (8.4%). The source of the unique optical gain properties of lanthanides resides in their very particular atomic structure. The classical image of an atom is that of a nucleus surrounded by shells of orbiting electrons. In general, as one progresses along the periodic table of elements, the electrons occupy shells with gradually increasing orbital radii. However, an abrupt discontinuity occurs at the element with atomic number Z = 57 (lanthanum). As shells *5s* and *5p* are fully occupied, the electrons start to occupy the lower radius inner *4f* shell [41]. Lanthanides (rare-earths) are elements with Z between 57 and 71 and a gradually increasing number of *4f* electrons. The last rare-earth element, Lutetium, has a complete *4f* shell. The number of *4f* electrons dictates the optical properties of each rare-earth element. Optical absorption and emission in lanthanides lead to electronic transitions within the *4f* shell. Being surrounded by two fully occupied electronic shells, the *4f* shell is electrostatically shielded (akin to inclusion in a metal sphere) by its larger radius neighbors. The *4f* shell sensitivity to external electrical fields is thus low, resulting in an atomic-like behavior of lanthanides in ordered (crystal) or unordered (glass) environments. Due to the special electrostatic condition of the *4f* shell, the absorption and emission bands of lanthanides exhibit reduced sensitivity to external electrical fields in contrast to transition elements lacking a similar shielding [42–43]. Ionization of the rare-earth atoms typically results in trivalent ions and involves the removal of two loosely-bound *6s* electrons and one inner *4f* electron. Thus the *5s* and *5p* shells remain intact, providing continued electrostatic shielding to the remaining *4f* electrons.

2.2.2 Host glass composition

As rare-earth ions are placed inside a glass host (as in the case of doped optical fibers), their energy levels experience splitting and broadening [44] because the *4f* electrons interact with each other and (albeit weakly) with the electrical fields of the glass lattice [42, 44–46]. As such, the composition of the host glass influences the spectroscopic properties of the rare-earth elements. Such dependence has been investigated experimentally for the case of Er- and Nd-doped fibers [47–49]. The most common active fibers are silica-based, with rare-earth ions embedded in the core. An approximate composition of the host silica glass is 94.5 SiO_2, 5 GeO_2, and 0.5 P_2O_5 (% mol). The influence of host glass composition on the fluorescence spectrum of rare-earth ions can be exploited by employing different glass compositions to effectively tune the gain spectra and relative intensities of the fluorescence peaks for different rare-earth doped fibers. For instance, altering the concentration of P_2O_5 in a Nd-doped silica fiber core leads to a substantial change of the emission and absorption spectra of the fiber [50]. Alternatively, host glass composition can be used to control the waveguiding properties of the gain fiber. In silica-based doped fibers, the germanium impurities in the core can be replaced by alumina (Al_2O_3) to increase the refractive index of the fiber core. Used in conjunction with a small amount of P_2O_5 to prevent devitrification [44], alumina enables the manufacturing of small-core, high index step fibers with improved single-mode operation. In addition, alumina allows for higher concentrations of rare-earth ions without the onset of clustering (discussed in section 2.2.3). High gain, large index contrast fibers can be manufactured using alumina-doped cores. Studies of fluorescence spectra in alumina core fibers doped with Nd have been performed [51]. More recently, a novel type of glass was investigated as primary material for gain optical fibers. It was called ZBLAN, an acronym related to its composition (ZrF - BaF - LaF - AlF - NaF), and it is sometimes referred to as fluoride glass. ZBLAN exhibits some very interesting optical properties and ZBLAN-based doped fibers received considerable attention. Built for more exotic applications (such as upconversion lasers for UV generation [52] or mode-locked upconversion lasers operating in the visible wavelength range [53]), such fibers are still of limited applicability.

2.2.3 Fiber doping level

The doping level of an optical fiber is defined either as the number of laser-active atoms per unit volume of glass or as the concentration of such ions specified in parts per million (ppm) by weight or mol. The concentration of the rare-earth ions in the fiber glass matrix determines a number of important laser parameters such as pump absorption and gain coefficient.

In fibers with low doping levels, the ground level is depleted once the number of incident photons exceeds the number of available ions. Signal amplification is thus quickly saturated. To a certain extent, increasing the optical gain can be done by using long spans of doped fiber. However, such measure may result in deleterious effects on laser operation, especially in pulsed regime (excessive nonlinearity or pulse broadening).

It would thus appear that the solution to high gain requirements of fiber lasers is a high doping level of gain fibers. Such action is not straightforward, as highly doped glass faces a series of technological problems related to uniform distribution of rare-earth ions within the glass matrix, such as concentration quenching, ion clustering, and crystallization.

Concentration quenching refers to energy transfer between laser active ions situated in close proximity. It causes a reduction in the population of the upper laser levels and thus limits the attainable gain. Quenching phenomena are assisted by clustering. Rare-earth ions tend to group inside the glass (forming clusters) rather than spreading evenly, thus enhancing inter-ion energy transfers. The contradicting requirements of low clustering/quenching and high doping levels in optical fibers are addressed (within certain physical and chemical limits) by introducing the rare-earth dopants into the glass composition by a crystal precursor with large ion spacing [54]. The precursor is subsequently melted away, but the large spacing between rare-earth ions remains, enabling a certain control over clustering. At large doping levels, rare-earth ions may crystallize within the amorphous silica [55] creating novel narrow lines within the fluorescence spectrum along with a parasitic dependence of the lasing characteristics on the pumping wavelength.

2.2.4 Neodymium (Nd), erbium (Er), and ytterbium (Yb) doped fibers

The three most important gain media of the moment are neodymium (Nd), erbium (Er), and ytterbium (Yb). Over the years, several rare-earth elements were considered (and used) for optical amplification and lasing at various wavelengths: praseodymium (Pr)–1300 nm in fluoride glass host [56], thulium (Tm)–1470–2000 nm [57–58], samarium (Sm)–used as optical gain equalizer at 1550 nm [59], and holmium (Ho)–2000–3000 nm in fluorozirconate glass host [60–61]. This section concentrates only on the gain media relevant to the work performed in this thesis.

Neodymium (Nd) doped fibers

Historically, Nd was the first dopant used in glass host for optical gain. Both glass-strand and single-mode fiber lasers were first reported using Nd as dopant [26, 36]. The absorption and fluorescence spectra of Nd, measured in a silica host, are shown in Fig. 2.1.

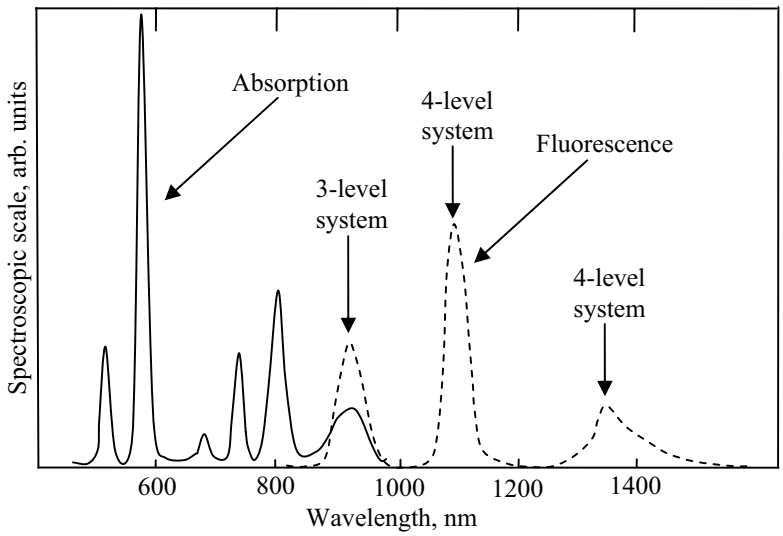

Fig. 2.1. Absorption and fluorescence spectra of Nd (adapted from [44, 62]).

The composition of the silica glass host is 94.5 SiO_2, 5 GeO_2, and 0.5 P_2O_5 (% mol) [62]. The spectrum reveals several absorption peaks around 800 nm making Nd particularly appealing, given the wide availability of pump lasers at this wavelength. An interesting feature is the very strong absorption peak situated just below 600 nm. Initially disregarded by laser scientists due to the lack of suitable pump lasers [44], this absorption peak may become important with the advent of visible single mode lasers [63], owing mostly to the very high absorption value. Remarkably, the Nd fluorescence spectrum exhibits both 3- and 4-level system emission peaks. This peculiar behavior has been ascertained by analyzing the dependence of the relaxation oscillations of an Nd fiber laser on the lasing wavelength [64–65]. The existence of a 3-level system emission peak around 900 nm has been confirmed both theoretically and experimentally [64]. The overlapping absorption and emission spectra at 900 nm (as seen in Fig. 2.1) constitutes additional proof of the existence of a 3-level lasing system in this wavelength range. The 800 nm absorption band (suitable for the mature diode laser technology) and emission band at 900 nm are interesting as a way to achieve short wavelength lasing in fibers. Mode-locked operation of an Nd doped fiber laser at wavelengths shorter than 900 nm has been reported **[P1]** in what is believed to be the shortest operation wavelength mode-locked fiber laser. It is worth noting that several other elements (Pr, for example) have short wavelength emission bands. However, laser operation at those wavelengths would require pump sources in the blue-green wavelength range, unavailable as of this moment.

Erbium (Er) doped fibers

The existence of a very low loss transmission window (1550 nm) made silica fibers ideal candidates for optical telecommunications. Owing to its strong fluorescence around 1550 nm, erbium received immediate attention as dopant for optical fibers targeting data-train amplification. Historically, Er-doped fibers were suggested as fiber-based light sources even before silica fibers were developed [66]. With the advent of low-loss silica fibers and the increasing demand for optical telecommunication amplifiers, Er-doped fibers became an important tool for the optical system designer [35]. The absorption and transmission spectra of Er ions in silica glass host are given in Fig. 2.2.

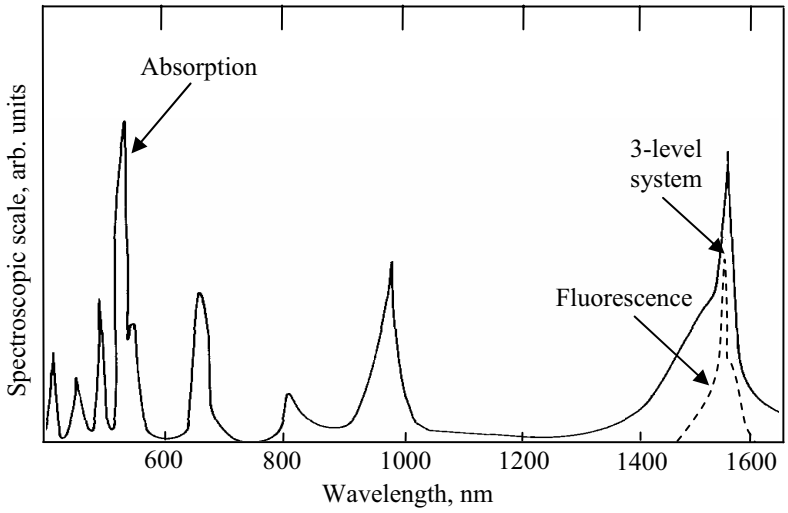

Fig. 2.2. Absorption and fluorescence spectra of Er (adapted from [44, 62]).

Er exhibits only one fluorescence peak, situated in the middle of the low loss telecommunications window (1550 nm). Several absorption peaks are present, some of which conveniently located at the operation wavelength of semiconductor lasers (980 nm and 1480 nm). Efficient pumping is possible at both wavelengths owing to the large absorption values. Laser operation is based on a 3-level system. This fact is confirmed by the overlapping absorption and fluorescence bands and demonstrated by the relaxation oscillations method [65]. Efficient pumping and the low loss of the waveguide overcome the deficiencies of a 3 level laser system (threshold dependence on fiber length and signal reabsorption). In ultrashort pulse operation, Er-doped fibers benefit from the anomalous dispersion of standard single-mode waveguides. Er-doped systems support soliton operation, a regime associated with short, self-adjusting pulses, resilient to noise and losses. Such pulses are beneficial to high speed optical telecommunications.

Ytterbium (Yb) doped fibers

Optical gain and laser action in Yb-doped glass has been demonstrated as early as 1962 [67]. However, Yb received little attention for the next decades owing mostly to its gain spectrum overlapping with Nd, a much better explored material. In crystalline media, Nd ions proved generally more efficient than Yb. In 1988, the first Yb-doped fiber was reported in laser operation [68]. Due to incorporation of the Yb ions in a silica fiber, the obtained laser efficiency was increased to 15%, comparable to Nd-based oscillators in similar conditions. Benefiting from the advanced silica technology, Yb-fiber lasers eventually became superior to Nd-based systems. There are strong reasons to investigate Yb-doped fibers as gain media, mostly related to the special properties of Yb-ions. Yb-based systems lack excited state absorption, as Yb has only one transition in infrared, all other transitions being in UV range. Some additional interesting features of Yb-based systems are visible in the absorption and fluorescence spectra of Yb in silica glass host, shown in Fig. 2.3.

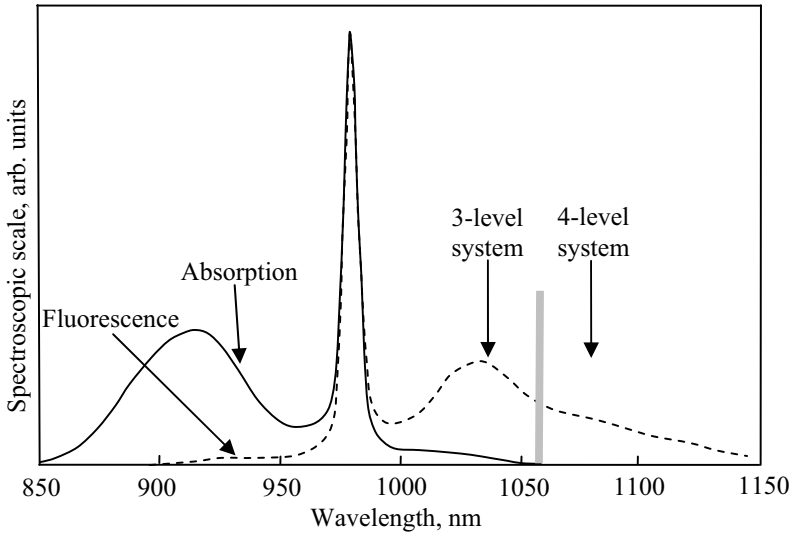

Fig. 2.3. Absorption and fluorescence spectra of Yb (adapted from [69]).

As can be seen by comparing Figs. 2.1 and 2.3, Yb ions exhibit a broader fluorescence spectrum than Nd. In consequence, Yb-doped fibers allow for broadly tunable lasers and

support ultrashort pulse operation. The broad absorption spectrum, covering the range of commercial semiconductor lasers (850–980 nm), relaxes the wavelength requirements of pump lasers for Yb-based systems. Indeed, Yb-doped fibers can be efficiently pumped with a broad range of semiconductor laser diodes and even with high power Nd lasers. In addition, Yb ions exhibit significantly lower concentration quenching than Nd and Er [69]. High doping levels are therefore possible, enabling high gain in short spans of fiber. Doped fibers exhibiting high gain per unit length are a very favorable case to ultrashort pulse amplification. Remarkably, Yb ions hosted in silica glass manifest as 3- and 4-level laser systems in immediately adjacent wavelength ranges. This phenomenon has been experimentally confirmed by analyzing the relaxation oscillations of an Yb fiber laser [70]. A sharp transition between the two regimes occurs at 1060 nm. Additional support for this assumption is given by Fig. 2.3, where the overlap between the fluorescence and absorption bands comes to an abrupt end at 1060 nm. The phenomenon is all the more interesting, as the switch between 3-level and 4-level operation can occur in the same laser setup by changing the operation wavelength. Such effects are relevant to fiber laser operation. In ultrashort pulse regime, Yb-based systems constitute a special case. Single-mode silica fibers exhibit large positive chromatic dispersion at Yb operation wavelength. This increases the amount of energy that can be stored in a single pulse without triggering pulse breakup (associated with solitons) and enables special schemes for high power pulse amplification (chirped pulse amplification - CPA) [71]. In addition, the large saturation energy of Yb-ions supports high energy pulses.

2.2.5 Advantages of fiber laser technology

Optical fibers are waveguiding structures and therefore confine light within the small area of the core. This opens up a path for large optical nonlinearity. The fibers are in most cases silica-based, thus benefiting from the low loss mature technology developed for telecom applications. In single-mode fibers the pump energy is transferred efficiently to the laser-active ions owing to the good overlap between pump and signal modes, yielding low lasing thresholds. The amorphous silica glass host causes the fluorescence spectra of the rare-earth ions to broaden, thus supporting short optical pulses or providing wide tuning range. The particularly large aspect ratio of optical fibers makes heat dissipation facile and alleviates the need for forced air or liquid cooling. Room-temperature CW operation of fiber lasers was reported at wavelengths where bulk lasers could only operate in pulsed mode. In a fiber laser, the light is waveguided at all times and coupling to transmission or sensor fibers is natural. The fiber cavity architecture enables facile insertion of intracavity fused fiber components (such as wavelength division multiplexers, beam splitters, and loop mirrors) which have no diffraction losses and do not require tedious aligning, as opposed to their bulk counterparts. In addition, fused fiber components can be easily engineered to exhibit custom spectral characteristics.

2.3 Mode-locked lasers

Mode-locking is a special operating regime of lasers, characterized by very short pulses of light being emitted from the laser cavity. The following sections provide a brief theoretical approach to mode-locking and explore various means of achieving such an operation regime in lasers. It should be noted that the introductory part is generally valid

for all solid state lasers; particularization for the case of fiber lasers is done whenever necessary.

2.3.1 Theoretical considerations

Let us consider a linear cavity laser containing *2n+1* oscillating longitudinal modes of equal amplitude, and let $\Delta\omega$ be the frequency spacing between two consecutive modes. The optical spectrum of such a laser is shown in Fig. 2.4.

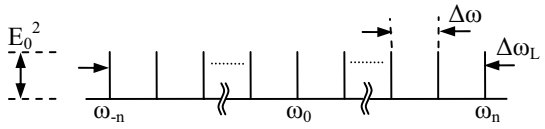

Fig. 2.4. Optical spectrum of a laser with uniform modal amplitude.

The optical bandwidth of the laser gain medium is $\Delta\omega_L = (2n+1)\Delta\omega$. In an ordinary laser, the *2n+1* modes oscillate randomly and the laser output is a noise-like trace with the average intensity $(2n+1)E_0^2$. The total electric field of a single oscillating mode can be written as:

$$E_l(t) = E_0 \exp\left[j\left(\omega_l t + \varphi_l\right)\right], \tag{2.1}$$

where φ_l and ω_l are the mode phase and frequency, respectively. Mode-locking occurs if, by means of a special action, the phases of the oscillating modes are locked to each other in a relation of the form:

$$\varphi_l = \varphi_0 + \varphi_{l-1} + \varphi = \varphi_0 + l\varphi, \tag{2.2}$$

where φ is the phase difference between two adjacent modes and φ_0 is the phase of the central mode ($l = 0$). The output of the laser can be expressed as the sum of all oscillating modes:

$$E(t) = \sum_{l=-n}^{l=n} E_0 \exp\left\{j\left[\left(\omega_0 + l\Delta\omega\right)t + l\varphi\right]\right\}, \tag{2.3}$$

where ω_0 is the frequency of the central mode and the phase of the central mode was assumed to be zero ($\varphi_0 = 0$). The laser output field in Eq. (2.3) can be expressed as:

$$E(t) = A(t)\exp(j\omega_0 t), \tag{2.4}$$

with

$$A(t) = \sum_{l=-n}^{l=n} E_0 \exp\left[jl\left(\Delta\omega t + \varphi\right)\right]. \tag{2.5}$$

The output field of the laser can thus be seen as a carrier wave oscillating at ω_0 modulated by a time-dependent amplitude *A(t)*. By introducing a new time axis *t'* so that:

$$\Delta\omega t' = \Delta\omega t + \varphi, \tag{2.6}$$

the time-dependent amplitude becomes:

$$A(t) = \sum_{l=-n}^{l=n} E_0 \exp\left(jl\Delta\omega t'\right). \tag{2.7}$$

Equation (2.7) is a geometric series with the ratio $\exp(j\Delta\omega t')$ and the scale factor E_0. It can be readily summed to give:

$$A(t) = E_0 \frac{1-\exp[j\Delta\omega t'(2n+1)]}{1-\exp[j\Delta\omega t']}, \tag{2.8}$$

which transforms into:

$$A(t) = E_0 \frac{\sin\left[\frac{(2n+1)\Delta\omega t'}{2}\right]}{\sin\left[\frac{\Delta\omega t'}{2}\right]}. \tag{2.9}$$

In Fig. 2.5, Eq. (2.9) is plotted as a function of *t'*, for *2n+1*=9 oscillating modes (corresponding to Fig. 2.4).

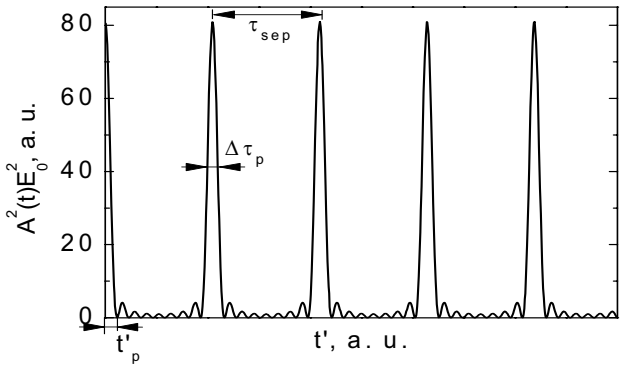

Fig. 2.5. Temporal output of a mode-locked laser.

As seen from the figure, under the assumption made in Eq. (2.2), the output of the laser consists of a train of regularly-spaced pulses. Consecutive pulses are separated by a time τ_{sep} and the full-width-at-half-maximum (FWHM) of the pulse amplitude is $\Delta\tau_p$. The maxima of *A(t)* occur when the denominator in Eq. (2.9) equals zero, i.e. when

$$\frac{\Delta\omega t'}{2} = k\pi \text{ , with } k \text{ integer.} \tag{2.10}$$

This implies that

$$t' = k\frac{2\pi}{\Delta\omega} = k\frac{1}{\Delta\nu}, \tag{2.11}$$

with $\Delta\nu$ the frequency spacing between adjacent cavity modes. The optical pulses in the output train are thus separated by a time interval equal to the inverse of the cavity modes frequency spacing. For each peak in Eq. (2.9), $\sin\left[\frac{(2n+1)\Delta\omega t'}{2}\right] \approx 2n+1$. The amplitude of the pulse is:

$$A(t)^2 = (2n+1)^2 E_0^2, \tag{2.12}$$

much larger than the amplitude of a singular mode. This can be seen in Fig. 2.5, where the mode locked pulses are $9^2 = 81$ times greater than E_0^2. Such behavior can be understood by considering that a mode-locked laser delivers its output energy in short bursts of light as opposed to a continuous output. Since the long time span between two consecutive pulses is essentially devoid of optical power, the entire laser energy is concentrated in a short duration pulse with large amplitude. Intense, ultrashort laser pulses are the main achievement of mode-locked lasers.

The first minimum of *A(t)* occurs when the numerator in Eq. (2.9) is zero. This leads to (see. Fig. 2.5):

$$t_p' = \frac{2\pi}{(2n+1)\Delta\omega}. \tag{2.13}$$

It is obvious in Fig. 2.5 that $\Delta\tau_p \approx t_p'$. Therefore,

$$\Delta\tau_p = \frac{2\pi}{\Delta\omega_L} = \frac{1}{\Delta\nu_L}, \tag{2.14}$$

where $\Delta\nu_L$ is the gain bandwidth of the laser. The pulsewidth is inversely proportional to the gain bandwidth of the laser. Active fibers, having gain bandwidths of several tens of nm, can support sub-picosecond pulses.

Thus far, the laser gain spectrum was assumed to be flat and all longitudinal modes had equal amplitudes. However, this is not always the case. The gain spectra of practical lasers exhibit one or more maxima and decrease smoothly towards zero on either side of the gain peak(s). Therefore the amplitudes of the oscillating longitudinal cavity modes are no longer equal. For a numerical analysis of mode-locking under such circumstances, a laser with a Gaussian-shaped gain spectrum is considered in the next paragraph. Figure 2.6 shows the laser spectrum under the new gain profile assumption.

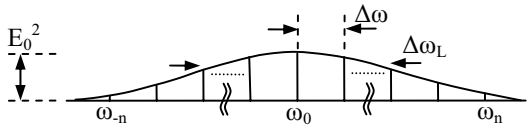

Fig. 2.6. Optical spectrum of a laser with Gaussian modal amplitude.

The electric field amplitude of the *l*-th cavity longitudinal mode can be expressed as:

$$E_l = E_0 \exp\left[-\left(\frac{2l\Delta\omega}{\Delta\omega_L}\right)^2 \frac{\ln 2}{2}\right]. \tag{2.15}$$

Assuming that the modes are phase-locked and that the phase of the central mode is zero, the electric field at the output of the laser can be expressed as in Eq. (2.4), with *A(t')* being

$$A(t') = \sum_{l=-\infty}^{l=+\infty} E_l \exp\left(jl\Delta\omega t'\right). \tag{2.16}$$

Given the narrow spectral lines of the longitudinal cavity modes, the time-varying amplitude of the laser output can be expressed in integral form as:

$$A(t') = \int_{-\infty}^{+\infty} E_l \exp(jl\Delta\omega t')dl \,. \tag{2.17}$$

Rearranging the phase terms in Eq. (2.17), one obtains:

$$A(t') = \int_{-\infty}^{+\infty} E_l \exp\left[-2\pi j\left(\frac{\Delta\omega t'}{2\pi}\right)l\right]dl \,. \tag{2.18}$$

Equation (2.19) closely resembles the Fourier transform of E_l, with the Fourier space variable $\Delta\omega t'/(2\pi)$. Since E_l in Eq. (2.15) is a Gaussian function, one may use the identity:

$$F\left[\exp\left(-ax^2\right)\right] = \sqrt{\frac{\pi}{a}}\exp\left(-\frac{\pi^2 k^2}{a}\right), \tag{2.19}$$

to obtain:

$$A(t') = E_0 \exp(-2)\frac{\Delta\omega_L}{2\Delta\omega}\sqrt{\frac{2\pi}{\ln 2}}\exp\left(-\frac{t^2}{2\ln 2}\frac{\Delta\omega^2}{4}\right). \tag{2.20}$$

Therefore, the mode-locked pulse has a Gaussian envelope, with a pulsewidth given by:

$$\Delta\tau_p = \frac{2\ln 2}{\pi\Delta\nu_L} = \frac{0.441}{\Delta\nu_L} \,. \tag{2.21}$$

The pulsewidth depends on gain bandwidth in a manner similar to Eq. (2.14), but multiplied with an additional coefficient of 0.441. In general, in lasers with finite gain spectra of various profiles, the pulse width is related to the gain bandwidth by a relation of the form:

$$\Delta\tau_p = \frac{m}{\Delta\nu_L}, \tag{2.22}$$

with m a factor of the order of unity. Table 2.1 lists the values of m for the three of the most common pulse shapes.

Table 2.1. The m parameter values for most common pulse shapes.

No	*Pulse shape*	*M value*	*Ref*
1.	Gaussian	0.441	Eq. (2.21)
2.	Hyperbolic secant (sech)	0.315	[72]
3.	Lorentz	0.38 (depending on the pulse edges)	[73]

The with characteristics fulfilling Eq. (2.22) are called *transform-limited*, in that their temporal and spectral widths are related by a Fourier transform, as described by Eq. (2.20). A transform-limited pulse is the shortest pulse that can be supported by a given optical spectrum with the width $\Delta\nu_L$. In reality, linear and nonlinear optical effects may cause the pulse to differ from the ideal case in Eq. (2.22), i.e. $\Delta\tau_P\Delta\nu_L > m$. Referring

back to the discussed mode-locking example, if the locking condition in Eq. (2.1) changes to:

$$\varphi_l = l\varphi_1 + l^2\varphi_2\,, \tag{2.23}$$

(φ_1, φ_2 – constants), the electric field of the mode-locked laser output is shown to be [74]:

$$E(t) \propto \exp\left(-\alpha t^2\right)\exp\left[j\left(\omega_0 t + \beta t^2\right)\right], \tag{2.24}$$

where α and β are functions of $\Delta\omega_L$ and φ_2. The phase term in Eq. (2.24) contains a quadratic factor of time. The instantaneous frequency

$$\omega(t) = \frac{d\left(\omega_0 t + \beta t^2\right)}{d(t)} = \omega_0 + 2\beta t\,, \tag{2.25}$$

is linearly dependent on time. Such a pulse is termed *chirped*. To understand the influence of chirp on pulse characteristics, the spectral width of *E(t)* in Eq. (2.24) is expressed as [74]:

$$\Delta\nu_L = \frac{0.441}{\Delta\tau_P}\sqrt{1+\left(\frac{\beta\Delta\tau_p^2}{2\ln 2}\right)^2}\,, \tag{2.26}$$

with

$$\Delta\tau_P = 2\sqrt{\frac{\ln 2}{\alpha}}\,. \tag{2.27}$$

For nonzero values of β, the product $\Delta\tau_P\Delta\nu_L$ (called time-bandwidth product) is larger than 0.441. A chirped pulse is a non-ideal case since it occupies broad time and spectral slots.

The time domain picture

Mode-locking is often considered in time domain. It was shown in Eq. (2.11) that the output pulses of a mode-locked laser are separated by a time interval equal to $1/\Delta\nu$, where $\Delta\nu$ is the frequency spacing between adjacent longitudinal modes of the cavity. Assuming for simplicity that the laser has a Fabry-Perot cavity, one has:

$$\Delta\nu = \frac{c}{2L} \Rightarrow \tau_{sp} = \frac{2L}{c}\,, \tag{2.28}$$

where c is the speed of light in the laser cavity and L is the cavity length. Thus, the spacing between two consecutive pulses equals the roundtrip time of the light inside the laser cavity. The mode-locked laser can thus be seen as a laser with a single pulse circulating in the cavity (Fig. 2.7). Each time the pulse bounces off the output coupler its replica is added to the output train.

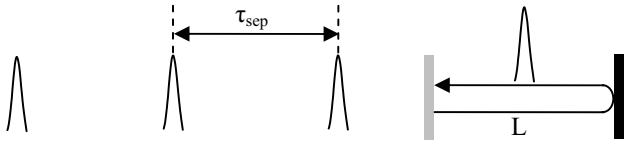

Fig. 2.7. Fundamental mode-locking: the time-domain picture.

The mode-locked operation described in Fig. 2.7 is called fundamental mode-locking in reference to the single pulse in the cavity. If n pulses circulate in the cavity, the output pulse separation decreases by a factor of n. In this case, the laser is said to be *harmonically mode-locked.*

2.3.2 Methods of mode-locking

Mode-locking of a laser requires the presence of an optical element (mode-locker) that provides periodic changes in the amplitude or phase of the light in the laser cavity. One distinguishes between mode-locking techniques by the control method of the optical element: *external control* (usually by electric signal) which leads to active mode-locking or *internal control* (the optical element reacts to the presence of the laser pulse), resulting in passive mode-locking.

2.3.2.1 Active mode-locking

In this case, the mode-locker is controlled externally. The laser pulsewidth and repetition rate are therefore subject to external control. There are two important variants of active mode-locking: amplitude modulation (AM) mode-locking and frequency modulation (FM) mode-locking.

AM mode-locking

For AM mode-locked operation, an amplitude modulator (hence the acronym AM) is inserted into the laser cavity. The sinusoidal drive of the modulator causes the cavity losses to drop periodically and laser pulses occur within the resulting low loss windows. Figure 2.8 depicts the temporal operation of an AM mode-locked laser.

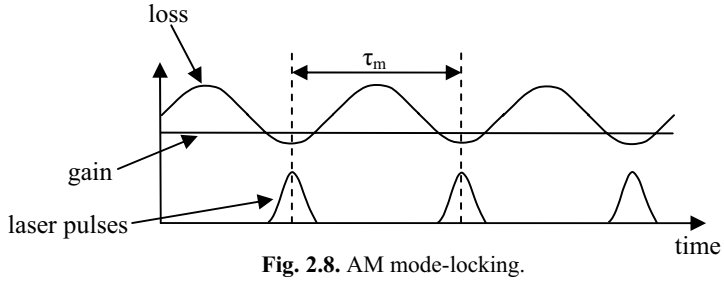

Fig. 2.8. AM mode-locking.

If the modulator drive frequency is ω_m, the electric field of the l-th cavity mode can be expressed as:

$$E_l(t) = E_0\left\{1-\frac{\delta}{2}\left[1-\cos\left(\omega_m t\right)\right]\right\}\cos\left(\omega_l t+\varphi_l\right), \tag{2.29}$$

where ω_l and φ_l are the frequency and phase of the mode, and δ is the depth of the amplitude modulation. Rearranging the terms of Eq. (2.29), one obtains:

$$E_l(t) = E_0\left(1-\frac{\delta}{2}\right)\cos(\omega_l t+\varphi_l)+E_0\frac{\delta}{2}\cos(\omega_m t)\cos(\omega_l t+\varphi_l)\ . \qquad (2.30)$$

Re-expressing the last term of Eq. (2.30), the electric field of the *l*-th mode becomes:

$$E_l(t) = M + E_0\frac{\delta}{4}\cos[(\omega_l+\omega_m)t+\varphi_l]\cos[(\omega_l-\omega_m)t+\varphi_l], \qquad (2.31)$$

where M is the first right-hand term of Eq. (2.30). Equation (2.31) reveals the presence of side-bands in the spectrum of E_l, at frequencies equal to $\omega_l+\omega_m$ and $\omega_l-\omega_m$, respectively. If the modulator frequency is chosen to equal the frequency spacing between adjacent cavity modes ($\omega_m = \Delta\omega$), the side-bands in the spectrum of E_l overlap with the neighboring modes. This causes phase-locking between modes, similar to Eq. (2.2).
The AM mode-locking mechanism can be easier understood in time domain. The light pulse occurs at the low loss window of the modulator, where the laser gain exceeds the cavity losses. If a pulse is offset in respect to the center of the low loss window, one of its wings will be attenuated more than the other, the overall effect being that of "pulling" the pulse towards the center of the low loss window. This effect is shown in Fig. 2.9.

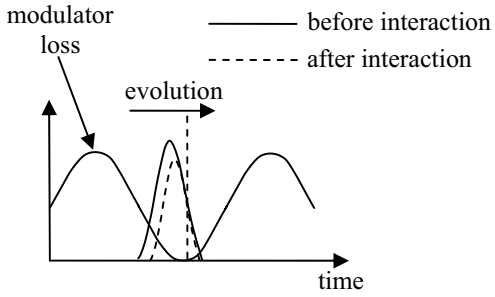

Fig. 2.9. Pulse tracking in AM mode-locking.

Pulse attenuation in the amplitude modulator is subsequently compensated for by amplification in the gain region of the laser. Once centered on the low loss window, both wings of the pulse are continuously and symmetrically attenuated. At each pass through the modulator, the pulse shortens. This process does not continue indefinitely since the pulse width is eventually limited by the gain spectrum, in accordance to Eq. (2.14). Figure 2.10 is a graphical illustration of the pulse shortening phenomenon.

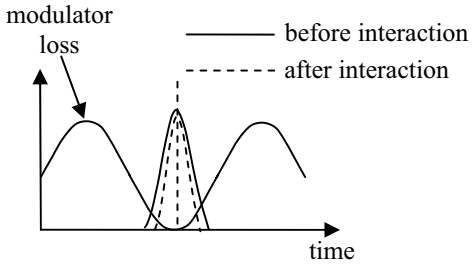

Fig. 2.10. Pulse shaping in AM mode-locking.

In a practical fiber laser, a steady state pulsewidth is reached when the pulse narrowing in the modulator is exactly balanced by the chromatic dispersion-induced pulse broadening in the fiber cavity. For the AM mode-locking regime, the pulse and spectral widths of a Gaussian-shaped pulse are given by [75]:

$$\tau_{p,AM} = \frac{\sqrt{\sqrt{2}\ln 2}}{\pi}\left(\frac{g}{\delta}\right)^{1/4}\left(\frac{1}{f_m \Delta f_L}\right)^{1/2}$$
$$\Delta f_{p,AM} = \sqrt{2\sqrt{2}\ln 2}\left(\frac{\delta}{g}\right)^{1/4}\left(f_m \Delta f_L\right)^{1/2} \quad , \tag{2.32}$$

where g is the saturated gain of the active medium at the center line of the spectrum for one roundtrip in the cavity, δ is the modulation depth, f_m is the frequency of the modulator driving signal, and $\Delta f_L = (\Delta\omega_L/2\pi)$ is the width of the laser gain spectrum. It should be noted that $\tau_{p,\,AM}\,\Delta f_{p,\,AM} = 0.44$. It is possible, in principle, to obtain transform-limited pulses from an AM actively mode-locked laser unless other cavity parameters (chromatic dispersion and nonlinearity) distort the pulse. Some interesting features of AM mode-locked lasers are revealed by Eq. (2.32). Firstly, the pulsewidth is inversely proportional to $\delta^{1/4}$ and therefore to $P_m^{1/8}$, with P_m being the RF power of the modulator drive signal. Therefore the pulsewidth depends weakly on the RF power fed to the modulator, rendering the modulator drive an ineffective way to shorten the pulse. On the other hand, the pulsewidth is inversely proportional to $f_m^{1/2}$. Modulation frequency is thus much more efficient in controlling the pulsewidth. AM active mode-locking produces pulsewidths in the range of a few picoseconds. Indeed, pulses as short as 1.9 ps have been reported at 1.3 μm in fiber ring lasers using semiconductor gain media [76]. Decreasing the pulsewidth below the theoretical value given by Eq. (2.32) (called the Kuizenga-Siegman limit) is seemingly impossible. However, by employing solitonic effects in a fiber cavity, the mode-locked pulsewidth can be decreased below the Kuizenga-Siegman limit by a factor given by [25, 77].

$$R \le 1.38\Delta\omega_L\sqrt{\frac{\beta_2 L}{g}}\,, \tag{2.33}$$

where β_2 is the cavity fiber dispersion. Using soliton effects in fiber cavities, pulses as short as 630 fs were generated from an AM actively mode-locked fiber laser [78]. The pulsewidth reduction factor was in this case 4.4.

FM mode-locking

To obtain FM mode-locking, a phase modulator is inserted into the laser cavity. The modulator is driven by a sinusoidal electrical signal and thus induces a periodic phase shift to the light passing through it. The l-th mode of the laser can be expressed as:

$$E_l(t) = E_0\cos\left\{\omega_l t + \varphi_l\left\{1 - \frac{\delta}{2}\left[1 - \cos(\omega_m t)\right]\right\}\right\}. \tag{2.34}$$

Fourier analysis of Eq. (2.34) reveals side-bands similar to AM modulation. For a Gaussian shaped pulse, the temporal and spectral widths of the pulse in FM mode-locking are given by [75]:

$$\tau_{p,FM} = \frac{\sqrt{2\sqrt{2}\ln 2}}{\pi}\left(\frac{g}{\delta}\right)^{1/4}\left(\frac{1}{f_m \Delta f_L}\right)^{1/2}$$
$$\Delta f_{p,FM} = \sqrt{2\sqrt{2}\ln 2}\left(\frac{\delta}{g}\right)^{1/4}\left(f_m \Delta f_L\right)^{1/2} \quad . \tag{2.35}$$

Except for the $\sqrt{2}$ factor in the pulsewidth, the equations are similar to Eq. (2.32). The time-bandwidth product is in this case: $\tau_{p,\,FM}\,\Delta f_{p,\,FM} = 0.626$. Therefore, the Gaussian pulses produced by an FM mode-locked laser are not transform-limited. FM mode-locking produces chirped pulses and is, in that respect, inferior to AM mode-locking. In what concerns pulsewidth reduction, precepts identical to AM mode-locking apply given the similar pulse and spectral width expressions (Eqs. (2.32) and (2.35)). Pulse evolution in FM mode-locking can be easily understood in spectral domain. At each pass through the modulator, the optical pulse acquires a certain frequency chirp which causes the pulse spectrum to broaden. Steady-state mode-locking is achieved when the spectral broadening in the modulator is exactly compensated by spectral narrowing in the gain medium. In time domain, the periodic phase modulation applied to the pulse by the modulator is equivalent to a periodic change in the cavity length given by:

$$L(t) = L \pm \frac{\lambda}{\pi}\delta\cos\left(2\pi f_m t\right), \tag{2.36}$$

where λ is the central wavelength of the pulse. A stable optical pulse is created at either extremum of the cavity length, corresponding to an extreme phase shift (as shown in Fig. 2.11). Herein lies the second drawback of FM mode-locking: pulse formation is possible at two different time instants and practical systems may uncontrollably switch between the two operating modes. Such instability is disturbing to most applications.

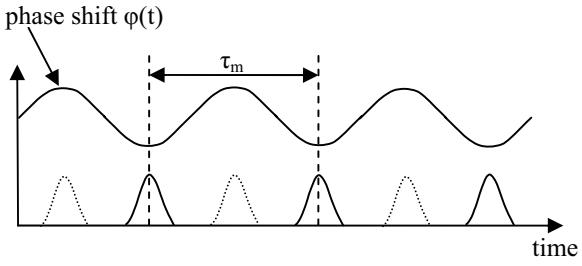

Fig. 2.11. FM mode-locking instability caused two possible operating regimes.

2.3.2.2 Passive mode-locking

In passive mode-locking, the mode locker is driven by the laser pulse itself. The mode-locker is designed so that its insertion losses decrease with high incident signal intensity. The central part of an optical pulse has high optical intensity and therefore experiences low losses, whereas the low intensity pulse wings are attenuated. The pulse emerging from the mode-locking element is shorter than the incident pulse. The steady-state mode-locking operation is self-sustaining, as pulse shortening is balanced by cavity-induced pulse broadening. However, the startup procedure (i.e. the onset of mode-locked operation) is more difficult. At the beginning of laser operation, a multitude of pulses circulate randomly in the laser cavity, arising from the unlocked longitudinal cavity

modes. At a certain point, one of the pulses is strong enough to lower the mode-locking element loss and thus promote itself in the cavity. Eventually, this pulse prevails and all other pulses become extinct. This mechanism occurs on a random time scale and the lack of an external driving signal makes self-starting of passively mode-locked lasers problematic. In some practical systems, an additional starting element is required to initiate mode-locking. Depending upon the laser type, mode-locking startup can be achieved by using an amplitude modulator, by vibrating one of the cavity mirrors, or by employing special cavity designs (restrictive cavity designs). Besides additional burden on cavity design, mode-lock starters can prove deleterious to steady-state mode-locking operation. In general, passive mode-locking produces shorter pulses, as the response of the mode-locker is dictated by the pulse itself. Three passive mode-locking methods relevant to fiber lasers will be introduced.

Nonlinear loop mirror mode-locking

The use of a nonlinear loop mirror (NOLM) as fast switching device has been first suggested in the late 80s [79]. The device consists of a fiber tap-coupler with a splitting ratio α, where the two output ports have been spliced together, as in Fig. 2.12.

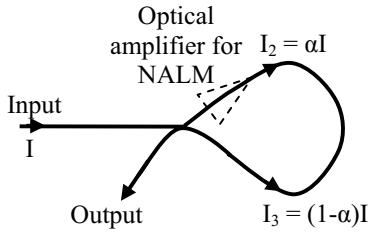

Fig. 2.12. Nonlinear loop mirror (NOLM). The dashed-line triangle indicates the position of the optical amplifier in the case of NALM.

The input signal is split in two counter-propagating signals that travel along the same path to recombine in the coupler. In the absence of nonlinear effects, the device behaves like a broadband mirror [80]. If the nonlinearity of the fiber is taken into account and if the splitting ratio fulfills $\alpha \neq 0.5$, the optical paths of the counter-propagating signals I_2 and I_3 are no longer the same, as the phase velocity is intensity-dependent. In this case, the output of the device changes with input intensity. The NOLM acts as a fast switch, performing an intensity-dependent routing between the input and output ports. Unfortunately, full switching (all input power is routed to the output port) requires very large optical power and $\alpha \cong 0.5$, being thus difficult to achieve in practice. This problem can be overcome by inserting an optical amplifier in the loop, close to the splitting coupler (as marked in Fig. 2.12) [81–82]. The resulting device is called *nonlinear amplifying loop mirror* (NALM). The key to NALM operation is the fact that the amplitudes of the counter-propagating signals are very different owing to the asymmetric positioning of the amplifier in the loop. The output signal level is given by [82]:

$$I(t+\delta) = GI_S(t)\sin^2\left[\frac{\pi}{2\lambda A_{eff}} n_2 (G-1) I_S(t) L\right], \tag{2.37}$$

where G is the amplifier saturated gain value, λ is the signal wavelength, A_{eff} is the effective mode area of the fiber (assumed the same in the gain and standard fibers), n_2 is the nonlinear refractive index of the fiber, L is the loop length, and δ is the loop transit

time. I_S is the full switching intensity, i.e. the input signal intensity that causes the loop to route the all the input signal to the output port. Owing to the built-in amplifier, full signal switching can be achieved for very low input signals (in the order of μW [82]). The potential of a fast switching NOLM to mode-lock an all-fiber laser was theoretically demonstrated less than 2 years from the introduction of NOLM [83]. The idea was quickly recognized as an attractive source of very short optical pulses and was followed by a burst of publications reporting practical implementations of such laser in a configuration known as *figure of eight laser (F8L)* [83]. Practical F8L's made use of the much less demanding NALM, due to its low power switching ability [84–86]. Providing in-depth theoretical analysis of F8L operation, the contributions reported a rapid decrease in obtained pulsewidth from the initial 150 ps [83] to an amazing 314 fs [85]. The optical setup of an F8L is presented in Fig. 2.13.

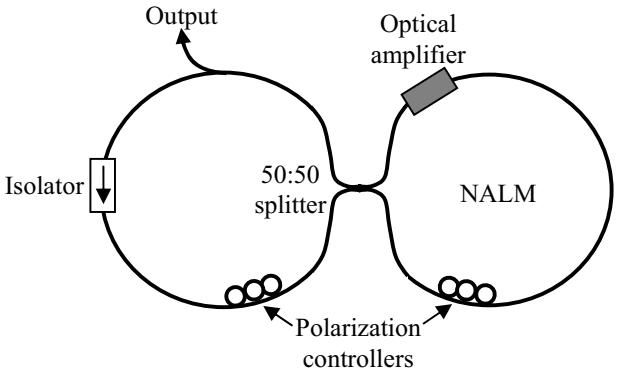

Fig. 2.13. Figure of eight laser based on NALM.

The NALM transmits only the high intensity parts of the input signal. The low intensity fraction of the laser pulse is reflected back and rejected by the isolator. The isolator is instrumental to laser operation, as it rejects the low intensity wings of the propagating optical pulse. The role of the polarization controllers is to set the polarization direction of propagating pulses and compensate for birefringence changes in the loop mirror. If the cavity fiber dispersion is negative, the laser pulses are solitonic in nature. It has been demonstrated [87] that solitons can propagate through a NOLM without losses or changes in pulse shape. Increasing the intracavity power of a F8L leads to pulse breakup and harmonic mode-locking. The phenomenon was first reported by Richardson [88], being later attributed by Grudinin [89] to energy quantization in the cavity owing to the solitonic character of the laser pulses. There is no fundamental limit for the repetition rate of such lasers since there is no external conditioning of the cavity. Using a special cavity design embedding a nonlinear semiconductor amplifier, a F8L was operated at a repetition rate of 40 GHz and used for clock extraction in a high speed telecom network [90]. Placing the output coupler in the NALM, high optical power can be extracted from the F8L while maintaining single pulse operation. An output level of 35 W at 1550 nm in 1.3 ps transform-limited pulses has been reported [91]. Nonlinear switching in fiber loop mirrors is fast and, combined with soliton compression, allows for ultrashort pulse operation. Pulsewidths of 350 fs have been obtained from an Er/Yb-doped F8L benefiting from intracavity dispersion management [92].

Nonlinear polarization rotation mode-locking

Another mode-locking mechanism suitable for fiber lasers is based on nonlinear polarization evolution in optical fiber. This phenomenon is the combined result of self-phase modulation (SPM) and cross phase modulation (XPM) in a fiber when the optical pulse is split in two orthogonally polarized components. Figure 2.14 describes the nonlinear polarization rotation mechanism in a fiber laser cavity.

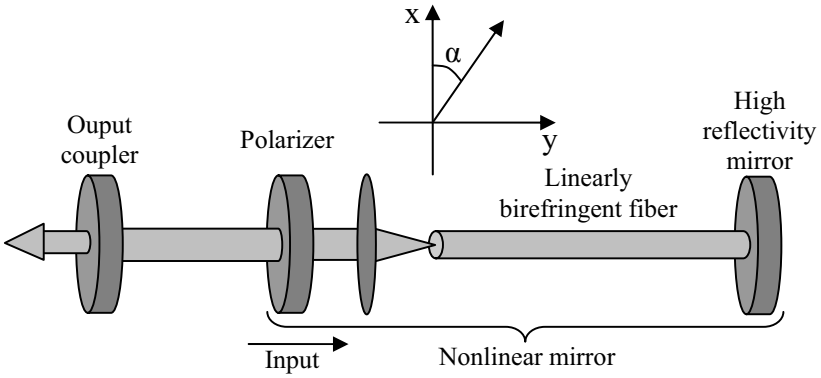

Fig. 2.14. Nonlinear polarization rotation in a fiber cavity.

The cavity comprises a span of linearly birefringent optical fiber and a polarizer. The polarizer axis makes an angle α with the orthogonal eigenmodes of the fiber (directions x and y in Fig. 2.14). The linearly polarized pulse that exits the polarizer excites the orthogonal eigenmodes of the fiber with amplitudes given by:

$$\begin{aligned} A_x &= A\cos(\alpha) \\ A_y &= A\sin(\alpha) \end{aligned}, \tag{2.41}$$

where A is the input signal amplitude and α is defined in Fig. 2.14. Both x and y polarized modes suffer linear and non-linear phase delays. With certain approximations [93], the phase delays along the x and y axes are given by [94]:

$$\begin{aligned} \Phi_x &= 2L\left[\beta_x + kn_2\left(|A_x|^2 + \frac{2}{3}|A_y|^2\right)\right] \\ \Phi_y &= 2L\left[\beta_y + kn_2\left(|A_y|^2 + \frac{2}{3}|A_x|^2\right)\right] \end{aligned}, \tag{2.42}$$

where L is the fiber length, $\beta_{x,y}$ are the propagation constants along the x and y axes, and k is the free space propagation constant. The intensity-dependent relative delay between the x and y polarized modes alters the polarization state across the pulse propagating through the fiber and influences the losses that different parts of the pulse experience at the polarizer. The assembly comprising the polarizer, fiber, and high reflectivity mirror acts as a nonlinear mirror, whose reflectivity is given by [94]:

$$R_{nl} = \cos^4(\alpha) + \sin^4(\alpha) + 2\cos^2(\alpha)\sin^2(\alpha)\cos(\Delta\phi), \tag{2.43}$$

where $\Delta\Phi = \Phi_x - \Phi_y$. The nonlinear reflectivity can be written as:

$$R_{nl} = \cos^4(\alpha) + \sin^4(\alpha) + 2\cos^2(\alpha)\sin^2(\alpha)\cos\left\{2L\left[\left(\beta_x - \beta_y\right) - \frac{1}{3}kn_2|A|^2\cos(2\alpha)\right]\right\}. \quad (2.44)$$

The dependence of reflectivity on input intensity can be seen in Eq. (2.44). For certain values of the input intensity $|A|^2$, the third cosine of the rightmost term in Eq. (2.44) becomes 1, and the nonlinear reflectivity equals unity. The portions of the pulse fulfilling this condition are losslessly reflected by the nonlinear mirror. The effectiveness of the pulse shaping mechanism provided by nonlinear polarization rotation is given by dR_{nl}/dI. One obtains:

$$\frac{dR_{nl}}{dI} = \frac{4}{3}Lkn_2\cos(2\alpha)\cos^2(\alpha)\sin^2(\alpha)\sin\left\{2L\left[\left(\beta_x - \beta_y\right) - \frac{1}{3}kn_2|A|^2\cos(2\alpha)\right]\right\}. \quad (2.45)$$

Pulse shaping efficiency depends on pulse intensity and on the polarizer angle α.

A suggestive description of mode-locking with nonlinear polarization rotation is as follows: the polarizer launches linearly polarized light upon the birefringent fiber. Following one round trip through the fiber, the state of polarization across the pulse will be nonuniform owing to the intensity-dependent phase shift, as described by Eq. (2.42). Therefore, different parts of the pulse experience different losses at the polarizer. If the peak of a pulse propagating in the cavity is linearly polarized and aligned with the polarizer, it is transmitted with minimal losses. The wings of the pulse experience more losses and the pulse is shortened. The effect is similar to the pulse shortening effect in a fast saturable absorber. Nonlinear polarization rotation can be used in both Fabry-Perot fiber cavities (such as that described in Fig. 2.14) and in ring cavity configurations, as shown in Fig. 2.15.

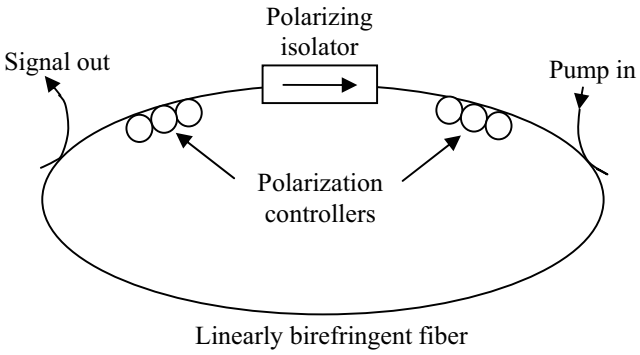

Fig. 2.15. Nonlinear polarization rotation mode-locked ring cavity fiber laser.

In this configuration, the isolator also works as a polarizer, so that the pulses leaving it are linearly polarized. The polarization controller on the right changes the pulse polarization state to elliptical. Nonlinearity in the optical fiber causes the pulse polarization state to evolve owing to nonlinear phase shift (Eq. (2.42)). The polarization controller before the isolator forces the central part of the pulse to be linearly polarized. The polarizing isolator acts as a pulse shaper. Nonlinear polarization rotation was used since the early 90s to mode-lock fiber lasers, markedly improving laser performance [94–96]. In the following years, considerable effort has been put into understanding the nonlinear polarization rotation pulse shaping mechanism and the role of cavity dispersion in pulse formation and temporal duration [97]. Optimizing nonlinear polarization rotation mode-locked fiber lasers led to remarkable results such as 452 fs in Er loop fiber laser [98]

or pulses as short as 42 fs in a Fabry-Perot cavity Nd-doped fiber laser [99]. As with all passively mode-locked lasers, the onset of mode-locked operation is problematic. However, once started, such lasers can operate without external control. Fiber lasers mode-locked by nonlinear polarization rotation may exhibit stability problems, particularly due to the long spans of fiber required to produce sufficient nonlinear phase shift (Eq. (2.42)). Moreover, temperature and mechanical stress variations can lead to fluctuating birefringence, resulting in additional instabilities in the operation of the laser. These deficiencies can be addressed by limiting the amount of fiber inside the laser cavity and employing fibers with built-in birefringence (polarization-maintaining fibers). In this way, the linear birefringence is not affected by environmental fluctuations. In an alternative approach, the use of a Faraday rotating mirror was suggested to compensate for the changes in the linear phase shift [100]. At each roundtrip, the linear phase shift is exactly compensated thus canceling out most environmental influences. The Faraday mirror also serves to reduce the walk-off caused by chromatic dispersion in high birefringence fibers.

Semiconductor saturable absorbers

Saturable absorbers are a class of mode-locking elements whose transmission increases with incident optical intensity and exhibits saturation for high input levels. Saturable absorbers are particularly attractive to ultrafast laser science because their optimization can be performed independently of cavity design. This way, the mode-locker and laser cavity can be separately designed for best performance. The possibility of shortening intense optical pulses in a medium exhibiting saturable absorption was first recognized in 1967 [101] and passively mode-locked lasers making use of this phenomenon were quickly developed. Being initially poisonous chemicals (dyes), absorbers were neither easy to handle nor cheap. It was the mid 70's that witnessed the birth of semiconductor saturable absorbers [102] as clean alternatives to dye absorbers. In 1991, semiconductor saturable absorbers were first used to mode-lock fiber lasers [103]. The semiconductor saturable absorber is probably the mode-locker of choice for fiber lasers. Nonlinear loop mirrors and nonlinear polarization rotation are unstable and sensitive to environmental changes, and mode-locking powered by such devices is difficult to start. Good as they were, fiber lasers yearned for a stable, fast mode-locking element which would enable simple cavity designs and reliable self-starting. Semiconductor saturable absorbers provided a viable solution to all these problems.

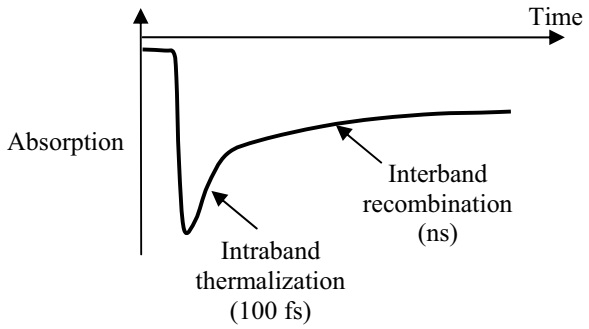

Fig. 2.16. Absorption recovery of a semiconductor saturable absorber (after [24]).

Light absorption in semiconductors is due to excitation of carriers from the valence band to conduction band. At large signal levels, the valence band levels are depleted and the

absorption saturates. One of the key parameters of a semiconductor saturable absorber used for mode-locking is its dynamic response. Figure 2.16 shows the temporal evolution of the absorption of a semiconductor saturable absorber following excitation with a very short optical pulse. Within 60–300 fs of the excitation, the carriers thermalize in either band and the absorption is partially recovered. On a longer time scale (ps to ns), the carriers are removed by recombination and trapping [104]. The presence of the two time-scales (visible in Fig. 2.16) is actually beneficial to mode-locking. The longer time scale reduces the optical intensity that saturates the absorption and thus facilitates self-starting of the laser, whereas the shorter time scale assists in shaping of sub-picosecond pulses [105].

In practice, semiconductor saturable absorbers are implemented as large stacks of quantum well layers, grown by molecular beam epitaxy (MBE). Semiconductor saturable absorbers are routinely embedded into one of the laser cavity mirrors, leading to a simple and compact cavity design. Such devices are called semiconductor saturable absorber mirrors (SESAMs) [105]. SESAM structures are the main focus of this section, as they constitute the key element of the lasers used throughout the thesis. Several lasers employing semiconductor saturable absorbers used in transmission have been reported [106–107]. The structure of a typical semiconductor saturable absorber is shown in Fig. 2.17.

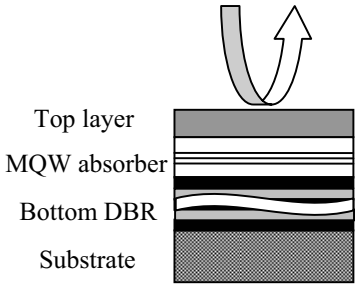

Fig. 2.17. Typical SESAM structure.

The substrate supports the bottom distributed Bragg reflector (DBR) that acts as one of the laser cavity mirrors. The multiple quantum well (MQW) structure constitutes the source of saturable absorption and is grown on top of the DBR. For the top layer, the designer is presented with a multitude of choices. One can use a second DBR for the top layer, thus encasing the MQW structure in a Fabry-Perot cavity or a dielectric anti-reflection coating, leading to a broadband absorber.

Absorbers having a top DBR are referred to as Fabry-Perot saturable absorbers (FPSA). The Fabry-Perot cavity controls the optical field in the MQW absorber region and thus the fluence (incident energy per unit area) that leads to absorption saturation. The Fabry-Perot cavity can be operated at resonance (R-FPSA) or antiresonance (A-FPSA). When operated at antiresonance (in the frequency span between two consecutive resonances of the Fabry-Perot cavity of the absorber) the FPSA exhibits broad operation bandwidth along with low insertion losses and group delay [108]. The optical intensity in the A-FPSA is low, resulting in large saturation fluence (defined in Fig. 2.18) and high optical damage threshold. In addition, A-FPSAs are insensitive to temperature fluctuations and provide loose design tolerances. However, the low intensity of the optical field in the A-FPSA causes little nonlinear reflectivity changes and thus a weak pulse shaping mechanism. By contrast, the optical field within an R-FPSA is more intense, leading to

large nonlinear modulation and low saturation fluence. Since R-FPSAs operate at a cavity resonance, their operation bandwidth is narrow and the insertion losses are relatively high. Such features make R-FPSAs usable only in fiber lasers, where optical gain is large enough to tolerate the relatively large insertion losses. R-FPSAs can be designed to exhibit significant chromatic dispersion and thus play an important role in the steady-state pulse characteristics [109]. Moreover, the low saturation fluence and large nonlinear modulation contribute to easy self-starting of the mode-locking operation [110].
An anti-reflection dielectric coating can be used as an alternative top layer. Albeit larger insertion losses, this absorber structure has a wide operation bandwidth; its parameters can be controlled by changing the diameter of the incident laser beam [105].
The reflectivity of a SESAM can be expressed as a function of incident signal fluence [111]:

$$R = 1 - R_{ns} - \Delta R \frac{1 - \exp\left(- F \big/ F_{sat} \right)}{F \big/ F_{sat}}. \tag{2.46}$$

R_{ns} is the nonsaturable reflectivity, ΔR is the nonlinear reflectivity modulation, F_{sat} is the saturation fluence, and F is the incident signal fluence. In Fig. 2.18, the SESAM reflectivity is plotted against incident fluence.

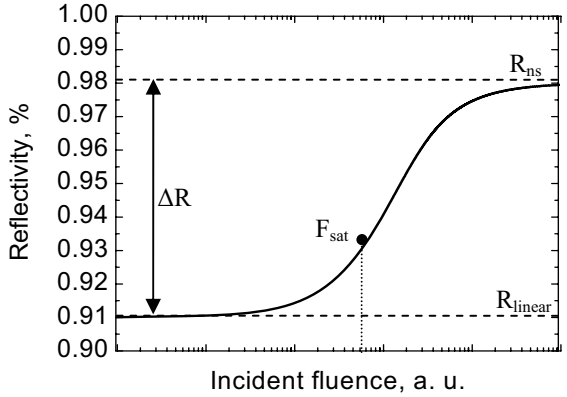

Fig. 2.18. Fluence-dependent reflectivity of a SESAM.

The SESAM reflectivity increases with incident fluence; this feature enables pulse shaping in SESAMs. Two important reflectivity levels are outlined on the Figure. The first is the minimum reflectivity (R_{linear}) which corresponds to the low-intensity (or linear) reflectivity of the SESAM at the operating wavelength. The second is the highest reflectivity point (R_{ns}), corresponding to the fully saturated absorber. The difference between this point and 100% is generally referred to as *nonsaturable losses* of the absorber. They are equivalent to the insertion losses of any optical device and are not affected by the incident light. Nonsaturable losses are an unwanted feature and their reduction is targeted by "smart" structure designs [105]. Between R_{linear} and R_{ns}, the SESAM reflectivity is fully controllable by the incident signal. The maximum change in reflectivity is termed *nonlinear reflectivity modulation* or simply *modulation depth (ΔR)*. The modulation depth value influences the laser performance. The *saturation fluence* is another important parameter of a SESAM. It gives the fluence of a pulse that raises the

absorber reflectivity to 1/e of its fully saturated value. In practical lasers, absorbers are operated several times over this value to ensure strong saturation. Strong absorber saturation is shown to reduce pulse instability and assist short pulse creation even in the presence of slow recovering absorbers [117].

Absorption recovery in the semiconductor saturable absorber is caused by recombination of the free carriers generated during light absorption. Based on the how the absorption recovery time compares to the pulsewidth of the laser, absorbers can be fast or slow. The absorption recovery time of fast saturable absorbers is much shorter than the width of the pulse circulating in the laser cavity. In the absence of additional pulse shaping phenomena (such as soliton effects), the short net gain window opened by fast saturable absorbers determines the width of the mode-locked pulses [112–113]. SESAMs are inherently slow and decreasing their recovery time is accomplished by providing carrier recombination centers [114] or by applying a sweep-out electrical field [115]. Lasers embedding fast saturable absorbers exhibit difficult starting of mode-locked operation owing to poor shaping of the long pulses present during laser startup.

In slow saturable absorbers, absorption recovery occurs on a time scale that is comparable to or longer than the pulsewidth of the laser. The pulses produced by mode-locked fiber lasers with slow saturable absorbers exhibit a trailing wing owing to the slowly recovering absorption. However, due to strong saturation of slow saturable absorbers even in the presence of long pulses, the mode-locking startup is facile [112]. It becomes clear that a good pulse quality, self-starting laser imposes contradicting requirements on the absorber. There exist several ways to overcome this limitation. For instance, soliton pulse shaping in a fiber cavity exhibiting negative average dispersion has been shown to generate pulses much shorter than the recovery time of the slow absorber used for mode-locking [116–117]. Pulsewidths of 13 fs were obtained from a laser mode-locked by a SESAM whose shortest recovery time was 60 fs (by carrier thermalization). In another approach, a dual-SESAM fiber laser having a slow and a fast absorber at either end of the cavity was suggested [118]. Placed at the end of properly designed dispersive segments of fiber, the SESAMS were simultaneously used for self-starting (slow SESAM) and pulse shaping (fast SESAM), respectively. The laser pulses were externally compressed to 135 fs.

The typical layout of a linear-cavity fiber laser mode-locked by a SESAM is presented in Fig. 2.19.

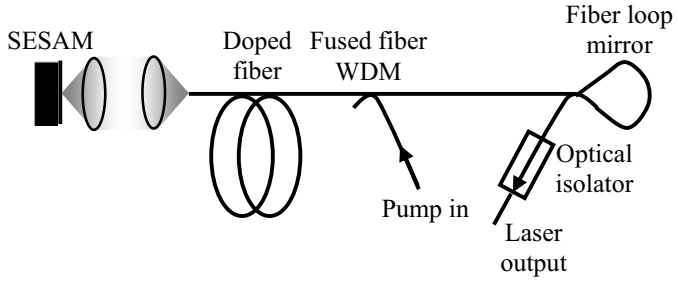

Fig. 2.19. Typical setup of a fiber laser mode-locked by SESAM.

The fiber cavity is delimited by the SESAM mirror at one end and by a linear (short) fiber loop mirror at the other. The fiber loop mirror acts also as a broadband output coupler. An optical isolator is placed at the laser output to protect the laser from external reflections that may disturb the mode-locked operation. The laser is typically pumped by

a pigtailed semiconductor laser diode, selected according to the doped fiber absorption band. The pump power is coupled into the laser cavity by a fiber wavelength-division multiplexer (WDM), fusion-spliced to the gain fiber. For laboratory experiments, a lens system is employed to couple light to the SESAM structure. For applications requiring a more compact approach, the SESAM can be butt-coupled to the fiber cavity. In some spectral ranges of fiber lasers (1060 nm, for example), optical fibers exhibit large positive dispersion. The short pulse operation of fiber lasers is hindered by this dispersion regime. To overcome this problem, chromatic dispersion compensation modules are placed inside the laser cavity. These modules offset the average cavity dispersion to negative values, which enables soliton creation and thus short pulse operation of the laser. The quest for low loss, small-sized, all-fiber dispersion compensation modules that provide negative dispersion with minimal disturbance in laser operation and seamless integration with laser cavity is ongoing. A novel dispersion compensation module is reported in this thesis **[P2]**.

SESAM technology has proven very beneficial to fiber lasers. High performance fiber lasers using SESAM structures for mode-locking have been reported in nearly every wavelength range covered by doped fibers. Careful cavity optimization has led to fiber lasers with simple cavity layout producing pulses as short as 180 fs at 1550 nm, a range of particular interest to optical telecommunications [119]. At 1060 nm (a spectral range particularly useful to life sciences), a linear cavity mode-locked fiber laser that could be tuned over 50 nm has been reported [120]. The broad wavelength tuning range with little penalty on the pulse quality and output power of the laser, stands proof to the powerful combination between SESAM technology and the broad gain spectrum of doped fibers. The novel wavelength region of 2000 nm, recently made available to fiber lasers by the advent of Tm-doped fibers, received its first ultrafast member in 1996 [121]. Producing 190 fs pulses at 1900 nm, the reported SESAM mode-locked fiber laser opens up new possibilities in this spectral region.

2.3.3 Power scaling in fiber lasers

Mode-locked fiber lasers deliver high quality optical pulses with wide wavelength tuning capabilities, benefiting from the large gain of rare-earth doped fibers and the emerging SESAM technology. Many applications, however, require high optical power as added value to the existing fiber laser qualities. This section is devoted to discussing the means of producing high power ultrashort pulses using mode-locked fiber lasers.

2.3.3.1 High intracavity power lasers

A straightforward way of obtaining high power pulses is increasing the optical power circulating in the mode-locked laser cavity. Past its apparent simplicity, this method faces some challenging technical problems.

In the 1550 nm wavelength range, the intracavity power is limited by the onset of pulse breakup [122]. Such effects are an unavoidable consequence of energy quantization in the soliton pulses produced by mode-locked lasers in this wavelength range. Several ways to overcome this problem have been suggested. A linear lossy element (as opposed to the nonlinear saturable absorber) has been used to limit the pulse energy, and thus prevent pulse breakup [122]. Using SESAM technology, 2.3 nJ, 5.5 ps pulses have been achieved in a simple mode-locked Er-fiber laser. Over-saturating the SESAM has been shown to

be an important action towards preventing pulse instabilities [116] and adjusting the spot size of the laser beam on the absorber proved beneficial for high energy pulse generation [118]. An alternative approach to preventing pulse breakup is employing a positive-dispersion fiber-cavity. In this dispersion regime, pulses are non-solitonic and exhibit frequency chirp dictated by the cavity dispersion value. Increasing the energy of such pulses does not lead to pulse breakup. Moreover, the peak power of a pulse propagating in positive dispersion regime is lower than that of a soliton with equal energy, resulting in less spectral distortion by SPM effects. An Er-doped fiber laser passively mode-locked by a nonlinear loop mirror (NOLM) and exhibiting positive cavity dispersion has been used to generate 1 nJ, 100 fs pulses at 1550 nm [123]. Even though the pulse breakup problem has been alleviated by positive-dispersion laser-cavities, nonlinear effects still play a role in limiting the attainable pulse energy. In particular, SPM causes the spectrum of intense laser pulses to broaden and thus become unsuitable for spectrum-sensitive applications such as frequency conversion in nonlinear crystals. A novel type of doped optical fibers, called *large mode-area (LMA)* fibers alleviates the problem of nonlinearity in the laser cavity. Using a special refractive index profile, the core size (and implicitly the mode field area) of the fiber can be increased up to 30 μm [124], while preserving the output close to diffraction-limited. The special index-profile increases the bending losses of the higher order modes of the fiber and thus promotes the fundamental mode. Large-core fibers can host more rare-earth ions than standard fibers and thus higher gain per unit length of fiber is achievable [124]. In one experiment, a 20 μm core LMA Er-doped mode-locked fiber laser delivered 20 nJ pulses at 1550 nm [125]. High power fiber lasers also benefit from increased power pump modules. The output power of currently available single-mode pigtailed pump modules is limited to about 1 W. Cladding pumping techniques allow for multimode pump modules to be used while the single-mode operation of the laser is retained [126]. Special fibers (called *double-clad fibers* due to their special structure featuring two claddings – a signal cladding a pump cladding) are used in cladding-pumped systems. High cladding-pumping efficiency can be achieved by *side-pumping*, where light from the pump laser chip is coupled by means of a microlens to a groove etched in the fiber cladding [127]. Such a scheme has been used in a fiber laser mode-locked by a SESAM to obtain 1.2 nJ, 130 fs pulses at 1550 nm [128].

At 1060 nm (the operation wavelength of Yb-doped fiber lasers), single mode optical fibers exhibit positive dispersion. Therefore, pulse breakup does not constitute a power limiting issue. The average dispersion of the laser cavity can be easily tuned by employing dispersion compensation modules. However, SPM effects and available pump power continue to raise difficulties in the path of high power Yb fiber lasers. These limitations can be overcome by tuning the chromatic dispersion of the laser cavity and employing multimode pumping modules in suitable arrangements. Careful dispersion management combined with the high saturation value of the gain in Yb-doped fibers allows for very efficient systems, such as the one reported in [129], where 6 nJ, 50 fs pulses were obtained from an Yb-doped fiber laser mode-locked by nonlinear polarization rotation techniques. The amount of available pump power can be increased by employing cladding-pumping schemes. Using a custom-designed SESAM, an all-fiber cladding-pumped mode-locked Yb fiber laser has been demonstrated **[SP1]**. Operating in positive dispersion regime, the laser produced 63 nJ, 2.5 ps-long pulses. The pulses were externally compressed by a hollow-core photonic-bandgap fiber to 160 fs. Recently, a

novel type of LMA fiber based on photonic-crystal technology has been demonstrated [130–131]. Nearly transform-limited 100 fs, 7.4-nJ pulses with 54-kW peak power at 1550 nm were achieved from an Er-doped amplifier without employing chirped-pulse amplification techniques.

2.3.3.2 High power amplifiers

High intracavity-power fiber lasers are not the ultimate high-power tools. Their output power is eventually limited by the onset of optical damage of the SESAM and cavity elements. Moreover, increasing the intracavity power is often done at the expense of pulse quality. An alternative approach to obtaining highly energetic pulses from fiber systems is the use of oscillator-amplifier schemes, generally known as master-oscillator power-amplifier (MOPA) systems. In this approach, the oscillator produces low power pulses that are further amplified by an optical amplifier. The major advantage of such an approach is that the optimization of laser and amplifier systems can be carried out independently. Naturally, the fibers and technologies developed for intracavity power augmentation were also used for high-power amplifiers. Table 2.2 lists some of the achievements in the field.

Table 2.2. Milestones of high power ultrashort pulse technology.

Power mode	*Technology*	*Pulse energy (nJ)*	*Pulse width (ps)*	*Wavelength (nm)*	*Ref.*
Large intracavity power	SESAM, core-pumped fiber	2.3	5.5	1550	[122]
	Positive dispersion cavity	1	0.1	1550	[123]
	Intracavity LMA fiber	20	20	1550	[125]
	Side-pumped double clad fiber	1.2	0.13	1550	[128]
	Dispersion-managed Yb fiber laser	6	0.05	1064	[129]
	SESAM, double-clad fiber	63	2.5	1064	[130]
Power amplifier	Double clad fiber amplifier	640	10	1064	[135]
	Photonic crystal LMA amplifier	600	10	1064	[136]
	Chirped pulse amplification	1000	0.4	1064	[133]

A solid limit for optical power in amplifier systems is imposed by fiber nonlinearities. Nonlinear effects in fiber amplifiers lead to spectral broadening of the amplified pulses. A special technique to alleviate such issues relies on modifying the temporal shape of optical pulses produced by the master oscillator by using optical elements with appropriate chromatic dispersion. The technique is called *chirped-pulse amplification (CPA)* in reference to its modus operandi [71]. The master oscillator pulse is initially stretched, typically several times over its transform-limited value. The resulting long optical pulse is amplified in the power amplifier. Given the long time span, the pulse accumulates energy without triggering nonlinear effects in the amplifier fiber owing to its low peak power value. After passing through the amplifier, the pulse is recompressed using a low nonlinearity pulse compressor with chromatic dispersion parameters opposite to those of the stretcher. Special attention must be paid so that the amplifier does not impose nonlinear chirp on the pulse, as nonlinear chirp cannot be removed by the pulse compressor. Using CPA techniques, 1 μJ pulses with peak powers in excess of 2 TW

have been reported in an Yb-doped fiber amplifier operating at 1060 nm [133]. The pulse stretchers and compressors used in CPA systems were traditionally pairs of diffraction gratings. Presently, the maturing photonic crystal technology allows for low nonlinearity, all-fiber pulse compressors [134].

3 Towards optimized all-fiber mode-locked lasers with broad wavelength selection

This chapter is concerned with the development of mode-locked lasers in all-fiber format suitable for short wavelength generation by frequency conversion. Aside brief literature reviews and theoretical considerations, the chapter consists of original work performed by the author and his collaborators. The work described aims at optimizing the fiber laser (regarded as a system) in terms of operation wavelength, pulsewidth, repetition rate controllability, and cavity setup in order to meet the requirements of nonlinear frequency conversion. Output power optimization is addressed in Chapter 4, as part of the frequency conversion process using nonlinear crystals.

3.1 Short wavelength mode-locked Nd-doped fiber laser

While the 980 nm to 1100 nm and the 1500 nm to 1600 nm spectral regions are well covered by mode-locked lasers, several applications requiring ultrashort pulses around 900 nm have difficulties in finding a suitable laser source. Intense laser radiation at 900 nm is particularly interesting as a starting point for blue light generation by frequency doubling. Powerful, compact blue-light sources are key tools for high density optical storage [137], LIDAR, and the emerging (red-green-blue) RGB laser displays. To date, blue light generation by frequency doubling has been performed using CW semiconductor laser diodes [138] or Q-switched lasers [139] delivering ns-long pulses. A source of ultrashort pulses in the blue range would be beneficial for applications requiring good temporal resolution and high peak power. A mode-locked laser is probably the ideal source of ultrashort pulses for frequency doubling. The well-established SESAM technology applied to mode-locked lasers allows for background-free, high-quality pulses and promises high conversion efficiency along with high quality of the frequency-converted output. Of the available laser gain media, Nd is the most eligible candidate for lasing around 900 nm. However, building a Nd-based laser for operation at 900 nm is not straightforward. As shown in Fig. 2.1, Nd exhibits two gain regions in close proximity, one centered at 900 nm and the other at 1060 nm. The 900-nm transition of Nd constitutes a 3-level laser system [64], whereas the 1060-nm band exhibits a 4-level behavior. This poses a great challenge to the laser designer, as the 1060-nm transition is more pump-efficient, exhibits no signal reabsorption, and thus has a low lasing threshold. In contrast, owing to the significant ground level population at room temperature, the 900-nm signal is reabsorbed and therefore the 900 nm transition requires a large amount of pump power to develop enough optical gain and sustain laser operation. An Nd-based laser system would naturally oscillate at 1060 nm, inhibiting the 900-nm emission. Operating such a laser around 900 nm requires special measures to prevent lasing at 1060 nm and provide enough pump power for the 900-nm transition to work. Nd-doped fibers are an excellent environment for such designs, as the good overlap between pump and signal modes and the long interaction length make it possible to extract enough gain even from a 3-level system. In addition, spectrally-selective fiber-couplers (WDMs) can be readily added to the cavity, enabling efficient filtering of the Nd gain spectrum and consequently precise selection of the lasing wavelength. Mode-locked

Nd-doped fiber lasers can overcome the problems associated with ultrashort pulse operation at 900 nm and thus constitute good candidates for practical and compact sources of ultrashort pulses in the blue range.
To investigate the mode-locking performance of Nd fiber lasers, a linear cavity laser has been assembled as shown in Fig. 3.1 **[P1]**.

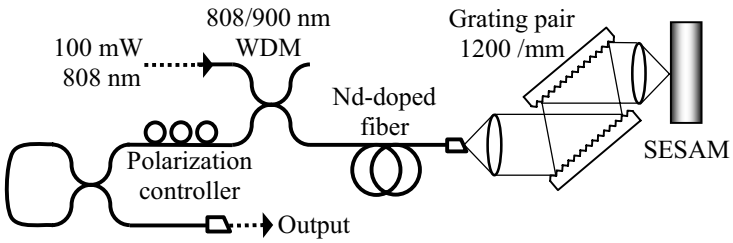

Fig. 3.1. Cavity layout of the Nd-based mode-locked fiber laser.
Mode-locking was initiated and sustained by a SESAM.

The laser cavity is similar to the typical fiber laser described in Fig. 2.19. The large positive dispersion of the fiber cavity is compensated by a pair of diffraction gratings inserted in the free-space section of the laser cavity. When properly aligned, the grating pair has a single-pass transmission of 75%. Besides providing dispersion compensation, the grating pair acts as a filter, enabling laser wavelength-tuning and filtering out the unwanted 1060-nm oscillation. In the proposed setup, the wavelength selective properties of both the WDM and the grating pair were sufficient to promote 900 nm lasing and suppress unwanted radiation at 1060 nm. The polarization controller compensates for stress birefringence in the fiber cavity. The output pulse duration exhibited a fair dependence on the polarization controller setting, which indicates that nonlinear polarization rotation played a role in pulse shaping. In the absence of a suitable isolator at 900 nm, an angle polished connector was used at the output of the laser to prevent deleterious back-reflections. The Nd-doped fiber is pumped by a single-mode pigtailed laser diode delivering 100 mW at 808 nm. The available pump power is the main limiting factor of the laser power output.

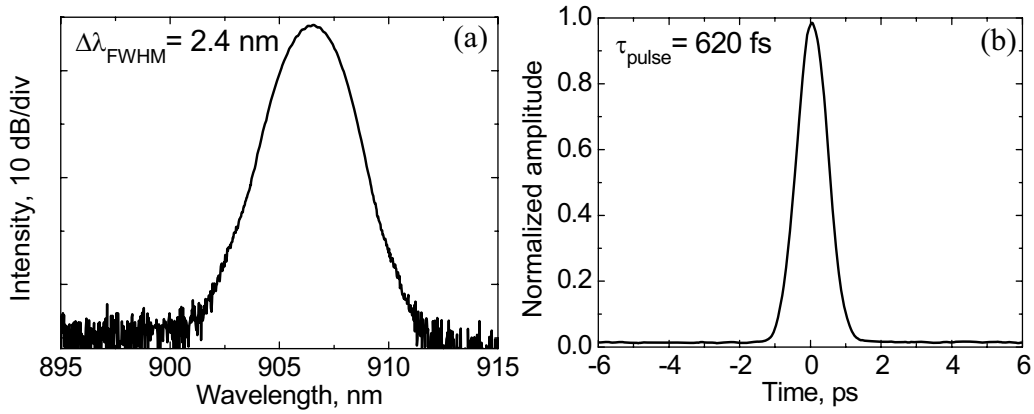

Fig. 3.2. (a) Output spectrum and (b) autocorrelation trace of the mode-locked Nd-doped fiber laser.

Special attention was paid to the manufacturing of the fused fiber WDM used as pump/signal combiner. The targeted operation wavelength of the laser (900 nm) is situated close to the cutoff of the LP_{11} mode of the optical fiber. Therefore, the fiber

fusing and tapering process in involved in coupler manufacturing have to be smooth and gradual to avoid microbends which would excite higher order modes [140]. For that purpose, a ceramic microheater with a uniform temperature distribution [141] was employed in a computer-controlled fiber drawing rig. The SESAM mirror was grown by MBE and its structure closely resembles the one shown in Fig. 2.17. A detailed description of the SESAM structure is given in **[P1]**. Upon proper optical alignment, the laser mode-locking is self-started and a stable train of pulses is produced. The optical spectrum and autocorrelation trace of the pulse (extracted from the laser through an 18 cm-long pigtail) are given in Fig. 3.2. The slight asymmetry of the autocorrelation trace is an artifact of the measuring instrument.

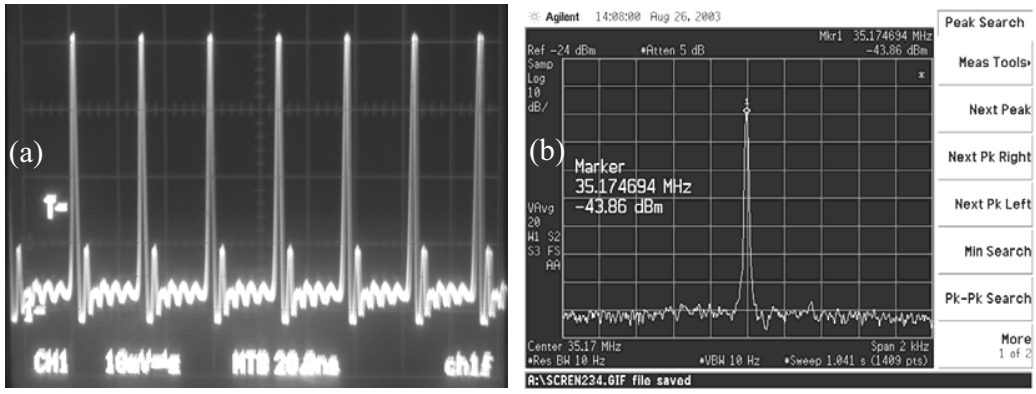

Fig. 3.3. (a) Pulse train and (b) RF spectrum of the mode-locked Nd fiber laser.

The average output power of the laser was 1 mW, yielding no nonlinear spectral broadening of the pulse in the output pigtail. Based on the laser spectral width and the estimated fiber dispersion (30 ps^2/km), the pulsewidth at the output of the laser (before the pigtail) was inferred to be 360 fs, corresponding to a time-bandwidth product of 0.32. The pulse is thus nearly transform-limited, assuming a sech shape (Table 2.1). Figure 3.3(a) shows the train of mode-locked laser pulses obtained with a high-bandwidth analog oscilloscope. To ascertain the repetition rate stability, the RF spectrum of the pulse train detected by a 1 GHz photodiode was measured with a resolution of 10 Hz. The clean, sharp RF peak at the repetition rate of the laser (shown in Fig. 3.3(b)) confirms the low interpulse jitter.

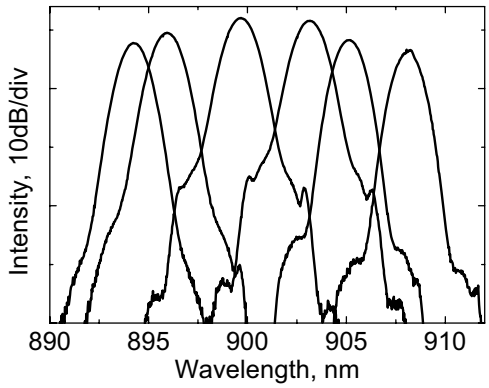

Fig. 3.4. Sequential spectra of the tunable mode-locked Nd fiber laser.

By tilting the diffraction gratings, the laser was continuously tuned from 894 nm to 909 nm while preserving the clean mode-locked operation and the spectral width, as shown in Fig. 3.4.
By increasing the available pump power, Nd-doped fiber lasers could challenge the Ti:Sapphire technology in this wavelength range.

3.2 Dispersion compensation in all-fiber format

Owing to the large peak power of the pulses circulating in a mode-locked laser cavity, self-phase modulation (SPM) effects play an important role in laser operation. Above a certain threshold, SPM effects become deleterious and lead to pulse broadening and temporal instability [117]. In the particular case of sub-picosecond pulses, SPM effects influence pulse parameters even at low intracavity powers. This constitutes a serious limitation for the output power of mode-locked lasers. Operating the lasers in a long pulse regime alleviates the problem; however such long pulses need to be compressed externally, which adds more optical elements to the setup thus increasing the complexity of the cavity. It has been shown that, in combination with the proper amount of chromatic dispersion, SPM effects in a laser cavity can be tamed and even used to generate shorter pulses. This particular regime is called *soliton mode-locking* and is associated with high quality optical pulses. In soliton mode-locking, the pulsewidth is the result of an interplay between pulse peak power and cavity dispersion. For a long time it was believed that short mode-lock pulses can only be achieved by using fast saturable absorbers (such as nonlinear polarization rotation [97]) or a complex interplay of slow saturable absorber and gain saturation (as in the case of dye lasers [142]). Soliton mode-locking proved the contrary, as pulses much shorter than the response time of the saturable absorber can be generated in this regime [77]. In SESAM mode-locking, soliton pulse stabilization by slow semiconductor saturable absorbers was used to generate 300 fs-long pulses using a 10 ps absorption recovery time SESAM [143, 144]. Soliton pulse mode-locking is especially attractive for mode-locked fiber lasers, in which dispersion and nonlinearity are evenly distributed throughout the fiber cavity.
Fiber lasers operating in the 1310 nm region and beyond are by nature soliton lasers, since standard single-mode fibers exhibit negative dispersion in this spectral range. However, the situation is more complicated for Yb-based fiber lasers operating around 1060 nm. In this spectral range, optical fibers exhibit significant positive dispersion and soliton pulses are not directly supported. As discussed in Chapter 2, the problem is solved by adding a dispersion compensating module to the cavity. The module should have enough negative dispersion to compensate for the entire fiber section of the cavity. Traditionally, dispersion compensation is achieved by a pair of fused-silica prisms [145] or diffraction gratings [146, 147]. Obtaining enough negative chromatic dispersion to compensate a typical fiber laser cavity requires the fused silica prisms to be placed several meters apart, which makes the use of prism pairs impractical. Grating pairs offer much larger negative dispersion for a small separation distance and are commonly used in laboratory versions of fiber lasers. However, grating pairs are polarization dependent and difficult to align, which makes them less attractive for compact lasers intended for maintenance-free operation. Moreover, both gratings and prisms are bulky optical elements and consequently incompatible with compact all-fiber lasers. Recently, the use of Gires-Tournois interferometers (GTIs) as intracavity dispersion compensators has been

suggested [148]. GTIs are also bulk optical devices and have a narrow operating bandwidth given by the resonance of the structure. However, easy integration with SESAM mirrors [149] makes GTIs attractive for fiber laser technology. In another approach, the extraordinary properties of photonic-bandgap fibers can be trimmed to obtain large negative dispersion at virtually any wavelength. Recent work [150] demonstrated intracavity dispersion compensation using photonic bandgap fiber in an all-fiber Yb-doped mode-locked laser. The inherently difficult fusion splicing between photonic crystal and single-mode fibers slows down the pace at which photonic crystal-based dispersion compensators enter the ultrafast laser field. Dispersion compensation, particularly in all-fiber format, continues to be of great interest to the field of mode-locked fiber lasers. The quest to find the ultimate dispersion compensation method is not, by far, over.

To overcome many of the issues associated with traditional dispersion compensation devices, a novel technique –based on single mode fiber tapers– has been proposed **[P2]**. Fiber tapers provide enough negative dispersion to compensate a short cavity fiber laser and can be losslessly integrated in the cavity by fusion splicing. Being made of standard single mode fiber, the insertion of a fiber taper in the cavity does not cause any disturbance to laser operation (back-reflections or higher order mode excitation). A fiber taper, whose fabrication and characterization are presented below, was successfully used to compensate dispersion in a mode-locked fiber laser, resulting in a simple all-fiber cavity supporting soliton pulses.

3.2.1 Fabrication and characterization of fiber tapers

A biconical fiber taper is manufactured by heating a short piece of optical fiber to the melting point and stretching it by pulling its ends in opposite directions. The resulting structure is a cylindrical waveguide with a smoothly decreasing diameter from that of the original fiber to the very thin region in the middle of the heated zone, as shown in Fig. 3.5. The length of the waist (thinnest portion of the taper) is roughly dictated by the extent of the heated zone.

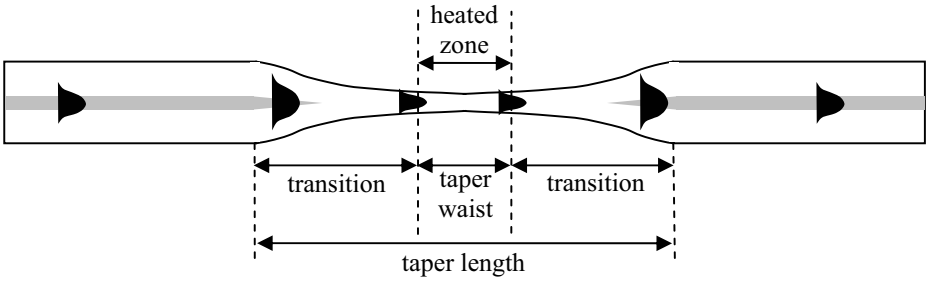

Fig. 3.5. Profile of a biconical fiber taper.

The key to the special properties of the fiber taper lies in the gradual change of the light guiding conditions within the transitions and the strong optical field confinement of the waist. Owing to the decreasing fiber diameter, the optical field detaches from the fiber core and spreads to the cladding boundaries, eventually being guided by the glass-to-air interface. The very strong guiding interface of the thin taper waist confines the optical field in an area much smaller than the original fiber core. The abrupt and large refractive index change of the waveguide creates a large amount of negative chromatic dispersion, whereas the large light intensity in the thin taper gives rise to strong nonlinear effects.

The region of interest in a fiber taper is the waist where the interesting dispersion and nonlinearity properties arise. Therefore, during taper manufacturing, one seeks to maximize the length of the taper waist and minimize the transitions.
The taper used in the experiments was manufactured using a "flame brush" technique [151]. A hydrogen-oxygen burner producing a small tip flame is swept across the fiber at a speed of a few millimeters per second, whereas the fiber ends are pulled apart at several micrometers per second. The heated zone is defined by the extent of the flame sweep. This procedure allows for accurate control of the heating and eliminates the need for an impractically wide heater. To minimize the length of the taper transitions and thus maximize the taper waist, a double stage fiber pulling fabrication method was employed. Initially, the fiber was tapered using a constant heated zone until the waist diameter reached about 10 μm. During this pulling stage, the fiber diameter varies as [151]:

$$d_1 = d_0 \exp\left(-\frac{x}{2L}\right), \tag{3.1}$$

where d_0 is the untapered fiber diameter, x is the taper extension (or pulling distance) and L is the heated zone length, identical to the flame sweep length. In the second stage, the heated zone length was increased at the same rate as fiber stretching [151]. This process results in extremely short taper transitions, as the amount of glass in the heated zone stays constant. For this pulling procedure, the reduction in taper waist diameter after n passes of the torch is [152]:

$$\frac{d_{n+1}}{d_n} = \sqrt{\frac{1-v/2u}{1+v/2u}}, \tag{3.2}$$

where u is the velocity of the torch scan, and v is the fiber stretching speed. Tight control over the manufacturing parameters results in tapers with long waists and short transitions. The 1.8-μm taper used in dispersion compensation experiments had a waist length of 13 cm and only 7 cm-long transitions. Upon fabrication, the tapers are promptly packaged in stainless steel or aluminum tubes and sealed with silicon rubber at the ends. Within the package, the tapers are surrounded by air. Using Eqs. (3.1) and (3.2), a computer program was designed to optimize the taper fabrication parameters.

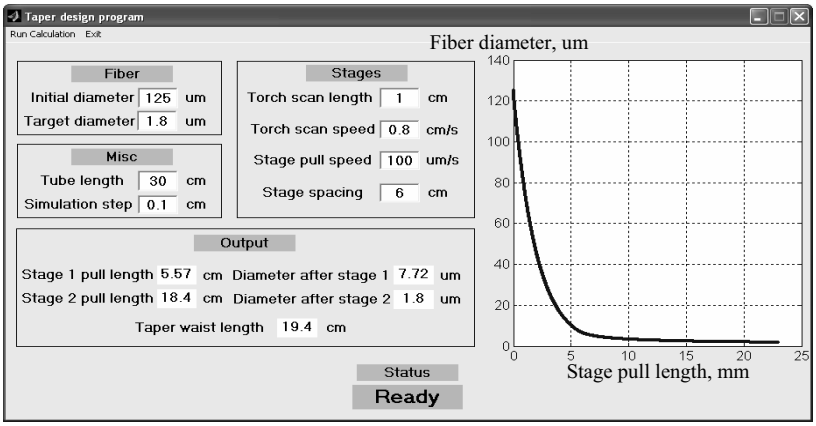

Fig. 3.6. Dual stage fiber taper design software.

The sole constraint on the taper is the length of the available packaging tube that dictates the taper length. The program determines the optimum switch point between the first and second pulling stages, ensuring that the taper waist length is maximized. The output of the program matches reasonably well with the data obtained during fabrication. Figure 3.6 shows a screenshot of the software interface. The tapers are fabricated on a computer controlled rig featuring two high precision translation stages for fiber stretching and a long-travel stage for hydrogen burner positioning. The fiber pulling data for the two stages is entered separately into the system and taper transmission at the targeted operation wavelength is continuously monitored. Using this method, taper waists as thin as 0.9 μm with losses of only 0.13 dB/cm can be obtained. It should be mentioned that more sophisticated fabrication methods have resulted in remarkably thin tapers (down to 0.28 μm) [152]. Such ultra-thin tapers, however, have little application in fiber lasers, owing to their large nonlinearity.

The chromatic dispersion of the fiber taper waist is determined based on the propagation constants of different wavelength signals in the taper, calculated by solving the eigenvalue equation for waveguides with cylindrical symmetry [153]:

$$\left[\frac{J_m'(ka)}{kJ_m(ka)}+\frac{K_m'(\gamma a)}{\gamma K_m(\gamma a)}\right]\cdot\left[\frac{J_m'(ka)}{kJ_m(ka)}+\frac{n_2^2}{n_1^2}\frac{K_m'(\gamma a)}{\gamma K_m(\gamma a)}\right]=\left[\frac{2m\beta(n_1-n_2)^2}{ak^2\gamma^2}\right], \tag{3.3}$$

with

$$\begin{aligned} k^2 &= n_1^2k_0^2-\beta^2 \\ \gamma^2 &= \beta^2-n_2^2k_0^2 \end{aligned}, \tag{3.4}$$

where $k_0=2\pi/\lambda$ is the wave vector, β the propagation constant of the wave in the waveguide, a the diameter of the waveguide core, n_1, n_2 the refractive indices of the core and cladding, respectively. m is a constant limited to integer values and commonly referred to as mode order. Symbols J and K represent Bessel functions and the prime sign denotes derivation in respect to the argument. Equation 3.3 is valid for any refractive index step and works for standard untapered fiber as well as thin tapers. The propagation constant β of a signal at a wavelength λ in a fiber defined by a, n_1, and n_2 was found by solving Eq. (3.3) numerically using a combination of bisection, secant, and inverse quadratic interpolation methods [155]. Once the propagation constant is known, the second order chromatic dispersion is readily obtainable by double differentiation in respect to the optical frequency ω ($\beta_2 = d^2\beta/d\omega^2$). Throughout the work, only the chromatic dispersion of the taper waist was calculated, thereby neglecting the chromatic dispersion of the taper transitions. This assumption is supported by the large amount of dispersion in the taper waist compared to the transitions and the relatively short transitions of the fabricated tapers. Despite the approximation, the results agreed well with the data gathered during experiments.

3.2.2 Dispersion compensation using fiber tapers

Benefiting from advanced simulation tools and technology, we investigated the fabrication of tapers suitable for intracavity dispersion compensation in mode-locked fiber lasers **[P2]**. For a range of tapers with different waist diameters, manufactured with

the method described in the previous section, the calculated chromatic dispersion and measured insertion losses at 1048 nm are shown in Fig. 3.7.

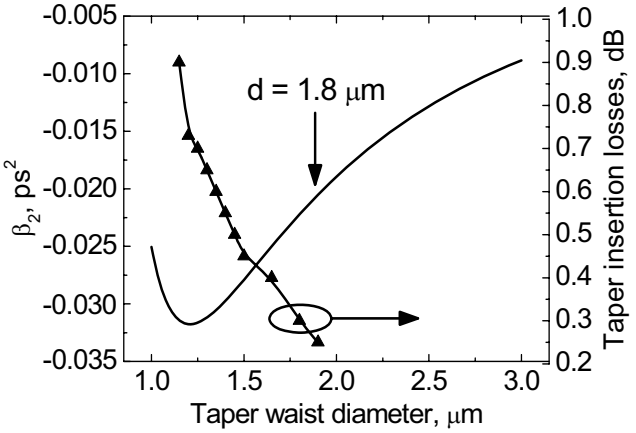

Fig. 3.7. Calculated chromatic dispersion and measured losses of tapers with a range of waist diameters at an operating wavelength of 1048 nm.

It can be seen that the largest negative dispersion is provided by the taper with a waist diameter of 1.2 μm. However, decreasing the diameter of the taper waist is accompanied by increasing insertion losses of the taper, owing to the small imperfections in the taper waist and prolonged exposure of the optical fiber to the intense heat of the hydrogen burner. To avoid mode-locking problems associated with lossy cavities, we settled for a taper with a waist diameter of 1.8 μm which constitutes a good compromise between chromatic dispersion value and insertion losses. Fig. 3.8(a) shows the profile of the fabricated taper measured with a high magnification (100X) optical microscope. The transmission spectrum of the taper obtained from a broadband white light source is shown in Fig. 3.8(b), along with the measured chromatic dispersion of the taper.

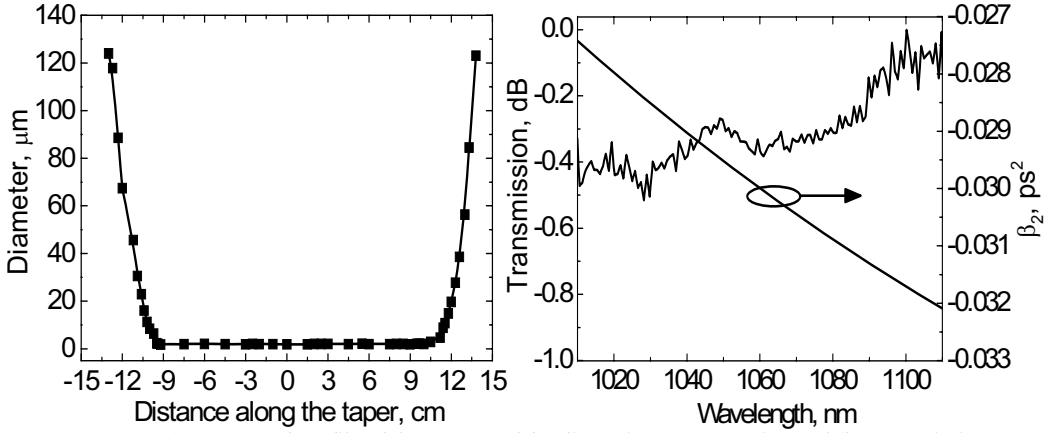

Fig. 3.8. (a) Measured profile of the taper used for dispersion compensation and (b) transmission spectrum and chromatic dispersion of the same taper.

To evaluate the dispersion compensation performance of the manufactured taper, a mode-locked fiber laser in linear-cavity configuration has been assembled shown in Fig. 3.9.

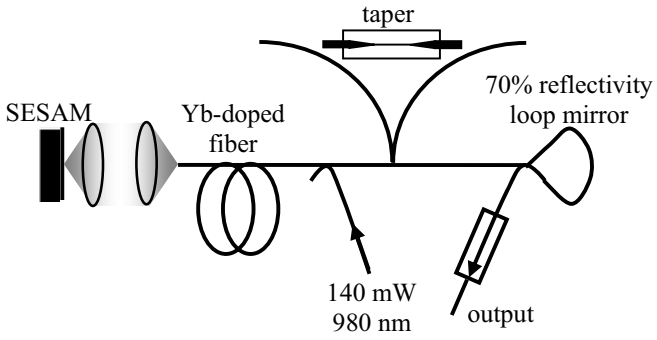

Fig. 3.9. Cavity setup of the mode-locked fiber laser using a fiber taper as dispersion compensator.

The laser is essentially similar to the one described in Fig. 2.19. The taper was inserted and removed from the fiber section of the cavity without disturbing the optical alignment of the SESAM mirror. Upon taper insertion, the only change experienced by the laser cavity was the average cavity dispersion switching from positive to negative. The experiment was carried out in two distinct phases to emphasize the influence of the taper on the laser operation. The laser was initially mode-locked without dispersion compensation. As expected, the laser produced long pulses with an optical spectrum exhibiting the flat-top shape characteristic to mode-locked operation in a positive dispersion regime and shown in Fig. 3.10(a). The taper was subsequently inserted in the laser cavity in the position shown in Fig. 3.9. The negative dispersion of the taper is large enough to offset the average cavity dispersion to negative values and the laser now operates in soliton pulse regime, as confirmed by the spectral side-bands, evident in Fig. 3.10(b). Autocorrelation traces of the pulses produced by the laser without and with dispersion compensation are shown as insets in the spectra plots. The small effective reduction of the output pulsewidth in soliton regime operation is caused by the large positive dispersion of the output fiber (loop mirror and isolator pigtails) that imposes a large chirp on the pulse.

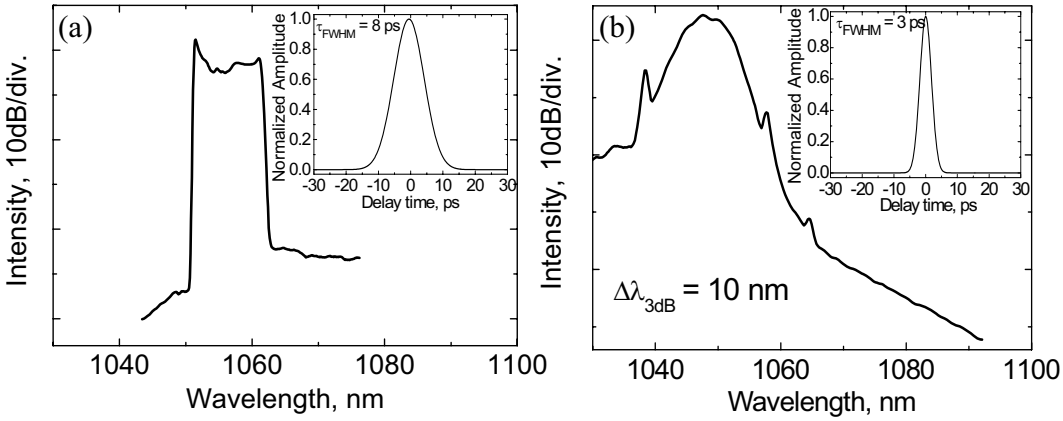

Fig. 3.10. Optical spectrum and autocorrelation traces of the mode-locked laser without (a) and with (b) dispersion compensation.

The large nonlinear coefficient of the fiber taper was not found to have any deleterious effects on the laser operation. The intracavity power (~ 6 mW) was low enough not to

trigger significant nonlinearities in the taper. Using much larger peak powers, the fiber taper can be turned into an efficient nonlinear medium, as discussed in Chapter 5.
With improvements in reliability and packaging, single-mode fiber tapers may become a serious candidate for all-fiber dispersion compensation in short cavity ultrafast fiber lasers.

3.3 Synchronization of mode-locked lasers by cross phase modulation in optical fibers

Timing and synchronization of ultrashort pulse lasers are key operations in applications addressing time domain processes. A laser system delivering ultrashort pulses at a stable rate is a priceless tool that enables accurate control of the experiment time scale, such as optical sampling and on-board optical clocking. Unfortunately, the timing accuracy of free-running mode-locked lasers is adversely affected by environmental changes (temperature fluctuations, cavity drift, mechanical vibrations, pump power variations), and intrinsic noise sources (variations of the lasing wavelength, amplified spontaneous emission). Laser timing can be done by locking the laser repetition rate to an external, accurate clock source (usually electronic). Timing of mode-locked lasers is traditionally achieved by active mode-locking methods, such as control of the laser cavity length [155], phase modulation in optical fibers [156], or gain modulation in semiconductor lasers [157]. Less progress has been recorded in *timing passively mode-locked lasers*, owing to the lack of a suitable control mechanism in such lasers. Cavity length adjustment with electronic feed-back has been used for synchronization of a passively mode-locked laser to an external clock, with inherent speed and flexibility problems [158].
Several applications such as pump-probe experiments and sum frequency generation by nonlinear interaction require direct *temporal synchronization of two passively mode-locked lasers*. Temporal synchronization of two passively mode-locked oscillators has been implemented using active control of the cavity length driven by the drift of the lasers' repetition rates. The error signal is supplied by balanced frequency mixers [159], balanced cross-correlators [160], or phase locked loops (PLLs) [161]. Albeit notable performance, these methods suffer from low tracking bandwidth (the maximum drift in the repetition rate of the laser that the system is still able to synchronize) and high complexity.
A special class of synchronized passively mode-locked lasers is constituted by *two-color sources*. A two color laser produces two synchronized trains of pulses at two different wavelengths, being a useful tool for pump-probe experiments and spectroscopy. Temporal synchronization between the two pulse trains is essential for applications. Two color laser sources have been implemented in Ti:Sapphire technology, providing stability and relatively broad wavelength tunability. Synchronization of the pulse trains was accomplished by tuning the cavity dispersion [162], gain interaction [163], cross-phase modulation [164], and Kerr interaction [165].
In terms of timing and synchronization, fiber lasers are a special case. The fiber embedded in the laser cavity constitutes a major source of noise to the laser repetition rate due to enhanced thermal interaction with the environment and stress-induced birefringence. In addition, cavity length control by mechanical means is not possible in all fiber systems owing to the lack of a freely-movable mirror. However, fiber lasers do

have a positive side. Nonlinear effects and stress-induced birefringence in optical fibers are readily available, providing efficient mechanisms for laser repetition rate control. By assembling two fiber lasers in close environmental contact, the inter-laser drift is eliminated and a simple synchronization system based on cavity length adjustment is possible [166]. Such lasers are said to be environmentally coupled. In another approach, two passively mode-locked fiber lasers were synchronized by employing a special cavity design, embedding an acousto-optical modulator and a diffraction grating [167]. Neither of these synchronization schemes is simple or easily implemented in all-fiber lasers.
Cross-phase modulation (XPM) in optical fibers provides a powerful solution to altering the repetition rate of a mode-locked fiber laser and thus achieving temporal synchronization with a clock source. The following section reports on the use of XPM in optical fibers to achieve both timing and synchronization of mode-locked fiber lasers. Employing the strong phase modulation mechanism offered by XPM, we achieved robust synchronization between two mode-locked fiber lasers in a master-slave cavity configuration **[P3]**, synchronized a mode-locked fiber laser to an external electronic clock **[P4]**, and realized a two-color source emitting pulse trains at very dissimilar wavelengths **[P5]**. The demonstrated systems are suitable for all-fiber integration.

3.3.1 Theoretical considerations

This section provides a brief theoretical account on how XPM can cause two ultrashort pulse sources to interact. In all that follows we shall consider two short (200 fs – 10 ps) pulses having different wavelengths and co-propagating in a single mode optical fiber. The refractive index experienced by one of the propagating pulses can be expressed as [214]:

$$n = n_0 + \Delta n_j \approx n_0 + n_2\left(\left|E_j\right|^2 + 2\left|E_{3-j}\right|^2\right), j = 1,2\,, \tag{3.5}$$

where n_0 is the linear refractive index, n_2 is a nonlinear parameter and $\left|E_j\right|^2$ is the power of the pulse j. Thus, the pulse propagates through a medium whose refractive index is altered by the pulse itself (SPM) and by the co-propagating pulse (XPM). Equation 3.5 shows that applications requiring efficient XPM are relatively safe from the deleterious influence of SPM, since XPM is twice as efficient as SPM and thus dominates the nonlinear effects.
The propagation of a light pulse in optical fiber can be mathematically described by considering the influence of chromatic dispersion and optical nonlinearity on the pulse shape and spectrum, in a propagation differential equation of the form [214]:

$$\frac{\partial A}{\partial z} + \beta_1\frac{\partial A}{\partial t} + \frac{i\beta_2}{2}\frac{\partial^2 A}{\partial t^2} + \frac{\alpha}{2} = i\gamma\left|A\right|^2 A\,, \tag{3.6}$$

where z and t are the distance along the fiber and time coordinates respectively, A is the slowly varying pulse envelope, α relates to fiber losses, and β_1, β_2 are the first and second order chromatic dispersion parameters. The nonlinear factor γ is defined as:

$$\gamma = \frac{n_2\omega_0}{cA_{eff}}\,, \tag{3.7}$$

with ω_0 the carrier frequency and A_{eff} the effective mode area of the propagating pulse. An optical pulse is uniquely defined by its time-dependent complex envelope A. The pulse spectrum is related to its temporal shape by Fourier transformation. Following propagation through a known optical fiber (defined in terms of losses, chromatic dispersion, and nonlinearity), the time and spectral shapes of an input optical pulse can be found by solving Eq. (3.6). Equation (3.6) is very flexible in that it allows the inclusion of multiple dispersion and nonlinear phenomena, as long as they are expressed in a form compatible with the terms depicted in Eq. (3.6).

The behavior of two co-propagating optical pulses that interact through XPM can be modeled by modifying the nonlinear right-hand term of Eq. (3.6) to reflect the changes that each pulse imposes on its pair. The result is a set of coupled equations of the form:

$$\begin{aligned}\frac{\partial A_1}{\partial z}+\beta_{11}\frac{\partial A_1}{\partial t}+\frac{i\beta_{21}}{2}\frac{\partial^2 A_1}{\partial t^2}+\frac{\alpha_1}{2}&=i\gamma_1\left(\left|A_1\right|^2+2\left|A_2\right|^2\right)A_1\\ \frac{\partial A_2}{\partial z}+\beta_{12}\frac{\partial A_2}{\partial t}+\frac{i\beta_{22}}{2}\frac{\partial^2 A_2}{\partial t^2}+\frac{\alpha_2}{2}&=i\gamma_2\left(\left|A_2\right|^2+2\left|A_1\right|^2\right)A_2\end{aligned}. \tag{3.8}$$

The subscripts 1 and 2 indicate which pulse the equation refers to. The interaction of the two pulses is expressed in the right-hand term of Eq. (3.8) in a manner similar to Eq. (3.5). For the particular case of fiber lasers, the losses α can be neglected due to the short cavity length and the set of equations 3.8 changes to:

$$\begin{aligned}\frac{\partial A_1}{\partial z}+\frac{i\beta_{21}}{2}\frac{\partial^2 A_1}{\partial T^2}&=i\gamma_1\left(\left|A_1\right|^2+2\left|A_2\right|^2\right)A_1\\ \frac{\partial A_2}{\partial z}+d\frac{\partial A_2}{\partial t}+\frac{i\beta_{22}}{2}\frac{\partial^2 A_2}{\partial T^2}&=i\gamma_2\left(\left|A_2\right|^2+2\left|A_1\right|^2\right)A_2\end{aligned}, \tag{3.9}$$

where

$$T=t-\frac{z}{v_{g1}}, \qquad d=\beta_{11}-\beta_{12}=\frac{v_{g2}-v_{g1}}{v_{g2}v_{g1}}. \tag{3.10}$$

The time T is measured in a reference frame traveling synchronously with one of the pulses. The parameter d quantifies the group velocity mismatch between the two propagating pulses. For a specified fiber, the evolution of the temporal and spectral shapes of two input pulses A_1 and A_2 can be investigated by solving the set of equations 3.9. The solution consists of a pair of pulses whose characteristics are dictated by fiber propagation and inter-pulse interaction. In the context of co-propagating pulses, an important parameter, called walk-off length (L_W), is defined as:

$$L_W=\frac{T_0}{|d|}, \tag{3.11}$$

where T_0 the width of one of the propagating pulses. L_W represents the length of fiber over which the pulses overlap temporally, therefore interacting by XPM. The walk-off length and the way it compares to the length of the propagation fiber play a seminal role in the performance of XPM systems and dictate the relative importance of SPM and XPM in practical systems.

The set of equations 3.9 can be solved analytically only in particular cases. A general solution, valid for any pulse and fiber parameters, can be found by using the split-step Fourier transform (SSFT) procedure [167]. A purposely-designed program has been implemented in MATLAB to simulate pulse propagation under the conjugated influence of chromatic dispersion, SPM, and XPM. In accordance to the SSFT philosophy, the program separates the chromatic dispersion and nonlinearity of the optical fiber and their influence on pulse propagation is treated separately. Once the fiber parameters are defined, the program calculates the spectral and temporal shapes of the pulses propagating through it. Switching back and forth between the time and spectral domains is accomplished via an adaptive fast Fourier transform (FFT) algorithm that reduces the large sized transformation in several sub transformations [169]. The improved speed allows for investigation of pulse propagation over long spans of fiber, with improved time and spectral resolution.

For a realistic evaluation of the XPM interaction effects in fiber lasers, the simulation program was fed a set of data consistent with the parameters of the laser systems used for experimental investigations. Picosecond-long pulses at 1060 and 1550 nm were co-propagated in a typical single-mode fiber (4.4 μm core diameter and 0.45% refractive index step). For both pulses, the group velocity and second order dispersion were calculated from Eq. (3.3). The resulting values are shown in Table 3.1 along other with relevant input data. The SSFT was implemented taking into account second order dispersion, SPM and XPM, as in Eq. (3.9).

Table 3.1. Input data for XPM interaction simulator.

		Pulse 1	**Pulse 2**	
Parameter name	*Symbol*	*Value*	*Value*	*Unit*
Wavelength	λ	1060	1550	nm
Peak power	P_{pk}	75	1000	W
Pulse width (FWHM)	τ	2	1	ps
Group velocity	v_g	$2.0513 \cdot 10^{-7}$	$2.0554 \cdot 10^{-7}$	nm/ps
Chromatic dispersion	β_2	$25.26 \cdot 10^{-12}$	$2.57 \cdot 10^{-12}$	ps^2/nm
Mode field diameter	MFD	6.2	9.9	μm
Nonlinear coefficient	γ	$4.31 \cdot 10^{-3}$	$1.15 \cdot 10^{-3}$	$W^{-1}m^{-1}$

As simulation testbed, we used a 1.5 m-long span of single-mode optical fiber of the type described above. For the particular fiber and operating wavelengths used in the simulation, the *d* parameter value was 9.7 ps/m, which yields a walk off length of 0.2 m based on the duration of pulse 1. Notably in Table 3.1, the pulses have very dissimilar peak powers. This choice is enforced by the goal of the work, namely synchronization of a mode-locked laser to a powerful master source. The synchronized, "slave" laser is typically weak and its influence on the master pulse characteristics is irrelevant. The "master"/"slave" terminology becomes fully transparent when the laser synchronization setup is revealed.

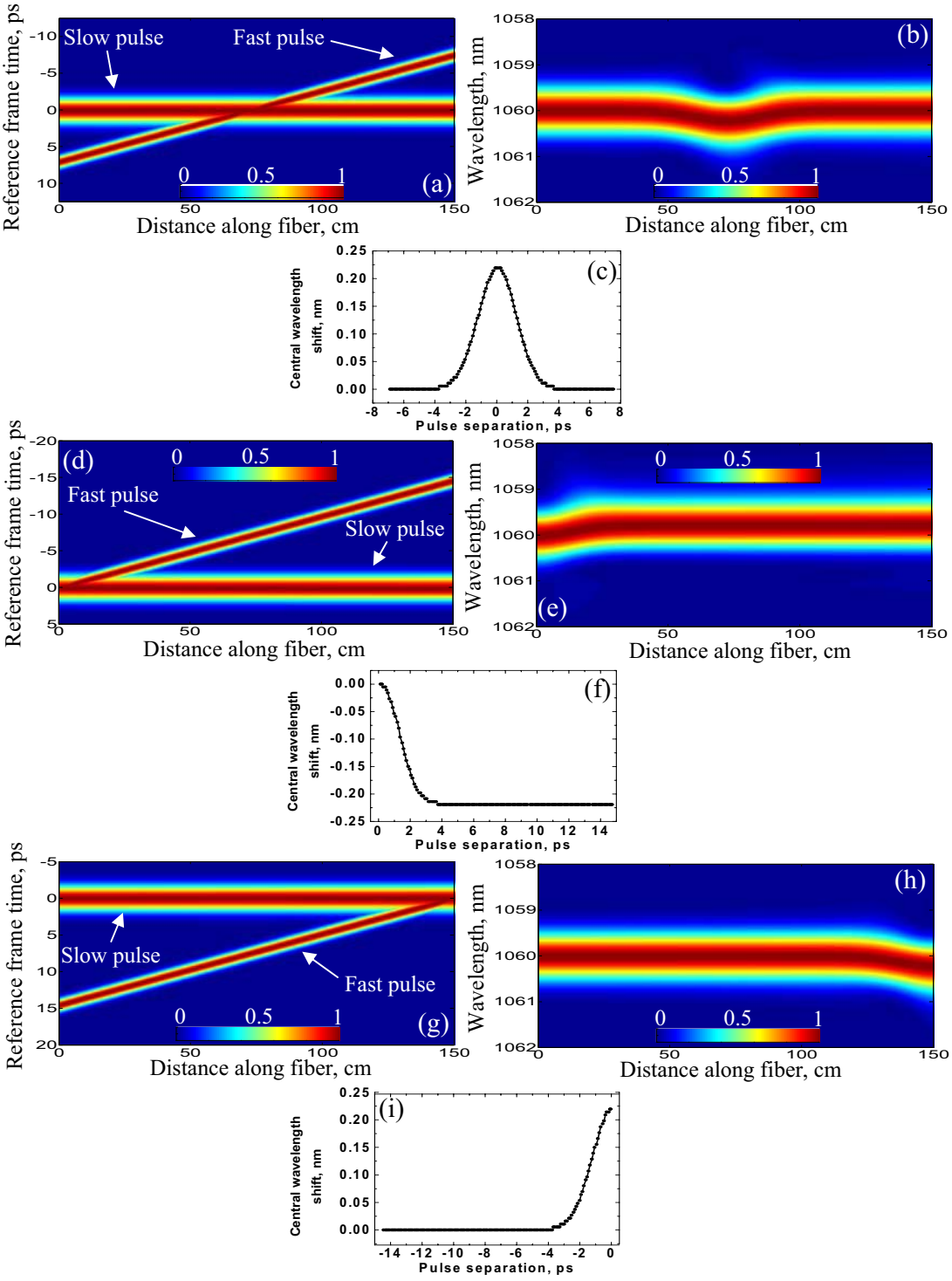

Fig. 3.11. Temporal and spectral evolution of two pulses interacting through XPM.
Case 1 – The fast pulse scans through the slow pulse (a, b, c),
Case 2 – The two pulses coincide at the beginning of the fiber (d, e, f),
Case 3 – The two pulses coincide at the end of the fiber (g, h, i).

Owing to dissimilar carrier frequencies, the pulses have different group velocities and thus propagate through the fiber at different speeds. This results in the faster pulse catching up with the slower and eventually overtaking it. From this perspective, the pulses are referred to as “fast” pulse and “slow” pulse. XPM interaction between the two optical pulses is analyzed in three distinct situations of great relevance to the laser synchronization experiments. Simulation parameters are identical in all three cases, the sole difference being the initial position of the fast pulse.

The first situation corresponds to the slow pulse being completely overtaken by the fast pulse, initially situated behind it. Figure 3.11(a) shows the evolution of the temporal pulses during propagation through the fiber. The corresponding optical spectrum of the slow pulse is shown in Fig. 3.11(b). Figure 3.11(c) reveals the shift of the slow pulse peak wavelength as a function of the temporal peak-to-peak separation between the fast and slow pulses. As the fast pulse catches up with the slow pulse, the optical spectrum of the slow pulse is shifted towards longer wavelengths; the opposite occurs as the fast pulse separates from the slow pulse. At the end of the interaction, the spectrum of the slow pulse is unchanged.

A second situation occurs when the pulse peaks coincide at the beginning of the propagation. As the pulses propagate down the fiber, the fast pulse decouples from its slow pair. The evolution of spectral and temporal shapes of the pulses is presented in Fig. 3.11(d–f). In this situation, the spectrum of the slow pulse is permanently shifted to shorter wavelengths. Owing to the low peak power of the slow pulse, no spectral distortion occurs when this pulse propagates alone in the fiber.

The third case corresponds to the pulse peaks overlapping at the very end of the propagation fiber. The characteristics of this case are plotted in Fig. 3.11(g–i). As in the second case, the spectrum of the slow pulse is permanently shifted, this time to longer wavelengths. The phenomena depicted in Fig. 3.11 have been experimentally investigated in [169]. By introducing a variable delay between the fast and slow pulses, researchers were able to record strong blue shift, red shift, or no shift at all in the spectrum of the slow pulse, depending upon the overlapping point of the pulses.

Several aspects of practical importance should be noted. In the presented simulation, the faster pulse was also assumed to be the most powerful. All results are perfectly valid if the slow pulse is more powerful than the fast one. The weak pulse will now catch up with the powerful pulse and the spectral shift presented in Fig. 3.11 occurs in the opposite direction, affecting the fast pulse spectrum. The magnitude of the spectral shift, however, is the same if all other simulation parameters are unchanged. Also, the two pulses involved in XPM interaction were considered co-propagating. It has been shown experimentally that XPM interaction is possible even if the pulses are counter-propagating. However, the interaction efficiency in such case is very low, owing to the short amount of time available for the pulses to interact. From a practical perspective, XPM interaction between counter-propagating pulses has little effect on laser synchronization.

3.3.2 Synchronization of mode-locked fiber lasers by cross-phase modulation

A simplified optical setup used for laser synchronization is shown in Fig. 3.12. The “master” pulse is typically more powerful and faster than the “slave”.

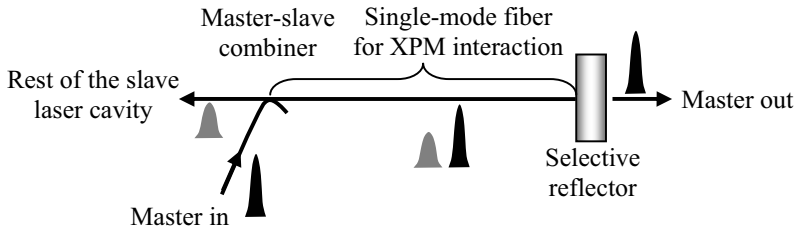

Fig. 3.12. Typical setup for mode-locked fiber laser synchronization.

Master pulses are seeded into the slave laser cavity by a dichroic fiber combiner, typically a fused fiber WDM. The XPM interaction fiber is part of the slave laser cavity and the selective reflector acts as one of the cavity mirrors. Upon arriving at the selective reflector, the master pulse is coupled out of the cavity while the slave pulse is back reflected and continues its trip through the laser cavity. XPM interaction takes place only in the shared span of fiber, whose length exceeds the walk-off length (L_W) of the two pulses. For consistency with the simulation results, we assume that the master (more powerful) pulse has a larger group velocity and thus propagates faster through the XPM fiber, and that the slave laser cavity contains only one pulse. The repetition rates of the master and slave lasers are brought close to each other by separate means.

At the beginning of the process, the two pulses propagate randomly through the XPM fiber until, due to asynchronism, the master pulse intersects the slave pulse. If the event occurs amidst the XPM fiber span, the spectrum of the slave pulse will be temporarily shifted, as described in Fig. 3.11, case 1. The slave laser operation is not affected by this type of interaction. The slight dissimilarity in the repetition rates of the lasers forces the pulse intersection point to migrate through the XPM fiber until the pulses overlap at one of the XPM fiber ends (cases 2 or 3 in Fig. 3.11). The spectrum of the slave laser is shifted in a permanent manner. At this point, the average dispersion of the slave laser cavity comes into play, as it translates the wavelength shift experienced by the slave laser into a variation of the group velocity of the pulse, effectively changing the pulse roundtrip time and thus the slave laser repetition rate. If the change in repetition rate brings the master and slave pulses closer together, the interaction proceeds until the slave laser spectrum is shifted enough to bring the repetition rates of the two lasers to equality. Conversely, if the mentioned wavelength shift causes the repetition rate of the slave laser to drift even further away from the master, random interaction will continue until the pulses meet at the opposite end of the fiber which will shift the slave laser wavelength in the right direction. In synchronized lasers, the master and slave pulses coincide either in the WDM combiner or at the selective reflector. The position of the overlapping pulses is dictated by whether the repetition rate of the slave laser was originally lower or higher than the master repetition rate.

Qualitatively, locking between two mode-locked lasers is possible when the repetition rates of the lasers are close enough for the pulses to be brought together by a relatively small change in the slave pulse spectrum. If the repetition rates are too dissimilar, XPM cannot produce enough amount of spectral shift to cause repetition rates to equalize. Once synchronized, the slave laser operates at the master repetition rate as long as external perturbations do not exceed the locking power of XPM. The chromatic dispersion of the slave laser cavity plays a seminal role in determining the locking bandwidth, as it relates spectral shift to group velocity change. As long as it does not hinder the operation of the

slave laser, large cavity dispersion improves the synchronization bandwidth. In conditions of large cavity dispersion, a small shift in the laser spectrum causes a large change in the group velocity of the slave pulse thus improving the locking capabilities of XPM.

The laser synchronization precepts presented above were applied in a series of experiments that confirmed the reliable and strong XPM interaction between co-propagating mode-locked laser pulses. The implementation that best mimics the described locking scheme is that of two synchronized mode-locked fiber lasers in a master-slave cavity configuration (and thus the terms "master" and "slave" pulses) **[P3]**. The setup is given in Fig. 3.13.

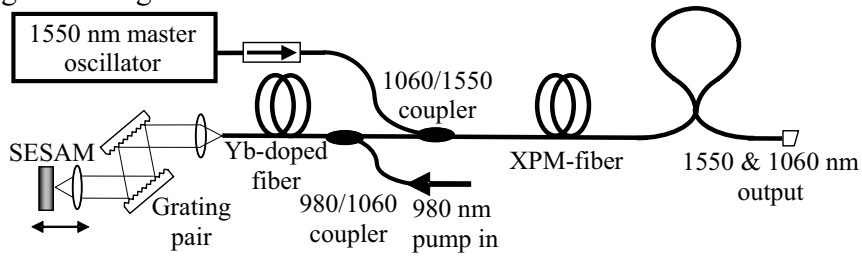

Fig. 3.13. Master-slave laser synchronization setup.

The slave laser cavity is a typical Yb-doped fiber laser in a linear cavity configuration, similar to Fig. 2.19 and producing 2 ps-long pulses at 1053 nm. The provisions for synchronization are evident on the right side of the cavity and consist of a 1060/1550 nm dichroic coupler, a 1.5 m-long span of single-mode fiber for XPM interaction, and a selective reflector. The loop mirror acts as a selective reflector, exhibiting 70% reflectivity at 1053 nm and high transmission at 1550 nm. XPM interaction takes place in the 1.5 m-long fiber spanning between the master/slave combiner and the loop mirror. The repetition rate of the slave laser can be adjusted by tuning the slave laser cavity length through a translation stage that changes the axial position of the SESAM mirror. The master laser is a compact and stable mode-locked Er fiber laser producing 1 ps-long pulses at 1550 nm. The peak powers of the master and slave pulses are 1 kW and 75 W, respectively.

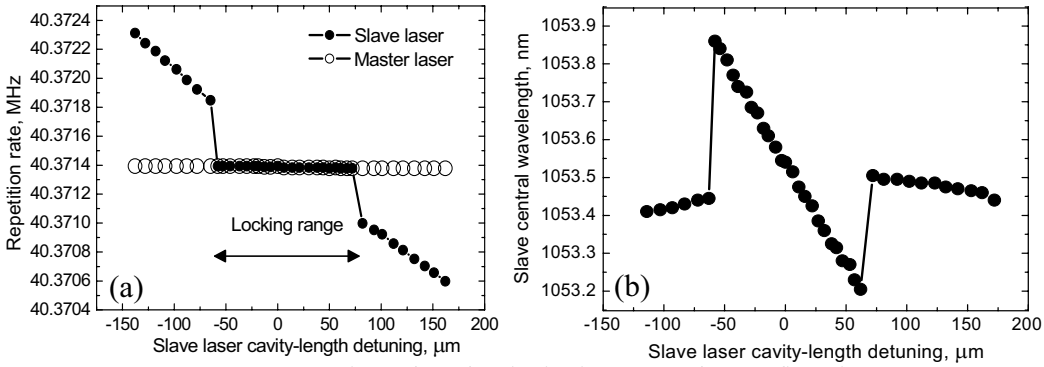

Fig. 3.14. Tuning and synchronization in a master-slave configuration.
(a) Repetition rate change and (b) spectral shift of the slave laser.

Upon switching on the master laser, the free-running slave laser is robustly synchronized to the more powerful master and the two oscillate in temporal coincidence. By continuously changing the slave laser cavity length, the laser is driven through the

synchronization band. Synchronization has been asserted by monitoring the slave laser repetition rate with the aid of a narrow-band RF spectrum analyzer. The tuning characteristics of the laser are shown in Fig. 3.14(a) and (b). The synchronization performance of the lasers is expressed in terms of maximum slave laser cavity detuning. Cavity detuning refers to changing the slave laser cavity length in respect to the optimal alignment (when the slave and master lasers exhibit precisely equal repetition rates). Outside the synchronization range, the laser repetition rare varies linearly with the amount of cavity detuning, as seen in Fig. 3.14(a). The synchronization (locking) range represents the largest change in the slave laser cavity length that does not cause loss of synchronism. Figure 3.14(b) shows the central wavelength of the slave laser during synchronization tests. As predicted by Eq. (3.11), the wavelength shifts proportionally with detuning in order to maintain the synchronization of the lasers. Synchronization is lost when the amount of cavity detuning requires a spectral shift beyond the capabilities of the XPM interaction. The recorded maximum spectral shift experienced by the slave laser (0.25 nm) matches well the value predicted by the simulation using similar pulses and fiber parameters. The synchronization stability has been tested by RF spectrum analysis, and the lasers have remained firmly synchronized for the entire 35 minutes duration of the experiment. Increasing the peak power of the master laser and the dispersion of the slave laser cavity improve the synchronization bandwidth.

Owing to the excellent overlapping between the master and slave modes, the optical fiber is an ideal synchronization environment. Using master pulse energies of only 1 nJ, an exceptionally large synchronization range of 140 μm has been obtained. These achievements exceed the performance of the systems reported to date. Synchronization between two passively mode-locked lasers has been achieved using XPM interaction in an optical fiber. The setup is robust and readily suitable for integration.

The very strong XPM interaction in single-mode optical fibers was employed to synchronize a mode-locked fiber laser to an external optical clock (optical clocking of a passively mode-locked laser) **[P4]**. The clock system is implemented using a 1540-nm telecom-grade diode laser, driven by a variable frequency pulse generator. The setup is shown in Fig. 3.15.

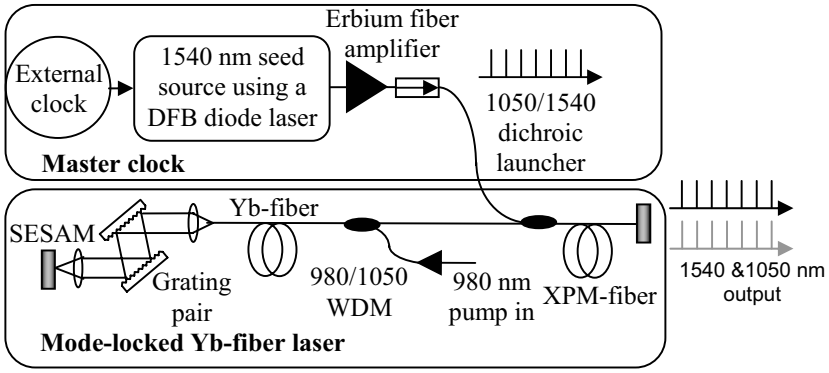

Fig. 3.15. Synchronizing a mode-locked fiber laser to an external clock by means of XPM interaction.

The signal from the telecom laser is amplified in an Er-doped fiber amplifier and coupled into the slave laser cavity by a dichroic coupler. The master clock source produces 100 ps-long pulses with 50 W of peak power. The slave source is a linear-cavity Yb-doped fiber laser, similar to the one depicted in Fig. 3.13, but operating at 20 MHz due to the

longer XPM interaction fiber (4 m). As in Fig. 3.13, the end reflector is selective and out-couples the master pulse. Owing to the low peak power of the master pulse, XPM interaction is much weaker. However, the long interaction fiber and walk-off length (L_W = 10 m), made XPM-driven synchronization possible. Owing to the weak interaction, the locking bandwidth is small and the slave laser cavity detuning test could not be performed. Laser synchronization was confirmed by monitoring the repetition rate of the slave laser with and without the master clock. Measurements were performed using a 10 Hz bandwidth RF spectrum analyzer and a 1 GHz photodetector. The results are presented in Fig. 3.16(a).

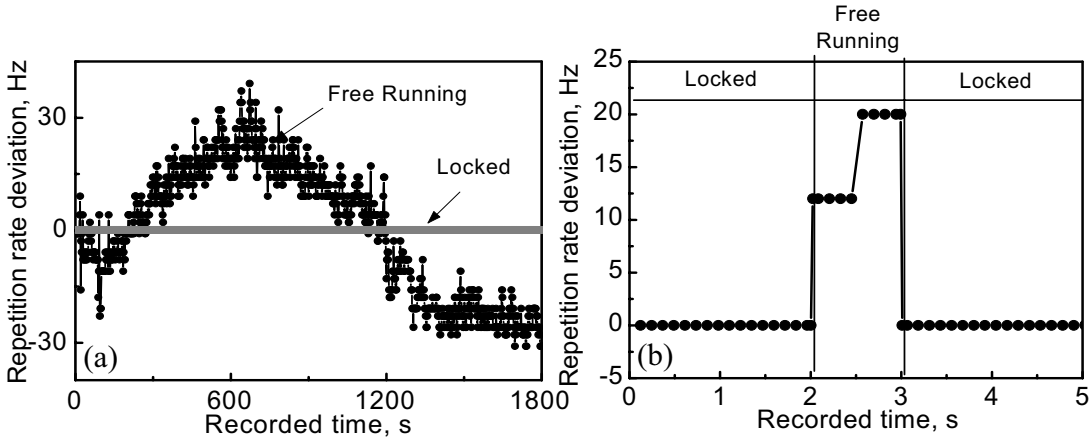

Fig. 3.16. Mode-locked fiber laser synchronized to an external clock. (a) Repetition rate and (b) re-acquiring of synchronization.

With the clock source turned off, the repetition rate of the slave laser changes continuously owing to thermal drift and mechanical vibrations of the cavity. In synchronized state, the slave laser operates at the repetition rate of the master clock and its fluctuations are below the resolution of the RF analyzer, resulting in a straight line in Fig. 3.16(a). By turning off the master clock laser, a temporary loss of synchronism is created. The slave laser is re-synchronized as soon as the master clock comes back online (Fig. 3.16(b)). The re-acquisition time was below the temporal resolution of our equipment.

Using state-of-the-art communication equipment, master clock pulses shorter than 100 ps can be generated. Such pulses should dramatically improve the performance of the proposed system. A gain-switched telecom laser diode producing 27 ps-long pulses was employed to synchronize an Er-doped fiber laser operating at 1550 nm, using an amplitude modulation scheme based on nonlinear semiconductor modulating mirror (SEMM) **[SP2]**.

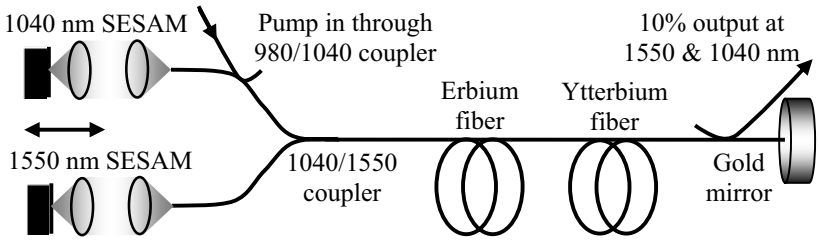

Fig. 3.17. Two-color laser source based on XPM interaction.

Using XPM interaction in a special cavity configuration, a two-color laser source has been assembled **[P5]** as shown in Fig. 3.17. The 1550-nm and 1040-nm lasers share a part of the cavity, including one end cavity mirror. The SESAM mirrors are the only separate components, owing to the very dissimilar operating wavelengths of the lasers. The lasers are pumped by a single 980 nm diode laser which reaches the doped fibers through the 1040/1550 nm dichroic combiner. System operation is based on the fact that the gain medium of each laser is transparent at the operating wavelength of the other, as seen from Figs. 2.2 and 2.3. This allows the two lasers to operate undisturbed in a shared cavity configuration. Moreover, the complete separation of the gain media prevents cross-gain modulation which may prove deleterious for XPM-based laser synchronization. Independent adjustment of the cavity lengths provides accurate control over the repetition rates of both slave and master lasers. All fiber components were manufactured "in-house" using a rig similar to the one depicted in 3.2.1. The 1550-nm laser produces 0.2-ps pulses with 2.6-kW peak power, whereas the 1040 nm laser pulses are 13 ps-long with a peak power of 40 W. Due to its shorter, more intense pulse, the 1550-nm laser was used as master laser. The walk-off length was 1.34 m, comparable to the cavity length. For the particular cavity arrangement in Fig. 3.17, the XPM interaction fiber, comprising both gain fibers and the output coupler pigtails, is traversed twice.

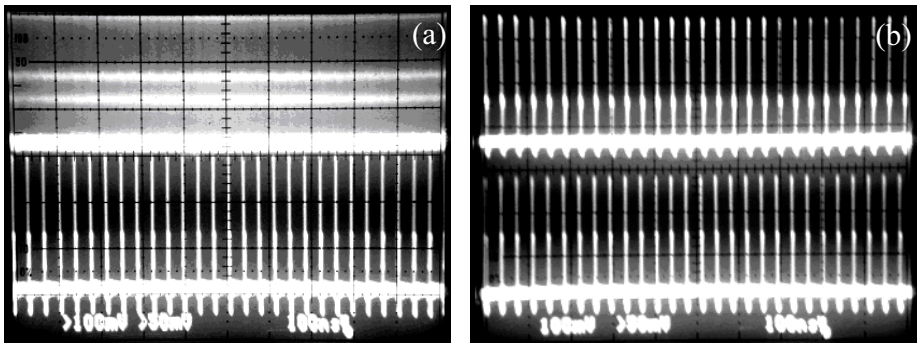

Fig. 3.18. Oscilloscope pattern of the two-color laser source in (a) free-running and (b) synchronized operation. The slave pulse train is displayed as the top trace.

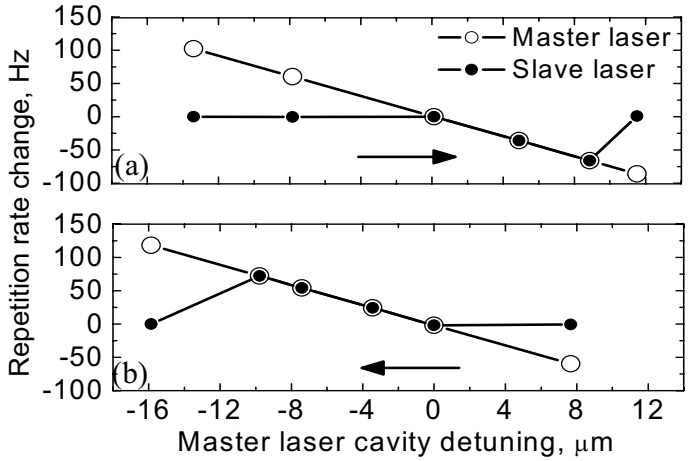

Fig. 3.19. Cavity mismatch test for a dual color laser based on XPM interaction. The arrow indicates the direction of slave laser cavity detuning.

The synchronization of the lasers was confirmed by displaying the pulse traces on an analog oscilloscope triggered by the master pulse. In the absence of synchronization, the slave pulse train cannot be clearly displayed on the scope. Once synchronization is achieved, the slave pulse train becomes stable. Both situations are shown in Fig. 3.18(a) and (b). The slave laser cavity mismatch test has been performed for the two color laser and the results are shown in Fig. 3.19, revealing a synchronization range of 18 μm. In accordance with the theory, the two pulses coincide temporally in the fiber dichroic splitter. However, the position of the extraction point in the cavity causes a constant amount of delay between the two-color output pulses. This deficiency could be corrected by using selective delay lines or by changing the position of the output coupler.

4 Frequency conversion in periodically-poled crystals

4.1 Fundamentals of frequency conversion

Frequency conversion is an essential step towards generation of ultrashort visible light pulses, being the process in which the pulses supplied by an infrared laser are converted into visible light pulses. This chapter addresses the main issues related to frequency conversion (particularly second and third harmonic generation) in nonlinear crystals. Several practical pump sources for frequency conversion experiments are described. Experimental results concerning second- and third-harmonic generation in custom-designed periodically-poled crystals starting from a 1060-nm pump laser are reported.

Frequency conversion is a very convenient method of generating novel wavelengths which are difficult or even impossible to obtain directly from lasers. In particular, visible light generation from mid and near infrared lasers has attracted a large amount of interest owing to its potential to replace the large and expensive gas laser systems dominating in this spectral range. Harmonic frequency generation was reported already in the early years of laser science [171–172]. Shortly thereafter, the chromatic dispersion of the nonlinear medium was identified as the main limiting factor to frequency conversion efficiency [173] and phase matching was suggested as an efficient way to overcome this hindrance [174]. The large interest raised by frequency doubling generated several early applications such as optical parametric oscillators [175]; however, it was not until the mid 80s that truly efficient nonlinear devices for frequency conversion were demonstrated [176].

The origins of frequency conversion can be understood by expressing the polarization of a material in the presence of an intense electric field as [177]:

$$P(r,t) = \varepsilon_0\left[\chi_1 E(r,t) + \chi_2 E^2(r,t) + ...\right], \tag{4.1}$$

where χ_n, $n=1, 2, ...$ is the susceptibility tensor. If the electric field is assumed to be of the form $E(r,t) = E(r)\cos(\omega t)$, Eq. (4.1) becomes:

$$P(r,t) = \varepsilon_0\left[\frac{\chi_2 E^2(r,t)}{2} + \chi_1 E(r,t)\cos(\omega t) - \frac{\chi_2 E^2(r,t)}{2}\cos(2\omega t) + ...\right]. \tag{4.2}$$

In Eq. (4.2) the material polarization receives contributions from the field itself (ω) as well as its harmonics (2ω, etc). If the term $\varepsilon_0 \frac{\chi_2 E^2(r,t)}{2}$ is large enough, a new wave oscillating at 2ω is generated in the material by the fundamental wave. The magnitude of the nonlinear interactions is determined by crystal structure and intensity of the fundamental wave.

In the simplified case of frequency doubling (only the second harmonic of the fundamental wave is generated), the material can be characterized by choosing a set of nonlinear coefficients d_{ij}, so that [177]:

$$\begin{bmatrix} P_X(2\omega) \\ P_Y(2\omega) \\ P_Z(2\omega) \end{bmatrix} = \begin{bmatrix} d_{11} & d_{12} & d_{13} & d_{14} & d_{15} & d_{16} \\ d_{21} & d_{22} & d_{23} & d_{24} & d_{25} & d_{26} \\ d_{31} & d_{32} & d_{33} & d_{34} & d_{35} & d_{36} \end{bmatrix} \times \begin{bmatrix} E_X^2(\omega) \\ E_Y^2(\omega) \\ E_Z^2(\omega) \\ 2E_Y(\omega)E_Z(\omega) \\ 2E_X(\omega)E_Z(\omega) \\ 2E_X(\omega)E_Y(\omega) \end{bmatrix}. \quad (4.3a)$$

This is the most general expression of the tensor d_{ij}. In most crystalline media, however, symmetry results in simpler forms of Eq. (4.3). For instance, in the case of lithium niobate ($LiNbO_3$), eq. 4.3 becomes [177]:

$$\begin{bmatrix} P_X(2\omega) \\ P_Y(2\omega) \\ P_Z(2\omega) \end{bmatrix} = \begin{bmatrix} 0 & 0 & 0 & 0 & d_{31} & -d_{22} \\ -d_{22} & d_{22} & 0 & d_{33} & 0 & 0 \\ d_{31} & d_{31} & d_{33} & 0 & 0 & 0 \end{bmatrix} \times \begin{bmatrix} E_X^2(\omega) \\ E_Y^2(\omega) \\ E_Z^2(\omega) \\ 2E_Y(\omega)E_Z(\omega) \\ 2E_X(\omega)E_Z(\omega) \\ 2E_X(\omega)E_Y(\omega) \end{bmatrix}. \quad (4.3b)$$

The optical axis is denoted by Z, whereas X and Y are the other two orthogonal axes of the 3D space. Table 4.1 lists some of the most commonly used crystalline materials for frequency conversion.

Table 4.1. Commonly used nonlinear crystals for frequency conversion (adapted from [177, 194]).

Commercial name	*Chemical formula*	*Nonlinear coefficient (pm/V)*	*Transparency range (nm)*	*Damage threshold (GW/cm^2)*
KDP	KH_2PO_4	$d_{36} = 0.38$ [194]	220–1500	0.2
LN	$LiNbO_3$	$d_{31} = -4.7$ [177]	400–5000	0.05
KTP	$KTiOPO_4$	$d_{36} = 5.7$ [177]	350–4500	1
BBO	β-BaB_2O_4	$\lvert d_{22}\rvert = 2.2$ [194]	190–3000	5

Of particular interest for the work in this thesis are KTP and LN, owing to their large nonlinearity and generous operating spectrum.
The efficiency of the frequency doubling process can be calculated as [177]:

$$\eta = \frac{P_{2\omega}}{P_\omega} = 2\left(\frac{\mu}{\varepsilon_0}\right)^{3/2} \frac{\omega^2 l^2 d_{eff}^2}{n^3} \frac{P_\omega}{A} \operatorname{sinc}^2\left(\frac{\Delta k l}{2}\right), \quad (4.4)$$

where P_ω, $P_{2\omega}$ are the powers of the fundamental and second-harmonic waves, l is the propagated length through the crystal, d_{eff} is the effective nonlinear coefficient (calculated from the d_{ij} tensor in Eq. (4.3)), $n^3 = n_\omega^2 n_{2\omega}$ is the refractive index, $\Delta k = k_{2\omega} - 2k_\omega$, $k_\omega = 2\pi n_\omega/\lambda_\omega$ is the wave-vector mismatch, and A is the interaction area between the pump and nonlinear medium. Equation 4.4 reveals some important aspects of practical interest. The second harmonic generation efficiency depends on the pump area A. Focusing the fundamental wave in the nonlinear medium can thus increase the amount of generated

harmonic radiation. If the fundamental wave is a Gaussian beam (as in most practical cases), some corrections should be applied to Eq. (4.4) in order to account for the limited focusing ability [178].

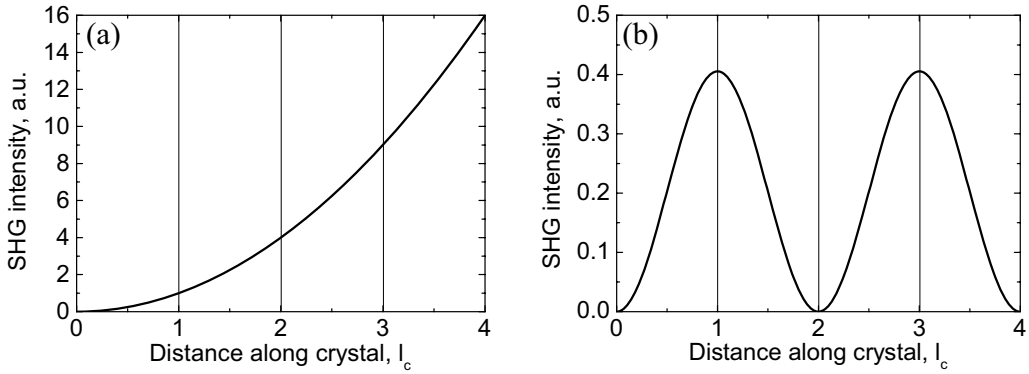

Fig. 4.1. (a) SHG intensity evolution in a crystal with birefringent phase matching and (b) without phase matching.

The optimum conversion efficiency is obtained when $\Delta k=0$, i.e. when the refractive index of the fundamental wave n_ω equals the refractive index of its second harmonic $n_{2\omega}$. The fundamental and the second-harmonic waves propagate in phase and are thus *phase-matched*. In this case, the second harmonic power builds up while traversing the crystal, as shown in Fig. 4.1(a). If the phase matching condition is not met, the phases of the second-harmonic wavelets generated throughout the crystal are different, causing destructive interference. The spatial coherence length of the fundamental and second harmonic waves is [177]:

$$l_c = \frac{\lambda_\omega}{4\left(n_{2\omega} - n_\omega\right)} = \frac{\pi}{\Delta k}\,. \tag{4.5}$$

Owing to interference between the second-harmonic wavelets, the intensity of the second harmonic radiation oscillates within the nonlinear medium and returns periodically to zero, as shown in Fig. 4.1(b).

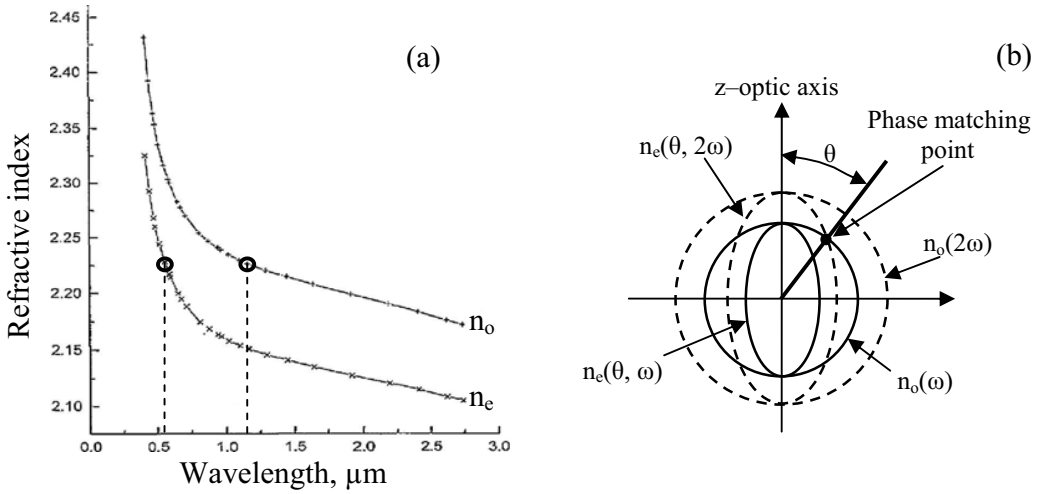

Fig. 4.2. (a) Ordinary and extraordinary refractive indices (after [177]) and (b) refractive index surfaces for LN.

Such an operation mode is far from optimum, as the generated second-harmonic radiation is periodically cancelled along the crystal. Therefore, highly efficient frequency conversion requires accurate phase matching between the fundamental and the second harmonic waves over a broad wavelength range.

Phase matching conditions will be detailed for the particular case of LN. Figure 4.2(a) shows the ordinary and extraordinary refractive indices for LN [177]. It can be seen that the ordinary refractive index of the fundamental wave at 1060 nm nearly equals the extraordinary refractive index of its second harmonic at 530 nm. This renders LN an almost ideal frequency doubler for this wavelength range, as the crystal's natural birefringence can be used for phase matching. Phase matching for longer wavelengths can be achieved in LN provided that the crystal birefringence is lowered, whereas a higher birefringence is required to achieve phase matching at shorter wavelengths. To a certain extent, tuning the crystal temperature can assist in changing its birefringence and thus the phase matching wavelength. The concept of phase matching is better illustrated in Fig. 4.2(b), which plots the ordinary and the extraordinary refractive indices within the crystal plane determined by the wave propagation vector and the optic axis of the crystal. Rotating the crystal by an angle θ, phase matching between the fundamental and the second harmonic can be achieved ($n_e(\theta, 2\omega) = n_o(\omega)$).

Despite its high theoretical efficiency, birefringent phase matching has several drawbacks of practical importance. In some crystals, birefringent phase matching over a broad wavelength range is difficult to obtain. Temperature tuning provides a limited degree of flexibility in the phase matching wavelength; however, the process is delicate and very slow. For several crystals (such as $LiTaO_3$) birefringent phase-matching is not possible at all (for any temperature) owing to the insufficient amount of birefringence exhibited by the material [179]. Moreover, since birefringent phase matching can only occur along certain axes, a select few d_{ij} parameters of the crystal (not necessarily the largest ones) are available for frequency doubling. This situation is particularly detrimental to $LiNbO_3$, as its largest nonlinear coefficient, d_{33}, is not available for birefringent phase matching [179]. The alternative, d_{31}, offers less nonlinearity and consequently poor conversion performance.

4.2 Quasi phase matching and periodic poling

The drawbacks of birefringent phase matching can be overcome by quasi-phase matching (QPM), illustrated in Fig. 4.3 [176, 177, 180].

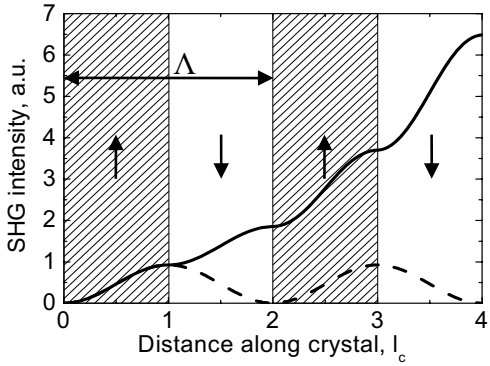

Fig. 4.3. SHG intensity evolution in a crystal with quasi phase matching.

QPM relies on repeated inversion of the relative phase between the fundamental and the second harmonic waves to prevent destructive interference between the second-harmonic wavelets. The falling segments of the "no phase matching" curve in Fig. 4.1(b) are thus replaced by rising segments in Fig. 4.3, owing to periodic zeroing of the phase mismatch. Fig. 4.3 shows the evolution of the second harmonic intensity in a crystal with QPM. The dashed line in Fig. 4.3 reproduces, for comparison, the evolution of the second harmonic light intensity inside an identical crystal with no phase matching. Although less efficient than birefringent phase matching, QPM yields significant improvement over the no phase matching case. The light domains in Fig. 4.3 show the regions where the nonlinear properties of the crystal have been altered (as opposed to shaded areas, where the crystal is pristine). A proper change in the nonlinear properties of the crystal causes the relative phase shift between the fundamental and second harmonic waves to change sign and thus the phase matching condition is preserved. In this manner, phase matching is ensured along the entire crystal without the assistance of birefringence. Such periodic alteration of the crystal nonlinear properties is referred to as *periodic polling*. It has been shown [180] that the most efficient QPM is obtained when crystal inversion occurs at every coherence length l_c as shown in Fig. 4.3. Periodic polling can be achieved by forming stacks of thin nonlinear crystal wafers, each wafer rotated by 180° in respect to its neighbor. The sign of the nonlinear coefficient d_{eff} changes in each portion of the stack, realizing the effect depicted in Fig. 4.3. However, for a large number of wafers, such a solution is impractical due to wafer-to-wafer thickness variations and intrinsic wafer alignment difficulty. In ferroelectric crystals, periodic polling can be achieved by forming regions with reversed spontaneous polarization (domains) [179–180]. The domains are created by applying a large electric field across a narrow region of the crystal, causing the crystal spontaneous polarization to change sign. Patterned electrodes are employed to create an alternation of inverted and non-inverted domains as seen in Fig. 4.3. An alternate solution for periodic poling is ion exchange in a chemical reaction [181]. This method enables simultaneous manufacturing of poled gratings and waveguides in a nonlinear crystal [182]. The polling period can be an integer multiple of coherence lengths. The situation described in Fig. 4.3 is called *first order QPM* since coherence length and poling period coincide. If the poling duty factor is 0.5, only odd order QPM occurs. Conversely, if the duty factor is different, even order QPM can be obtained. Compared to first order QPM, the efficiency of high order QPM is lower by a factor of $n^{-2}(4/\pi^2)$ [180], with n the QPM order.

QPM offers a number of advantages over birefringent phase matching. QPM can achieve phase matching in isotropic materials and in materials exhibiting too little or too much birefringence at the desired operating wavelength. In addition, QPM enables two waves with the same polarization to be phase matched, enabling the use of higher nonlinear coefficients. For example, in $LiNbO_3$, the d_{33} coefficient is accessible through QPM, with the result of enhancing nonlinear conversion efficiency [179]. By choosing the appropriate polling period (domain length), virtually any two wavelengths can be phase-matched at a given temperature. This allows $LiNbO_3$ to be used in second harmonic generation for wavelengths below 1000 nm, which was impossible using birefringent phase matching (as seen from Fig. 4.2(a)). The possibility of achieving phase matching at elevated temperatures is especially important for congruent $LiNbO_3$ whose performance power-wise is strongly limited by the *photorefractive effect*.

The photorefractive effect occurs in all ferroelectric materials and causes the refractive index of the crystal to change under the influence of an intense optical field. The refractive index change arises from the optically induced redistribution of charge carriers (electrons and holes). As electrons and holes are displaced, static charge builds up inside the crystal and the refractive index along the optical beam path is modulated. The photorefractive effect can be permanent and thus the crystal "memorizes" the input beam intensity. Several interesting applications of ferroelectric materials, such as holographic memory chips, emerged based on this peculiar characteristic [186]. For frequency-doubling applications, however, the photorefractive effect is deleterious, as it alters the phase matching condition $\Delta k = k_{2\omega} - 2k_{\omega}$ by virtue of refractive index change. The photorefractive effect can also disrupt the beam path inside the crystal, effectively shortening the interaction length.

The strength of the photorefractive effect can be diminished by increasing the crystal photoconductivity. This can be accomplished by operating the crystal at an elevated temperature [187–188]. The crystal is placed inside insulated enclosures heated by electrical elements. The fragile and often bulky heaters are one of the main limitations to manufacturing portable light sources based on frequency doubling. Moreover, heating and cooling of the crystal must be performed very slowly in order to avoid accumulation of static charge on the crystal surface and crystal breakage. An alternative way to achieve high photoconductivity is doping the ferroelectric crystal with magnesium [189]. This is regarded as a very promising way to suppress photorefractive effects in frequency conversion applications handling high optical power.

4.3 Performance assessment of periodically-poled crystals

QPM greatly relaxes the refractive index matching conditions required by birefringent phase matching. However, accurate overlap between the poling period of the crystal and the coherence length of the fundamental is instrumental to high conversion efficiency. Mismatch between crystal and fundamental wave parameters results in conversion efficiency penalty. This section analyzes the dependence of second harmonic generation efficiency on fundamental wave and crystal parameters. Acceptance bandwidths are defined for fundamental wavelength, crystal temperature, and input beam angle.

4.3.1 Input power variation

As shown by Eq. (4.4), the second harmonic generation efficiency depends linearly on the fundamental wave power and quadratically on device length. Increasing the total length of the crystal is an effective way to improve the conversion efficiency at a given input power. However, as shown below, long poled crystals suffer from several drawbacks, such as reduced wavelength acceptance bandwidth.

4.3.2 Fundamental wavelength variation

If the wavelength of the fundamental wave deviates from the value considered in crystal design, the crystal polling (constant) can no longer provide optimum phase matching between fundamental and second harmonic. A phase mismatch Δk arises as a result of fundamental wavelength variation. Assuming a device of length L designed for operation at a wavelength λ_O, the phase mismatch caused by the input fundamental wave at a wavelength λ_F (slightly different from λ_O) is [183]:

$$\Delta k(\lambda_F) = \frac{4\pi(n_{2\omega} - n_{\omega})}{\lambda_F} - \frac{2\pi}{\Lambda}, \tag{4.6}$$

where Λ is the period of the poled structure. The refractive indices of the crystal at the fundamental and second harmonic wavelengths (n_{ω} and $n_{2\omega}$) can be estimated from a Sellmeier-type equation [184]. The wavelength λ_{FWHM} of the fundamental radiation at which the conversion efficiency drops to half of its peak value can be found by solving the equation [183]:

$$\mathrm{sinc}^2\left[\frac{\Delta k(\lambda_{FWHM})L}{2}\right] = \frac{1}{2}. \tag{4.7}$$

The wavelength acceptance bandwidth of the crystal is [183]:

$$\delta\lambda_{FWHM} = 2(\lambda_{FWHM} - \lambda_O). \tag{4.8}$$

Figure 4.4(a) plots the wavelength acceptance bandwidth versus crystal length for a series of periodically-poled $LiNbO_3$ (PPLN) crystals with Λ = 6.54 μm, optimized for doubling of λ_O = 1.0632 μm at a temperature of 165°C.

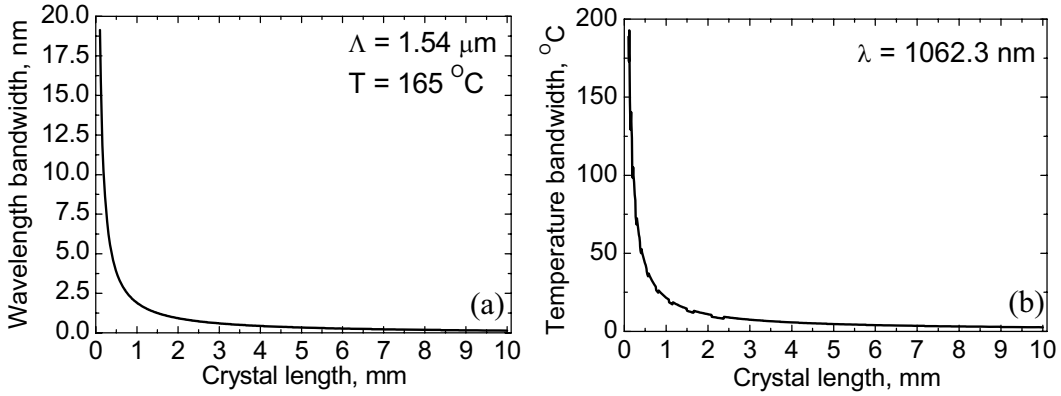

Fig. 4.4. Calculated (a) wavelength and (b) temperature acceptance bandwidths for a PPLN crystal.

4.3.3 Crystal temperature variation

Crystal temperature affects the second harmonic generation efficiency by two mechanisms: temperature-dependence of the refractive indices and thermal expansion of the crystal itself. The temperature-dependent refractive indices are well approximated by the temperature-dependent Sellmeier equation in [184]. Thermal expansion of the crystal causes the poling period Λ to change and adds an error factor to phase matching. The temperature-induced change in the crystal poling period Λ can be estimated as [183]:

$$\delta\Lambda = \alpha \cdot \Lambda \cdot \delta T, \tag{4.9}$$

where α is a temperature coefficient and δT is the temperature variation. For $LiNbO_3$, α = $1.54 \cdot 10^{-5}$ [185]. Similar to Eq. (4.6), the phase mismatch caused by the crystal temperature variation is:

$$\Delta k(T) = \frac{4\pi\left(n_{2\omega}(T) - n_{\omega}(T)\right)}{\lambda_F} - \frac{2\pi}{\Lambda(T)}. \tag{4.10}$$

The temperature acceptance bandwidth can be determined by the prescription in Eq. (4.7) and (4.8). Figure 4.4(b) shows the temperature acceptance bandwidth for the structure considered in Fig. 4.4(a).

4.3.4 Variation of the input beam angle

Angular acceptance of a periodically-poled crystal refers to the dependence of the second harmonic generation efficiency on the launch angle (in respect to the crystal normal direction). Tilting the input beam causes the poling period "seen" by the fundamental wave to change as [180]:

$$\Lambda \approx \Lambda_0 \cos(k-\nu)\left[1 + \frac{n_{2\omega} - n_{\omega}}{2n_{2\omega}} \tan^2(k-\nu)\right], \tag{4.11}$$

where the normal to the crystal makes an angle v with the fundamental wave vector and an angle k with the wave vector of the poled structure. The angular acceptance bandwidth is [180]:

$$\delta\nu \approx 0.886 \frac{\cos(\nu)}{\sin(k-\nu)} \frac{\Lambda}{L}. \tag{4.12}$$

The angular bandwidth is inversely proportional to the crystal length and has a maximum at normal incidence (v = 0). Angular acceptance bandwidth is important when the fundamental beam is focused in the crystal. The numerical aperture of the focused radiation has a considerable influence on the conversion efficiency, as peripheral rays are less efficiently converted than the central ones.

The analysis of second harmonic efficiency dependence on crystal and wave parameters reveals several interesting features of a periodically-poled device. For fixed poling period, the second harmonic efficiency scales as crystal length squared. Increasing the crystal length is thus beneficial to wavelength conversion. However, according to Fig. 4.3 the increase of the device length is done at the expense of wavelength and temperature acceptance bandwidths. Accurate control of the operating temperature of the crystal and spectral width of the pump source becomes necessary. This is particularly important for ultrashort pulse sources, where the crystal acceptance bandwidth must be designed to accommodate the typically broad spectrum of the fundamental wave pulses. Fiber lasers, where pulse amplification is usually accompanied by spectral broadening, constitute a serious challenge for periodically-poled crystals, as optimization for both temporal and spectral shapes of the pulses creates conflicting requirements for the device length.

The following sections address the problem of increasing the second-harmonic generation efficiency by two approaches: crystal optimization by built-in waveguides and laser source optimization by pulse and spectrum compression.

4.4 Waveguided periodically-poled KTP crystal for multi harmonic generation

The second harmonic generation efficiency depends on both the crystal length and the fundamental wave intensity. Typically, the fundamental wave is focused into the nonlinear crystal to achieve smaller spot size and thus higher power density. Small spot-size (and consequently high intensity) of the focused beam is achieved in a limited physical domain. For Gaussian beams, this domain is delimited by the Rayleigh range of the beam. Efficient interaction between the nonlinear crystal and the fundamental beam requires that the crystal be at least as long as the Rayleigh range. Tighter focusing results in a smaller Rayleigh range and thus requires a shorter crystal, offering a shorter interaction length. A tradeoff between the crystal length and the focusing strength of the fundamental beam is enforced.

This problem can be alleviated by embedding a waveguide structure in the periodically-poled crystal. The (typically) planar waveguide guides both fundamental and second harmonic waves through the crystal and thus eliminates the need for a trade-off between the focusing spot size and the crystal length. Since the fundamental light is confined within the waveguide along the entire crystal, the conversion efficiency is expected to improve significantly compared to the efficiency of non-waveguided structures where efficient interaction occurs only within the Rayleigh range of the beam. The situation can be better understood by referring to Eq. (4.4), where A is replaced by the waveguide cross-sectional area. Waveguides can be made very small (μm x μm) and thus large efficiency is expected. Waveguides are fabricated by a variety of techniques that allow the refractive index of the crystal to be changed, such as etching and cladding [190], impurity diffusion [191], proton exchange [192], a combination of proton exchange and ion implantation [181], or (in the case of ferroelectric materials) electrical inversion [179]. In waveguided nonlinear crystals, phase matching can be achieved by using the waveguide chromatic dispersion [177] or by standard QPM, leading to robust and efficient generators [192–193].

KTP is an attractive material for short wavelength frequency doubling owing to its broad transmission spectrum, large nonlinear coefficient, and high damage threshold [Table 4.1, 194]. In addition, KTP exhibits low coercive field (10 times lower than $LiNbO_3$) and quasi unidirectional structure which allows the fabrication of narrow inversion domains in relatively thick crystals [195]. The low photorefractive effect enables KTP crystals to handle high optical power at low operating temperatures, which alleviates the need for expensive and bulky ovens [196]. Conversion efficiency in excess of 50% has been obtained from bulk KTP crystals operated at room temperature [197]. With the added benefits of a waveguide, KTP crystals constitute an attractive solution for a compact frequency doubler suitable for intense visible light generation in small footprint applications.

Using a purposely designed fiber laser, we investigated the frequency conversion performance of a periodically-poled KTP (PP-KTP) crystal embedding a waveguide **[P6]**. Owing to strong nonlinear interactions, the second (532 nm) and third (355 nm) harmonics of the fundamental wavelength (1064 nm) light were generated simultaneously in the crystal. The 12 mm-long crystal was fabricated by an ion exchange technique [181] and periodic polling was achieved by chemical waveguide patterning. The structure embeds three parallel waveguides with poling periods varying between 8.22 μm and 8.72

μm and a duty cycle of 0.6. Precise matching between the crystal structure and the input laser wavelength is performed by choosing the appropriate waveguide (coarse tuning) followed by temperature adjustment (fine tuning). The setup used during the experiments is shown in Fig. 4.5.

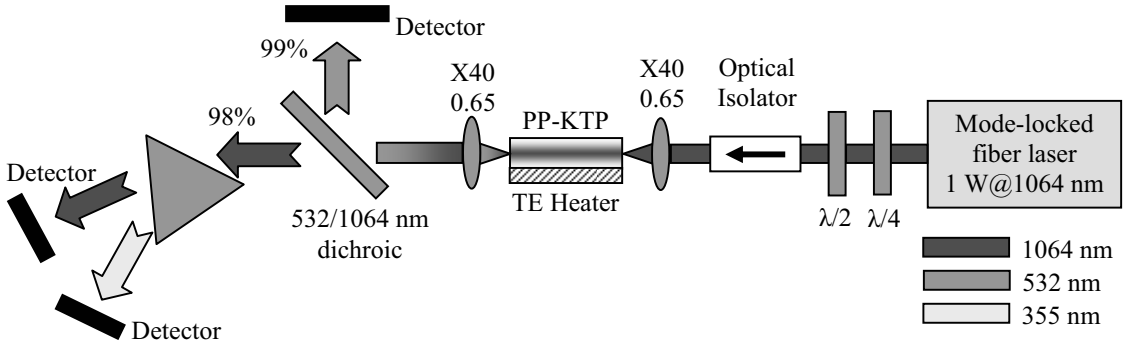

Fig. 4.5. Experimental setup for frequency conversion in a waveguided PP-KTP crystal.

The crystal is placed on a thermoelectric (TE) heater that keeps the crystal at 60 °C, the optimum operation temperature for a fundamental wavelength of 1064 nm. Light is coupled in and out of the crystal by a pair of X40 (NA = 0.65) microscope objectives. The waveguide structure confines the pump and second harmonic waves in the crystal, simplifying the tedious focusing procedure aimed at maximizing the Rayleigh range and light intensity in the crystal. The sole concern is matching the size of the focused beam with the waveguide area (4 x 7 μm^2). Separation between the fundamental and second harmonic radiations is performed by a dichroic splitter exhibiting high reflectivity at 532 nm and high transmission at 1064 nm and 355 nm. The fundamental is further separated from the third harmonic radiation by a BK7 glass prism. All beams are directed towards appropriate detectors. At full power, the fiber laser source delivers 1 W of light at 1064 nm in 3 ps-long pulses. For this regime of operation, 50 mW of second harmonic (corresponding to an effective conversion efficiency of 33%) and 3 mW of third harmonic light (effective conversion efficiency of 2%) were measured. The optical spectra of second and third harmonics are given in Fig. 4.6(a) and (b).

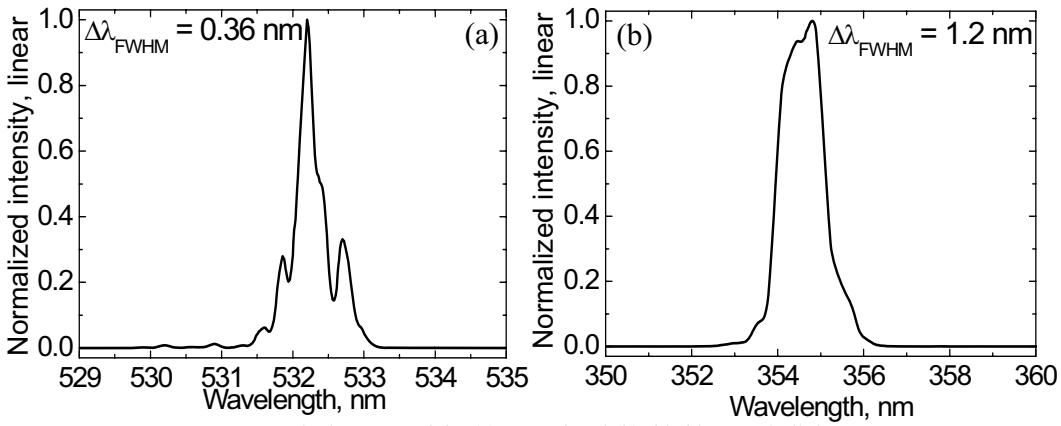

Fig. 4.6. Optical spectra of the (a) second and (b) third harmonic light.

The frequency conversion efficiency is limited by the mismatch between the laser spectrum and the crystal acceptance bandwidth as well as two-photon absorption (TPA) in the crystal bulk [198].
The second harmonic generation process is QPM-based. Following the theoretical analysis in **[P6]**, the third harmonic radiation is found to emerge from a two-step process consisting of quasi phase-matched second harmonic generation followed by non phase-matched sum frequency mixing between the non-depleted fundamental and the strong second-harmonic light generated in the waveguide. It can be shown that the intensity of the third order harmonic radiation varies within the crystal as **[P6]**:

$$\left|A_3\right|^2 \approx \left(\left|A_1\right|^3 L_{coh,4} L\right)^2, \tag{4.13}$$

where $\left|A_1\right|^2$ is the intensity of the fundamental wave, $L_{coh,4}$ is the coherence length of the sum frequency mixing process corresponding to 4th order QPM frequency doubling, and L is the propagated distance within the crystal. Remarkably, despite originating in a non-phase matched interaction, third harmonic generation behaves like a phase matched process and its efficiency does not oscillate with propagated distance (as in Fig. 4.1(b)). Third harmonic radiation intensity scales quadratically with crystal length and cubically with fundamental light intensity. For the crystal employed in the experiments, the coherence length $L_{coh,4}$ was 71 μm, which creates the premises for efficient third harmonic generation. The calculated value of third harmonic generation efficiency is 2.7%, which matches the measured value reasonably well.
Owing to the small footprint and relaxed requirements for optical alignment, waveguided PP-KTP crystals constitute a viable solution for portable generators of visible and UV light.

4.5 Ultrashort pulse sources for frequency conversion

Frequency conversion in periodically-poled nonlinear crystals requires custom-designed ultrashort pulse sources delivering large peak power in high quality pulses. The optical spectrum of such sources is a key issue, as it has to match the acceptance bandwidth of the periodically-poled crystal in order to yield good conversion efficiency. Optimal frequency conversion in a periodically-poled crystal is obtained when both input pulse width and spectrum are optimized for the available crystal. To achieve a satisfactory balance between optical spectrum and pulse width, we concentrated on two extreme situations: short pulses (and consequently broad spectrum) that require short nonlinear crystals exhibiting large acceptance bandwidth, and long pulses whose narrow spectra fit well within the acceptance bandwidth of long periodically-poled crystals. Both situations have the ability to bring the optical pulse close to its transform limited value. As experimental base, two mode-locked laser systems have been assembled as test sources for the described situations. One of the sources is based on the robust master oscillator-power amplifier (MOPA) architecture, whereas the other employs nonlinear effects in the power amplifier to compress the optical spectrum of the output pulse.

4.5.1 Master-oscillator power-amplifier ultrashort pulse laser source

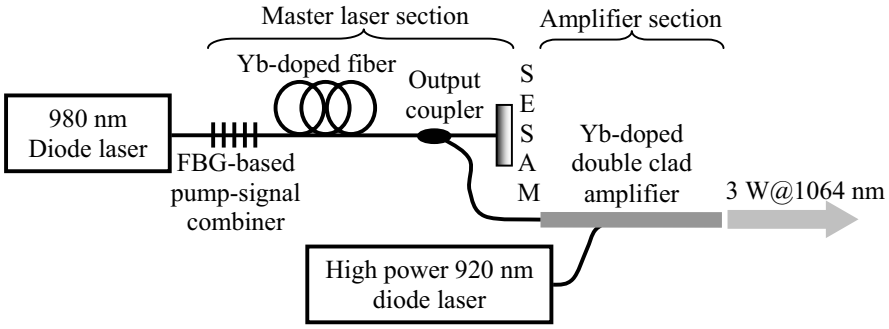

Fig. 4.7. Optical setup of the all-fiber MOPA system for frequency conversion.

The MOPA source was assembled as shown in Fig. 4.7. The master oscillator is a linear cavity Yb-doped fiber laser. Notably, the pump light is coupled into the laser cavity through a fiber Bragg grating (FBG) acting as a dichroic cavity mirror. This arrangement results in a short laser cavity with reduced positive dispersion ballast. In addition, chirped FBGs can have large negative dispersion and provide intracavity chromatic dispersion compensation [199]. The laser is mode-locked by a butt-coupled SESAM mirror. The all-fiber character of the laser cavity enables compact packaging and improved stability.

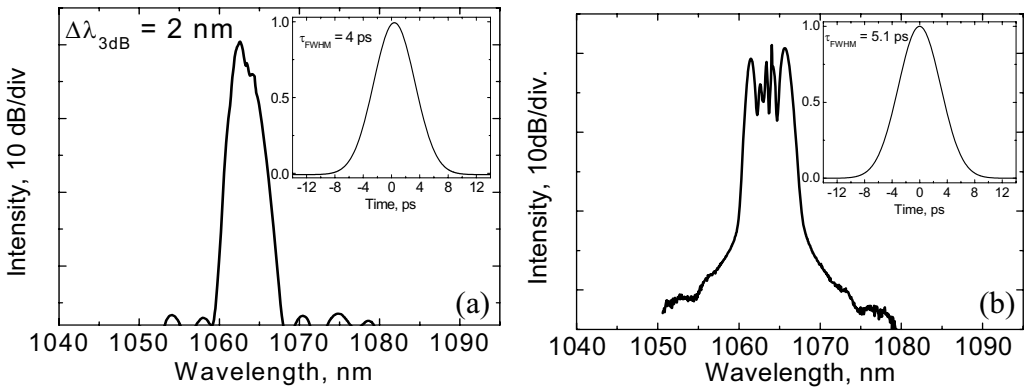

Fig. 4.8. Optical spectrum and autocorrelation of (a) the master oscillator and (b) MOPA source for an output power of 3 W.

Output signal is extracted through a broadband output coupler. Upon switching on the pump laser, the laser self-initiates mode-locking and produces a stable train of 4 ps-long pulses at a repetition rate of 100 MHz. The average output power of the master oscillator is 10 mW. The optical spectrum and autocorrelation (inset) of the master oscillator are presented in Fig. 4.8(a). The pulses are coupled into the power amplifier through an isolator that prevents amplifier noise from leaking into the laser cavity and disturb the mode-locked operation. The amplifier consists of a span of large mode area fiber (LMA) with a core diameter of 20 μm, pumped by a high power multimode laser diode operating at 920 nm. At full power, the laser diode produces 7 W in a 100 μm core pigtail. Coupling between the multimode pump and LMA amplifier fiber is done through a commercial fused coupler. The output of the amplifier is angle polished to avoid back reflections. The choice of a collimated beam free-space output was enforced by the use of

bulk diffraction gratings for pulse compression, as shown later. The device used for experiments was assembled by Fianium Ltd. UK.

Figure 4.8(b) shows the optical spectrum and autocorrelation trace of a 30 nJ output pulse corresponding to a source output power of 3 W. SPM-induced spectral broadening is evident in the spectrum shape. The estimated time-bandwidth product of the pulse is 10, well above the transform-limited value. This is an expected effect of intense SPM effects in the amplifier fiber. To recover the pulse quality, a pair of 1200 lines/mm diffraction gratings was placed at the output of the MOPA source. In this configuration, the grating pair exhibits negative dispersion and removes the linear chirp from the temporal pulse, working as a pulse compressor. Without *a priori* knowledge of the extent of SPM-induced chirp on the output pulse, a set of consecutive measurements was performed, targeted at minimizing the output pulse width. The grating pair compressor was adjusted several times, each time with a slightly increasing separation between the gratings. The dispersion of the grating pair compressor was thus varied until an optimal value was found, corresponding to the shortest pulse duration. Figure 4.9 shows the measured pulsewidths for various grating separations, along with the autocorrelation of the shortest obtained pulse.

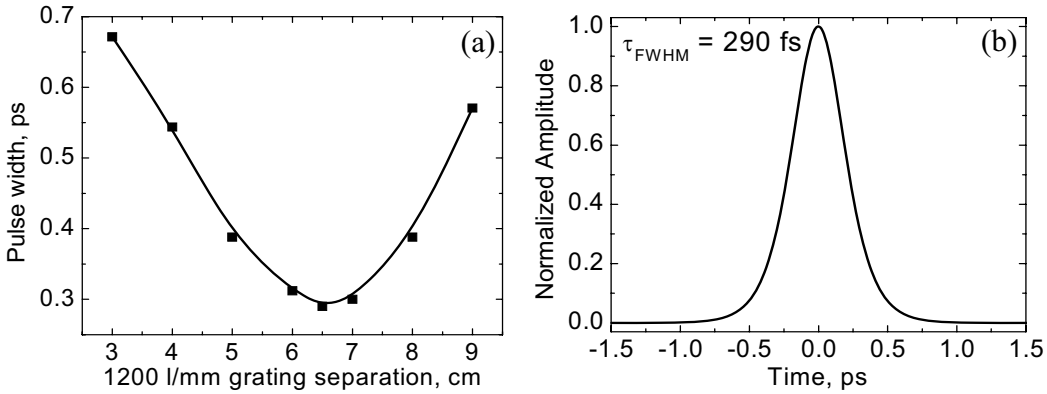

Fig. 4.9. (a) Compression curve and (b) autocorrelation of the shortest pulse at an output power of 1 W.

The time-bandwidth product of the compressed pulse is 0.38, assuming a sech envelope. The pulse is thus nearly transform-limited. Since the grating pair has virtually no nonlinearity, the pulse spectrum is not disturbed by the compressor. However, polarization rotation effects in the MOPA fiber amplifier cause the pulse compression efficiency to be dependent on the output power of the laser. The best pulse compression efficiency, corresponding to Fig. 4.9, was obtained for a laser output power of 1 W.

The MOPA source was used in two independent frequency doubling experiments in order to asses the attainable frequency conversion performance using such a laser. In a first experiment, we used the uncompressed MOPA system to pump a 10 mm-long PPLN crystal (supplied by Stratophase Ltd. UK) which was optimized for frequency doubling at 1064 nm. The crystal had three parallel gratings with poling periods of 6.5 μm, 6.54 μm, and 6.58 μm. Periodic polling was realized by electric field inversion. The PPLN crystal was pumped with the pulses extracted directly from the MOPA output. Despite the narrow acceptance bandwidth (0.3 nm, far below the extent of the MOPA output spectrum) the crystal length is a good match for the picosecond pulses of the source and a fair conversion efficiency is expected. The crystal, whose facets were anti-reflection

coated to minimize reflection losses, was placed in an electric oven for temperature control. A digital feed-back loop controller allowed for setting and maintaining the crystal temperature with a precision of 0.1 °C. The experimental setup is shown in Fig. 4.10.

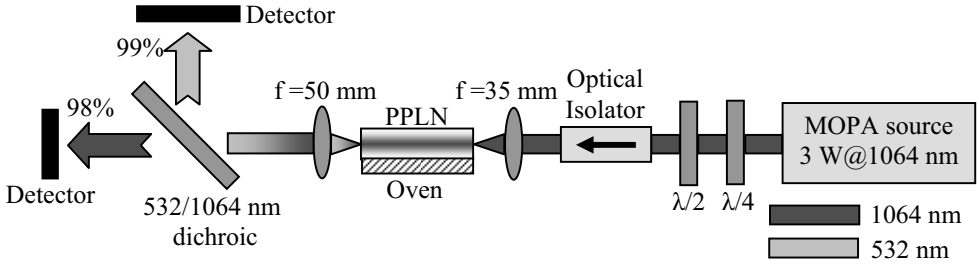

Fig. 4.10. Optical setup for second-harmonic generation using picosecond pulses.

The light was focused through the crystal by a 35 mm lens, yielding a spot size of 40 μm and a Rayleigh range of 2 mm. These values were found to yield the best conversion efficiency. The second-harmonic light was separated from the fundamental by a dichroic mirror and the two beams were independently monitored by suitable detectors. When the polarization plates and focusing optics were properly set, a bright green light (second harmonic) emerges from the PPLN crystal.

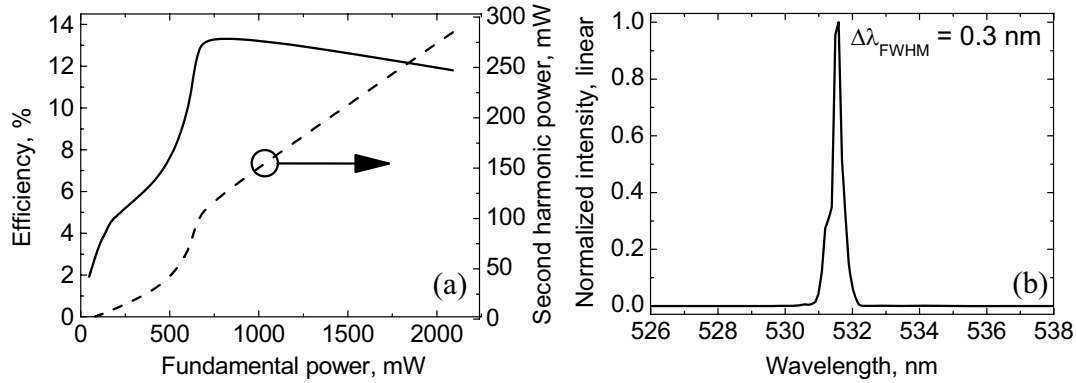

Fig. 4.11. (a) Second harmonic conversion efficiency vs. input power and (b) optical spectrum of the converted radiation (corresponding to 120 mW output) for a 10 mm PPLN pumped with picosecond pulses.

Figure 4.11(a) plots the second harmonic conversion efficiency as a function of the infrared power launched into the crystal. The maximum conversion efficiency was 13.8% at a crystal temperature of 165 °C. Figure 4.11(b) shows the spectrum of the green second-harmonic radiation at an output power of 120 mW corresponding to the highest conversion efficiency. Owing to polarization rotation effects in the MOPA amplifier fiber at high optical power, the polarization sensitive isolator in Fig. 4.10 causes certain insertion losses which limit the maximum available pump power to 2.1 W, corresponding to a pulse peak power of 4.2 kW. The frequency conversion efficiency exhibits saturation caused by two-photon absorption (visible in Fig. 4.11). The drop in second harmonic output at full laser power is likely due to laser-induced heating of the periodically-poled crystal that causes detuning from the optimal operation conditions. The effects of temperature detuning were investigated by monitoring the second-harmonic output while varying the operating temperature of the crystal. The pump power was set to 750 mW to

avoid permanent damage to the crystal caused by the photorefractive effect. The measured temperature tuning curve is shown in Fig. 4.12.

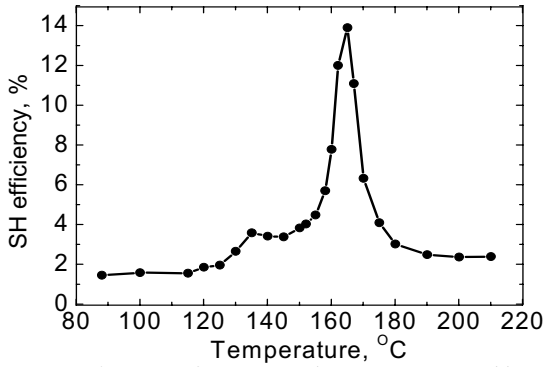

Fig. 4.12. Temperature tuning curve for a 10 mm-long PPLN pumped by picosecond pulses.

The 10 mm-long crystal appears to have a temperature acceptance bandwidth of 10 °C. The dissimilarity between the measured and calculated values in Fig. 4.4(b), indicating a bandwidth of 3 °C, is ascribed to the broad laser spectrum. As the temperature is detuned, the optimal conversion wavelength of the crystal is scanned across the broad laser spectrum causing the temperature acceptance bandwidth to appear wider. Notably, the second-harmonic efficiency drops by several percents for a temperature variation of less than 2 °C, emphasizing the importance of accurate temperature control in systems embedding periodically-poled crystals. As indicated by the spectra of MOPA output (Fig. 4.8(b)) and second-harmonic radiation (Fig. 4.11(b)), frequency conversion efficiency is limited by the acceptance bandwidth of the crystal, in that the crystal will only accept and convert a narrow "slice" of the input laser spectrum. The use of a short periodically-poled crystal (with broad acceptance bandwidth) should alleviate this problem. However, owing to the limited interaction length, short crystals require very intense pulses to achieve good conversion efficiency.

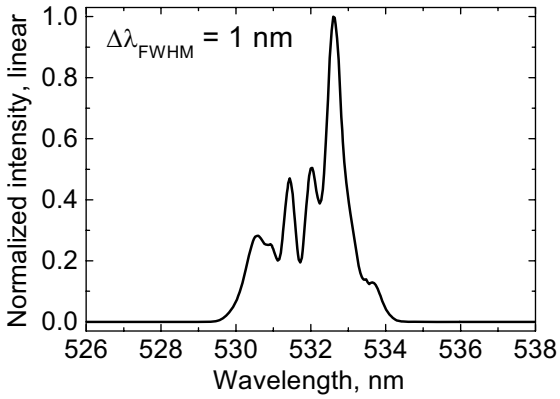

Fig. 4.13. Optical spectrum of the converted radiation (corresponding to 135 mW output) for a 0.3 mm PPLN pumped with femtosecond pulses.

We used the compressed pulse version of the MOPA system to investigate the possibility of increasing the conversion efficiency in short crystals. The MOPA source and pulse compressor were adjusted for best pulse shape, as shown in Fig. 4.9(b). The optical setup

is similar to the one depicted in Fig. 4.10, where the isolator is replaced by the grating pair compressor. At optimal power, the source produces 700 mW in 290 fs pulses with a peak power of 24 kW. A 0.3 mm-long PPLN crystal was used as frequency doubling medium. Except for its length, the crystal is identical to the 10 mm version used with uncompressed pulses. A second harmonic output of 135 mW was obtained from 600 mW of infrared input, corresponding to a conversion efficiency of 18.3%. The spectrum of the second harmonic radiation at maximum power is shown in Fig. 4.13. The large spectral bandwidth of the second harmonic radiation indicates that the short periodically-poled crystal accepts a wider input spectrum than its 10 mm counterpart. In consequence, the conversion efficiency increased by 5%. However, further optimization of the laser source is necessary, as the spectral width of the laser is still in excess of the crystal acceptance bandwidth.

4.5.2 Spectrally-compressed source of ultrashort pulses for frequency conversion

The MOPA experiments indicate that the spectral broadening associated with pulse amplification in an optical fiber can seriously affect the frequency conversion efficiency. Limiting the spectral broadening effects in high power fiber lasers would thus seem to be the best option for efficient frequency conversion in periodically-poled crystals. It has been shown [200] that the SPM-induced effects on the spectrum of an optical pulse can be limited or even reversed by applying a certain amount of negative chirp on the pulse prior to its propagation through the nonlinear medium. This prescription can be readily applied to optical fibers: the SPM-induced spectral broadening experienced by a pulse in an optical fiber can be controlled by applying a negative chirp (pre-chirp) on the pulse before it is launched into the fiber. In fact, owing to the negative pre-chirp, SPM effects cause the pulse spectrum to narrow instead of broaden. This phenomenon relies on the balance between the chirp imposed on the pulse by SPM and the pre-chirping operation. The SPM-induced positive chirp of the pulse interacts with the pre-existing negative chirp, effectively re-distributing the spectral components of the pulse towards the center of the spectrum. The pulse spectrum is compressed. Spectral compression is intensity-dependent and accumulates with propagation down the nonlinear fiber section. Therefore an exact balance between the amount of pre-chirp and SPM effects is required to obtain the narrowest spectrum pulse at the end of the fiber.

To estimate the effects of pulse pre-chirping, a computer routine has been devised to simulate the propagation of an optical pulse through a length of negative dispersion fiber for pre-chirp followed by a span of nonlinear fiber. As in chapter 3, pulse propagation has been simulated by solving Eq. (3.6) using a split-step Fourier transform algorithm, taking into account second order dispersion, SPM, self-steepening, and shock formation. Figure 4.14 shows the time-domain and spectral characteristics of a transform-limited pulse propagating through the nonlinear fiber (a, b) and the same situation when the pulse undergoes initial pre-chirping (c, d). The insets on the right side reveal the shapes of the pulse and its associated spectrum at the far end of the nonlinear fiber. The relevant simulation parameters are given in Table 4.2.

Table 4.2. Input data for simulation of pre-chirped pulse amplification.

	Parameter name	*Symbol*	*Value*	*Unit*
Pulse	Wavelength	λ	1060	nm
	Initial pulse width (FWHM)	τ_{FWHM}	0.5	ps
	Initial spectral width (FWHM)	$\Delta\lambda_{FWHM}$	3.3	nm
	Peak power	P_{pk}	1500	W
Pre-chirp fiber	2nd order chromatic dispersion	$\beta_{2,\,P}$	-94	ps^2/km
	3rd order chromatic dispersion	$\beta_{3,\,P}$	1.64	ps^3/km
	Nonlinear coefficient	γ_P	0	$W^{-1}m^{-1}$
	Fiber length	l_P	5	m
Nonlinear fiber	2nd order chromatic dispersion	$\beta_{2,\,NL}$	24	ps^2/km
	3rd order chromatic dispersion	$\beta_{3,\,P}$	0.0229	ps^3/km
	Nonlinear coefficient	γ_{NL}	0.004	$W^{-1}m^{-1}$
	Fiber length	l_{NL}	4	m
Free space	2nd order chromatic dispersion	$\beta_{2,\,FS}$	0	ps^2/km
	3rd order chromatic dispersion	$\beta_{3,\,P}$	0	ps^3/km
	Nonlinear coefficient	γ_{FS}	0	$W^{-1}m^{-1}$
	Length	L_{FS}	5	m

The pulse temporal shape is measured in a reference frame traveling with the pulse. Case (a, b) corresponds to typical propagation in a nonlinear fiber with positive chromatic dispersion. The (initially transform-limited) pulse experiences massive SPM-induced spectral broadening, while the time domain pulse is stretched by the positive dispersion of the fiber. Due to spectral broadening, the pulse stretching rate increases with pulse propagation through the nonlinear fiber. By contrast, in Fig. 4.14(c) and (d), the initial pulse undergoes pre-chirping for the first 500 cm of propagation followed by propagation in the nonlinear fiber segment. The pre-chirping module does not exhibit optical nonlinearity and leaves the pulse spectrum intact. Low nonlinearity pulse stretchers can be realized in practice using bulk diffraction elements or special optical fibers such as hollow-core fibers. During pre-chirping, the pulse is stretched to about 7 times its transform-limited width. Owing to the negative pre-chirping, the pulse experiences spectral compression in the nonlinear fiber. The sidebands in the compressed spectrum and the slight asymmetry of the pulse shape are caused by the third order dispersion of the pre-chirping fiber, as discussed in [200]. The positive dispersion of the nonlinear fiber strand has little effect on the temporal shape of the narrow spectrum pulse, which propagates undisturbed through the entire 400 cm-long section. This constitutes an added bonus of pulse pre-chirping. The simulated system is optimized in that the minimum spectral width is achieved at the very end of the nonlinear segment. However, this may not always be the case. If the SPM effects are too strong or if the pre-chirping is too weak, the pulse spectrum will go through a minimum width point before being broadened again by the excessive SPM. Obviously this is not an optimized situation. Correcting this problem requires a reduction in the pulse peak power or a larger amount of pre-chirp.

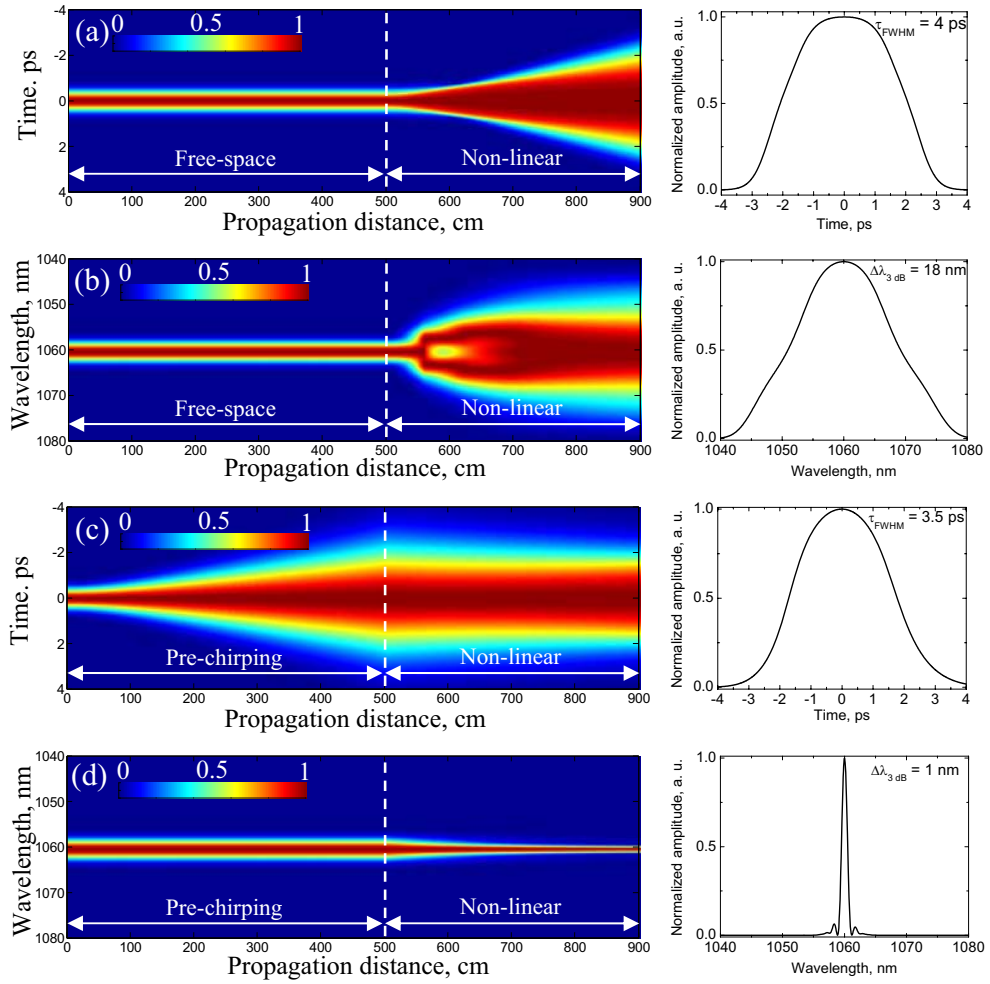

Fig. 4.14. Temporal and spectral shapes of an ultrashort optical pulse propagating through a fiber amplifier (a, b) without and (c, d) with initial pre-chirping. The free-space section has been included to provide identical propagation length in the two cases. It has no influence on the time-domain pulse or its spectrum, being merely "propagation ballast".

The results in Fig. 4.14 can be applied in practice if the nonlinear fiber segment is replaced by a fiber amplifier. The pulses (produced by a low power oscillator and pre-chirped by a proper optical fiber) experience spectral compression in the power amplifier stage thus canceling out the SPM-induced spectral distortion seen in most MOPA systems. This type of spectrally compressed source is very useful in frequency conversion, where narrow pulse spectrum is essential. SPM-induced spectral compression was employed in a series of experiments [201, 202], resulting in nearly transform-limited pulses with large peak power. However, the reported experimental setups employ grating pair pulse stretchers and massive cladding-pumped amplifiers which are hardly compatible with compact fiber lasers.

Based on the considerations above, we constructed an all-fiber spectrally-compressed source of ultrashort pulses suitable for frequency conversion **[P7]**. The optical setup is given in Fig. 4.15. Pulses from an Yb-doped mode-locked fiber laser are pre-chirped in a 5 m-long piece of hollow-core photonic bandgap fiber. This type of optical fiber relies on

photonic crystal effects to guide light and thus the core of the fiber can consist of a variety of optical media, with much less emphasis on the refractive index. In the fiber used for this experiment, the fiber core consists of air (hollow core) and thus fiber nonlinearity is practically zero. The fiber is mechanically spliced to both laser output and amplifier input, resulting in a low-loss (typically 0.2 dB) compact connection.

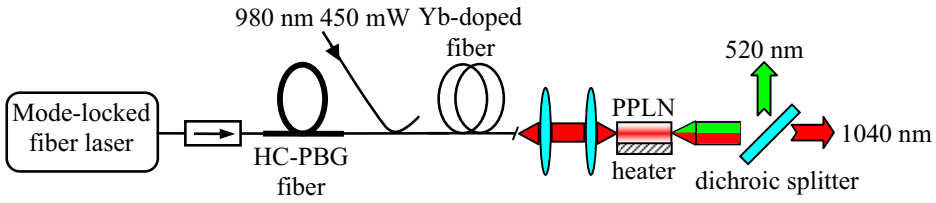

Fig. 4.15. Optical setup of the picosecond fiber laser source employing spectral compression.

Following propagation through the pre-chirping fiber, the 1.4 ps-long pulse of the laser stretches to 3.5 ps, while the optical spectrum is unchanged. After pre-chirping, the pulses are launched into a 4 m-long single mode Yb-fiber amplifier, core-pumped by a pigtailed laser diode delivering 450 mW at 980 nm. The performance of the source is monitored at the output of the amplifier by an autocorrelator and an optical spectrum analyzer. The pulse and spectrum width as a function of the amplifier power are shown in Fig. 4.16(a). Figure 4.16(b) reveals a series of spectra collected at the output of the amplifier for various output powers.

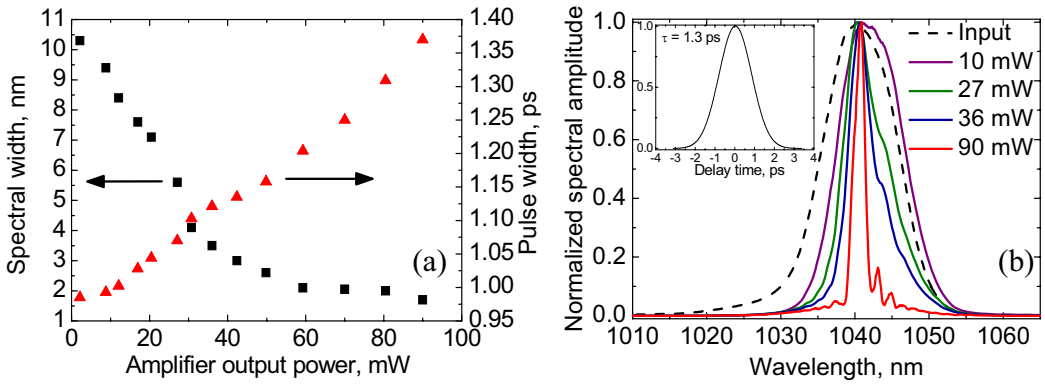

Fig. 4.16. (a) Temporal and spectral widths after the amplifier for different output powers and (b) a set of optical spectra for selected output power settings. Inset shows the autocorrelation of the narrowest spectrum pulse.

As the amplifier output power is ramped up, the increasingly strong SPM effects cause spectral narrowing. For this experimental setup, the amount of pre-chirp was chosen to exactly balance the SPM in the amplifier at full power, which corresponds to the narrowest spectrum of the output pulses. Owing to spectral compression, the time-bandwidth product of the output pulses decreases from 3.16 to 0.58 corresponding to a full-range sweep of the amplifier power. At the best output setting (90 mW), the system delivers 1.4 ps-long, nearly transform-limited pulses with a peak power of 1.25 kW.

The suitability of the laser source for frequency conversion has been assessed by placing a PPLN crystal in the output of the source, as shown in Fig. 4.15. A (slightly out of range) 10 mm-long crystal has been used, owing to the unavailability of a more suitable device. A second-harmonic output of 12 mW was measured, corresponding to an effective conversion efficiency of 66%. We demonstrated the potential of SPM-induced

spectral narrowing to generate transform-limited pulses and consequently boost the conversion efficiency as a result of better matching between the pulse and crystal parameters. Owing to its all-fiber architecture, such a fiber source is an attractive solution for compact visible light generators.

5 Supercontinuum generation in optical fibers

Frequency conversion is a robust and reliable source of short wavelength radiation. With mode-locked fiber lasers for pumping, frequency conversion in periodically-poled crystals produces intense ultrashort pulses at a wide selection of wavelengths. However, the tuning range and spectral width of these sources is limited by the phase matching bandwidth of the nonlinear crystal. Several important fields of science draw great benefit from low coherence broadband optical sources covering the infrared and visible wavelength domains. Traditional sources of broadband radiation (thermal or ionization sources) are unreliable and offer poor spectral power density, directionality, and coupling efficiency into optical waveguides. A light source offering high brightness and directionality with the added bonus of broad optical spectrum is therefore in great demand.

A possible solution to building such a source is the supercontinuum radiation. The term supercontinuum refers to the large spectral broadening experienced by intense laser pulses propagating in a nonlinear medium. Supercontinuum broadening is the combined result of several nonlinear optical phenomena, such as self phase modulation (SPM), four-wave mixing (FWM), and stimulated Rayleigh scattering (SRS). Originating from laser radiation, supercontinuum fulfills most of the requirements formulated above: it is directional, has large spectral power density, and in special cases can be formed inside a waveguide, alleviating the need for delicate waveguide coupling techniques.

The origins of supercontinuum generation can be traced back to the groundbreaking work of Alfano and Shapiro who, in 1970, reported the generation of novel wavelengths in a gas medium irradiated with an intense laser beam [203]. The results were received with interest by the scientific community and efforts to improve the efficiency of nonlinear spectral broadening were reported in the next decade [204–205]. In 1987, supercontinuum spectral broadening was reported for the first time in multimode optical fibers [206] and, just two years later, the nonlinearity of single-mode fibers was used for supercontinuum generation [207]. From this moment on, supercontinuum radiation became a phenomenon of practical interest undergoing constant progress and benefiting from the latest advances in laser and fiber technology. Recently, supercontinuum generation was reported in novel waveguide structures such as photonic bandgap fibers (PBGF) [208], single mode fiber tapers [209], as well as more exotic devices such as soft glass Kagome crystal fibers [210]. All mentioned waveguides exhibit appealing nonlinear and dispersion properties and can be optimized for operation with a large selection of lasers. Innovative technologies enable very compact sources of supercontinuum radiation which are presently available in commercial form [211].

Supercontinuum radiation has found multiple applications in science and engineering, wherever intense broadband radiation was required. The large spectral power density of supercontinuum radiation is especially beneficial to spectroscopy [20] and biology [21], whereas the controlled coherence was exploited in metrological applications [23]. The large spectral bandwidth and uniform power distribution renders supercontinuum an almost ideal source for dense wavelength division multiplexed (DWDM) optical communications [212–213]. Therefore, research aimed at understanding the intimate mechanisms of supercontinuum generation as well as generating novel experimental

systems for broadband light generation is by no means futile, as progress in the light source triggers progress in the application.
This chapter details the research work performed on supercontinuum generation mechanisms and practical broadband systems. Using self-made laser sources operating at both infrared and visible wavelengths, supercontinuum radiation has been generated in PBGF and single-mode fiber tapers. Experimental proof of soliton fission during the formation of broadband radiation has been found.

5.1 Analysis of supercontinuum generation mechanisms in optical fibers

Supercontinuum radiation arises as interplay between a large number of nonlinear phenomena. The mechanism behind such extensive spectral broadening is fairly complex and its understanding requires breaking up supercontinuum generation in small steps that can be analyzed separately. In this section, supercontinuum generation is split in two major steps: the onset of spectral broadening caused by solitonic effects, followed by propagation-induced evolution of the spectrum. The influence of various pump and fiber parameters is discussed. The initial spectral broadening is found to be particularly important for supercontinuum formation, as it sets the stage for later spectral evolution. Most important parameters of the supercontinuum radiation are determined in the initial stage of spectral broadening.
The early stages of supercontinuum formation from an ultrashort optical pulse are described by simulating the propagation of the pulse inside an optical fiber under the influence of nonlinearity. For this purpose, Eq.(3.6) is modified to include self-steepening and Raman gain [214]:

$$\frac{\partial A}{\partial z}+\beta_1\frac{\partial A}{\partial t}+\frac{i\beta_2}{2}\frac{\partial^2 A}{\partial t^2}+\frac{\alpha}{2}=i\gamma\left[|A|^2A+\frac{i}{\omega_0}\frac{\partial}{\partial t}\left(|A|^2A\right)-T_RA\frac{\partial|A|^2}{\partial t}\right], \tag{5.1}$$

where T_R is the Raman response of the fiber which includes both electronic and vibrational (Raman) interactions between wave and medium. The optical fiber used for supercontinuum generation in the model mimics the commercial photonic crystal fiber employed in subsequent experimental work (NL–5.0–1065 from Crystal Fibre).

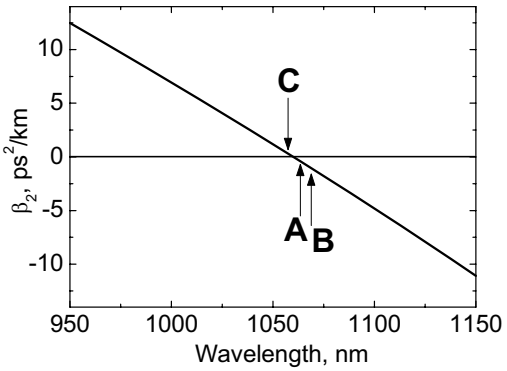

Fig. 5.1. Calculated chromatic dispersion of the nonlinear fiber used for SC generation. The arrows indicate the pumping wavelength.

The fiber has a zero dispersion wavelength (ZDW) at 1060 nm and the third order dispersion parameter is: $\beta_3 = 0.07\ ps^3/km$. The nonlinear coefficient of the fiber has been estimated to $\gamma = 11\ W^{-1}\ km^{-1}$, whereas the Raman response parameter has been assumed to be $T_R = 9\ fs$. The calculated second order chromatic dispersion of the fiber in a range relevant to initial supercontinuum formation is shown in Fig. 5.1. Broadband supercontinuum radiation is typically obtained by pumping the nonlinear fiber with intense ultrashort pulses at a wavelength situated on the negative dispersion side, close to the ZDW (point A in Fig. 5.1). Owing to the negative dispersion experienced inside the fiber, the pump pulses are converted into solitons. The order of the soliton resulting from a single pump pulse is given by:

$$N = \sqrt{\frac{\gamma P_0 T_{FWHM}^2}{3.11|\beta_2|}}, \tag{5.2}$$

where P_0 is the peak power of the pump pulse and T_{FWHM} is the FWHM value of the pulsewidth. In the conditions of large second order dispersion (β_2) and long pulsewidth, the soliton undergoes periodic changes in time and frequency domains with a spatial period given by:

$$z_d = \frac{T_{FWHM}^2}{|\beta_2|}. \tag{5.3}$$

For the particular case of supercontinuum pumping, the combined nonlinear and dispersion effects (modulation instability, SPM, third order dispersion, and the proximity of ZDW) cause the high order solitons ($N>1$) to decay into their constituent pulses (N fundamental solitons), in a process referred to as soliton fission [214–215]. During soliton decay, the excess energy is emitted as blue-shifted nonsolitonic radiation at a wavelength determined by phase matching [216]. For a better description of the process, the propagation of an ultrashort pulse through the fiber described above has been simulated. A transform limited, 100 fs-long pulse at 1064 nm has been used for pump pulse. To obtain clear soliton fission, the pulse parameters were adjusted to result in a third order soliton ($N = 3$), low enough to resolve the fundamental solitons. The simulation setup is characterized in Table 5.1.

Table 5.1. Pulse and fiber parameters for supercontinuum generation by pumping close to ZDW.

	Parameter name	*Symbol*	*Parameter value*	*Unit*
Input pulse	Wavelength	λ	1064	nm
	Peak power	P_0	117	W
	Width	T_{FWHM}	0.1	ps
	Chirp parameter [214]	C	0	-
Fiber soliton	Order	N	3	-
	Spatial period	z_d	10.9	m
Fiber	Second order dispersion at pump wavelength	β_2	-0.46	ps^2/km
	Nonlinear coefficient	γ	11	$W^{-1}km^{-1}$
	Length	L	10.9	m

The soliton order (*N*) and spatial period were calculated from Eq. (5.2) and (5.3). To obtain a good separation of the fundamental solitons, the pulse was propagated in the fiber over a distance equal to the soliton period. The resulting temporal and spectral shapes are shown in Fig. 5.2.

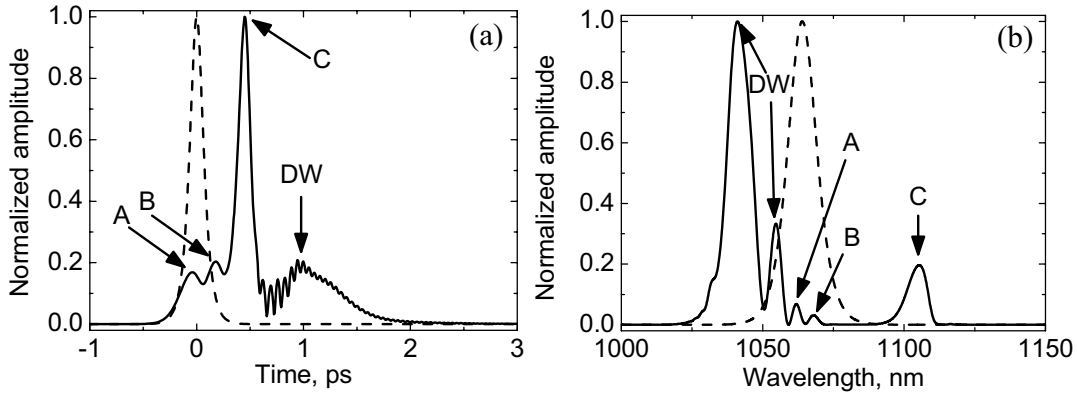

Fig. 5.2. (a) Temporal and (b) spectral description of the fission of a third order soliton during supercontinuum formation starting from an unchirped 100 fs-long pulse. The temporal and spectral shapes of the input pulse are shown in dashed line.

The third order soliton (*N=3*) created by the pump pulse splits into three fundamental solitons shown as A, B, and C in Fig. 5.2(a). Owing to intrapulse Raman scattering, the spectrum of the fundamental solitons shifts to longer wavelengths during propagation, as seen in Fig. 5.2(b). This phenomenon is referred to as soliton self-frequency shifting (SSFS). The amount of red shift experienced by each soliton is given by [214]:

$$\Delta\omega_R(z) = -\frac{5.16|\beta_2|T_R L}{T_{FWHM,S}^4}, \tag{5.4}$$

where $T_{FWHM,\,S}$ is the fundamental soliton pulsewidth. The shorter the soliton pulse, the more red shift it experiences. According to Eq.(5.2), the shortest fundamental soliton must have the largest peak power to maintain its solitonic character. It infers that the most powerful soliton in Fig. 5.2(a) (soliton C) experiences the largest red shift, as indicated in Fig. 5.2(b). Owing to the negative dispersion of the fiber the red-shifted soliton is slower than its peers and accumulates delay with propagation. This causes soliton C to appear behind solitons A and B in Fig. 5.2(a). Each of the two splitting solitons emits a nonsolitonic dispersive wave (DW in Fig 5.2(b)). The blue shifted dispersive wave propagates in the positive dispersion regime of the fiber and consists of a long pulse situated on the trailing edge of the solitons, as shown in Fig. 5.2(a). Similar temporal features have been reported elsewhere [217]. Figure 5.2 describes the first moments of supercontinuum generation. If the pulses are allowed to propagate further in the fiber, the Raman solitons (A, B, C) will experience more red shift (according to Eq.(5.4), where the amount of red shift is linearly dependent on L, the propagated fiber length) whereas the blue shifted radiation will be broadened by conventional SPM in the positive dispersion regime of the fiber. At the end of the propagation, the spectral output will consist of a smooth spectrum spanning from the longest wavelength soliton to the shortest wavelength blue shifted dispersive wave.

It now becomes obvious that the shape of the final supercontinuum spectrum is largely dictated by the soliton fission phenomena in the early stages of spectral broadening. The influence of pump pulse and fiber parameters on soliton fission is valuable knowledge, as it helps to identify ways to optimize the supercontinuum radiation.

5.2 Influence of pump and fiber parameters on the supercontinuum spectrum

5.2.1 Pumping wavelength

In Fig. 5.2, the pump pulses were close to the ZDW of the fiber and experienced negative dispersion. If the pump wavelength is tuned, the new chromatic dispersion conditions may significantly alter the supercontinuum spectrum. When the pump wavelength is situated deep into the negative dispersion region of the fiber (large $|\beta_2|$, point B in Fig. 5.1), the initial soliton order N of the pump pulse decreases as indicated by Eq.(5.2). The fission process results in fewer fundamental solitons and thus less blue-shifted nonsolitonic radiation. However, according to Eq.(5.4), fundamental solitons experience larger Raman shift in conditions of high $|\beta_2|$, resulting in a larger extension of the long wavelength side of the supercontinuum. As shown before, soliton fission is associated with the emission of phase matched blue shifted radiation at short wavelengths. It has been demonstrated [218] that if soliton fission occurs at large $|\beta_2|$, the wavelength of the resulting nonsolitonic radiation is shorter. Therefore, if pumping is done at wavelengths corresponding to large values of $|\beta_2|$, the end-to-end supercontinuum bandwidth is wider than for pumping close to ZDW. However, given the fewer solitons, the spectrum is very fragmented. This behavior has been confirmed in several experiments [216, 218].
Numerical simulations showed that the main source of soliton jitter (which causes noise in supercontinuum radiation) is modulation instability in the presence of input pulse noise [219–220]. The modulation instability bandwidth can be calculated as [221]:

$$B = 2\sqrt{\frac{\gamma P_0}{|\beta_2|}}. \tag{5.5}$$

Therefore, large $|\beta_2|$ also helps reduce the soliton jitter noise resulting in a quieter supercontinuum source.
Conversely, if pumping is performed at wavelength situated in the positive dispersion region of the fiber (point C in Fig. 5.1), soliton formation cannot occur. The spectrum is initially broadened by SPM alone and only the part of the spectrum that crosses the ZDW point can result in solitons. This operating mode is obviously non optimal and in most cases should be avoided.

5.2.2 Pump pulse chirp

The spectral broadening depicted in Fig. 5.2 assumes that the pump pulse is transform limited. In practice however, transform-limited pump pulses are not always available. The section analyzes the influence of pump pulse chirp on supercontinuum formation.
If the pump pulse is positively chirped, it undergoes temporal compression before forming a high order soliton [222]. A portion of the nonlinear fiber will be thus used as pulse compressor reducing the supercontinuum generation efficiency. This phenomenon

is particularly important when using fiber laser pump sources, where high power pulses can exhibit significant frequency chirp. If the frequency chirp is too large, soliton formation may not occur at all despite the negative dispersion of the fiber. The supercontinuum spectrum is thus restricted to SPM-induced broadening.
If the pump pulse is negatively chirped, the anomalous dispersion of the supercontinuum fiber imposes further chirp on the pump pulse. Soliton formation is even more difficult and supercontinuum generation efficiency is low.

5.2.3 Pump pulse duration

According to Eq.(5.2), if the peak power is kept constant, a long pump pulse results in a large soliton order and consequently more fundamental solitons. The resulting supercontinuum spectrum is smoother. In fact, it is this effect that indicated the soliton fission effect as the first step in supercontinuum formation [223]. For practical applications, however, the situation is more complex, as longer pump pulses can be delivered at the expense of pulse peak power. Where pump pulse duration can be freely selected at constant peak power, the longer pulse yields better results. A fiber laser source delivering pulses of adjustable width was used to generate supercontinuum in the nonlinear fiber depicted in Fig. 5.1 **[P8]**. The fiber was first pumped by 3 ps-long pulses with a peak power of 13 kW and the resulting supercontinuum spectrum is shown in Fig. 5.3(a). By placing a grating pair compressor after the laser, the output pulses were compressed down to 0.4 ps corresponding to a peak power of 60 kW. The launching conditions were identical in both cases. The supercontinuum spectrum obtained with compressed pulse pumping is shown in Fig. 5.3(b).

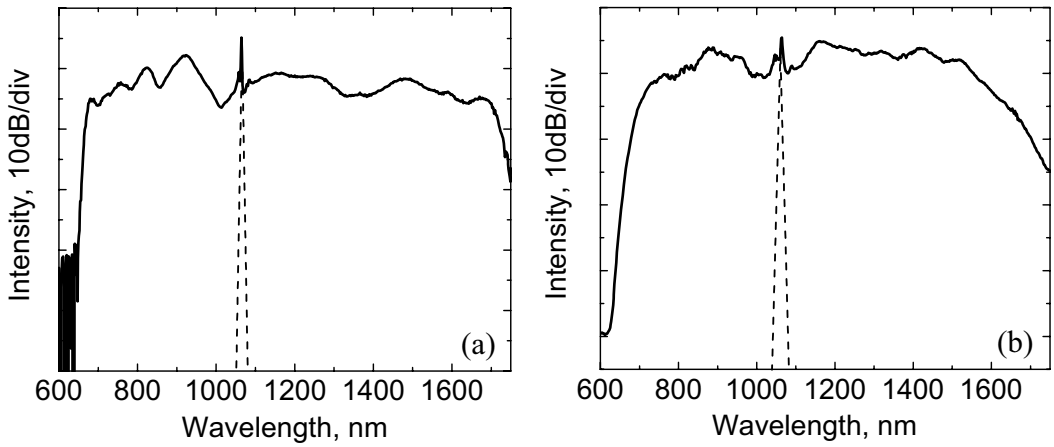

Fig. 5.3. Supercontinuum spectra generated by (a) 3 ps, 13 kW pulses and (b) 0.4 ps, 60 kW pulses. Dashed lines indicate pump laser spectra.

Despite the 4-fold increase in the peak power, the supercontinuum spectrum obtained by short pulse pumping is narrower than the spectrum generated by long pulses. This behavior is a direct proof of soliton fission effects, the narrower spectrum in Fig. 5.3(b) being ascribed to the 8-fold decrease in the order of the pump pulse-induced soliton.

5.2.4 Pump power

Increase of pump power is always beneficial to supercontinuum generation. Large pump power increases the soliton order and promotes SPM broadening of nonsolitonic radiation. The ultimate limit for pump power is given by the onset of catastrophic optical damage in the nonlinear fiber.

5.2.5 Fiber length

The extent of the nonlinear effects involved in supercontinuum generation depends linearly on fiber length (Raman shifting and SPM broadening). Therefore, in a first approximation, supercontinuum spectrum is broader and smoother with increasing fiber length. However, if the fiber length exceeds $100/(\gamma P_0)$, the evolution of nonlinear effects saturates [224] and little improvement in the supercontinuum spectrum is expected past this limit. Using a very long fiber is thus inefficient. For the fiber and pulse considered in Table 5.1, the limit length of the fiber is 78 m.

5.2.6 Dispersion profile of the fiber

The position of the ZDW of the nonlinear fiber in respect to the pumping wavelength has a major influence on the shape and extent of the supercontinuum radiation. In addition, the supercontinuum radiation is conditioned by the dispersion profile of the nonlinear fiber. Figure 5.1 shows the dispersion profile of the most commonly used supercontinuum generators, exhibiting negative dispersion on the long-wavelength side of the ZDW. This configuration supports soliton pulses at the pumping wavelength and enables Raman shifting of the fundamental solitons, leading to long wavelength broadening. An alternative dispersion profile (parabolic dispersion profile) has been suggested as an effective way to control the amount of Raman shift experienced by the fundamental solitons during supercontinuum broadening [227]. An example of parabolic dispersion fiber is shown in Fig. 5.4.

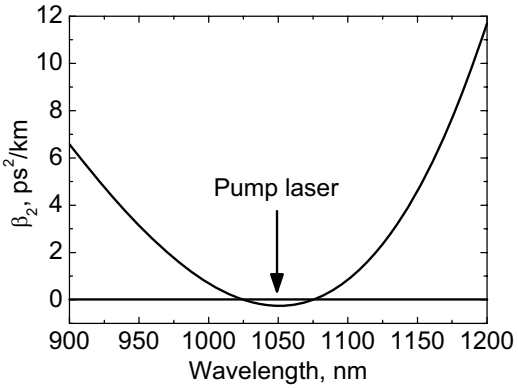

Fig. 5.4. Parabolic chromatic dispersion profile fiber (Crystal Fibre NL–1050–ZERO2).

The fiber exhibits a limited region with negative dispersion encompassed by two ZDW. Outside the mentioned region, the fiber has positive dispersion. The chromatic dispersion profile can be closely approximated by a parabola, as indicated by its name. Efficient supercontinuum generation is obtained if the pump wavelength is situated within the negative dispersion region (indicated by the arrow in Fig. 5.4). Soliton pulses can only

exist within the negative dispersion region and thus Raman shifting is limited by the long-wavelength side ZDW. This constitutes an efficient mechanism for limiting the extent of infrared radiation. Owing to the symmetric dispersion profile, a symmetric supercontinuum broadening is expected to occur.
A high power fiber laser source was used to test the parabolic dispersion fiber in Fig 5.4 as supercontinuum generator versus the single ZDW fiber in Fig. 5.1. The equally long (20 m) spools of fiber were pumped with 5 ps-long pulses at 1064 nm, carrying a peak power of 5 kW. The resulting supercontinuum spectra are shown in Fig. 5.5(a) and (b).

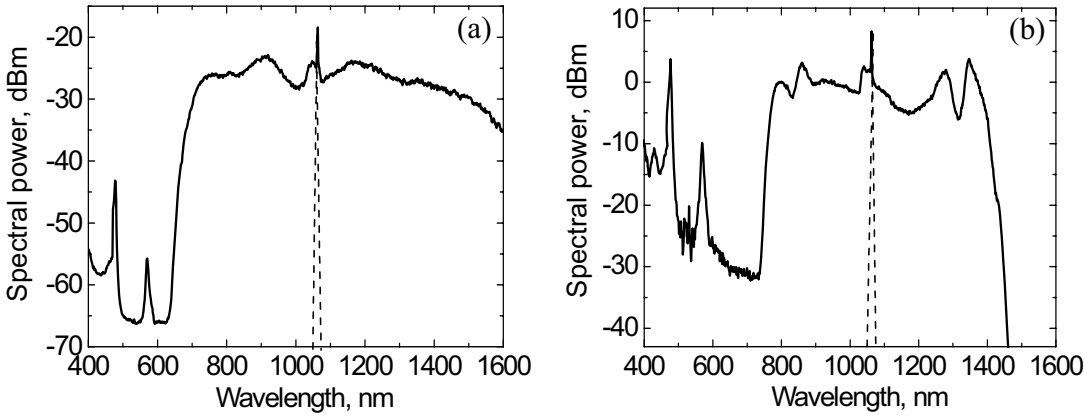

Fig. 5.5. Supercontinuum spectra generated by a picosecond fiber source in a single ZDW fiber (a) and a parabolic profile fiber (b).

The spectrum of the input laser is indicated by dotted lines in Fig. 5.5. The parabolic dispersion fiber yields a symmetric spectrum with limited extension in the infrared range. Non-solitonic phase matched radiation peaks are visible on both sides of the flat-top peak in Fig. 5.5(b). Owing to the positive dispersion value at long wavelengths, soliton self-frequency shift is limited and the energy transferred to long wavelengths is reduced.

5.3 Optimizing the supercontinuum parameters

Supercontinuum radiation emerges from a complex set of nonlinear effects and offers a generous optical spectrum spanning across several octaves. However, various systems require supercontinuum spectra which are optimized in respect to the parameters important for the application (spectral width, spectral power density, coherence, dominant wavelength range, etc.) even at the expense of other parameters. This section reviews methods to improve the supercontinuum radiation in several aspects useful to applications.

5.3.1 Degree of coherence

The usefulness of supercontinuum in metrological applications is limited by its degree of coherence [225]. Owing to the strong nonlinear interactions involved in supercontinuum generation, the degree of coherence is expected to degrade significantly for very wide spectra. If one aims at highly coherent supercontinuum radiation, certain precautions must be taken to avoid excessive noise during spectral broadening. As discussed before, one of the main sources of noise in supercontinuum is modulation instability, whose bandwidth can be significantly reduced by pumping the nonlinear fiber at wavelengths

associated with large $|\beta_2|$. In extreme cases where large spectral width is not required, the nonlinear fiber can be pumped in the positive dispersion region. Although detrimental to supercontinuum generation, the positive dispersion region of the fiber inhibits modulation instability leading to negligible coherence degradation [219, 226]. For short pump pulses, SPM plays a major role in spectrum broadening and thus the importance of modulation instability is diminished. Therefore, pumping with short pulses improves the coherence of supercontinuum. To meet the current metrological needs, one needs to employ supercontinuum radiation generated with pulsewidths of 50 fs or less [220]. This puts a significant burden on the pump source. It should also be noted that supercontinuum radiation is particularly sensitive to input pulse parameters (amplitude and temporal noise). A "quiet" pump source is a prerequisite for highly coherent supercontinuum.

5.3.2 Spectral width and smoothness

Spectral smoothness of supercontinuum radiation is important for characterization of passive components, as well as for telecommunication systems, ensuring uniform channel power. Smooth supercontinua can be achieved by pumping very close to ZDW [218]. In most cases, spectral smoothness conflicts with spectral width [218] and degree of coherence [220]. It has been suggested [227] that a smooth supercontinuum spectrum can be achieved by employing a parabolic dispersion optical fiber exhibiting two ZDWs (as shown in Fig. 5.3). The pump power is launched in the negative dispersion region between the ZDWs. By appropriately choosing the peak chromatic dispersion, a smooth supercontinuum spectrum is obtained.

5.3.3 Extended blue range

Several applications require short wavelength supercontinua with a limited amount of long wavelength components. The blue-shifted radiation originates in soliton fission processes and increasing the initial soliton order leads to improved blue-shifted output. However, increasing the amount of blue-shifted radiation while preventing a simultaneous increase in the long-wavelength content of the supercontinuum is not straightforward. Input pump power can be used to improve the extent and intensity of the blue shifted radiation. However, the influence of pump power on supercontinuum spectral width saturates after a certain threshold is reached [224]. Moreover, simply increasing the pump power causes the long wavelength side of the supercontinuum to extend as well, which may prove deleterious to some applications. As with spectral width, the extent of the blue shifted radiation can be controlled by the pulsewidth and wavelength of the pump, with the limitation of simultaneously extending the infrared side of the spectrum. The shortest wavelength of the supercontinuum spectrum can be pushed further into the blue range by parametric processes using advanced fiber designs. In one approach [228], a customized dispersion profile optical fiber has been used to stimulate FWM processes in the short wavelength range of the spectrum, thus improving the blue side content of the supercontinuum. An alternative solution relies upon cascading a typical photonic crystal fiber (like the one shown in Fig. 5.1) with a fiber exhibiting a parabolic dispersion profile (as in Fig. 5.3) [229]. Careful phase matching promotes FWM processes and leads to a significant increase in the short wavelength span of the supercontinuum.

5.4 Experimental investigation of soliton fission phenomenon during supercontinuum formation

The supercontinuum formation mechanism discussed in section 5.1 was experimentally investigated using a set of spectrally resolved autocorrelation measurements **[P8]**. The experimental setup is shown in Fig. 5.6.

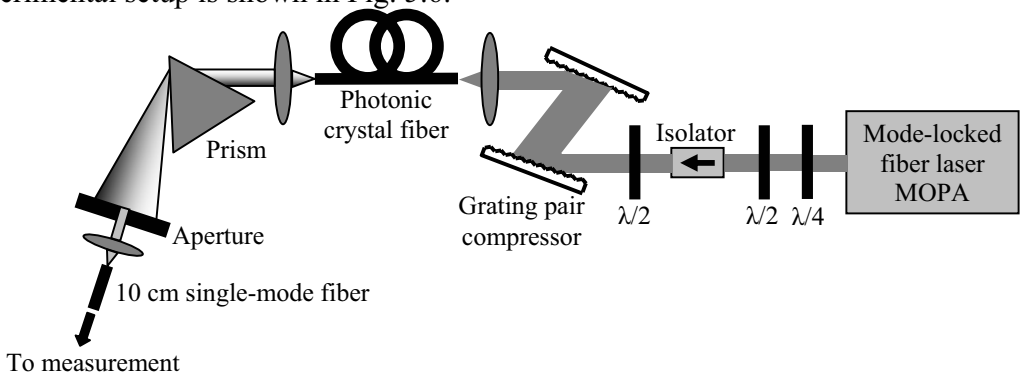

Fig. 5.6. Optical setup for investigation of supercontinuum generation mechanisms.

Supercontinuum radiation is produced in a 20 m-long span of photonic crystal fiber of the sort described in Fig. 5.1. The fiber is pumped with the pulses produced by a high power mode-locked fiber laser and compressed in a grating compressor. After compression, the pulses are 0.4 ps wide and carry a peak power of 60 kW. The supercontinuum spectrum measured after the photonic crystal fiber is shown in Fig. 5.7.

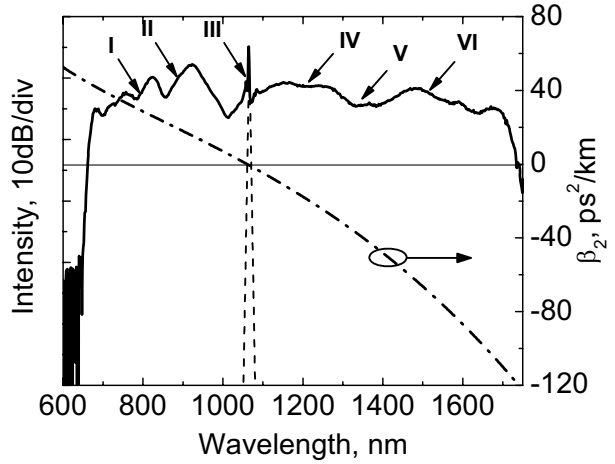

Fig. 5.7. Spectrum of the supercontinuum radiation used for investigation of soliton fission phenomena. The dash-dotted line shows the chromatic dispersion of the photonic bandgap fiber used for supercontinuum generation.

The structure of the supercontinuum radiation was investigated by slicing the ultrawide spectrum in several points (marked by roman numerals in Fig. 5.7) and analyzing the second harmonic intensity autocorrelation of the pulses comprised within the sliced section. Spectral slicing was performed by a tunable filter made from a rotating prism followed by a variable aperture. By tuning the central wavelength of the filter, portions of the supercontinuum spectrum from the positive, near zero, and negative fiber dispersion regimes were selected and investigated by autocorrelation measurements. Figure 5.8(a–h)

present selected autocorrelation traces and spectra obtained from the supercontinuum radiation.

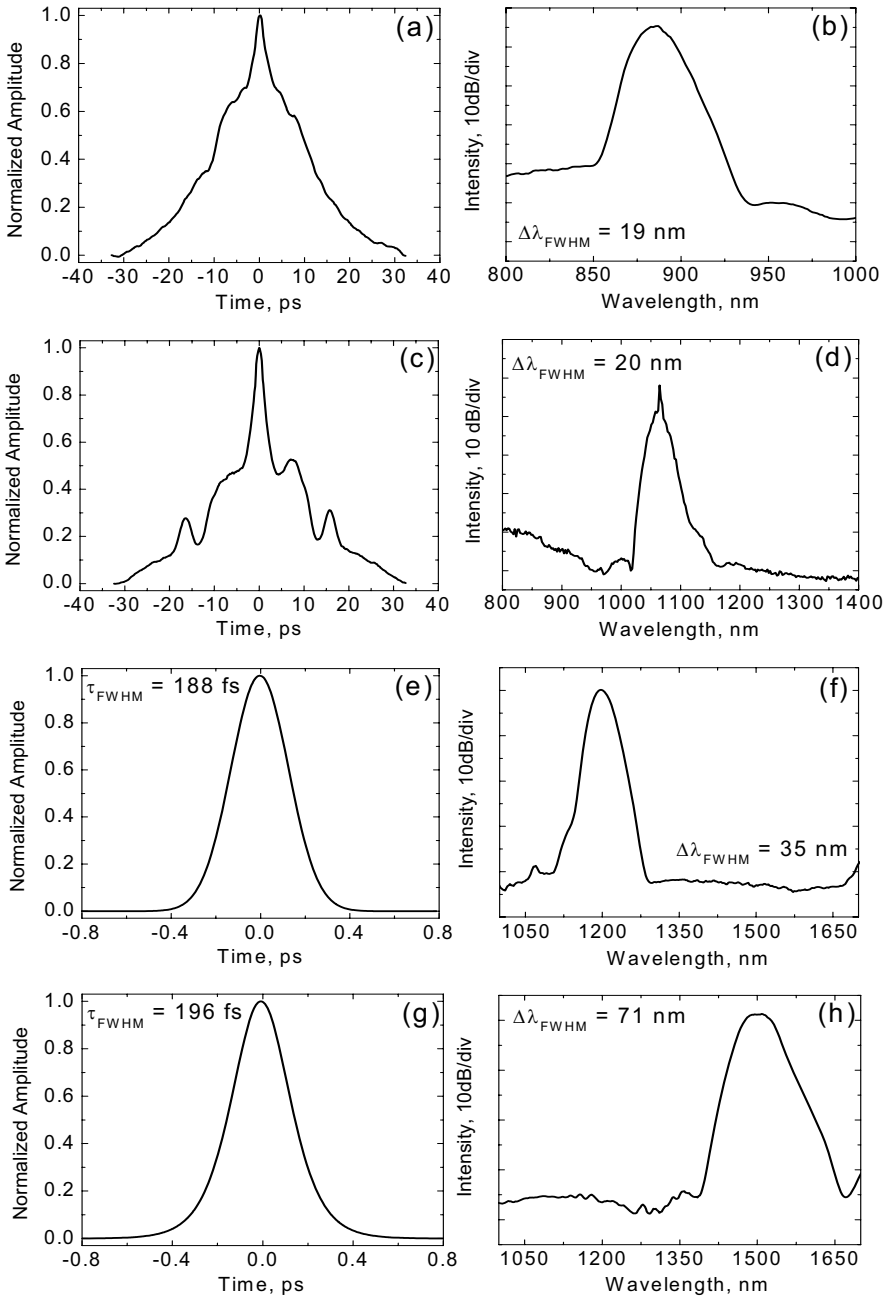

Fig. 5.8. Autocorrelation traces and optical spectra corresponding to points II, III, IV, and VI in Fig. 5.7.

In the positive dispersion regime, the non-solitonic radiation propagates as long pulses under the influence of dispersion and SPM. This behavior is illustrated in Fig. 5.8(a) and (b). Around ZDW the autocorrelation trace shows clear evidence of pulse breakup (Fig. 5.8(c)). The side peaks correspond to low energy solitons which experience small frequency shift. The central feature is a 140 fs-long pulse attributed to residual pump. The very short duration of the central feature (much shorter than the original pump pulse

width) is a proof of soliton effect compression undergone by pump pulses before breaking up into fundamental solitons. This is in agreement with the theoretical predictions of [222]. Fig. 5.8(e–h) show Raman solitons originating in the pump pulse and red shifted by SSFS. The clean autocorrelation trace is a clear indication of fundamental soliton pulses that propagate undisturbed through the fiber. From this perspective, the obtained supercontinuum radiation constitutes an ideal source of ultrashort pulses tunable over 600 nm. The temporal behavior of pulses extracted from the supercontinuum radiation at both positive and negative sides of the fiber dispersion has been tested by displaying the pulse trains on an analog oscilloscope. The soliton pulses formed a well defined trace of the screen, whereas the tops of the pulses extracted from the positive dispersion side could not be clearly visualized owing to the large amplitude noise.
The structure of the supercontinuum radiation has been investigated and clear evidence of soliton fission effects has been found. The supercontinuum radiation is an attractive tunable source of ultrashort pulses.

5.5 Generation of all-visible supercontinuum in fiber tapers

Selected applications of supercontinuum in biology, medical sciences, and machine vision require visible-only supercontinuum without parasitic infrared components. For such applications, broad spectra generated using infrared lasers (such as the one in Fig. 5.7) are not only inefficient but also deleterious, as the large amount of energy hosted in the infrared spectral range can damage the biological samples or saturate the vision sensors. Novel solutions are required to provide continuum radiation suitable for these applications. Filtering out the infrared part of the spectrum in Fig. 5.7 is difficult, owing to the wide bandwidth and the large amount of power contained therein. Based on the current understanding of supercontinuum formation mechanisms, the best option for generating a customized broadband radiation is employing a pump source emitting at a wavelength close to the center of the required spectrum, backed by a suitable nonlinear fiber exhibiting ZDW at the pump wavelength. For the particular case of visible light, the pump and the ZDW of the nonlinear fiber should be in the green light range (500 nm). Until recently, the unavailability of ultrashort pulse lasers at 500 nm and difficulty in manufacturing fibers with ZDW in this range made this solution impractical.

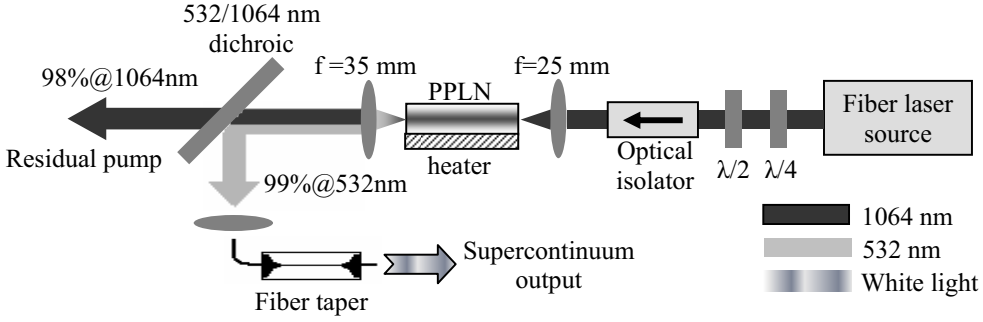

Fig. 5.9. Optical setup for visible supercontinuum generation

Using the technology and methods developed within the scope of this thesis, we generated pure white light supercontinuum in tapered optical fibers pumped with a frequency-doubled mode-locked Yb fiber laser **[P9]**. Efficient QPM frequency doubling of a robust mode-locked Yb fiber laser provided a high-power ultrashort pulse source

operating at 531 nm, conveniently located amidst the visible range. The precise fiber tapering technique described in chapter 3 allowed us to accurately control the ZDW of the taper to match the pumping wavelength. The optical setup is detailed in Fig. 5.9. The fiber laser source is frequency doubled in a 10 mm-long PPLN crystal similar to those described in chapter 4. The second harmonic light was separated from the residual fundamental by a dichroic mirror. The second harmonic light was then coupled into the fiber taper.

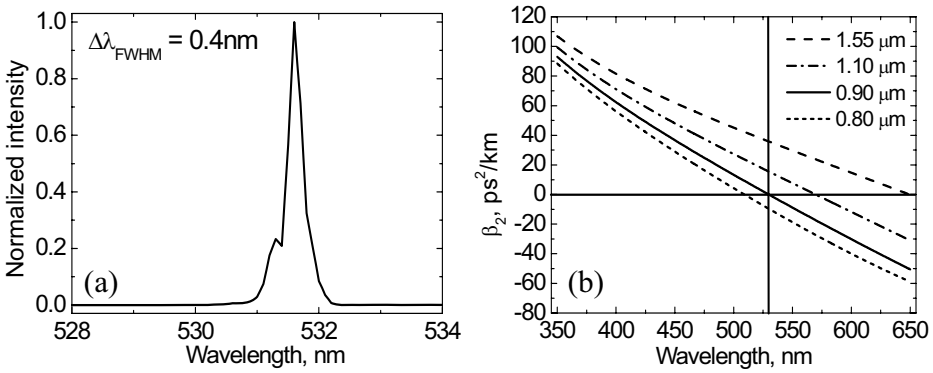

Fig. 5.10. (a) Optical spectrum of the second harmonic light used as pump and (b) chromatic dispersion characteristics of the tapers.

Figure 5.10 shows the optical spectrum of the second harmonic light and the chromatic dispersion characteristic of the tapers used for supercontinuum generation.

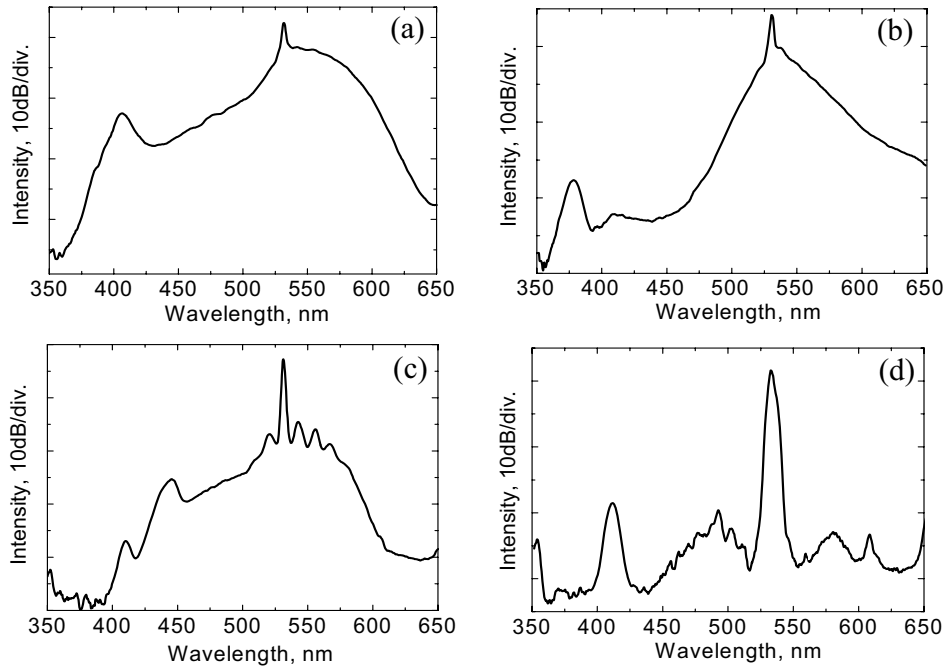

Fig. 5.11. Supercontinuum spectra obtained using tapers with waist diameters of (a) 0.9 μm, (b) 0.8 μm, (c) 1.1 μm, and (d) 1.55 μm.

A series of four tapers with increasing waist diameters exhibiting both positive, zero, and negative dispersion at the pump wavelength (as shown in Fig. 5.10(b)) has been

manufactured. This enables determining of the most efficient supercontinuum generator configuration. The supercontinuum spectra obtained by placing the tapers in sequence at the output of the frequency converted system are shown in Fig. 5.11(a–d). For each taper, 80 mW of 531.6 nm light was coupled into the single-mode input pigtail. The widest spectrum is obtained by the 0.9 μm waist taper (Fig. 5.11(a)) due to its ZDW being closest to the pump wavelength. The nonsolitonic radiation peak is visible in the spectrum at 402 nm. At full input power, the supercontinuum average power is 55 mW, yielding a spectral power density of 0.17 mW/nm. The 0.8 μm waist taper (Fig. 5.11(b)) exhibits higher negative dispersion at pump wavelength and behaves as discussed in the previous section: the spectrum is less smooth (owing to the lower soliton number) and the amount of red shifted radiation is larger (the amount of SSFS experienced by the fundamental solitons increases with chromatic dispersion). The nonsolitonic radiation peak extends further into the blue range (375 nm) owing to phase matching occurring at shorter wavelengths. The end-to-end spectral width is larger than in the previous case but at the expense of spectral smoothness. Figures 5.11(c) and (d) show the supercontinuum spectra obtained with positive dispersion tapers (consequently less efficient). Owing to the positive dispersion regime, traces of SSFS are barely visible on the right-hand side of Fig. 5.11(c). Also, the phase matched nonsolitonic radiation is formed at longer wavelengths. In the particular case of fiber tapers, large positive dispersion is always associated with low nonlinearity (due to thicker taper waist, as seen in Fig. 5.10(b)). This explains the poor broadening seen in Fig. 5.11(d), where only discreet peaks can be noticed. The results in Fig. 5.11 indicate that the supercontinuum generation efficiency depends strongly on the taper waist diameter accuracy. A waist diameter deviation of only 0.2 μm from the optimal value (0.9 μm) leads to significant changes in the supercontinuum spectrum.

Using the mature fiber taper technology, all-visible supercontinuum radiation can be obtained in a compact and stable setup. Intense ultrashort pulses in the green range (531.6 nm) have been obtained from a frequency-doubled Yb fiber source using a robust PPLN crystal. The described supercontinuum source may provide a solution to the all-visible broadband radiation problem.

6 Conclusions

This thesis aims at designing fiber lasers optimized for frequency conversion and supercontinuum generation applications. The research work addresses various aspects of frequency-converted laser sources, such as the mode-locked laser used as pump source, the fiber-based power amplifier, the frequency doubling and tripling stages, and the nonlinear waveguides for supercontinuum generation.

Short wavelength (~900 nm) generation directly from a mode-locked laser was demonstrated using Nd-doped single mode fiber as gain medium. Despite its widespread use as gain material in bulk lasers, Nd has only recently earned recognition in fiber lasers. The work performed in this thesis resulted in the shortest wavelength mode-locked fiber laser at the time (880 nm). The use of all-fiber intracavity components allowed for efficient suppression of the parasitic 1060-nm radiation, characteristic to Nd-based systems. The laser was self-starting and produced sub-picosecond pulses with an average power of 1 mW. The grating pair used for dispersion compensation allowed for tuning of the laser operation wavelength within a 30-nm band.

A custom designed single-mode fiber taper was used to provide intracavity dispersion compensation to a short Yb-doped fiber laser. This resulted in a very compact cavity layout, suitable for small footprint laser sources. A three-fold reduction in the pulsewidth has been recorded, following the insertion of the fiber taper in the laser cavity. Soliton sidebands were identified in the laser spectrum, which constituted a clear indication of soliton pulse operation as a result of dispersion compensation.

Stable synchronization between two mode-locked fiber lasers was achieved using cross phase modulation (XPM) in a single-mode optical fiber. Owing to the fiber-based interaction medium, the repetition rates of the lasers were robustly locked to each other. The lasers tolerated a change in the cavity length of up to 150 μm without losing synchronization. This constitutes a very reliable noise-cancellation mechanism, particularly useful for time-sensitive applications.
Using a similar cavity design, an all-optical clocking mechanism suitable for mode-locked fiber lasers was devised. An Yb-doped fiber laser was synchronized to an external optical clock supplied by a standard telecom diode laser. Precise timing of the laser could be accomplished using an electronic synthesizer used as driver for the diode laser. The system was tested against clock failure, and fast reacquisition of the clock signal was demonstrated.
The dissimilar gain spectra of Er- and Yb-doped fibers were used to assemble a dual-color laser. This special laser source emitted two synchronized trains of pulses at 1550 nm and 1040 nm. Pulse synchronization was performed by XPM interaction in a shared fiber cavity.

Having an Yb-doped fiber laser as pump source, simultaneous second and third harmonic generation was demonstrated in a waveguided periodically-poled KTP crystal. A conversion efficiency of 33% for second harmonic and 2% for third harmonic waves was

recorded. Following a brief theoretical analysis, the third harmonic light was found to emerge from a non phase-matched process based on fourth order second harmonic generation in the periodically-poled crystal. The system constitutes a promising source of visible and UV laser pulses using a single frequency conversion stage.

Employing a pre-chirping technique, spectral compression of an ultrashort optical pulse was obtained in a fiber amplifier. This allowed for nearly transform-limited pulses to be obtained at the output of a fiber amplifier stage. The narrow-spectrum pulses are useful in frequency conversion experiments, as it provides a better matching with the small acceptance bandwidth of periodically-poled crystals. A frequency conversion efficiency of 66% was obtained using a 10 mm-long crystal pumped by the spectrally-compressed source.

Supercontinuum formation in photonic crystal fibers was investigated using spectrally-resolved autocorrelations. Soliton fission was found to be the key factor in spectral broadening, as it converts the pump pulses into multiple fundamental solitons, associated with the long-wavelength extension of the supercontinuum spectrum. The short-wavelength side of the broadband spectrum is given by phase-matched nonsolitonic radiation emitted during soliton fission. Experimental evidence of soliton fission was found and the measured features were consistent with the theory. Using a tunable filter, the supercontinuum radiation was proved to be a reliable source of ultrashort pulses in a broad wavelength range.

For biological applications, where the large amount of infrared radiation present in ordinary supercontinuum is deleterious, an all-visible supercontinuum source was demonstrated. Starting from a frequency-doubled Yb fiber laser, truly all-visible broadband light spanning from 400 nm to 650 nm was generated in a custom designed (and rather unique) fiber taper exhibiting zero-dispersion wavelength at 532 nm. A special fiber pulling technique was developed to manufacture the thin (0.9 μm) and long (20 cm) fiber taper with low losses and good uniformity.

References

[1] O. Svelto, "Principles of lasers 4th ed.," Plenum Press, 330 (1998).
[2] R. Knox, "Ultrashort processes and biology," *J. Photochem. Photobiol. B: Biol.* **49**, 81–88 (1999).
[3] G. Feher, "Three decades of research in bacterial photosynthesis and the road leading to it: A personal account," *Photosynthesis Research* **55,** 1–40 (1998).
[4] A. H. Zewail, "Femtochemistry: Recent Progress in Studies of Dynamics and Control of Reactions and Their Transition States," *J. Phys. Chem.* **100**, 12701–12724 (1996).
[5] Erwin J.G. Peterman, René Monshouwer, Ivo H.M. van Stokkum, Rienk van Grondelle, and Herbert van Amerongen, "Ultrafast singlet excitation transfer from carotenoids to chlorophylls via different pathways in light-harvesting complex II of higher plants," *Chem. Phys. Lett.* **264**, 279–284 (1997).
[6] W. Rudolph, P. Dorn, X. Liu, N. Vretenar, and R. Stock, "Microscopy with femtosecond laser pulses: applications in engineering, physics, and biomedicine," *Appl. Surf. Sci.* **208–209**, 327–332 (2003).
[7] J. Jasapara and W. Rudolph, "Characterization of sub-10-fs pulse focusing with high numerical-aperture microscope objectives," *Opt. Lett.* **24**, 777–779 (1999).
[8] G. A. Keeler, B. E. Nelson, D. Agarwal, C. Debaes, N. C. Helman, A. Bhatnagar, D. A. B. Miller, "The benefits of ultrashort optical pulses in optically interconnected systems," *IEEE Sel. Topics in Quantum Electron.* **9**, 477–485 (2003).
[9] B. Agate, C. T. A. Brown, W. Sibbett, and K. Dholakia, "Femtosecond optical tweezers for *in-situ* control of two-photon fluorescence," *Opt. Express* **12**, 3011–3017 (2004).
[10] Paul J. Campagnola, Mei-de Wei, Aaron Lewis, and Leslie M. Loew, "High-Resolution Nonlinear Optical Imaging of Live Cells by Second Harmonic Generation," *Biophys. J.* **77**, 3341–3349 (1999).
[11] E. Bordenave, E. Abraham, G. Jonusauskas, J. Oberlé and C. Rullière, "Longitudinal imaging in biological tissues with a single laser shot correlation system," *Opt. Express* **10**, 35–40 (2002).
[12] Q. Ye, L. Shah, J. Eichenholzb, D. Hammons, R. Peale, M. Richardson, A. Chin, B.H.T. Chai, "Investigation of diode-pumped, self-frequency doubled RGB lasers from Nd:YCOB crystals," *Opt. Commun.* **164**, 33–37 (1999).
[13] D. Jaque, J. Capmany, and J. García Solé, "Red, green, and blue laser light from a single Nd:$YAl_3(BO_3)_4$ crystal based on laser oscillation at 1.3 μm," *Appl. Phys. Lett.* **75**, 325–327 (1999).
[14] B. H. T. Chai, J. M. Eichenholz, Q. Ye, W. K. Jang, M. Richardson, *Technical Digest of CLEO'98*, Vol.**6**, CThA6, (1998).
[15] F. H. Loesel, M. H. Niemz, J. F. Bille, and T. Juhasz, "Laser-Induced Optical Breakdown on Hard and Soft Tissues and Its Dependence on the Pulse Duration: Experiment and Model," *IEEE J. Quantum Electron.* **32**, 1717–1722 (1996).
[16] T. Juhasz, F. H. Loesel, R. M. Kurtz, C. Horvath, J. F. Bille, and G. Mourou, "Corneal Refractive Surgery with Femtosecond Lasers," *IEEE Sel. Topics in Quantum Electron.* **5**, 902–910 (1999).

[17] F. Korte, S. Adams, A. Egbert, C. Fallnich, A. Ostendorf, S. Nolte, M. Will, J. -P. Ruske, B. Chichkov, and A. Tunnermann, "Sub-diffraction limited structuring of solid targets with femtosecond laser pulses," *Opt. Express* **7**, 41–49 (2000).
[18] N. N. Nedialkov, S. E. Imamova, and P. A. Atanasov, "Ablation of metals by ultrashort laser pulses," *J. Phys. D: Appl. Phys.* **37,** 638–643 (2004).
[19] G. Korn, A. Thoss, H. Stiel, U. Vogt, M. Richardson, T. Elsaesser, and M. Faubel, "Ultrashort 1-kHz laser plasma hard x-ray source," *Opt. Lett.* **27**, 866–868 (2002).
[20] H. Kano and H. -o. Hamaguchi, "Characterization of a supercontinuum generated from a photonic crystal fiber and its application to coherent Raman spectroscopy," *Opt. Lett.* **28**, 2360–2362 (2003).
[21] D. L. Marks, A. L. Oldenburg, J. J. Reynolds, and S. A. Boppart, "Study of an ultrahigh-numerical-aperture fiber continuum generation source for optical coherence tomography," *Opt. Lett.* **27**, 2010–2012 (2002).
[22] J. H. V. Price, T. M. Monro, K. Furusawa, W. Belardi, J. C. Baggett, S. Coyle, C. Netti, J. J. Baumberg, R. Paschotta, and D. J. Richardson, "UV generation in a pure-silica holey fiber," *Appl. Phys. B* **77**, 291–298 (2003).
[23] M. Bellini and T. W. Hänsch, "Phase-locked white-light continuum pulses: toward a universal optical frequency-comb synthesizer," *Opt. Lett.* **25**, 1049–1051 (2000).
[24] U. Keller, "Recent developments in compact ultrafast lasers," *Nature* **424**, 831–838 (2003).
[25] M. E. Fermann, A. Galvanauskas, G. Sucha, and D. Harter, "Fiber-lasers for ultrafast optics," *Appl. Phys. B* **65**, 259–275 (1997).
[26] E. Snitzer, "Optical maser action of Nd^{+3} in a Barium crown glass," *Phys. Rev. Lett.* **7**, 444–446 (1961).
[27] C. J. Koester and E. Snitzer, "Amplification in a Fiber Laser," *Appl. Opt.* **3**, 1182–1186 (1964).
[28] C. A. Burrus and J. Stone, "Single crystal fiber optical devices: a Nd:YAG fiber laser," *Appl. Phys. Lett.* **26,** 318–320 (1975).
[29] C. A. Burrus and J. Stone, "Room-temperature continuous operation of a ruby fiber laser," *J. Appl. Phys.* **49**, 3118–3123 (1978).
[30] J. L. Nightingale and R. L. Byer, "A guided wave monolithic resonator ruby fiber laser," *Opt. Commun.* **56**, 41–45 (1985).
[31] C. J. Koester, "Laser Action by Enhanced Total Internal Reflection," *IEEE J. Quantum Electron.* **QE–2**, 580–584 (1966).
[32] J. Stone and C. A. Burrus, "Nd : Y_2O_3 single-crystal fiber laser: Room-temperature cw operation at 1.07- and 1.35-μm wavelength," *J. Appl. Phys.* **49**, 2281–2287 (1978).
[33] J. Stone, C. A. Burrus, A. G. Dentai, and B. I. Miller, "Nd:YAG single-crystal fiber laser: Room-temperature cw operation using a single LED as an end pump," *Appl. Phys. Lett.* **29,** 37–39 (1976).
[34] J. Stone and C.A. Burrus, "Neodymium-doped silica lasers in end-pumped fiber geometry," *Appl. Phys. Lett.* **23,** 388–389 (1973).
[35] S. B. Poole, D. N. Payne, and M. E. Fermann, "Fabrication of low-loss optical fibres containing rare-earth ions," *Electron. Lett.* **21**, 737–738 (1985).
[36] R. J. Mears, L. Reekie, S. B. Poole, and D. N. Payne, "Neodymium-doped silica single-mode fibre lasers," *Electron. Lett.* **21**, 738–740 (1985).

[37] S. B. Poole, D. N. Payne, R. J. Mears, M. E. Fermann, and R. I. Laming, "Fabrication and Characterization of Low-Loss Optical Fibers Containing Rare-Earth Ions," *J. Lightwave Technol.* **LT–4**, 870–876 (1986).
[38] S. B. Poole, J. E. Townsend, D. N. Payne, M. E. Fermann, C. J. Cowle, R. I. Laming, and P. R. Morkel, "Characterization of Special Fibers and Fiber Devices," *J. Lightwave Technol.* **LT–7**, 1242–1255 (1989).
[39] L. Reekie, R. J. Mears, S. B. Poole, and D. N. Payne, "Tunable Single-Mode Fiber Lasers," *J. Lightwave Technol.* **LT–4**, 956-960 (1986).
[40] K. C. Kao and G. A. Hockham, "Dielectric-fibre surface waveguides for optical frequencies," *IEE Proc. J.* **133**, 191–198 (1986) – originally published in 1966 in *IEE Proc. J.*.
[41] M. G. Mayer, "Rare-Earth and Transuranic Elements," *Appl. Phys.* **60**, 184–187 (1941).
[42] P. C: Becker, N. A. Olsson, and J. R. Simpson, "Erbium-doped fiber amplifiers," Academic Press, San Diego, USA, 88 (1999).
[43] J. Becquerel, *Le Radium* **4**, 328 (1907).
[44] P. Urquhart, "Review of rare earth doped fibre lasers and amplifiers," *IEE Proc. J.* **135**, 385–407 (1988).
[45] B. R. Judd, "Complex Atomic Spectra," *Rep. Prog. Phys.* **48**, 907–954 (1985).
[46] M. Zurn, J. Voigt, E. Brinkmeyer, R. Ulrich, and S. B. Poole, "Line narrowing and spectral hole burning in single-mode Nd^{3+}-fiber lasers," *Opt. Lett.* **12**, 316–318 (1987).
[47] C. Brecher, L. A. Riseberg, and M. J. Weber, "Line-narrowed fluorescence spectra and site-dependent transition probabilities of Nd^{3+} in oxide and fluoride glasses," *Phys. Rev. B* **18**, 5799–5811 (1978).
[48] S. Tanabe, "Optical transitions of rare earth ions for amplifiers: how the local structure works in glass," *J. Non-Cryst. Sol.* **259,** 1–9 (1999).
[49] H. Ebendorff-Heidepriem, D. Ehrt, M. Bettinelli and A. Speghini, "Effect of glass composition on Judd–Ofelt parameters and radiative decay rates of Er^{3+} in fluoride phosphate and phosphate glasses," *J. Non–Cryst. Sol.* **240,** 66–78 (1998).
[50] B. J. Ainslie, S. P. Craig and S. T. Davey, "The fabrication and optical properties of Nd^{3+} in silica-based optical fibres," *Mat. Lett.* **5**, 143–146 (1987).
[51] B. J. Ainslie, S. P. Craig, S. T. Davey and B. Wakefield, "The fabrication, assessment and optical properties of high-concentration Nd^{3+}- and Er^{3+}-doped silica-based fibres," *Mat. Lett.* **6**, 139–144 (1988).
[52] W. Tian and B. Rami Reddy, "Ultraviolet upconversion in thulium-doped fluorozirconate fiber observed under two-color excitation," *Opt. Lett.* **26**, 1580–1582 (2001).
[53] D. M. Costantini, H. G. Limberger, T. Lasser, C. A. P. Muller, H. Zellmer, P. Riedel, and A. Tünnermann, "Actively mode-locked visible upconversion fiber laser," *Opt. Lett.* **25**, 1445–1447 (2000).
[54] F. Auzel and P. Goldner, "Towards rare-earth clustering control in doped glasses," *Opt. Mater.* **16**, 93–103 (2001).
[55] B. J. Ainslie, S. P. Craig, S. T. Davey, D. J. Barber, J. R. Taylor, and A. S. L. Gomes, "Optical and structural investigation of Nd^{3+} in silica-based fibres," *J. Mater. Sci. Lett.* **6**, 1361–1363 (1987).

[56] Y. Nishida, M. Yamada, T. Kanamori, K. Kobayashi, J. Temmyo, S. Sudo, and Y. Ohishi, "Development of an Efficient Praseodymium-Doped Fiber Amplifier," *IEEE J. Quantum Electron.* **34**, 1332–1339 (1998).
[57] Tadashi Kasamatsu, Yutaka Yano, and Takashi Ono, "Gain-Shifted Dual-Wavelength-Pumped Thulium-Doped Fiber Amplifier for WDM Signals in the 1.48–1.51-μm Wavelength Region," *IEEE Photon. Technol. Lett.* **13**, 31–33 (2001).
[58] W. A. Clarkson, N. P. Barnes, P. W. Turner, J. Nilsson, and D. C. Hanna, "High-power cladding-pumped Tm-doped silica fiber laser with wavelength tuning from 1860 to 2090 nm," *Opt. Lett.* **27**, 1989–1991 (2002).
[59] S.-K. Liaw and Y.-K. Chen, "Passive Gain-Equalized Wide-Band Erbium-Doped Fiber Amplifier Using Samarium-Doped Fiber," *IEEE Photon. Technol. Lett.* **8**, 879–881 (1996).
[60] S. D. Jackson, "Single-transverse-mode 2.5-W holmium-doped fluoride fiber laser operating at 2.86 μm ," *Opt. Lett.* **29**, 334–336 (2004).
[61] L. Wetenkamp, "Efficient CW operation of a 2.9 μm Ho^{3+}-doped fluorozirconate fibre laser pumped at 640 nm," *Electron. Lett.* **13**, 883–884 (1990).
[62] B. J. Ainslie, S. P. Craig, S. T. Davey, "The Absorption and Fluorescence Spectra of Rare Earth Ions in Silica-Based Monomode Fiber," *IEEE J. Lightwave Technol.* **6**, 287–293 (1988).
[63] A. Liu, M. A. Norsen, and R. D. Mead, "60-W green output by frequency doubling of a polarized Yb-doped fiber laser," *Opt. Lett.* **30**, 67–69 (2005).
[64] O. G. Okhotnikov and J. R. Salcedo, "Spectroscopy of the transient oscillations in a Nd^{3+}-doped fiber laser for the four-level $^4F_{3/2}$-$^4I_{11/2}$ (1060 nm) and three-level $^4F_{3/2}$-$^4I_{9/2}$ (900 nm) transitions," *Appl. Phys. Lett.* **64,** 2619–2621 (1994).
[65] O. G. Okhotnikov, V. V. Kuzmin, and J. R. Salcedo, "General Intracavity Method for Laser Transition Characterization by Relaxation Oscillations Spectral Analysis," *IEEE Photon. Technol. Lett.* **6**, 362–364 (1994).
[66] R. Reisfeld, G. Katz, C. Jacoboni, R. De Pape, M. G. Drexhage, R. N. Brown, and C. K. Jørgensen, "The comparison of calculated transition probabilities with luminescence characteristics of erbium(III) in fluoride glasses and in the mixed yttrium-zirconium oxide crystal," *J. Sol. Stat. Chem.* **48**, 323–332 (1983).
[67] H. W. Etzel, H. W. Gandy, and R. J. Ginther, "Stimulated Emission of Infrared Radiation from Ytterbium Activated Silicate Glass," *Appl. Opt.* **1**, 534–536 (1962).
[68] D.C. Hanna, R.M. Percival, I.R. Perry, R.G. Smart, P.J. Suni, J.E. Townsend, and A.C. Tropper, "Continuous-wave oscillation of a monomode ytterbium-doped fibre laser," *Electron. Lett.* **24**, 1111–1113 (1988).
[69] R. Paschotta, J. Nilsson, A. C. Tropper, and D. C. Hanna, "Ytterbium-Doped Fiber Amplifiers," *IEEE J. Quantum Electron.* **33**, 1049–1056 (1997).
[70] L. Orsila and O. Okhotnikov, "Three- and four-level transition dynamics in Yb-fiber laser," *Opt. Express* **13**, 3218–3223 (2005).
[71] D. Strickland and G. Mourou, "Compression of amplified chirped optical pulses," *Opt. Comm.* **56**, 219–221 (1985).
[72] A. Baltuška, Z.Wei, M.S. Pshenichnikov, D.A. Wiersma, R. Szipocs, "All-solid-state cavity-dumped sub-5-fs laser," *Appl. Phys. B* **65**, 175–188 (1997).

[73] N. Onodera, H. Ito, and H. Inaba, “Fourier-transform-limited, single-mode picosecond optical pulse generation by a distributed feedback InGaAsP diode laser,” *Appl. Phys. Lett.* **45**, 843–845 (1984).
[74] O. Svelto, “Principles of lasers 4th ed.,” Plenum Press, 335 (1998).
[75] D. J. Kuizenga and A. E. Siegman, “FM and AM Mode-locking of the homogeneous laser – Part I: Theory,” *IEEE J. Quantum Electron.* **QE–6**, 694–708 (1970).
[76] M.J. Guy, J.R. Taylor, and K. Wakita, “10 GHz 1.9 ps actively modelocked fibre integrated ring laser at 1.3μm,” *Electron. Lett.* **33**, 1630–1631 (1997).
[77] F. X. Kärtner, D. Kopf, and U. Keller, "Solitary-pulse stabilization and shortening in actively mode-locked lasers," *J. Opt. Soc. Am. B* **12**, 486–496 (1995).
[78] D. J. Jones, H. A. Haus, and E. P. Ippen, "Subpicosecond solitons in an actively mode-locked fiber laser," *Opt. Lett.* **21**, 1818–1820 (1996).
[79] N. J. Doran and D. Wood, "Nonlinear-optical loop mirror," *Opt. Lett.* **13**, 56–58 (1988).
[80] D. B. Mortimore, “Fibre loop reflectors,” *J. Lightwave. Technol.* **6**, 1217–1224 (1988).
[81] M. E. Fermann, F. Haberl, M. Hofer, and H. Hochreiter, "Nonlinear amplifying loop mirror," *Opt. Lett.* **15**, 752–754 (1990).
[82] D. J. Richardson, R. I..Laming, and D. N. Payne, “Very low threshold Sagnac switch incorporating an erbium doped fibre amplifier,” *Electron. Lett.* **26**, 1779–1781 (1990).
[83] A. G. Bulushev, E. M. Dianov, and O. G. Okhotnikov, "Passive mode locking of a laser with a nonlinear fiber reflector," *Opt. Lett.* **15**, 968–970 (1990).
[84] D. I. Richardson, R. I. Laming, D. N. Payne, V. Matsas, and M. W. Phillips, “Selfstarting, Passively Modelocked Erbium Fibre Ring Laser Based on the Amplifying Sagnac Switch,” *Electron. Lett.* **27**, 542–543 (1991).
[85] I. N. Duling III, “Subpicosecond All-Fibre Erbium Laser,” *Electron. Lett.* **27**, 543–544 (1991).
[86] I. N. Duling III, "All-fiber ring soliton laser mode locked with a nonlinear mirror," *Opt. Lett.* **16**, 539–541 (1991).
[87] K. J. Blow, N. J. Doran, and B. K. Nayar, "Experimental demonstration of optical soliton switching in an all-fiber nonlinear Sagnac interferometer," *Opt. Lett.* **14**, 754–756 (1989).
[88] D. I. Richardson, R. I. Laming, D. N. Payne, V. Matsas, and M. W. Phillips, “Pulse repetition rates in passive, selfstarting, femtosecond soliton fibre laser,” *Electron. Lett.* **27**, 1451–1453 (1991).
[89] A. B. Grudinin, D. J. Richardson and D. N. Payne, “Energy Quantisation in Figure Eight Fibre Laser,” *Electron. Lett.* **28**, 67–68 (1992).
[90] L.E. Adams, E.S. Kintzer and J.G. Fujimoto, “All-optical timing extraction at 40GHz using a mode-locked figure-eight laser with an SLA,” *Electron. Lett.* **31**, 1759–1761 (1995).
[91] W. Margulis, K. Rottwitt, and J. R. Taylor, “High-power figure-of-eight laser for soliton transmission experiments,” *Electron. Lett.* **31**, 645–647 (1995).
[92] A. Boskovic, S.V. Chernikov and J.R. Taylor, “Femtosecond figure of eight Yb:Er fibre laser incorporating a dispersion decreasing fibre,” *Electron. Lett.* **31**, 1446–1448 (1995).

[93] R. H. Stolen, J. Botineau, and A. Ashkin, "Intensity discrimination of optical pulses with birefringent fibers," *Opt. Lett.* **7**, 512–514 (1982).
[94] M. Hofer, M. E. Fermann, F. Haberl, M. H. Ober, and A. J. Schmidt, "Mode locking with cross-phase and self-phase modulation," *Opt. Lett.* **16**, 502–504 (1991).
[95] C. -J. Chen, P. K. A. Wai, and C. R. Menyuk, "Soliton fiber ring laser," *Opt. Lett.* **17**, 417–419 (1992).
[96] V. J. Matsas, W. H. Loh, D. J. Richardson, "Self-starting, passively mode-locked Fabry-Perot fiber soliton laser using nonlinear polarization evolution," *IEEE Photon. Technol. Lett.* **5**, 492–494 (1993).
[97] H. A. Haus, E. P. Ippen, and K. Tamura, "Additive-Pulse Modelocking in Fiber Lasers," *IEEE J. Quantum Electron.* **30**, 200–208 (1994).
[98] K. Tamura, H. A. Haus, E. P. Ippen, "Self-starting additive pulse mode-locked erbium fibre ring laser," *Electron. Lett.* **28**, 2226–2228 (1992).
[99] M. H. Ober, M. Hofer, and M. E. Fermann, "42-fs pulse generation from a mode-locked fiber laser started with a moving mirror," *Opt. Lett.* **18**, 367–369 (1993).
[100] T. F. Carruthers and I. N. Duling III, "10-GHz, 1.3-ps erbium fiber laser employing soliton pulse shortening," *Opt. Lett.* **21**, 1927–1929 (1996).
[101] A. C. Selden, "Pulse transmission through a saturable absorber," *Br. J. Appl. Phys.* **18** 743–748 (1967).
[102] A. F. Gibson, M. F. Kimmitt, and B. Norris, "Generation of bandwidth-limited pulses from a TEA CO_2 laser using p-type germanium," *Appl. Phys. Lett.* **24**, 306–307 (1974).
[103] M. Zirngibl, L. W. Stulz, J. Stone, J. Hugi, D. DiGiovanni, P.B. Hansen, "1.2 ps pulses from passively mode-locked laser diode pumped Er-doped fibre ring laser," *Electron. Lett.* **27**, 1734–1735 (1991).
[104] U. Siegner, R. Fluck, G. Zhang, and U. Keller, "Ultrafast high-intensity nonlinear absorption dynamics in low-temperature grown gallium arsenide," *Appl. Phys. Lett.* **69**, 2566–2568 (1996).
[105] U. Keller, K. J. Weingarten, F. X. Kärtner, D. Kopf, B. Braun, I. D. Jung, R. Fluck, C. Hönninger, N. Matuschek, and J. A. der Au, "Semiconductor Saturable Absorber Mirrors (SESAM's) for Femtosecond to Nanosecond Pulse Generation in Solid-State Lasers," *IEEE Sel. Topics Quantum Electron.* **2**, 435–453 (1996).
[106] Y. Deng, M. Koch, F. Lu, G. Wicks, and W. Knox, "Colliding-pulse passive harmonic mode-locking in a femtosecond Yb-doped fiber laser with a semiconductor saturable absorber," *Opt. Express* **12**, 3872–3877 (2004).
[107] A. Isomäki, M. D. Guina, P. Tuomisto, and O. G. Okhotnikov, "Fiber Laser Mode-Locked with a Semiconductor Saturable Absorber Etalon Operating in Transmission," *IEEE Photon. Technol. Lett.* **18**, (2006).
[108] U. Keller, D. A. B. Miller, G. D. Boyd, T. H. Chiu, J. F. Ferguson, and M. T. Asom, "Solid-state low-loss intracavity saturable absorber for Nd:YLF lasers: an antiresonant semiconductor Fabry - Perot saturable absorber," *Opt. Lett.* **17**, 505–507 (1992).
[109] M. Guina, N. Xiang, and O.G. Okhotnikov, "Stretched-pulse fiber lasers based on semiconductor saturable absorbers," *Appl. Phys. B* **47** (suppl.), S193–S200 (2002).
[110] R. Herda and O. G. Okhotnikov, "Dispersion compensation-free fiber laser mode-locked and stabilized by high-contrast saturable absorber mirror," *IEEE J. Quantum Electron.* **40**, 893–899 (2004).

[111] M. Haiml, R. Grange, and U. Keller, “Optical characterization of semiconductor saturable absorbers,” *Appl. Phys. B* **79**, 331–339 (2004).
[112] F. X. Kärtner, J. A. der Au, and Ursula Keller, “Mode-Locking with Slow and Fast Saturable Absorbers-What’s the Difference?,” *IEEE Sel. Topics Quantum Electron.* **4**, 159–168 (1998).
[113] H. A. Haus, “Theory of mode locking with a fast saturable absorber,” *J. Appl. Phys.* **46**, 3049–3058 (1975).
[114] M. J. Lederer, B. Luther-Davies, H. H. Tan, C. Jagadish, M. Haiml, U. Siegner, and U. Keller, “Nonlinear optical absorption and temporal response of arsenic- and oxygen-implanted GaAs,” *Appl. Phys. Lett.* **74**, 1993–1995 (1999).
[115] E. P. Burr, J. B. Song, A. J. Seeds, and C. C. Button, “28 ps recovery time in an InGaAsP/InGaAsP multiple-quantum-well saturable absorber employing carrier sweepout,” *J. Appl Phys.* **90**, 3566–3569 (2001).
[116] F. X. Kärtner, I. D. Jung, and U. Keller, “Soliton Mode-Locking with Saturable Absorbers,” *IEEE Sel. Topics Quantum Electron.* **2**, 540–556 (1996).
[117] R: Paschotta and U. Keller, “Passive mode locking with slow saturable absorbers,” *Appl. Phys. B* **73**, 653–662 (2001).
[118] M. Guina, N. Xiang, A. Vainionp, O. G. Okhotnikov, T. Sajavaara, and J. Keinonen, "Self-starting stretched-pulse fiber laser mode locked and stabilized with slow and fast semiconductor saturable absorbers ," *Opt. Lett.* **26**, 1809–1811 (2001).
[119] M. E. Fermann, M. J. Andrejco, Y. Silberberg, and A. M. Weiner, "Generation of pulses shorter than 200 fs from a passively mode-locked Er fiber laser," *Opt. Lett.* **18**, 48–50 (1993).
[120] O. G. Okhotnikov, L. Gomes, N. Xiang, T. Jouhti, and A. B. Grudinin, "Mode-locked ytterbium fiber laser tunable in the 980–1070-nm spectral range ," *Opt. Lett.* **28**, 1522–1524 (2003).
[121] R. C. Sharp, D. E. Spock, N. Pan, and J. Elliot, "190-fs passively mode-locked thulium fiber laser with a low threshold," *Opt. Lett.* **21**, 881–883 (1996).
[122] B. C. Barnett, L. Rahman, M. N. Islam, Y. C. Chen, P. Bhattacharya, W. Riha, K. V. Reddy, A. T. Howe, K. A. Stair, H. Iwamura, S. R. Friberg, and T. Mukai, "High-power erbium-doped fiber laser mode locked by a semiconductor saturable absorber," *Opt. Lett.* **20**, 471–473 (1995).
[123] F. Ö. Ilday, F. W. Wise, and T. Sosnowski, "High-energy femtosecond stretched-pulse fiber laser with a nonlinear optical loop mirror ," *Opt. Lett.* **27**, 1531–1533 (2002).
[124] S. Höfer, A. Liem, J. Limpert, H. Zellmer, A. Tünnermann, S. Unger, S. Jetschke, H. -R. Müller, and I. Freitag, "Single-frequency master-oscillator fiber power amplifier system emitting 20 W of power," *Opt. Lett.* **26**, 1326–1328 (2001).
[125] N. G. R. Broderick, H. L. Offerhaus, D. J. Richardson, and R. A. Sammut, “Power Scaling in Passively Mode-Locked Large-Mode Area Fiber Lasers,” *IEEE Photon. Technol. Lett.* **10**, 1718–1720 (1998).
[126] J. Nilsson, W. A. Clarkson, R. Selvas, J. K. Sahu, P. W. Turner, S. -U. Alam, and A. B. Grudinin, “High-power wavelength-tunable cladding-pumped rare-earth-doped silica fiber lasers,” *Opt. Fiber Technol.* **10**, 5–30 (2004).
[127] L. Goldberg, B. Cole, and E. Snitzer, “V-groove side-pumped 1.5 μm fibre amplifier,” *Electron. Lett.* **33**, 2127–2129 (1997).
[128] M. Hofer, M. E. Fermann, and L. Goldberg, “High-Power Side-Pumped Passively

Mode-Locked Er-Yb Fiber Laser," *IEEE Photon. Technol. Lett.* **10**, 1247–1249 (1998).
[129] F. Ö. Ilday, J. R. Buckley, H. Lim, F. W. Wise, and W. G. Clark, "Generation of 50-fs, 5-nJ pulses at 1.03 μm from a wave-breaking-free fiber laser," *Opt. Lett.* **28**, 1365–1367 (2003).
[130] A. Shirakawa, J. Ota, M. Musha, K. 'i. Nakagawa, K. -i. Ueda, J. R. Folkenberg, and J. Broeng, "Large-mode-area erbium-ytterbium-doped photonic-crystal fiber amplifier for high-energy femtosecond pulses at 1.55 μm," *Opt. Express* **13**, 1221–1227 (2005)
[131] J.C. Knight, T.A. Birks, R.F. Cregan, P.St. J. Russell, and J.-P. de Sandro, "Large mode area photonic crystal fibre," *Electron. Lett.* **34**, 1347–1348 (1998).
[132] J. Limpert, T. Schreiber, S. Nolte, H. Zellmer, T. Tunnermann, R. Iliew, F. Lederer, J. Broeng, G. Vienne, A. Petersson, and C. Jakobsen, "High-power air-clad large-mode-area photonic crystal fiber laser," *Opt. Express* **11**, 818–823 (2003).
[133] J. Limpert, T. Clausnitzer, A. Liem, T. Schreiber, H. -J. Fuchs, H. Zellmer, E. -B. Kley, and A. Tünnermann, "High-average-power femtosecond fiber chirped-pulse amplification system ," *Opt. Lett.* **28**, 1984–1986 (2003).
[134] J. Limpert, T. Schreiber, S. Nolte, H. Zellmer, and A. Tünnermann, "All fiber chirped-pulse amplification system based on compression in air-guiding photonic bandgap fiber," *Opt. Express* **11**, 3332–3337 (2003).
[135] J. Limpert, A. Liem, T. Gabler, H. Zellmer, A. Tünnermann, S. Unger, S. Jetschke, and H. -R. Müller, "High-average-power picosecond Yb-doped fiber amplifier," *Opt. Lett.* **26**, 1849–1851 (2001).
[136] J. Limpert, A. Liem, M. Reich, T. Schreiber, S. Nolte, H. Zellmer, A. Tünnermann, J. Broeng, A. Petersson, and C. Jakobsen, "Low-nonlinearity single-transverse-mode ytterbium-doped photonic crystal fiber amplifier," *Opt. Express* **12**, 1313–1319 (2004).
[137] H. Jones-Bey, "Expiring license opens field for solid-state blue lasers," *Laser Focus World* **36**, 133–137, (2000).
[138] W. J. Kozlovsky, W. Lenth, E. E. Latta, A. Moser, and G. L. Bona, "Generation of 41 mW of blue radiation by frequency doubling of a GaAlAs diode laser," *Appl. Phys. Lett.* **56**, 2291–2292 (1990).
[139] C.-W. Wang, Y.-L. Weng, P.-L. Huang, H.-Z. Cheng, and S.-L. Huang, "Passively Q -Switched Quasi-three-level laser and its intracavity frequency Doubling" *Appl. Opt.*, **41**, 1075–1081 (2002).
[140] C. D. Hussey, E. M. O'Brien, P. F. O'Sullivan, K. P. Oakley, "Adiabatic fused tapered couplers," *Electron. Lett.* **37**, 1009–1010 (2001).
[141] Y. Takeuchi, J. Noda, "Novel fiber coupler tapering process using a microheater," *IEEE J. Lightwave Technol.* **17**, 2356–2360 (1999).
[142] G. H. C. New, "Pulse Evoultion in Mode-Locked Quasi-Continuous Lasers," *IEEE J. Quantum Electron.* **QE–10**, 115–124 (1974).
[143] F. X. Kärtner and U. Keller, "Stabilization of solitonlike pulses with a slow saturable absorber," *Opt. Lett.* **20**, 16–18 (1995).
[144] I. D. Jung, F. X. Kärtner, L. R. Brovelli, M. Kamp, and U. Keller, "Experimental verification of soliton mode locking using only a slow saturable absorber," *Opt. Lett.* **20**, 1892–1894 (1995).
[145] R. L. Fork, O. E. Martinez, and J. P. Gordon, "Negative dispersion using pairs of prisms," *Opt. Lett.* **9**, 150–152 (1984).

[146] E. B. Treacy, “Optical pulse compression with diffraction gratings,” *IEEE J. Quantum Electron.* **QE–5**, 454–458 (1969).
[147] J. E. Roman and K. A. Winick, “Waveguide Grating Filters for Dispersion Compensation and Pulse Compression,” *IEEE J. Quantum Electron.* **29**, 975–982 (1993).
[148] J. Kuhl and J. Heppner, “Compression of femtosecond optical pulses with dielectric multilayer interferometers,” *IEEE J. Quantum Electron.* **QE–22**, 182–185 (1986).
[149] L. Orsila, L. A. Gomes, N. Xiang, T. Jouhti, O. G. Okhotnikov, “Mode-locked ytterbium fiber lasers,” *Appl. Opt.* **43**, 1902–1906 (2004).
[150] A. Isomäki, O. G. Okhotnikov, “All-fiber ytterbium soliton mode-locked laser with dispersion control by solid-core photonic bandgap fiber,” *Opt. Express* **14**, 4368–4373 (2006).
[151] T. A. Birks and Y. W. Li, “The Shape of Fiber Tapers,” *IEEE J. Lightwave Technol.* **10**, 432–438 (1992).
[152] S. Leon-Saval, T. Birks, W. Wadsworth, P. St. J. Russell, and M. Mason, "Supercontinuum generation in submicron fibre waveguides," *Opt. Express* **12**, 2864–2869 (2004).
[153] G. P. Agrawal, “Fiber-Optic Communication Systems,” John Wiley and sons, New York (1997).
[154] G. E. Forsythe, M. A. Malcolm, and C. B. Moler, “Computer Methods for Mathematical Computations,” *Prentice-Hall* ed., 1976.
[155] S. B. Darack, D. R. Dykaar, and G. T. Harvey, "Timing-jitter stabilization of a colliding-pulse mode-locked laser by active control of the cavity length," *Opt. Lett.* **16**, 1677–1679 (1991).
[156] K. Smith, and J. K. Lucek, “All-optical clock recovery using a mode-locked laser,” *Electron. Lett.* **28**, 1814–1816 (1992).
[157] D. M. Patrick, “Modelocked ring laser using nonlinearity in a semiconductor laser amplifier,” *Electron. Lett.* **30**, 43–44 (1994).
[158] D. E. Spence, W. E. Sleat, J. M. Evans, W. Sibbett, and J. D. Kafka, “Time synchronisation measurements between two self-modelocked Ti:sapphire lasers,” *Opt. Commun.* **101**, 286–296 (1993).
[159] S. A. Crooker, F. D. Betz, J. Levy, and D. D. Awschalom, “Femtosecond synchronization of two passively mode-locked Ti:sapphire lasers,” *Rev. Sci. Instrum.* **67**, 2068–2071 (1996).
[160] T. R. Schibli, J. Kim, O. Kuzucu, J. T. Gopinath, S. N. Tandon, G. S. Petrich, L. A. Kolodziejski, J. G. Fujimoto, E. P. Ippen, and F. X. Kaertner, "Attosecond active synchronization of passively mode-locked lasers by balanced cross correlation ," *Opt. Lett.* **28**, 947–949 (2003).
[161] L.-S. Ma, R. K. Shelton, H. C. Kapteyn, M. M. Murnane, and J. Ye, “Sub-10-femtosecond active synchronization of two passively mode-locked Ti:sapphire oscillators,” *Phys. Rev. A* **64**, 021802(1–4) (2001).
[162] M. R. X. de Barros and P. C. Becker, "Two-color synchronously mode-locked femtosecond Ti:sapphire laser," *Opt. Lett.* **18**, 631–633 (1993).
[163] A. Leitenstorfer, C. Furst, and A. Laubereau, "Widely tunable two-color mode-locked Ti:sapphire laser with pulse jitter of less than 2 fs," *Opt. Lett.* **20**, 916–918 (1995).
[164] M. Betz, F. Sotier, F. Tauser, S. Trumm, A. Laubereau, and A. Leitenstorfer, "All-optical phase locking of two femtosecond Ti:sapphire lasers: a passive coupling

mechanism beyond the slowly varying amplitude approximation," *Opt. Lett.* **29**, 629–631 (2004).
[165] Z. Wei, Y. Kobayashi, Z. Zhang, and K. Torizuka, "Generation of two-color femtosecond pulses by self-synchronizing Ti:sapphire and Cr:forsterite lasers ," *Opt. Lett.* **26**, 1806–1808 (2001).
[166] M. Jiang, W. Sha, L. Rahman, B. C. Barnett, J. K. Andersen, M. N. Islam, and K. V. Reddy, "Synchronization of two passively mode-locked erbium-doped fiber lasers by an acousto-optic modulator and grating scheme," *Opt. Lett.* **21**, 809–811 (1996).
[167] R. H. Hardin and F. D. Tappert, "Applications of the Split-Step Fourier Method to the Numerical Solution of Nonlinear and Variable Coefficient Wave Equations," *SIAM Rev. Chronicle* **15**, 423 (1973).
[168] M. Frigo and S. G. Johnson, "FFTW: An Adaptive Software Architecture for the FFT," *Proceedings of the International Conference on Acoustics, Speech, and Signal Processing*, **3,** 1381–1384 (1998).
[169] P. L. Baldeck, R. R. Alfano, and G. P. Agrawal, "Induced-frequency shift of copropagating ultrafast optical pulses," *Appl. Phys. Lett.* **52**, 1939–1941 (1988).
[170] B. -T. V. Vu, A. Szoke, and O. L. Landen, "Induced frequency shifts by counterpropagating subpicosecond optical pulses," *Opt. Lett.* **18**, 723–725 (1993).
[171] P. A. Franken, A. E. Hill, C. W. Peters, and G. Weinreich, "Generation of optical harmonics," *Phys. Rev. Lett.* **7**, 118–120 (1961).
[172] R. C. Miller, "Optical harmonic generation in single crystal $BaTiO_3$," *Phys. Rev.* **134**, A1313–A1319 (1964).
[173] D. A. Kleinman, "Nonlinear Dielectric Polarization in Optical Media," *Phys. Rev.* **126**, 1977–1979 (1962).
[174] J. A. Armstrong, N. Bloembergen, J. Ducuing, and P. S. Pershan, "Interactions between Light Waves in a Nonlinear Dielectric," *Phys. Rev.* **127**, 1918–1939 (1962).
[175] J. A. Giordmaine and R. C. Miller, "Tunable coherent parametric oscillation in $LiNbO_3$ at optical frequencies," *Phys. Rev. Lett.* **14**, 973–976 (1965).
[176] A. Feisst and P. Koidl, "Current induced periodic ferroelectric domain structures in $LiNbO_3$ applied for efficient nonlinear optical frequency mixing," *Appl. Phys. Lett.* **47**, 1125–1127 (1985).
[177] M. Houe and P. D. Townsend, "An introduction to methods of periodic poling for second-harmonic generation," *J. Phys. D Appl. Phys.* **28**, 1747–1763 (1995).
[178] G. D. Boyd and D. A. Kleinman, "Parametric Interaction of Focused Gaussian Beams," *J. Appl. Phys.* **39**, 3597–3638 (1968).
[179] C. B. E. Gawith, "Novel Active Waveguide Devices in Direct-Bonded Structures," PhD Thesis, Univ. of Southampton, Sept. (2001).
[180] M. M. Fejer, G. A. Magel, D. H. Jundt, and R. L. Byer, "Quasi-Phase-Matched Second Harmonic Generation: Tuning and Tolerances," *IEEE J. Quantum Electron.* **28**, 2631–2654 (1992).
[181] G.W. Arnold, G. De Marchi, F. Gonella, P. Mazzoldi, A. Quaranta, G. Battaglin, M. Catalan, F. Garrido, and R.F. Haglund, Jr., "Formation of nonlinear optical waveguides by using ion-exchange and implantation techniques," *Nucl. Instrum. Methods Phys. Res. B* **116**, 507–510 (1996).
[182] B. Agate, E. U. Rafailov, W. Sibbett, S. M. Saltiel, K. Koynov, M. Tiihonen, S. Wang, F. Laurell, P. Battle, T. Fry, T. Roberts, and E. Noonan, "Efficient frequency-

doubling of femtosecond pulses in waveguide and bulk nonlinear crystals: Design, fabrication, theory and experiment," *Frontiers in Planar Lightwave Circuit Technology: Design, Simulation, and Fabrication; NATO Science Series II: Mathematics, Physics and Chemistry, Janz Siegfried Ed.*, **216**, 191–231 (2006).
[183] Y. Chen, X. Chen, S. Xie, X. Zeng, Y. Xia, and Y. Chen, "Polarization dependence of quasi-phase-matched second-harmonic generation in bulk periodically-poled $LiNbO_3$," *J. Opt. A: Pure and Appl. Opt.* **4**, 324–328 (2002).
[184] D. H. Jundt, "Temperature-dependent Sellmeier equation for the index of refraction, n_e, in congruent lithium niobate," *Opt. Lett.* **22**, 1553–1555 (1997).
[185] G. J. Edwards and M. Lawrence, "A temperature-dependent dispersion equation for congruently grown lithium niobate," *Opt. Quantum Electron.* **16**, 373–375 (1984).
[186] M. Carrascosa and L. Arizmendi, "High-temperature photorefractive effects in LiNbQ3:Fe," *J. Appt. Phys.* **73**, 2709–2713 (1993).
[187] K. Buse, "Light-induced charge transport processes in photorefractive crystals I: Models and experimental methods," *Appl. Phys B* **64**, 273–291, (2004).
[188] R. L. Byer, Y. K. Park, R. S. Feigelson, and W. L. Kway, "Efficient second-harmonic generation of Nd:YAG laser radiation using warm phasematching $LiNbO_3$," *Appl. Phys. Lett.* **39**, 17–19 (1981).
[189] A. Yamada, H. Tamada, and M. Saitoh, "Photorefractive damage in $LiNbO_3$ thin-film optical waveguides grown by liquid phase epitaxy," *J. Appl. Phys.* **76**, 1776–1783 (1994).
[190] B. U. Chen, C. C. Ghizoni, and C. L. Tang, "Phase-matched second-harmonic generation in solid thin films using modulation of the nonlinear susceptibilties," *Appl. Phys. Lett.* **28**, 651–653 (1976).
[191] B. Jaskorzynska, G. Arvidsson, and F. Laurell, "Periodic structures for phase-matching in second harmonic generation in titanium lithium niobate waveguides," *Proc. SPIE* **651**, 221–228 (1986).
[192] E. J. Lim, M. M. Fejer, and R. L. Byer, "Second-harmonic generation of green light in periodically poled planar lithium niobate waveguide," *Electron. Lett.* **25**, 174–175 (1989).
[193] T. Suhara and H. Nishihara, "Theoretical Analysis of Waveguide Second-Harmonic Generation Phase Matched with Uniform and Chirped Gratings," *IEEE J. Quantum Electron.* **26**, 1265–1276 (1990).
[194] R. C. Eckardt, H. Masuda, Y. X. Fan, and R. L. Byer, "Absolute and relative nonlinear optical coefficients of KDP, KD*P, BaB_2O_4, $LiIO_3$, MgO:$LiNbO_3$, and KTP measured by phase-matched second-harmonic generation," *IEEE J. Quantum Electron.* **26**, 922–933 (1990).
[195] F. Laurell, "Periodically poled $KTiOPO_4$," *Proceedings Conf. Lasers and Electro-Optics (CLEO)*, 383 (1999).
[196] J. K. Tyminski, "Photorefractive damage in KTP used as second-harmonic generator," *J. Appl. Phys.* **70**, 5570–5576 (1991).
[197] T. A. Driscoll, H. J. Hoffman, and R. E. Stone, "Efficient second-harmonic generation in KTP crystals," *J. Opt. Soc. Am. B* **3**, 683–686 (1986).
[198] B. Agate, E. U. Rafailov, W. Sibbett, S. M. Saltiel, P. Battle, T. Fry, and E. Noonan, "Highly efficient blue-light generation from a compact, diode-pumped femtosecond laser by use of a periodically poled KTP waveguide crystal ," *Opt. Lett.* **28**, 1963–1965 (2003).

[199] O. Katz, Y. Sintov, Y. Nafcha and Y. Glick, “Passively mode-locked ytterbium fiber laser utilizing chirped-fiber-Bragg-gratings for dispersion control”, *Opt. Commun.* (2006), doi:10.1016/j.optcom.2006.07.034.
[200] M. Oberthaler and R. A. Höpfel, “Special narrowing of ultrashort laser pulses by self-phase modulation in optical fibers,” *Appl. Phys. Lett.* **63**, 1017–1019 (1993).
[201] J. Limpert, T. Gabler, A. Liem, H. Zellmer, and A. Tünnermann, “SPM-induced spectral compression of picosecond pulses in a single-mode Yb-doped fiber amplifier,” *Appl. Phys. B* **74**, 191–195 (2002).
[202] J. Limpert, N. Deguil-Robin, I. Manek-Hönninger, F. Salin, T. Schreiber, A. Liem, F. Röser, H. Zellmer, A. Tünnermann, A. Courjaud, C. Hönninger, E. Mottay, “High-power picosecond fiber amplifier based on nonlinear spectral compression,” *Opt. Lett.* **30**, 714–716 (2005).
[203] R. R. Alfano and S. L. Shapiro, “Emission in the Region 4000 to 7000 Å Via Four-Photon Coupling in Glass,” *Phys. Rev. Lett.* **24**, 584–587 (1970).
[204] R. R. Alfano and S. L. Shapiro, “Observation of Self Phase Modulation and small scale filaments in crystals and glasses,” *Phys. Rev. Lett.*, **24**, 592–594 (1970).
[205] J. I. Gersten, R. R. Alfano, and M. Belic, “Combined stimulated Raman scattering and continuum self-phase modulations,” *Phys. Rev. A* **21**, 1222–1224 (1980).
[206] P. Baldeck, and R. Alfano, “Intensity effects on the stimulated four photon spectra generated by picosecond pulses in optical fibers,” *IEEE J. Lightwave Technol.* **5**, 1712–1715 (1987).
[207] M. N. Islam, G. Sucha, I. Bar-Joseph, M. Wegener, J. P. Gordon, and D. S. Chemla, "Broad bandwidths from frequency-shifting solitons in fibers," *Opt. Lett.* **14**, 370–372 (1989).
[208] J. K. Ranka, R. S. Windeler, and A. J. Stentz, "Visible continuum generation in air silica microstructure optical fibers with anomalous dispersion at 800nm," *Opt. Lett.* **25**, 25–27 (2000).
[209] T. A. Birks, W. J. Wadsworth, and P. S. J. Russell, "Supercontinuum generation in tapered fibers," *Opt. Lett.* **25**, 1415–1417 (2000).
[210] P. Glas, D. Fischer, G. Steinmeyer, A. Husakou, J. Herrmann, R. Iliew, N. B. Skibina, V. I. Beloglasov, and Y. S. Skibina, “Supercontinuum generation in a two-dimensional photonic kagome crystal,” *Appl. Phys. B* **81**, 209–217 (2005).
[211] Fianium SC450–2 supercontinuum source.
http://www.fianium.com/products/sc.htm
[212] T. Morioka, H. Takara, S. Kawanishi, O. Kamatani, K. Takiguchi, K. Uchiyama, M. Saruwatari, H. Takahashi, M. Yamada, T. Kanamori, and H. Ono, “1 Tbit/s (100 Gbit/s×10 channel) OTDM/WDM transmission using a single supercontinuum WDM source,” *Electron Lett.* **32**, 906–907 (1996).
[213] E. Yamada, H. Takara, T. Ohara, K. Sato, T. Morioka, K. Jinguji, M. Itoh, and M. Ishii, “A high SNR, 150 ch supercontinuum CW optical source with precise 25 GHz spacing for 10 Gbit/s DWDM systems,” *Proceedings of Optical Fiber Communication Conference (OFC)* **1**, ME2(1–3) (2001).
[214] G. P. Agrawal, “Nonlinear fiber optics,” Academic Press, San Diego, USA (2001).
[215] A. V. Housakou and J. Herrmann, “Supercontinuum Generation of Higher-Order Solitons by Fission in Photonic Crystal Fibers,” *Phys. Rev. Lett.* **87**, 203901(1–4), 2001.

[216] K. M. Hilligsøe, H. N. Paulsen, J. Thøgersen, S. R. Keiding, and J. J. Larsen, "Initial steps of supercontinuum generation in photonic crystal fibers ," *J. Opt. Soc. Am. B* **20**, 1887–1893 (2003).
[217] J. Dudley, X. Gu, L. Xu, M. Kimmel, E. Zeek, P. O'Shea, R. Trebino, S. Coen, and R. Windeler, "Cross-correlation frequency resolved optical gating analysis of broadband continuum generation in photonic crystal fiber: simulations and experiments," *Opt. Express* **10**, 1215–1221 (2002).
[218] K. Sakamaki, M. Nakao, M. Naganuma, and M. Izutsu, "Soliton Induced Supercontinuum Generation in Photonic Crystal Fiber," *IEEE Sel. Top. Quantum Electron.* **10**, 876–884 (2004).
[219] J. M. Dudley and S. Coen, "Coherence properties of supercontinuum spectra generated in photonic crystal and tapered optical fibers ," *Opt. Lett.* **27**, 1180–1182 (2002).
[220] J. M. Dudley, S. Coen, "Numerical simulations and coherence properties of supercontinuum generation in photonic crystal and tapered optical fibers," *IEEE Sel. Top. Quantum Electron.* **8**, 651–659 (2002).
[221] I. Zeylikovich, V. Kartazaev, and R. R. Alfano, "Spectral, temporal, and coherence properties of supercontinuum generation in microstructure fiber," *J. Opt. Soc. Am. B* **22**, 1453–1460 (2005).
[222] T. Schreiber, J. Limpert, H. Zellmer, A. Tunnermann and K. P. Hansen, "High average power supercontinuum generation in photonic crystal fibers," *Opt. Commun.* **228**, 71–78 (2003).
[223] J. Herrmann, U. Griebner, N. Zhavoronkov, A. Husakou, D. Nickel, J. C. Knight, W. J. Wadsworth, P. St. J. Russell, and G. Korn, "Experimental Evidence for Supercontinuum Generation by Fission of Higher-Order Solitons in Photonic Fibers," *Phys. Rev. Lett.* **88**, 173901(1–4), (2002).
[224] T. Hori, N. Nishizawa, T. Goto, and M. Yoshida, "Experimental and numerical analysis of widely broadened supercontinuum generation in highly nonlinear dispersion-shifted fiber with a femtosecond pulse," *J. Opt. Soc. Am. B* **21**, 1969–1980 (2004).
[225] R. Holzwarth, M. Zimmermann, T. Udem, T. W. Hänsch, P. Russbldt, K. Gbel, R. Poprawe, J. C. Knight, W. J. Wadsworth, and P. S. J. Russell, "White-light frequency comb generation with a diode-pumped CrLiSAF laser," *Opt. Lett.* **26**, 1376–1378 (2001).
[226] F. Lu and W. Knox, "Generation of a broadband continuum with high spectral coherence in tapered single-mode optical fibers," *Opt. Express* **12**, 347–353 (2004).
[227] K. Mori, H. Takara, and S. Kawanishi, "Analysis and design of supercontinuum pulse generation in a single-mode optical fiber," *J. Opt. Soc. Am. B* **18**, 1780–1792 (2001).
[228] N. I. Nikolov, T. Srensen, O. Bang, and A. Bjarklev, "Improving efficiency of supercontinuum generation in photonic crystal fibers by direct degenerate four-wave mixing," *J. Opt. Soc. Am. B* **20**, 2329–2337 (2003).
[229] J. C. Travers, S. V. Popov, and J. R. Taylor, "Extended blue supercontinuum generation in cascaded holey fibers," *Opt. Lett.* **30**, 3132–3134 (2005).

Appendices

Appendix 1

Publication 1

M. Rusu, S. Karirinne, M. Guina, A. B. Grudinin, O. G. Okhotnikov, "Femtosecond neodymium-doped fiber laser operating in the 894–909 nm spectral range," *IEEE Photon. Technol. Lett.* **16**, 1029–1031 (2004).

Femtosecond Neodymium-Doped Fiber Laser Operating in the 894–909-nm Spectral Range

M. Rusu, S. Karirinne, M. Guina, A. B. Grudinin, and O. G. Okhotnikov

***Abstract*—We demonstrate a practical ultrafast Nd-doped fiber laser operating in the 894–909-nm spectral range. Using purposely designed semiconductor saturable absorbers, a truly self-started mode-locking regime of operation with clean transform-limited 360-fs pulses was achieved.**

***Index Terms*—Mode-locked lasers, neodymium, optical fiber, quantum-well devices.**

ULTRAFAST fiber lasers are currently becoming very useful and reliable tools in many practically important applications such as micromachining, biomedicine, terahertz generation, and others. The main features of fiber-based devices—high efficiency, reliability, and small footprint—make them very attractive for applications traditionally occupied by conventional ultrafast lasers. Important activities in development of practical ultrafast fiber lasers have been recently focused on the use of semiconductor saturable absorber mirrors (SESAMs) as intracavity intensity discriminating element, and Yb-doped fiber as a gain medium [1], [2]. The SESAMs have been extensively used to mode-lock a large variety of laser systems [3], [4]. The passive mode-locking mechanism provided by an SESAM is very efficient and allows for implementation of very compact linear cavity lasers. Yb-doped fibers offer high efficiency, low threshold, and virtually unlimited ability to scale power up [5], [6]. Yb-doped fiber lasers can be easily tuned in a 1030–1120-nm spectral range. However, some applications require a wavelength close to 900 nm. This can be achieved with Nd-doped fibers [7], [8]. The quasi-three-level $^4F_{3/2} - ^4 I_{9/2}$ transition of a Nd- ion-doped laser around 900 nm has attracted much attention in recent years as a master source for generation of high power radiation at 460 nm (blue laser) and as a high power single-mode pump for 980-nm fiber lasers [9], [10]. However, the stimulated emission cross section is an order of magnitude smaller than that of commonly used four-level transition at 1064 nm. In addition, the lower laser level has a significant thermal population at room temperature resulting in losses due to reabsorption of laser light. Consequently, quasi-three-level laser systems require considerable pumping before exhibiting gain [6]. Optical fiber-based systems provide promising alternative to the bulk configuration because of their excellent mode confinement and long interaction length that allow us to extract sufficient gain even for quasi-three-level transitions [7], [8]. In this letter, we report on a passively mode-locked Nd^{3+}-doped fiber laser operating at the three-level $^4F_{3/2} - ^4 I_{9/2}$ transition near 900 nm.

Manuscript received September 22, 2003; revised December 2, 2003. This work was supported by the Finnish Academy under the TULE-QUEST Project.

M. Rusu, S. Karirinne, M. Guina, and O. G. Okhotnikov are with the Optoelectronics Research Centre, Tampere University of Technology, FIN-33101 Tampere, Finland (e-mail: Oleg.Okhotnikov@orc.tut.fi).

A. B. Grudinin is with the Fianium-NewOptics Ltd., Southampton, SO31 4RA, U.K.

Digital Object Identifier 10.1109/LPT.2004.824951

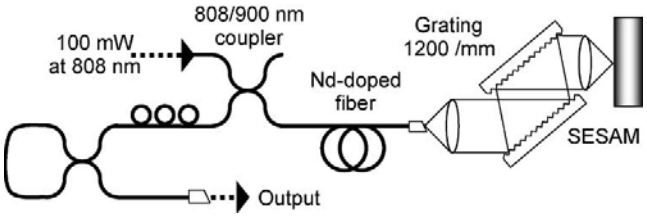

Fig. 1. Cavity configuration for a tunable mode-locked Nd fiber laser.

A schematic description of laser setup is shown in Fig. 1. The cavity contains a grating pair for intracavity dispersion compensation, a 1-m-long Nd^{3+}-doped fiber with angled-cleaved end to suppress intracavity reflections, a wavelength-division multiplexer, and a $\sim$92% reflectivity fiber loop mirror. The cavity was terminated by the loop mirror from one end and by an SESAM from the other. The neodymium-doped silica fiber (NA $= 0.14$, cutoff wavelength $\sim$800 nm) is pumped by a pigtailed single-mode laser diode operating at 808 nm. The unsaturated fiber absorption at 808 nm was $\sim$37 dB/m. The 808/900-nm pump wavelength-selective coupler and the loop mirror were made of fiber with a cutoff wavelength of $\sim$735 nm. The maximum launched pump power was 100 mW. The large normal group-velocity dispersion introduced into the cavity by the fiber is offset by the anomalous dispersion of the grating pair, so that total intracavity dispersion was anomalous which resulted in easy self starting of mode-locked operation. Mode locking was initiated and stabilized by the SESAM. The SESAM was grown by solid-source molecular beam epitaxy on n-type GaAs (100) substrate satisfying an antiresonant design [3]. The sample includes a bottom mirror comprising 20 pairs of AlAs–$Al_{0.2}Ga_{0.8}As$ quarter-wave layers forming a distributed Bragg reflector (DBR). The DBRs stopband had a center wavelength of 910 nm and approximately 100-nm bandwidth (860–960 nm). The absorber region consists of six 6-nm-thick $In_{0.12}Ga_{0.88}As$ quantum-wells separated by 16-nm GaAs barriers. The quantum-wells are placed between a 0.1-μm GaAs buffer layer and a 50-nm GaAs cap layer. The device was grown at 650 °C with the exception of the active region that was grown at 520 °C. The photoluminescence emission peak from quantum-wells was measured to be at 930 nm. The saturation fluence and nonlinear reflectivity have been estimated to be $\sim$ 3 μJ/cm^2 and 2%–3%, respectively. Recently, similar absorber mirrors were successfully used in broadly tunable mode-locked Yb-fiber lasers [2].

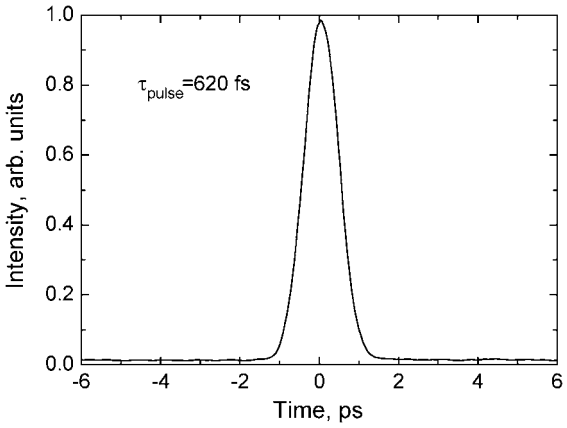

Fig. 2. Autocorrelation trace of the pulses observed at the output of the fiber lead with the length of 18 cm. The distance between gratings is 4.5 cm.

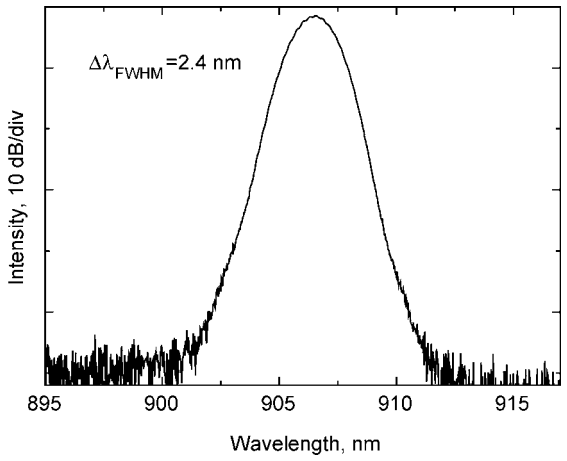

Fig. 3. Optical spectrum of the pulses shown in Fig. 2.

The proper alignment of the SESAM with the Nd-doped fiber resulted in self-starting mode-locking at the fundamental frequency of the laser cavity of 35.17 MHz. The laser threshold was 60 mW for CW operation and ∼70 mW for the mode-locked regime. Polarization dependence of the grating reflectivity led to the necessity to employ polarization controller in order to minimize intracavity loss. Although the mode locking could be started at virtually any position of polarization controller, the most stable operation with shortest pulses were achieved at only one orientation of the controller. This fact also suggests that nonlinear polarization had probably played some role in pulse shaping [11]. The shortest stable pulses were achieved with a grating separation of 4.5 cm, whereas, total second-order group velocity dispersion of the doped fiber was measured to be 0.05 ps^2. The total second-order dispersion in the cavity, including a double pass of the fiber and the grating pair set with the optimal grating separation, was -0.13 ps^2. The pulsewidth measurements were performed at the output of the fiber pigtail external to the loop mirror. The autocorrelation measurements presented in Fig. 2 reveals a pulsewidth of 620 fs [full-width at half-maximum (FWHM) assuming a $sech^2$ pulse shape] for the shortest length of the fiber pigtail of ∼18 cm. The corresponding pulse spectrum is presented in Fig. 3 and had FWHM

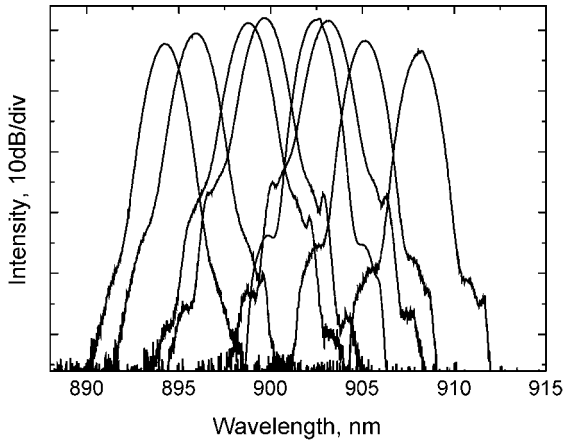

Fig. 4. Continuous wavelength tuning over 894–909-nm range obtained for mode-locked operation.

bandwidth of 2.4 nm. The average output power was ∼1 mW. The effect of the fiber pigtail on the pulsewidth was studied by changing the length of the fiber lead. The extrapolated value of the pulse duration corresponded to the pulsewidth generated by the laser was found to be 360 fs. Therefore, the time-bandwidth product of the pulse at the input of the fiber lead is 0.32, indicating that the pulses are transform limited. By tilting the diffraction grating or by shifting the lens focusing the light onto absorber, we were able to continuously tune the mode-locked laser from 894 to 909 nm, as shown in Fig. 4.

In conclusion, we have demonstrated a passively mode-locked Nd-fiber laser tunable over the three-level transition band from 894 to 909 nm. To our knowledge, this is the shortest wavelength obtained from mode-locked fiber laser. Continuous tuning of the pulses was accomplished by using an SESAM that initiates and stabilizes the mode-locking process. The low pump power (∼100 mW), supplied by a single-mode pump diode, makes this laser a very attractive fiber counterpart to the solid-state lasers now dominating in this wavelength range. As a final remark, we would like to note that by utilizing fiber cladding pumped technology for power amplification, it is feasible to scale the average power up to several watts [12], which will make such a tunable source of subpicosecond pulses very attractive for numerous applications.

REFERENCES

[1] L. Lefort, J. H. V. Price, D. J. Richardson, G. J. Spühler, R. Paschotta, U. Keller, A. R. Fry, and J. Weston, "Practical low-noise stretched-pulse Yb^{+3}-doped fiber laser," *Opt. Lett.*, vol. 27, pp. 291–293, 2002.

[2] O. G. Okhotnikov, L. Gomes, N. Xiang, T. Jouhti, and A. B. Grudinin, "Mode-locked ytterium fiber laser tunable in the 980–1070-nm spectral range," *Opt. Lett.*, vol. 28, pp. 1522–1524, 2003.

[3] U. Keller, D. A. B. Miller, G. D. Boyd, T. H. Chiu, J. F. Ferguson, and M. T. Asom, "Solid-state low-loss intracavity saturable absorber for Nd:YLF lasers: an antiresonant semiconductor Fabry-Perot saturable absorber," *Opt. Lett.*, vol. 17, pp. 505–507, 1992.

[4] U. Keller, K. J. Weingarten, F. X. Kartner, D. Kopf, B. Braun, I. D. Jung, R. Fluck, C. Hönninger, N. Matuschek, and J. Aus der Au, "Semiconductor saturable absorber mirrors (SESAMs) for femtosecond to nanosecond pulse generation in solid-state lasers," *IEEE J. Select. Topics Quantum Electron.*, vol. 2, pp. 435–452, Sept. 1996.

[5] H. Lim, F. Ö. Ilday, and F. W. Wise, "Generation of 2-nJ pulses from a femtosecond ytterbium fiber laser," *Opt. Lett.*, vol. 28, pp. 660–662, 2003.

[6] T. Y. Fan, "Optimizing the efficiency and stored energy in quasi-three-level lasers," *IEEE J. Quantum Electron.*, vol. 28, pp. 2692–2697, Dec. 1992.

[7] O. G. Okhotnikov and J. R. Salcedo, "Spectroscopy of the transient oscillations in a Nd^{3+}-doped fiber laser for the four-level ${}^4F_{3/2} - {}^4I_{11/2}$ (1060 nm) and three-level ${}^4F_{3/2} - {}^4I_{9/2}$ (900-nm) transitions," *Appl. Phys. Lett.*, vol. 64, pp. 2619–2621, 1994.

[8] R. Hofer, M. Hofer, G. A. Reider, M. Cernusca, and M. H. Ober, "Modelocking of a Nd-fiber laser at 920 nm," *Opt. Commun.*, vol. 140, pp. 242–244, 1997.

[9] C.-W. Wang, Y.-L. Weng, P.-L. Huang, H.-Z. Cheng, and S.-L. Huang, "Passively Q-switched quasithree-level laser and its intracavity frequency doubling," *Appl. Opt.*, vol. 41, pp. 1075–1081, 2002.

[10] T. Kellner, F. Heine, G. Huber, C. Hönninger, B. Braun, F. Morier-Genoud, M. Moser, and U. Keller, "Soliton mode-locked Nd:YAlO 3 laser at 930 nm," *J. Opt. Soc. Amer. B*, vol. 15, pp. 1663–1666, 1998.

[11] M. H. Ober, M. Hofer, U. Keller, and T. H. Chiu, "Self-starting diode-pumped femtosecond Nd fiber laser," *Opt. Lett.*, vol. 18, pp. 1532–1534, 1993.

[12] I. A. Bufetov, V. V. Dudin, A. V. Shubin, A. K. Senatorov, E. M. Dianov, A. B. Grudinin, S. E. Goncharov, I. D. Zalevskii, A. N. Gur'yanov, M. V. Yashkov, A. A. Umnikov, and N. N. Vechkanov, "Efficient 0.9-mm neodymium-doped single-mode fibre laser," *Quantum Electron.*, vol. 33, pp. 1035–1037, 2003.

Appendix 2

Publication 2

M. Rusu, R. Herda, S. Kivistö, and O. G. Okhotnikov, "Fiber taper for dispersion management in a mode-locked ytterbium fiber laser," *Opt. Lett.* **31**, 2257–2259 (2006).

Fiber taper for dispersion management in a mode-locked ytterbium fiber laser

Matei Rusu, Robert Herda, Samuli Kivistö, and Oleg G. Okhotnikov

Optoelectronics Research Center, Tampere University of Technology, P. O. Box 692, FIN-33101 Tampere, Finland

Received February 28, 2006; revised May 2, 2006; accepted May 8, 2006;
posted May 15, 2006 (Doc. ID 68551); published July 10, 2006

We exploit the large anomalous dispersion in the waist of a fiber taper to offset the intracavity normal chromatic dispersion of an Yb-doped fiber laser. The fiber taper provides sufficient anomalous dispersion to ensure soliton operation of the mode-locked laser. With the taper removed from the cavity, the laser operates in a net normal dispersion regime. © 2006 Optical Society of America

OCIS codes: 060.2340, 140.3510, 260.2030, 320.7090.

By combining the broad gain spectrum of Er- or Yb-doped fibers with semiconductor saturable absorber mirror (SESAM) structures, widely tunable sources delivering excellent pulse quality have been developed.[1–5] Yb-doped fiber lasers operating at a 1 μm band gained recognition as useful tools for medical science and material processing and as attractive sources for visible and UV light generation through frequency conversion[6] and supercontinuum broadening.[7] Despite excellent performance reported to date, Yb-doped fiber laser development remains hindered by the issue of chromatic dispersion compensation. Owing to both doped and standard single-mode fibers exhibiting normal chromatic dispersion, without proper dispersion management, mode-locked fiber lasers emitting at 1 μm operate in a net normal dispersion regime, associated with long pulse widths and a difficult start-up of mode-locked operation.[8] To overcome these problems, normal dispersion of the laser cavity should be compensated for by the anomalous dispersion of an additional intracavity element, generally referred to as the dispersion compensator. Consequently, the laser operates in a soliton regime, being more tolerant of cavity losses and reflections and delivering shorter pulses. Regularly, dispersion compensation is achieved with bulk optical components such as prisms[9] and waveguide and diffraction gratings.[10,11] These solutions suffer from disadvantages that limit their applicability to fiber lasers: prisms exhibit too low dispersion and require an impractically large separation, while diffraction gratings are strongly polarization dependent and introduce additional cavity losses. Moreover, the use of intracavity bulk optical elements violates the "all-fiber" character of fiber lasers. A more compact approach to dispersion compensation uses a Gires–Tournois interferometer embedded in one of the laser cavity mirrors.[12] However, the device operation bandwidth of such reflectors is small, while the magnitude of third-order dispersion is typically high. Recently, the emerging photonic crystal technology has been used to produce all-fiber dispersion compensators[13] as attractive alternatives to bulk elements.

In this Letter we report on the use of a tapered single-mode fiber to compensate for the dispersion of an Yb fiber laser. The laser could operate in both normal and anomalous dispersion regimes, whereas the switch between the two dispersion regimes was performed by simply inserting the taper in the laser cavity. When properly designed and manufactured, a fiber taper preserves the low-loss all-fiber character of the laser cavity and constitutes a strong candidate to practical dispersion compensators for fiber lasers.

The fiber taper was manufactured from a single-mode fiber using a flame brush technique.[14,15] A premixed hydrogen–oxygen burner was swept over a short span of fiber, while the ends of the fiber were pulled in opposite directions at low speed. To ensure good taper waist uniformity and short taper transitions, a double-stage pulling process was employed. First, the fiber was heated in a narrow region and tapered down to a diameter of 10 μm. Second, the torch sweep range was varied linearly with taper extension[16] to achieve conical transitions as short as possible. Tight control over the torch gas flow and brush speed resulted in a uniform taper waist with a length of 20 cm and a total conical transition length of 7 cm. Figure 1 shows the taper profile, as inferred from measurements with a 100× magnification optical microscope. After fabrication, the taper was promptly packaged in a rugged aluminum tube and sealed with silicon rubber at either end. Inside the package the taper remained surrounded by air. The chromatic dispersion of the taper waist was esti-

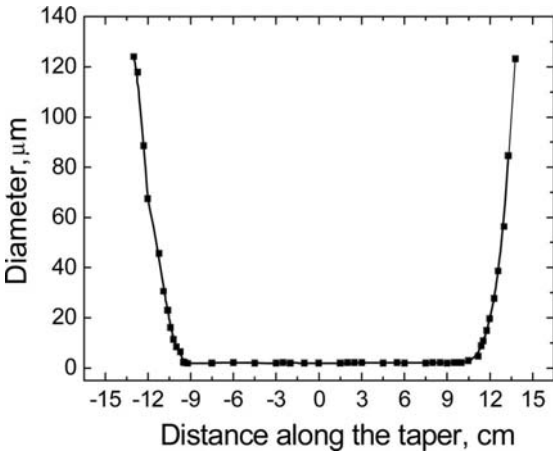

Fig. 1. Measured taper profile.

0146-9592/06/152257-3/$15.00

mated by solving the propagation constant eigenvalue equation[17,18] using a Newton–Raphson algorithm implemented in MATLAB. Figure 2 shows the calculated chromatic dispersion of the taper waist at a wavelength of 1.048 μm for a range of waist diameters, along with the measured taper insertion losses. It can be seen that the largest amount of anomalous dispersion could be obtained for a taper waist diameter of 1.2 μm. However, a gradual increase in the optical loss of the taper, ascribed to the nonoptimized manufacturing process, was observed with the reduction in waist diameter. Therefore, in practice, the choice of waist diameter value is a matter of a tradeoff between taper loss and dispersion. Since the taper is to be used inside the laser cavity, low insertion loss is an important prerequisite. The taper with a waist diameter of 1.8 μm exhibiting a dispersion value of 0.19 ps/nm/m at 1.048 μm was found to be optimal for our laser setup. With this taper, light was well confined in the waist, and the insertion losses were only 0.3 dB for the entire structure. Using a white-light interferometer,[19] we measured the total chromatic dispersion of the whole taper (waist plus pigtails) plotted in Fig. 3. A value of 50 fs/nm at 1.048 μm for a 20 cm long waist with two 15 cm standard fiber pigtails has been derived from the measurement. It should be noted that the chromatic dispersion of the taper can be altered by changing the refractive index of the medium surrounding the taper, for instance, by filling the housing tube with an optical material with selected refractive index.[18] The transmission spectrum of the taper was measured by using a broadband fiber source and a 0.05 nm resolution spectrum analyzer, and the result is presented in Fig. 3. As can be seen from the figure, the transmission spectrum is smooth, without spectral features. This confirms the single-mode light propagation in the taper and the good uniformity of the conical transitions.

The fiber laser used in the experiment is shown in Fig. 4. The laser cavity is composed of 50 cm of Yb-doped gain fiber with 434 dB/m absorption at 980 nm, a SESAM for initiating and sustaining mode-locked operation, and a 70% reflectivity fiber loop mirror, which also served as an output coupler. A polarization-insensitive pigtailed isolator is spliced to laser output to avoid back reflections. The laser was pumped with a 140 mW single-mode laser operating at 980 nm through an intracavity WDM coupler. In a mode-locked regime, the laser operates with a repetition rate of 65 MHz. The average output power was 2 mW. The optical spectrum and autocorrelation trace recorded at the output of the loop mirror are shown in Fig. 5(a). As inferred from the square-shaped spectrum, the laser operates in a net normal dispersion regime owing to the normal dispersion of the cavity. The corresponding pulse width is 8 ps.

The taper was fusion spliced to the cavity fiber just next to the loop mirror, leaving the alignment of the SESAM mirror undisturbed. Hence the normal dispersion of the fiber was offset by the dispersion of the taper, resulting in a net anomalous dispersion of the cavity. The optical spectrum of the laser operating in

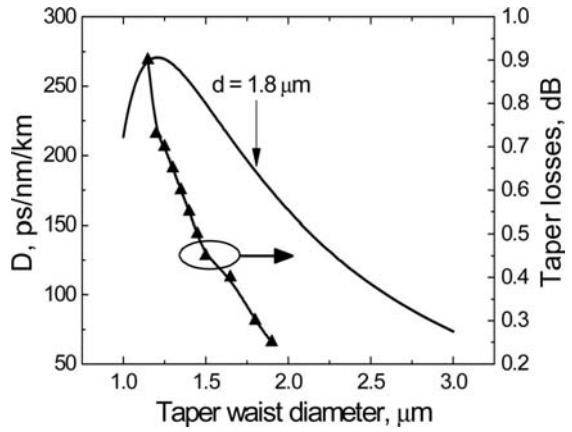

Fig. 2. Calculated dispersion of the taper waist versus diameter and measured taper losses. The chosen diameter is shown by an arrow.

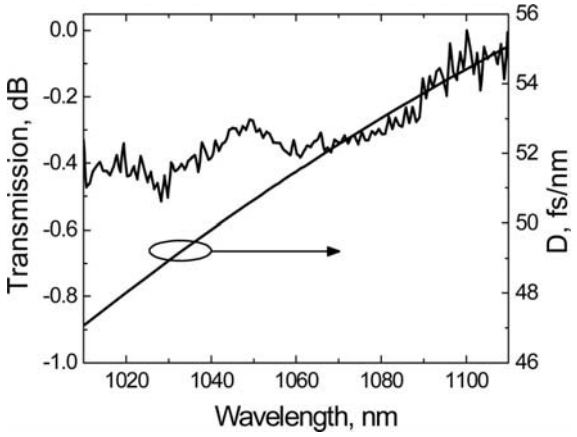

Fig. 3. Transmission spectrum and chromatic dispersion of the taper used in experiments.

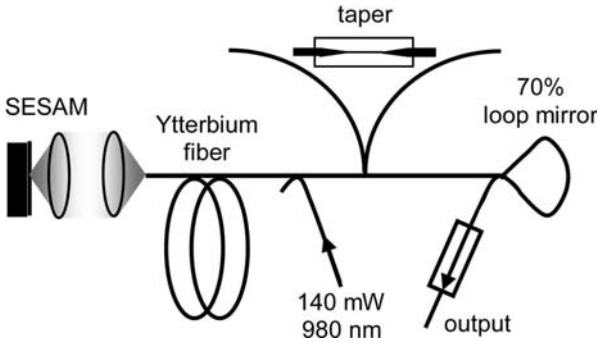

Fig. 4. Cavity setup of the mode-locked fiber laser.

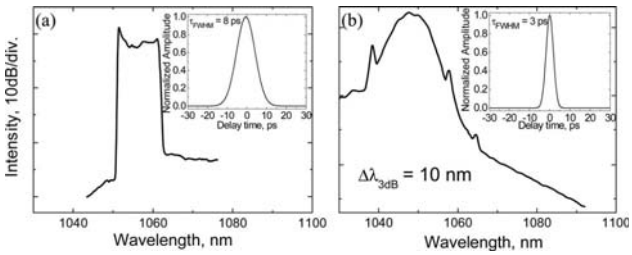

Fig. 5. Spectrum and autocorrelation trace of the laser operating in (a) net normal dispersion regime and (b) soliton regime.

the new configuration is presented in Fig. 5(b) showing solitonic sidebands, a clear indication of soliton pulse mode locking. The autocorrelation trace shows pulse width reduction to a value of 3 ps. The output of the laser is extracted through a loop mirror followed by a fiber pigtailed isolator, both exhibiting significant normal dispersion, which results in a large amount of chirp on the output pulse. In the soliton regime, the laser was operated continuously for hours without any noticeable performance degradation. Using the soliton sidebands in the spectrum, the average cavity dispersion after taper insertion was calculated.[20] A value of 0.03 ps/nm was deduced at 1.048 μm. By subtracting the taper dispersion, the initial laser cavity dispersion originating from single-mode fibers was estimated to be −0.02 ps/nm.

In summary, we demonstrated all-fiber intracavity chromatic dispersion compensation by using a tapered single-mode fiber. A short linear cavity fiber laser incorporating the taper exhibits evident soliton pulse mode-locked operation. Without the taper, the laser operates in a net normal dispersion regime owing to normal cavity dispersion. At the given intracavity power, optical nonlinearity of the taper did not perturb the laser operation. The tapers demonstrated reasonable stability in laboratory conditions. The use of these components in practical environments would, however, require advanced packaging suitable for long-term operation. With mature technology, tapers may constitute an important step toward all-fiber chromatic dispersion compensators suitable for short cavity mode-locked fiber lasers.

The authors acknowledge the financial support of the Academy of Finland (project GEMINI) and EU-FP6 project URANUS. Matei Rusu acknowledges financial support from the Nokia Foundation. M. Rusu's e-mail address is matei.rusu@tut.fi.

References

1. F. Ö. Ilday, J. R. Buckley, H. Lim, F. W. Wise, and W. G. Clark, Opt. Lett. **28**, 1365 (2003).
2. B. C. Collings, K. Bergman, S. T. Cundiff, S. Tsuda, J. N. Kutz, J. E. Cunningham, W. Y. Jan, M. Koch, and W. H. Knox, IEEE J. Sel. Top. Quantum Electron. **3**, 1065 (1997).
3. L. A. Gomes, L. Orsila, T. Jouhti, and O. G. Okhotnikov, IEEE J. Sel. Top. Quantum Electron. **10**, 129 (2004).
4. O. G. Okhotnikov, L. A. Gomes, N. Xiang, T. Jouhti, and A. B. Grudinin, Opt. Lett. **28**, 1522 (2003).
5. B. Barnett, L. Rahman, M. Islam, Y. Chen, P. Bhattacharya, W. Riha, K. Reddy, A. Howe, K. Stair, H. Iwamura, S. Friberg, and T. Mukai, Opt. Lett. **20**, 471 (1995).
6. A. Liu, M. A. Norsen, and R. D. Mead, Opt. Lett. **30**, 67 (2005).
7. M. Rusu, A. Grudinin, and O. G. Okhotnikov, Opt. Express **13**, 6390 (2005).
8. R. Herda and O. Okhotnikov, IEEE J. Quantum Electron. **40**, 893 (2004).
9. R. L. Fork, O. E. Martinez, and J. P. Gordon, Opt. Lett. **9**, 150 (1984).
10. J. E. Roman and K. A. Winick, IEEE J. Quantum Electron. **29**, 975 (1993).
11. E. B. Treacy, IEEE J. Quantum Electron. **QE-5**, 454 (1969).
12. L. Orsila, L. A. Gomes, N. Xiang, T. Jouhti, and O. G. Okhotnikov, Appl. Opt. **43**, 1902 (2004).
13. H. Lim, F. Ö. Ilday, and F. W. Wise, Opt. Express **10**, 1497 (2002).
14. F. Bilodeau, K. O. Hill, S. Faucher, and D. C. Johnson, J. Lightwave Technol. **6**, 1476 (1988).
15. M. Rusu, S. Kivistö, C. Gawith, and O. G. Okhotnikov, Opt. Express **13**, 8547 (2005).
16. T. A. Birks and Y. W. Li, J. Lightwave Technol. **10**, 432 (1992).
17. G. P. Agrawal, *Fiber-Optic Communication Systems*, 2nd ed. (Wiley, 1997).
18. C. M. B. Cordeiro, W. J. Wadsworth, T. A. Birks, and P. S. J. Russell, Opt. Lett. **30**, 1980 (2005).
19. H.-T. Shang, Electron. Lett. **17**, 603 (1981).
20. M. L. Dennis and I. N. Duling III, IEEE J. Quantum Electron. **30**, 1469 (1994).

Appendix 3

Publication 3

M. Rusu, R. Herda and O. G. Okhotnikov, "Passively synchronized two-color mode-locked fiber system based on master-slave lasers geometry," *Opt. Express* **12**, 4719–4724 (2004).

Passively synchronized two-color mode-locked fiber system based on master-slave lasers geometry

Matei Rusu, Robert Herda and Oleg G. Okhotnikov

Optoelectronics Research Centre, Tampere University of Technology,
P.O. Box 692, FIN-33101, Tampere, Finland
matei.a.rusu@orc.tut.fi, robert.herda@orc.tut.fi, oleg.okhotnikov@orc.tut.fi

Abstract: Using a master - slave configuration, a robust synchronization was achieved for two-color Erbium and Ytterbium mode-locked fiber lasers. Due to enhanced nonlinear interaction in the fiber, noise-free pulse-locking was achieved allowing for a cavity mismatch tolerance of 140 μm. This is the highest tolerable cavity-length difference ever been obtained for synchronized mode-locked oscillators.

OCIS codes: (140.3500) Lasers, erbium; (140.3510) Lasers, fiber; (140.4050) Mode-locked lasers; (320.7090) Ultrafast lasers

References and links

1. O. G. Okhotnikov, L. Gomes, N. Xiang, T. Jouhti, and A. B. Grudinin, "Mode-locked ytterbium fiber laser tunable in the 980-1070 -nm spectral range," Opt. Lett. **28**, 1522 (2003).
2. O. G. Okhotnikov, T. Jouhti, J. Konttinen, S. Karirinne and M. Pessa, "1.5- μm monolithic GaInNAs semiconductor saturable-absorber mode locking of an erbium fiber laser," Opt. Lett. **28**, 364 (2003).
3. M. Rusu, S. Karirinne, M. Guina, A. B. Grudinin, and O. G. Okhotnikov, "Femtosecond neodymium-doped fiber laser operating in the 894-909 nm spectral range," IEEE Photon Technology Lett. **16**, 1029 (2004).
4. T. R. Schibli, J. Kim, O. Kuzucu, J. T. Gopinath, S. N. Tandon, G. S. Petrich, L. A. Kolodziejski, J. G. Fujimoto, E. P. Ippen, and F. X. Kaertner, "Attosecond active synchronization of passively mode-locked lasers by balanced cross correlation," Opt. Lett. **28**, 947 (2003).
5. R. K. Shelton, S. M. Foreman, L-S Ma, J. L. Hall, H. C. Kapteyn, M. M. Murnane, M. Notcutt, and J. Ye, "Subfemtosecond timing jitter between two independent, actively synchronized, mode-locked lasers," Opt. Lett. **27**, 312 (2002).
6. A. Leitenstofer, C. Fürst, and A. Laubereau, "Widely tunable two-color mode-locked Ti:sapphire laser with pulse jitter of less than 2 fs," Opt. Lett. **20**, 916 (1995).
7. Z. Wei, Y. Kobayashi, Z. Zhang, and K. Torizuka, "Generation of two-color femtosecond pulses by self-synchronizing Ti:sapphire and Cr:forsterite lasers," Opt. Lett. **26**, 1806 (2001).
8. Z. Wei, Y. Kobayashi, and K. Torizuka, "Relative carrier-envelope phase dynamics between passively synchronized Ti:sapphire and Cr:forsterite lasers," Opt. Lett. **27**, 2121 (2002).
9. M. Betz, F. Sotier, F. Tauser, S. Trumm, A. Laubereau, and A. Leitenstorfer, "All-optical phase locking of two femtosecond Ti:sapphire lasers: a passive coupling mechanism beyond the slowly varying amplitude approximation," Opt. Lett. **29**, 629 (2004).
10. M. Rusu, R. Herda and O. G. Okhotnikov, "Passively synchronized Erbium (1550 nm) and Ytterbium (1040 nm) mode-locked fiber lasers sharing the cavity," Opt. Lett. **29**, (October 2004).
11. Femtomaster fibre laser, Fianium Ltd, http://www.fianium.com/products/femto.htm
12. C. Furst, A. Leitenstorfer and A. Laubereau, "Mechanism for Self-Synchronization of Femtosecond Pulses in a Two-Color Ti:Sapphire Laser," IEEE Sel. Topics in Quant. Electron. **2**, 473 (1996).

1. Introduction

The technology of Semiconductor Saturable Absorber Mirror (SESAM) has greatly pushed the development of mode-locked fiber laser. The main features of fiber-based devices – high efficiency, reliability and small footprint – make them promising for applications traditionally

#5148 - $15.00 US Received 27 August 2004; revised 13 September 2004; accepted 17 September 2004

occupied by ultrafast solid-state lasers. The broad fluorescence spectrum makes different fiber gain media attractive for tunable and ultrashort pulse sources. Recently pulse trains covering the vast wavelength range from 895 to 1560 nm were reported using neodymium, ytterbium and erbium doped mode-locked fiber lasers [1-3]. Different fields of science and technology have a strong need to pursue research using ultrafast lasers in an arrangement called two-color experiment. The two-color source appears to be a valuable instrument for ultrafast research including difference-, harmonic- and sum-frequency generation, coherent anti-Stokes Raman scattering microscopy and two-color pump-probe investigations. For the majority of the applications, the relative jitter between the pulses is a crucial factor severely limiting the performance of the system. Compared to the active synchronization of two-color mode-locked lasers with an electrical feedback scheme [4-5], the passive technique using cross-phase modulation (XPM) should result in a very small timing jitter [6-9]. It should also be noted that a two-color source using a single gain medium suffers from limited bandwidths, gain competition, poor tunability and close optical frequencies.

Using coupled-cavity lasers is shown to be a powerful technique for generation of a synchronized two-color mode-locked pulse train. In this approach, the two laser cavities share the same medium with Kerr-type nonlinearity that ensures synchronous mode-locking of the coupled oscillators. This technique is particularly attractive with fiber lasers because of long interaction length that can be conveniently constructed for coupled-cavity fiber lasers [10]. However, integrated two-color coupled-cavities usually require complicated dichroic components and should be carefully designed to avoid excessive noise due to laser coupling.

In this Letter we demonstrate an alternative approach for synchronized two-color mode-locked system based on master-slave configuration. In this set-up the highly stable master mode-locked erbium-fiber oscillator is isolated from the slave ytterbium-fiber laser and, therefore, it is free from any disturbing influences that may occur in the lasers sharing joint cavity. Synchronization is achieved by the cross-phase modulation (XPM) in the slave oscillator induced by the master laser. We demonstrate that the slave mode-locked laser can be tightly synchronized by the pulse train injected into its cavity from independent master source with a record cavity-length detuning exceeding 140 μm. We have found that the performance of the master-slave type technique is similar to the coupled-cavity set-up otherwise it is simpler, more robust and well suited for use in practical systems.

2. Experiment

The experimental setup is shown in Fig. 1. The output of the erbium-fiber master-laser operating at 1550 nm was injected into the 1060 nm slave laser cavity. The slave laser comprises a linear cavity terminated by the SESAM on one side and a fiber loop mirror on the other. The loop mirror acts as a dichroic output coupler providing ~90%-reflectivity at 1060 nm and high transmission at 1550 nm. Optical gain medium is a 70 cm of Yb-doped fiber with NA=0.13 and cutoff wavelength ~910 nm pumped by a 150 mW single-mode 980 nm semiconductor laser via a 980/1060 WDM coupler. The gain fiber has pump absorption of 434

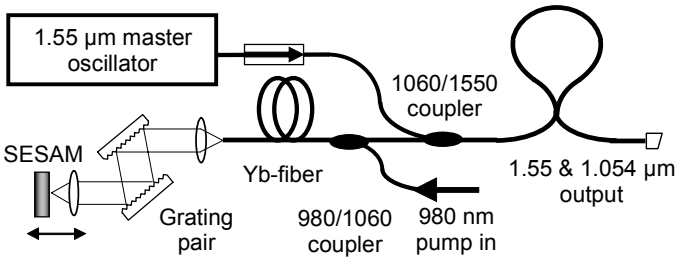

Fig. 1. Configuration of the master-slave ultrashort pulse lasers synchronization setup.

#5148 - $15.00 US Received 27 August 2004; revised 13 September 2004; accepted 17 September 2004

dB/m at 980 nm, a core diameter of 6.2 μm and normal group velocity dispersion of -30 ps/nm·km at 1060 nm. The large normal chromatic dispersion of the fiber in slave laser cavity is offset by a 1200 mm^{-1} grating pair placed in the free space section of the cavity that allows changing the overall cavity dispersion over a broad range, from normal to anomalous. The SESAM-lens assembly can be precisely translated axially providing us with a means of controlling the cavity length and thus the slave laser repetition rate.

The master laser is a stable, linear cavity laser passively mode-locked by a SESAM [2, 11]. Master laser is coupled to the slave laser cavity through a 1060/1550 dichroic fiber combiner. The fiber span between the combiner and the loop mirror acts as an interaction medium of the master and slave laser pulses. The segment of the slave laser cavity, where XPM occurs, has anomalous dispersion of the fiber at 1550 nm. The fiber dispersion was measured to be of 7.8 ps/nm·km. The low value of dispersion and short length of interaction fiber (~1.5 m) allowed concluding that the distortion of the 1.55-μm control pulse in a laser cavity was negligible. To ensure master laser protection against back reflections from the slave cavity, an optical isolator was placed at the input of the master/slave combiner to achieve one-way coupling from the master to the slave laser. The loop mirror supplies a two-color output from the master-slave system. The pump WDM, master-slave beam combiner and the loop mirror were made from Corning HI1060 fiber (NA=0.14, cutoff wavelength 939 nm) using computer-controlled fusing technology to achieve the required spectral characteristics.

The master laser repetition rate was measured to be around 40 MHz. By changing the fiber length and shifting the SESAM-lens holder, the cavity length of the slave laser was made to be essentially identical to cavity length of the master oscillator. The locking behavior was then investigated by only fine-tuning the slave cavity-length using the translation stage. Movement of the translation stage was monitored using an inductive transducer gauge with a reading precision of 1 μm. SESAM-enforced self starting mode-locking was obtained with both master and slave lasers. The pulse widths of 1 ps and 2 ps with the assumption of a $sech^2$ shape were deduced from the autocorrelation measurements for the master and slave oscillators, respectively, as shown in Fig. 2(a) and Fig. 2(b).

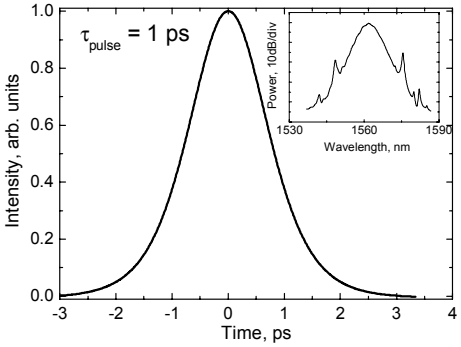

Fig. 2. (a) Autocorrelation trace of the master laser output pulse. Corresponding pulse spectrum is shown as an inset.

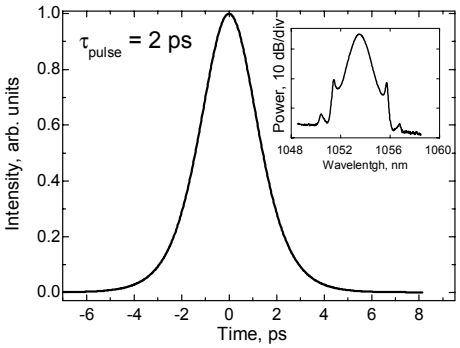

Fig. 2. (b) Autocorrelation trace of slave laser output pulse. Corresponding pulse spectrum is shown as an inset.

The combined output of the master and slave lasers was detected and fed to the input of an electrical spectrum analyzer with a resolution of 100 Hz. This allows for repetition rate monitoring of the master and slave lasers, simultaneously. By aligning the slave laser cavity-length while recording the cavity elongation together with repetition rate for both lasers, the slave laser pulse train could be easily set to be locked to the master pulses. Figure 3 shows the repetition rate of the slave laser as a function of the SESAM assembly displacement. As shown in Fig. 3, a slave cavity-length mismatch over 140 μm is tolerable without losing locking mode with the repetition rate identical to the master oscillator. The stable

#5148 - $15.00 US Received 27 August 2004; revised 13 September 2004; accepted 17 September 2004

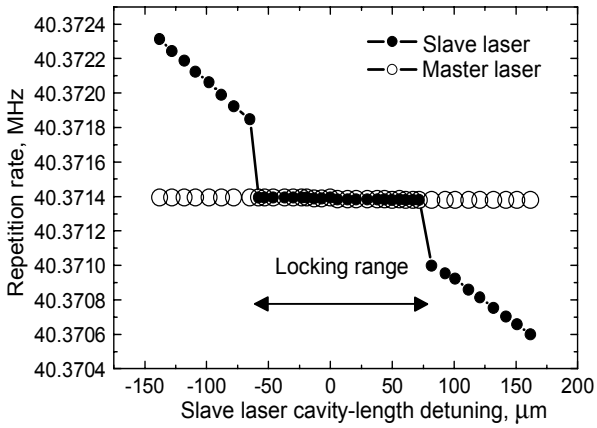

Fig. 3. Cavity detuning diagram for master/slave configuration: measured repetition rate of the Yb-fiber slave laser versus its cavity-length variation. The synchronization range is highlighted.

synchronization was maintained within the locking range even under continuous changing the slave cavity-length. In these measurements, the average output power of the master laser was 40 mW, whereas the slave laser average power was about 2 mW. The synchronized mode of the master-slave system was independently confirmed by monitoring pulse trains on an oscilloscope. Triggering the scope with the master pulse train allowed the slave laser train to be clearly visualized. Otherwise, the slave laser could not be displayed on the scope without synchronization. In the synchronized mode, when master and slave pulses coincide temporally, strong nonlinear effect causes the slave pulse spectrum to be affected by the control master train.

Figure 4 shows the wavelength shift in the slave laser spectrum recorded simultaneously with repetition rate monitoring, shown in Fig. 3. This feature is due to the XPM induced by the Er-fiber master laser in the Yb-fiber cavity [8, 9]. The wavelength shift of the slave laser pulses generated through the XPM allows compensating for cavity-length variations owing to adequate change in the pulse group velocity [12]. The synchronized operation was also

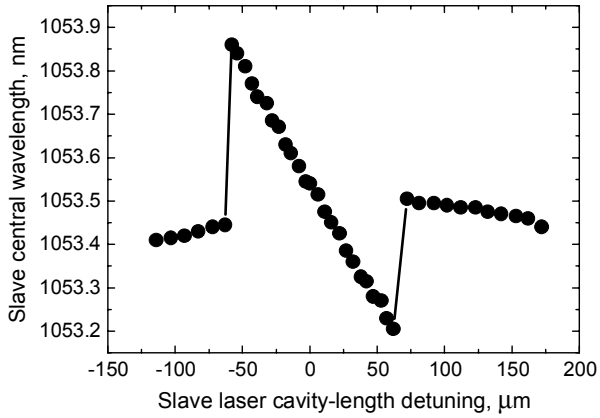

Fig. 4. The wavelength of the slave laser versus the offset of the cavity length. The anomalous dispersion of the slave laser cavity is 2 ps/nm.

#5148 - $15.00 US Received 27 August 2004; revised 13 September 2004; accepted 17 September 2004

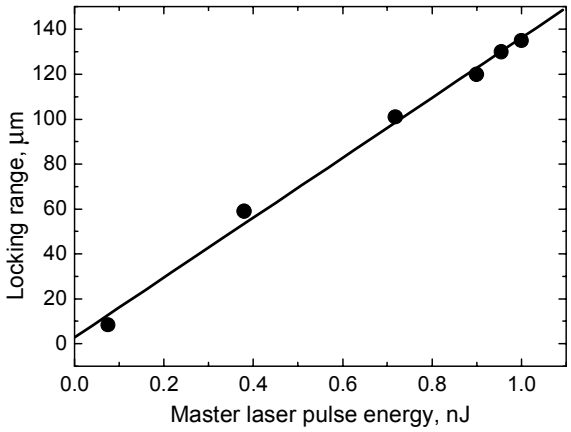

Fig. 5. Slave laser cavity mismatch tolerance versus master laser pulse energy. The anomalous dispersion of the slave laser cavity is 2 ps/nm.

possible with a spectral filter inserted in the slave laser cavity. However, with slave laser wavelength firmly set by the filter, the locking range vanished, as expected from the above discussions.

The average dispersion in the slave laser cavity obviously plays a crucial role in the locking procedure. The repetition rate of the slave laser was initially higher than that of the master oscillator (Fig. 3). Since the slave laser had anomalous cavity dispersion, the pulses experience abrupt red-shift to reach the locking state with an increase in the cavity-length (Fig. 4). With subsequent increase in the slave cavity-length in the synchronized mode, gradual blue-shift was detected, as seen from Fig. 4. As the cavity-mismatch reaches the locking limit, the slave laser wavelength returns to the free-running value.

With a decrease in the cavity dispersion, the same locking range can in principle be expected provided that a larger spectral shift is imposed on the slave laser pulses to compensate for the master-slave velocity mismatch. However, we found that the locking range for arbitrarily low cavity dispersion was ultimately limited by the spectral broadening generated by the master laser pulses through cross-phase modulation. This conclusion was derived from the behavior of the cavity mismatch tolerance with increasing master pulse energy, shown Fig. 5. The higher the master pulse energy, the stronger the phase modulation seen by the slave pulse and, consequently, the larger the spectral shift they acquire. Therefore,

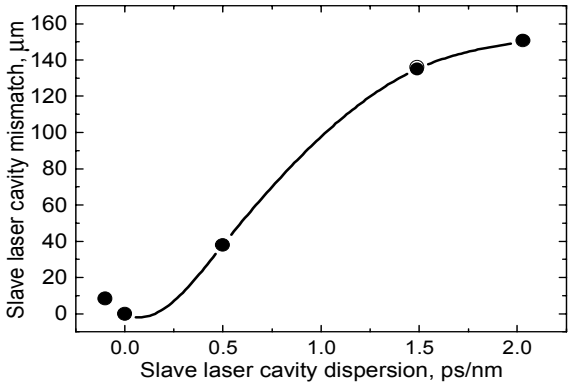

Fig. 6. Slave laser cavity mismatch tolerance versus average dispersion of the cavity. The master pulse energy is 1.0 nJ.

#5148 - $15.00 US Received 27 August 2004; revised 13 September 2004; accepted 17 September 2004

the locking range increases with increasing master pulse energy since larger mismatch tolerances can be compensated for a given dispersion of the cavity. From this observation, we conclude that the master pulse energy is a key parameter in our system limiting the locking range by setting a maximum value for wavelength variation.

The average dispersion of the slave laser cavity could be changed by altering the gratings separation. Figure 6 shows the change in slave laser cavity tolerance for several dispersion values of cavity. The decrease in the locking range with the decrease in the cavity dispersion originates from the limit in the wavelength shift capability set by the amount of the spectral broadening generated through the XPM. Alternatively, higher value of the chromatic dispersion of the slave laser cavity allows for larger change in the pulse group velocity for a given spectral shift, and thus leads to increased cavity mismatch tolerance.

Regardless the pulse energy limitation in our system, the strong mode overlap provided by the fiber as well as the long interaction length in the laser cavity make XPM-based synchronization very strong and, consequently, the locking range in a fiber system is shown to be approximately an order of magnitude larger than in bulk solid-state counterpart. With a large cavity tolerance, it was possible to maintain the synchronization state for long time without cavity stabilization. Figure 7 shows RF power variations in the slave laser output in the synchronized mode at the frequency corresponding to the repetition rate of the master oscillator. It should be noted that this enhancement in the locking mechanism is obtained with pulse energy of ~1 nJ that is at least by the 2-3 orders of magnitude lower than in typical solid-state lasers.

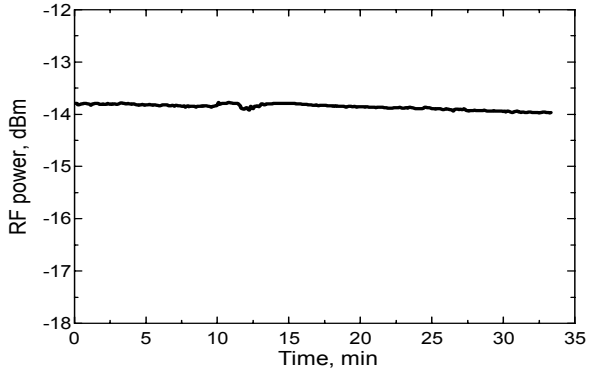

Fig. 7. Variation of RF power at the slave laser output in the synchronized mode. The central frequency corresponds to the repetition rate of the master laser. Bandwidth – 100 Hz.

3. Conclusion

In conclusion, we demonstrated synchronized 1.55 and 1.06 μm mode-locked fiber lasers using master-slave configuration. Using optically isolated noise-free master oscillator, we have achieved a record value of the locking tolerance for the slave laser cavity mismatch of 140 μm. This result has been achieved owing to fiber-cavity advantages and can be exploited in practical two-color synchronized ultrafast sources. Contrary to the solid-state lasers, where two laser beams need to be carefully adjusted to overlap spatially in the nonlinear gain medium, the waveguide properties of the single-mode fiber ensure automatically large overlap volume of the master-slave beams. Another benefit of the master-slave fiber system is that even with very large interaction volume no gain competition is expected owing to the passive nature of the nonlinear fiber.

#5148 - $15.00 US Received 27 August 2004; revised 13 September 2004; accepted 17 September 2004

Appendix 4

Publication 4

M. Rusu, R. Herda and O. G. Okhotnikov, "1.05-um mode-locked Ytterbium fiber laser stabilized with the pulse train from a 1.54-um laser diode," *Opt. Express* **12**, 5258–5262 (2004).

1.05-µm mode-locked Ytterbium fiber laser stabilized with the pulse train from a 1.54-µm laser diode

Matei Rusu, Robert Herda, and Oleg G. Okhotnikov

Optoelectronics Research Centre, Tampere University of Technology, P.O. Box 692, FIN-33101, Tampere, Finland
matei.a.rusu@orc.tut.fi

Abstract: Using cross-phase modulation in an optical fiber, we synchronized the pulse train from a mode-locked ytterbium fiber laser operating at 1.05 µm to an external optical master signal. The optical master source based on a 1.54 µm distributed feedback (DFB) diode laser was driven by the clock signal and was used as a seed source. The amplified seed pulses are launched into the fiber cavity and synchronize the mode-locked pulses through cross-phase modulation. The master clock signal is electronically generated, benefiting from inherent stability and repeatability. Due to its simplicity, this technique provides an attractive alternative to the traditional scheme that uses an independent mode-locked laser as source of seed signal. Since the approach is flexible and generally applicable, we expect this stabilization method to have a good potential for use in metrology and optical communications.

OCIS codes: (320.7160) Ultrafast technology; (190.4380) Nonlinear optics; (140.3510) Lasers, fibers; (140.4050) Mode-locked lasers

References and links

1. R.J. Jones and J.C. Diels, "Stabilization of Femtosecond Lasers for Optical Frequency Metrology and Direct Optical to Radio Frequency Synthesis," Phys. Rev. Lett. **86**, 3288-3291 (2001).
2. D.J. Jones, S.A. Diddams, J.K. Ranka, A. Stenz, R.S. Windeler, J.L. Hall, and S.T. Cundiff, "Carrier-envelope phase control of femtosecond mode-locked lasers and direct optical frequency synthesis," Science **288**, 635-639 (2000).
3. R.K. Shelton, L.S. Ma, H.C. Kapteyn, M.M. Murnane, J.L. Hall, and J. Ye, "Active synchronization and carrier phase locking of two separate mode-locked femtosecond lasers," J. Mod. Opt. **49**, 401-409 (2002).
4. S.T. Cundiff, "Phase stabilization of ultrashort optical pulses," J. Phys. D. **35**, R43 (2002).
5. J. Rauschenberger, T.M. Fortier, D.J. Jones, J. Ye, and S.T. Cundiff, "Control of the frequency comb from a mode-locked Erbium-doped fiber laser," Opt. Express **10**, 1404-1410 (2002), http://www.opticsexpress.org/abstract.cfm?URI=OPEX-10-24-1404
6. H. Hundertmark, D. Wandt, C. Fallnich, N. Haverkamp, and H.R. Telle, "Phase-locked carrier-envelope-offset frequency at 1560 nm," Opt. Express **12**, 770-775 (2004), http://www.opticsexpress.org/abstract.cfm?URI=OPEX-12-5-770
7. N.H. Bonadeo, W.H. Knox, J.M. Roth, and K. Bergman, "Passive harmonic mode-locked soliton fiber laser stabilized by an optically pumped saturable Bragg reflector," Opt. Lett. **25**, 1421-1423 (2000).
8. M. Guina, and O.G. Okhotnikov, "Harmonically mode-locked laser stabilized by semiconductor saturable absorber modulated with the residual pump," Appl. Phys. B. **75**, 127-130 (2002).
9. M. Guina and O.G. Okhotnikov, "Harmonic mode-locking by synchronous optical pumping of a saturable absorber with the residual pump," Opt. Lett. **28**, 358-360 (2003).
10. M. Rusu, R. Herda and O. G. Okhotnikov, "Passively synchronized Erbium (1550 nm) and Ytterbium (1040 nm) mode-locked fiber lasers sharing the cavity," Opt. Lett. **29**, 2246-2248 (2004).
11. M. Rusu, R. Herda and O. G. Okhotnikov, "Passively synchronized two-color mode-locked fiber system based on master-slave lasers geometry ," Opt. Express **12**, 4719-4724 (2004), http://www.opticsexpress.org/abstract.cfm?URI=OPEX-12-20-4719.
12. M. L. Dennis and I. L. Duling III, "Experimental study of sideband generation in femtosecond fiber lasers," IEEE J. Quantum Electron. **30**, 1469-1477 (1994).
13. Corning PureMode HI1060 optical fiber datasheet, Corning Inc., September 2001.

#5403 - $15.00 US Received 29 September 2004; revised 12 October 2004; accepted 12 October 2004

1. Introduction

Over the past years, mode-locked lasers have revolutionized frequency metrology and optical clocks [1]. Stabilized mode-locked lasers now allow scientists to perform synthesis of few-cycle optical pulses [2]. Diode pumped solid-state lasers currently dominate the area of ultrashort pulsed light sources for frequency comb generation offering not only extremely short optical pulses comprising several optical cycles, but also broad tunability [2-4].

Fiber lasers are being developed in many laboratories around the world as alternatives to bulky and expensive solid-state lasers. Recent unprecedented growth of telecom industry had resulted in development of mature fiber technology, and reliable and cost effective components which make suitably designed fiber lasers real contenders to conventional solid state lasers. The fiber laser technology is to replace bulk-optic ultrafast systems with simpler and hands-off alternatives. The broad fluorescence spectrum makes different fiber gain media attractive for tunable and ultrashort pulse sources. Additionally, fiber lasers offer attractive, new means of controlling the frequency comb, particularly the offset frequency [5].

The heart of any optical system used in frequency metrology is a stabilized mode-locked oscillator. Typical stabilization technique employs servo loop control feedback with piezoelectric actuator for active control of the cavity length and therefore of the repetition rate [3-5]. Using optical signal for controlling a passively mode-locked fiber laser has recently been demonstrated [7-11]. In this technique, repetition rate stabilization and timing jitter reduction were achieved with modulating the loss of the saturable absorber mirror by pumping it optically at the cavity fundamental frequency or its harmonic. Improved stability of the mode-locked pulse train owing to significant reduction of the unwanted harmonics has been demonstrated.

Here, we demonstrate a new and simple technique for mode-locked laser stabilization based on cross-phase modulation (XPM) in an optical fiber. Seed pulses are produced by a telecom DFB laser diode operating at 1540 nm. The stabilization technique we demonstrate here should be applicable to different types of mode-locked fiber lasers used in those systems that require low jitter ultrashort pulse oscillators.

2. Laser system

The master-slave geometry used for synchronization of the passively mode-locked laser to the external clock is shown in Fig 1.

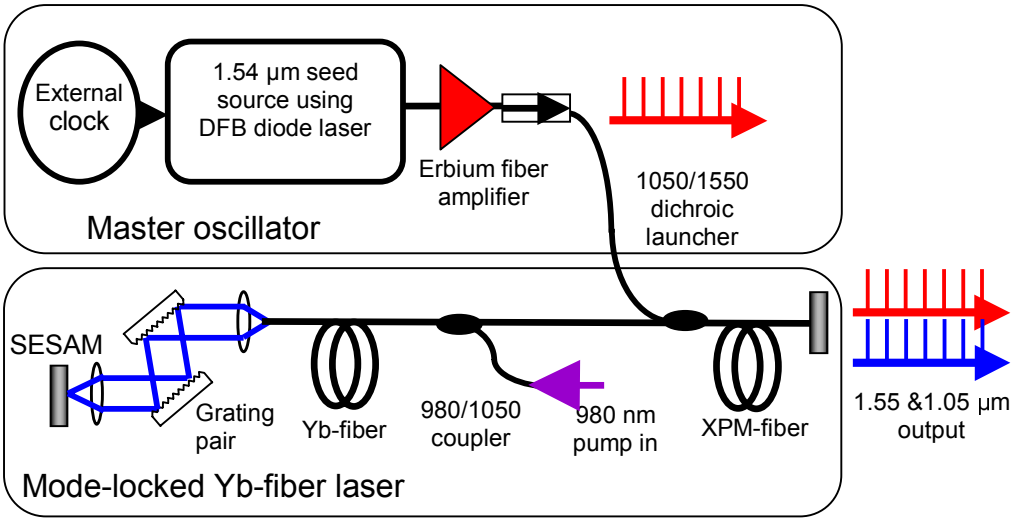

Fig. 1. Schematic of 1050 nm-fiber laser synchronized to the pulse train produced by a 1.54 µm laser diode.

#5403 - $15.00 US Received 29 September 2004; revised 12 October 2004; accepted 12 October 2004

The seed source, which comprises a distributed-feedback (DFB) laser diode and standard telecom components, emits optical pulses with tunable repetition rate. The repetition rate was determined by the frequency synthesizer that acts as a clock generator. After passing through an Er-doped fiber amplifier, the pulses are launched into the slave laser cavity. The shortest pulse duration obtained here was limited by the bandwidth of the components and drive electronics available for these experiments. The state-of-the-art telecom devices, however, allow the generation of much shorter pulses and may result in an improved performance of the technique described in this paper.

As a slave laser we used a passively mode-locked ytterbium fiber laser with an intra-cavity 1540/1050 nm dichroic combiner for launching the seeding signal from the master source (Fig 1). The Yb-laser comprises a linear cavity terminated by the SESAM used as a cavity end mirror. Another cavity mirror was a dichroic fiber loop mirror providing ~90%-reflectivity at 1050 nm and high transmission at 1540 nm. Optical gain is provided by a 70 cm Yb-doped fiber with NA=0.13 and cutoff wavelength of ~910 nm, pumped with a 150 mW, 980 nm semiconductor laser through a 980/1060 WDM combiner. The gain fiber has pump absorption of 434 dB/m at 980 nm, a core diameter of 6.2 μm and normal group velocity dispersion of -30 ps/nm·km at 1050 nm. The large normal chromatic dispersion of the fiber in mode-locked laser is offset by a 1200 mm^{-1} grating pair placed in the free space section of the cavity that allows changing the overall cavity dispersion over a broad range, from normal to anomalous. The overall cavity dispersion of the Yb slave laser was 0.7 ps/nm, as inferred from the soliton side-bands in the optical spectrum of the mode-locked pulses, shown in Fig. 3 [12]. The SESAM-lens assembly can be precisely translated axially providing us with a means of controlling the cavity length and thus the laser repetition rate. SESAM-enforced self-starting mode-locking was obtained in the Yb fiber laser. The slave laser operated at a fundamental repetition rate of 24 MHz.

The locking signal from the seed source was coupled into the mode-locked slave laser cavity through the 1.05 μm/1.54 μm dichroic fiber combiner. The 2m span of Corning HI1060 fiber between the combiner and the output coupler acts as a nonlinear interaction medium for seed master pulses and slave pulses. The interaction length also included the loop mirror, however because of its short length of 0.1 m, nonlinear interaction inside the loop can be ignored. The XPM interaction fiber has a MFD of 6.2 μm and normal dispersion of -29 ps/nm·km at 1.05 μm [13]. To avoid any optical coupling between seed and slave oscillators, an optical isolator was placed at the input of the master/slave combiner which resulted in one-way coupling from the seed to the mode-locked laser. The fiber loop-mirror acts as an output coupler which supplies the two-color pulse train from the system. All fiber components were made from Corning HI1060 fiber with NA=0.14 and cutoff wavelength of 939 nm using computer-controlled fusing technology that allows the required spectral characteristics to be achieved. The combined output of the system was detected and fed to the input of an electrical spectrum analyzer with 10 Hz resolution for simultaneous monitoring of the seed and mode-locked lasers repetition rates.

3. Results

First, by changing the frequency of the 1.54 μm seed pulsed signal, its repetition rate was brought close to the fundamental repetition rate of the 1.05 μm mode-locked laser. Then, the length of the free-space section of the slave laser cavity was precisely adjusted by moving the SESAM-assembly. The repetition rate was detected with a fast photodiode and analyzed by monitoring its radio-frequency (RF) spectrum. The cavity length of the mode-locked slave laser was tuned until the two pulse trains became locked owing to XPM-interaction in the common optical fiber path [10]. Monitoring the slave laser pulse train with the aid of an oscilloscope triggered by the clock signal allows the mode-locked pulse train to be viewed (stopped) in the synchronized state. In free-running regime, the pulse train could not be clearly

#5403 - $15.00 US Received 29 September 2004; revised 12 October 2004; accepted 12 October 2004

displayed on the oscilloscope. It should be noted that mode-locked operation of the slave laser was sustained during adjustment of the cavity length and with variations in the seed signal.

The master laser pulse spectrum and temporal shape are shown in Fig 2, revealing an optical pulse FWHM of 100 ps. The master pulse appears inverted on the oscilloscope screen due to the electronic amplifier employed in the fast photo-detection scheme.

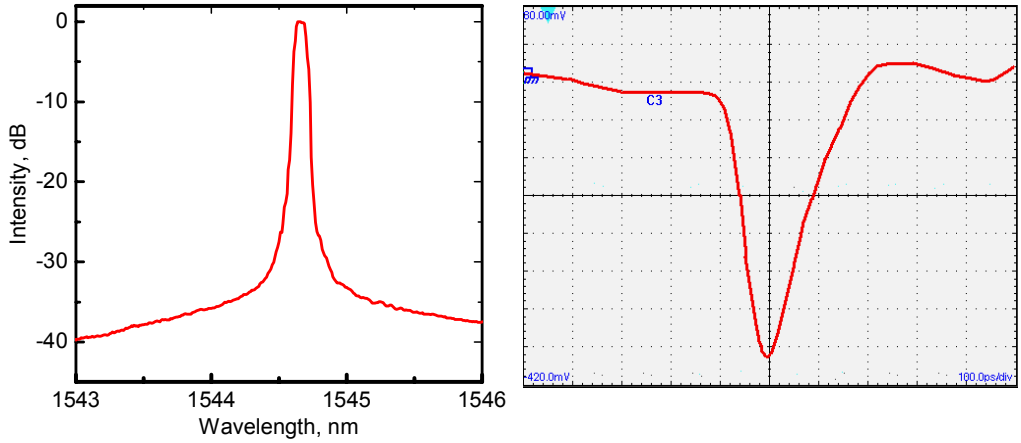

Fig. 2. (a) Optical spectrum of the seed pulses and (b) pulse shape obtained with a fast

The pulse spectrum for the 1.05 μm mode-locked laser operating in the synchronized mode is shown in Fig. 3. The corresponding autocorrelation trace in the insert reveals a clean pulse with 2 ps FWHM.

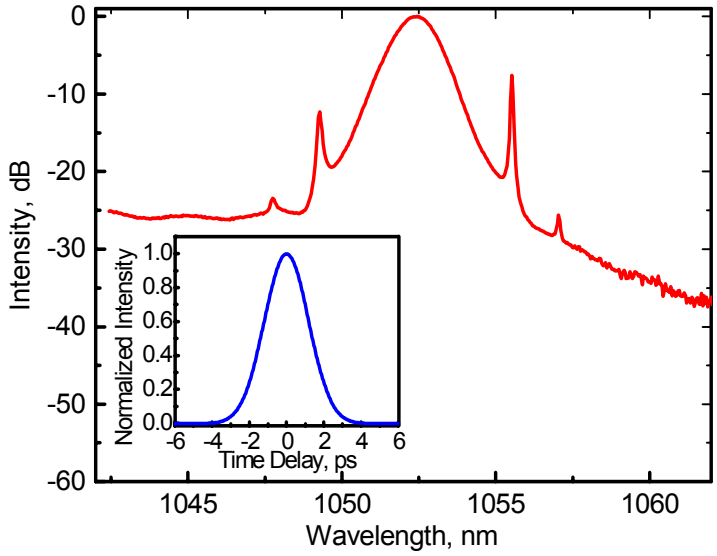

Fig. 3. Optical spectrum of the mode-locked pulses. Inset shows intensity autocorrelation corresponding to pulse duration of 2ps.

Figure 4 shows the change in repetition rate of the slave laser in free-running and synchronized regimes. The free-running laser repetition rate exhibits large environmental variation of ±30 Hz. When synchronized, the repetition rate of the mode-locked slave laser remained constant and equal to the repetition rate of the clock within the analyzer bandwidth,

#5403 - $15.00 US Received 29 September 2004; revised 12 October 2004; accepted 12 October 2004

for a measurement time of 30 minutes without any external cavity-length stabilization. In these measurements, the average power of the seed signal was 130 mW, whereas the 1.05 μm laser produced about 2 mW at the output.

By changing the cavity length of the slave laser until locking of the lasers was lost, we could estimate that the maximum tolerable cavity-length mismatch is about 15 μm, corresponding to a locking bandwidth of 60 Hz.

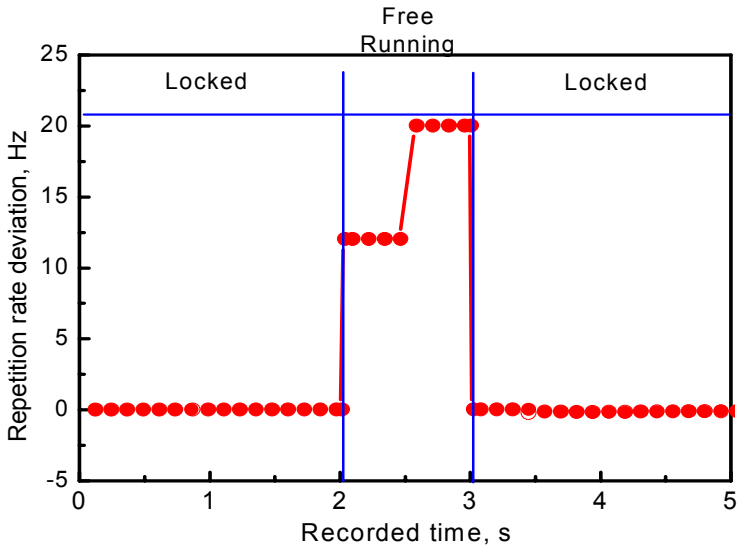

Fig. 5. Temporal evolution of the slave laser central frequency when the seed signal is switched periodically off and on.

To further study the strength of the locking mechanism based on the DFB diode-induced XPM in optical fiber, we periodically turned off the seed signal and monitored the slave laser transition from locked to free-running state and back. Fig. 5 shows a fragment of these actions. As observed from the scope and RF analyzer, when the seed signal is turned on, the slave Yb-fiber laser returns to the locked state in nearly instantaneous manner; the actual transition time, however, could not be measured.

4. Conclusion

We demonstrated optical synchronization of the repetition rate of a passively mode-locked fiber laser to a pulse train generated by a DFB laser diode-based seed source. The locking scheme used here to synchronize mode-locked laser to the external clock differs from conventional approaches in that the seed pulsed signal with tunable repetition rate is produced by modulating a laser diode with an external clock signal. The cross-phase modulation in the fiber cavity of the slave mode-locked oscillator enables the generation of pulse trains with highly stable repetition rate locked to the external clock. We have found that the phase modulation produced by the seed master pulses from the laser diode creates a sufficiently strong locking mechanism for interpulse spacing stabilization. Although shorter pulses would improve the strength of the locking mechanism, we demonstrate that tight control of the repetition rate can be achieved with seed pulse duration above 100 ps. The seed source and electronics components used in the synchronization scheme employ only standard communication components. Using state-of the art high-frequency telecom devices that allow ps-duration pulses generation will greatly improve the locking bandwidth and make this method applicable to different mode-locked laser systems in the picosecond and femtosecond regimes.

#5403 - $15.00 US Received 29 September 2004; revised 12 October 2004; accepted 12 October 2004

1.05-µm mode-locked Ytterbium fiber laser stabilized with the pulse train from a 1.54-µm laser diode: errata

Matei Rusu, Robert Herda, and Oleg G. Okhotnikov

Optoelectronics Research Centre, Tampere University of Technology,
P.O. Box 692, FIN-33101, Tampere, Finland
matei.a.rusu@orc.tut.fi

Abstract: Figures 2 and 4 have been altered during publication. Their correct version is presented herein.

OCIS codes: (320.7160) Ultrafast technology; (190.4380) Nonlinear optics; (140.3510) Lasers, fibers; (140.4050) Mode-locked lasers

References and Links

1. M. Rusu, R. Herda, and O. G. Okhotnikov, "1.05-µm mode-locked Ytterbium fiber laser stabilized with the pulse train from a 1.54-µm laser diode," Opt. Express 12, 5258-5262 (2004), http://www.opticsexpress.org/abstract.cfm?URI=OPEX-12-21-5258

During the publication process, some figures in [1] have been adversely modified. They are presented here in their original form for manuscript completeness and consistence.

The caption of Fig. 2 has been truncated during manuscript editing. Figure 2 is shown below with complete caption.

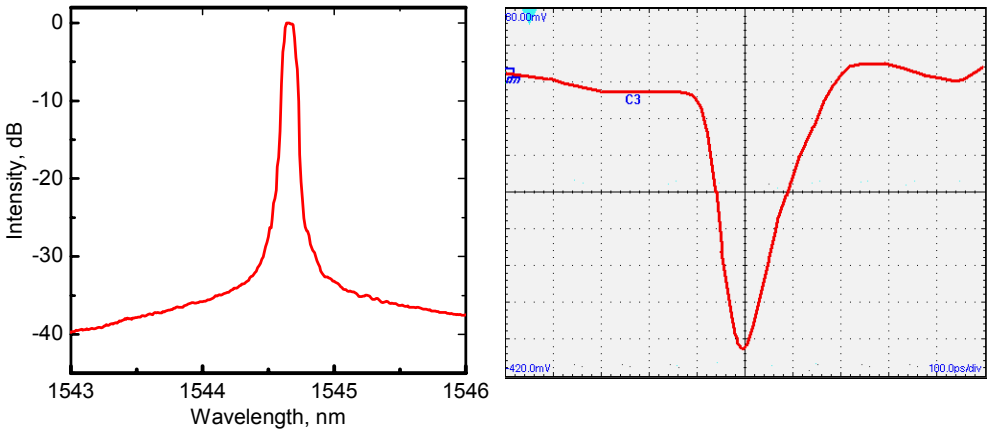

Fig. 2. (a) Optical spectrum of the seed pulses and (b) pulse shape obtained with a fast detector (100ps/div).

Figure 4 is missing in [1]. It is referred to in the manuscript body and we deem it very important to the work, since it helps the reader assess the strength of passive locking mechanism. Figure 4 is presented below.

#5587 - $15.00 US Received 27 October 2004; revised 27 October 2004; accepted 29 October 2004

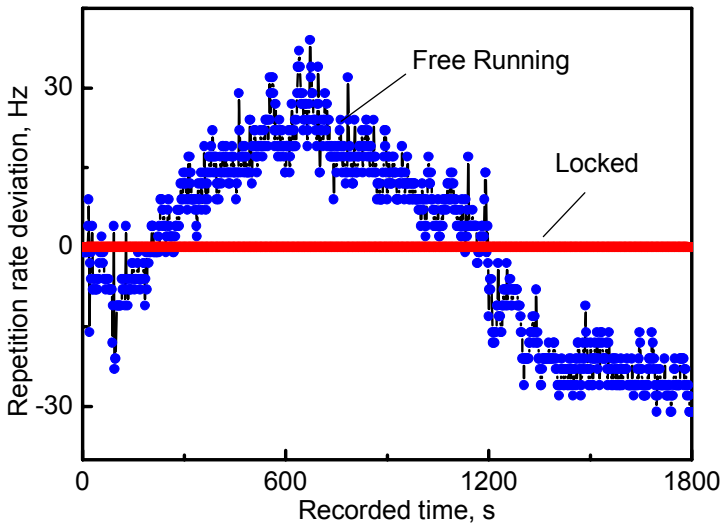

Fig. 4. Temporal variation of the repetition rate for the free running and locked states.

#5587 - $15.00 US Received 27 October 2004; revised 27 October 2004; accepted 29 October 2004

Appendix 5

Publication 5

M. Rusu, R. Herda and O. G. Okhotnikov, "Passively synchronized erbium (1550-nm) and ytterbium (1040-nm) mode-locked fiber lasers sharing a cavity," *Opt. Lett.* **29**, 2246–2248 (2004).

Passively synchronized erbium (1550-nm) and ytterbium (1040-nm) mode-locked fiber lasers sharing a cavity

Matei Rusu, Robert Herda, and Oleg G. Okhotnikov

Optoelectronics Research Centre, Tampere University of Technology, P.O. Box 692, Tampere FIN-33101, Finland

Received April 14, 2004

Erbium and ytterbium fiber lasers were firmly synchronized by nonlinear interaction in active media placed in the same cavity. A two-color femtosecond–picosecond pulse train at largely separate wavelengths of 1.55 and 1.04 μm was generated. Optimizing the laser cavity to enhance the cross-phase modulation in the gain materials has yielded a large mismatch of 20 μm between the two laser cavities. © 2004 Optical Society of America

OCIS codes: 140.3500, 140.3510, 140.4050, 320.7090.

Semiconductor saturable-absorber mirror (SESAM) technology has greatly advanced the development of mode-locked fiber lasers. The main properties of fiber-based devices—high efficiency, reliability, and small footprints—make these devices attractive for applications traditionally attributed to ultrafast solid-state lasers. The broad fluorescence spectrum makes different fiber gain media attractive for tunable and ultrashort pulse sources. Recently pulse trains that covered the vast wavelength range from 895 to 1560 nm were achieved with neodymium-, ytterbium-, and erbium-doped fiber lasers.[1–3]

Several fields of science and technology have strong needs to pursue research with two independent ultrafast lasers in an arrangement called a two-color experiment. The two-color source appears to be a promising instrument for ultrafast research including difference-, harmonic-, and sum-frequency generation; coherent anti-Stokes Raman scattering microscopy; and two-color pump–probe investigations. For a majority of applications, relative jitter between the pulses is a crucial factor that severely limits the performance of the system. Compared with the active synchronization of two-color mode-locked lasers with an electrical feedback scheme,[4,5] the passive technique that uses cross-phase modulation (XPM) results in a small timing jitter.[6–9] It should also be noted that a two-color source that uses a single gain medium suffers from limited bandwidths, gain competition, poor tunability, and limitation to closely spaced optical frequencies.

In this Letter we demonstrate a novel two-color ultrafast fiber source based on two gain materials, erbium and ytterbium fibers, that share the same cavity. The long XPM interaction length of the fiber enforces synchronous mode locking of both oscillators, making this approach particularly attractive in a fiber form. Owing to large overlap volume in the joint cavity, strong nonlinear coupling between the Er and the Yb lasers occurs, resulting in tight passive synchronization of the pulse train at the two wavelengths of 1040 and 1550 nm.

The experimental setup for a two-color mode-locked source is illustrated in Fig. 1. The laser configuration used Yb- and Er-doped fibers as gain media placed in a shared cavity. The fiber cavity comprised 50 cm of Er-doped fiber (N.A., 0.13; cutoff wavelength, ~920 nm) and 70-cm-long Yb-doped silica fiber (N.A., 0.13; cutoff wavelength, ~910 nm) pumped with a single-mode grating-stabilized laser diode, which provided a power of 150 mW at 980 nm. The unsaturated Yb fiber absorption at 980 nm was ~434 dB/m, and the fiber core diameter was 6.3 μm. The Er-doped fiber had an unpumped loss of 32 dB/m at 1.535 μm, a core diameter of 6.2 μm, and normal group-velocity dispersion of +0.01 ps^2/m at 1.56 μm.

The 980/1050 pump/signal, the output, and 1.04- and 1.55-μm wavelength-selective couplers were made from fiber with a cutoff wavelength of 910 nm. Ten percent of the signal was coupled out at both signal wavelengths. A 1.04–1.55-μm coupler separated signal wavelengths and directed them to the long- and short-wavelength SESAMs.

The large normal group-velocity dispersion of the Yb laser cavity at 1 μm was partially balanced by the anomalous dispersion of a gold-coated 1200-line/mm diffraction grating pair placed in the open-air section of the cavity (not shown in Fig. 1). The cavity dispersion for the Er fiber laser was balanced by use of fiber segments with normal and anomalous dispersion that had appropriate lengths. It is, however, obvious that, when the round-trip frequencies are equalized, the local cavity dispersion and the group velocity are still different at different wavelengths. Therefore interaction through XPM is strongly determined by the pulse walk-off time. Thus the role of dispersion compensation was to enhance XPM by minimizing the pulse duration of the master oscillator and to optimize the walk-off length for 1.04- and 1.55-μm pulses in the two-color section of the cavity containing the Er- and Yb-doped fibers. The passive synchronization mechanism is attributed to XPM. When master and slave pulses overlap temporally, the spectrum of the

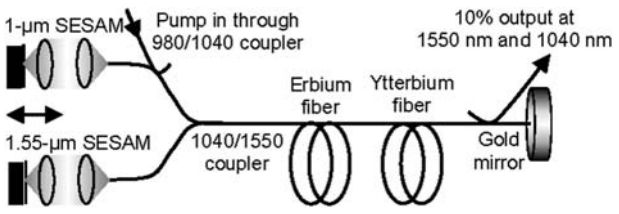

Fig. 1. Cavity configuration of the two-color Er fiber and Yb fiber self-synchronized mode-locked source.

0146-9592/04/192246-03$15.00/0

latter is shifted owing to strong phase modulation provided by the master pulse. As a result, the slave pulse's group velocity changes accordingly, driving the slave pulse train's repetition rate to match the repetition rate of the master source.

The cavity terminated in a Au mirror at one end and in SESAM structures at the other. Throughout this study, two types of quantum-well absorber material were used. The resonant 1-μm SESAM used in this study was fabricated by use of solid-source molecular-beam epitaxy upon an n-type GaAs (100) substrate. The samples include a bottom mirror that comprised 30 pairs of AlAs/GaAs quarter-wave layers forming a distributed Bragg reflector. The distributed Bragg reflector's stop band had a center wavelength of 1050 nm and a bandwidth of ~120 nm (990–1110 nm).

A 1.55-μm SESAM was grown by use of the same technique on a silicon-doped n-type InP (100) substrate. A highly reflective Burstein–Moss-shifted Bragg mirror composed of 19.5 pairs of quarter-wave n^+-$Ga_{0.47}In_{0.53}As$/InP layers is described in Ref. 8. The saturable absorber consisted of an InP spacer layer, four 7-nm-thick GaInAsP quantum wells separated by an 8-nm InP barrier, and an 80-nm-thick InP cap. For the SESAM we used a Fabry–Perot design that included a bottom semiconductor distributed Bragg reflector and a top dielectric Bragg reflector with a reflectivity of ~75%. Antireflection-coated aspheric lenses with focal lengths of 2.0 mm were used to focus the beam on the absorbers.

Self-starting passive mode locking was independently obtained for both lasers. Owing to the use of individual saturable absorbers and gain media for each color, the lasers interact solely through XPM. The passive mode-locking mechanism remains insensitive to the XPM interaction between the lasers. The synchronization scheme is based on the spectroscopic property of Er fiber that it is highly transparent at 1040 nm, whereas Yb fiber is transparent at 1550 nm. To start the synchronization between the lasers, first we measured the repetition rates of both lasers, using an electrical spectrum analyzer. By axially translating the SESAM mounts, we could tune the cavity length of one (or both) laser(s), which enabled us to set the repetition rates of the lasers with an accuracy of better than 10 Hz. The repetition rates of both lasers were measured to be ~29 MHz. With an additional (optional) dichroic splitter at the output, we could also analyze the trains independently, using two fast detectors. An analog scope without averaging was used for real-time monitoring of the two output pulse trains. The time scale was set to be 100 ns/division, corresponding to a full sweep time of 1 μs. The monitoring of the pulse train on the oscilloscope triggered by use of one pulse train allowed the other pulse train to be viewed (stopped), as shown in Fig. 2(a). Before equalization of the repetition rate, the second pulse train could not be clearly displayed on the oscilloscope [Fig. 2(b)]. Intensity autocorrelations for the two-color source in the synchronized regime are displayed in Fig. 3. To increase the synchronization range, we need to optimize the pulse walk-off length and thus the interaction length of the two-color pulse train. One can do this by lengthening the pulse width of one laser. High peak power and short pulse duration, however, are needed to enhance XPM nonlinearity. To cope with these conflicting requirements, we broadened the pulse of the slave laser, using the stretched-pulse technique,[10] while the pulse duration of the master source remained 65 times shorter. In this experiment, an Er fiber laser acted as a master oscillator because of its high power and shorter pulse duration. The pulse duration of the Er master laser was 200 fs, and the duration of the Yb slave laser was 13 ps. The pulse spectra are depicted as insets in Fig. 3. The estimated walk-off length was ~1.5 m, which is comparable with the total length of the cavity.

Figure 4 shows the repetition rates of the lasers versus the measured cavity detuning of the master laser. The length of the master laser cavity was measured with an inductive gauge that had a reading precision of 1 μm. Initially, both lasers oscillated independently with different round-trip frequencies. When the repetition rate of the Er fiber laser was close to the round-trip frequency of the Yb fiber laser, the Yb fiber laser became captured by the Er fiber laser; then its frequency remained equal to the repetition rate of the master laser and followed the changes induced by the variations in the master cavity length. For a cavity length mismatch that exceeded the locking (synchronization) limit, the Yb fiber slave laser returned to its initial (free-running) repetition rate. With increasing master cavity length, as shown in Fig. 4(a), the synchronized regime was

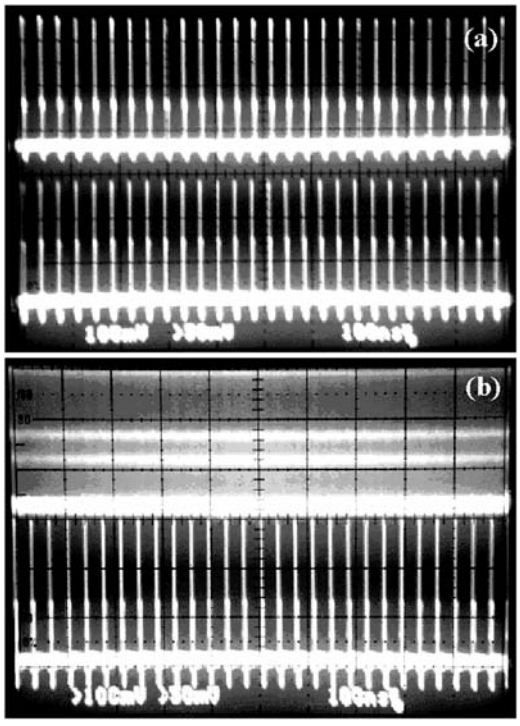

Fig. 2. Oscilloscope pulse traces of Er and Yb fiber lasers in (a) the synchronized and (b) the free-running regimes. The oscilloscope is triggered by the master Er fiber laser.

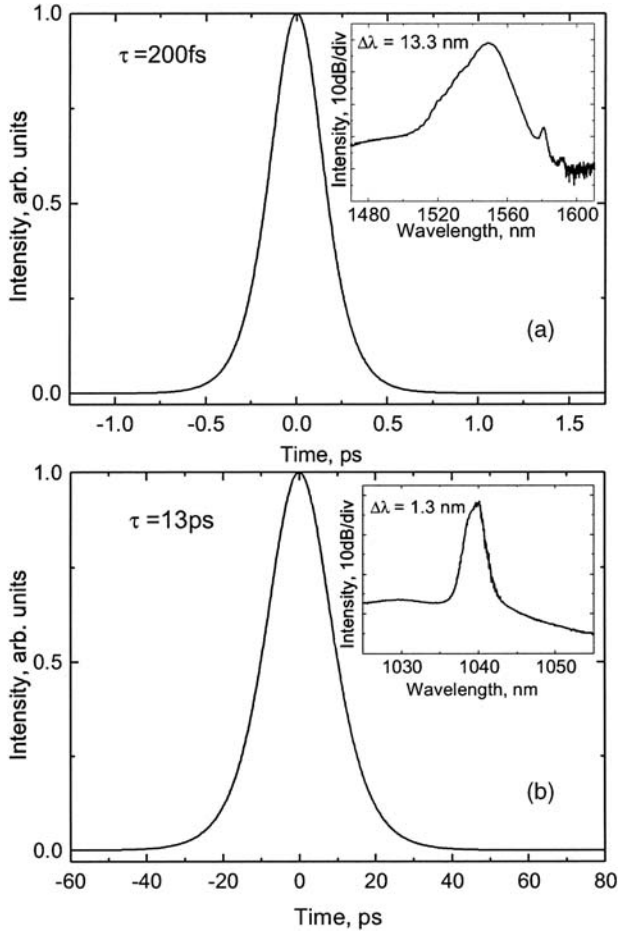

Fig. 3. Intensity autocorrelations and optical pulse spectra, displayed as insets, of (a) a 1.54-μm master Er fiber laser and (b) a 1.04-μm slave Yb fiber laser.

achieved for a difference in repetition rates of ~80 Hz between free-running and captured operation of the slave 1-μm laser. The corresponding tolerance in the cavity-length mismatch of the 1.54-μm master laser was ~9 μm. Synchronization for a change in the cavity in the opposite direction (length decreasing) showed nearly the same frequency locking range of ~90 Hz, resulting in a total cavity-length tolerance of ~20 μm, as shown in Fig. 4(b). The total output power of the source was ~3 mW, and no notable power changes were measured in either a synchronized or a free-running regime. The passive synchronization mechanism depicted in Fig. 4 implies that the master laser locks the repetition frequency of the slave laser and exhibits a large synchronization band, shown in the figure as overlapping dots. When they are synchronized, the two lasers maintain the same repetition frequency (within 10-Hz resolution of the analyzer) and the slave laser precisely tracks any variations in the master laser's frequency by changing its effective cavity length through shifting of the wavelength (as much as 3 nm at 1060 nm) and, consequently, the group velocity.

In conclusion, we have presented, for the first time to our knowledge, reliable synchronization between two

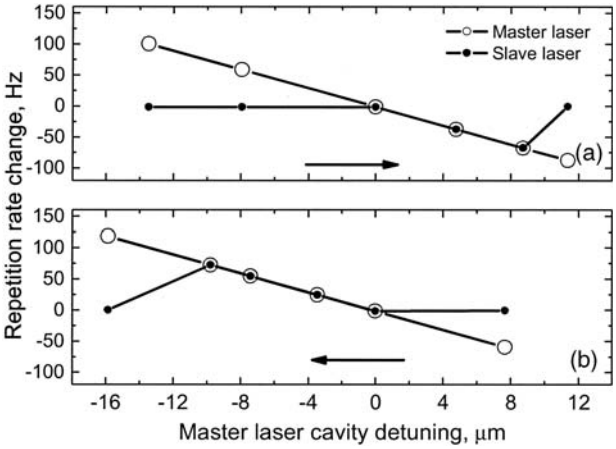

Fig. 4. Round-trip frequencies of the Er and Yb fiber lasers obtained by (a) lengthening and (b) shortening the cavity length of the Er fiber laser, plotted against the measured master laser cavity length. Arrows indicate the directions of the master cavity changes.

mode-locked fiber lasers that jointly share a cavity. Strong coupling, achieved by cross-phase modulation in a fiber, results in a large cavity mismatch tolerance of ~20 μm. This result, achieved because of the fiber cavity's advantages, can be exploited in practical two-color synchronized ultrafast sources.

This research was supported by the Academy of Finland (projects Supercontinuum Generation in Tapered Optical Fibers; Light Interaction with Microcavities and Photonic Crystal Structures; and Ultrafast Quantum-Regime Semiconductors, Components, and Subsystems) and the Technology Development Centre (project Towards Lighter Technologies). M. Rusu's e-mail address is matei.rusu@orc.tut.fi.

References

1. O. G. Okhotnikov, L. Gomes, N. Xiang, T. Jouhti, and A. B. Grudinin, Opt. Lett. **28,** 1522 (2003).
2. O. G. Okhotnikov, T. Jouhti, J. Konttinen, S. Karirinne, and M. Pessa, Opt. Lett. **28,** 364 (2003).
3. M. Rusu, S. Karirinne, M. Guina, A. B. Grudinin, and O. G. Okhotnikov, IEEE Photon. Technol. Lett. **16,** 1029 (2004).
4. T. R. Schibli, J. Kim, O. Kuzucu, J. T. Gopinath, S. N. Tandon, G. S. Petrich, L. A. Kolodziejski, J. G. Fujimoto, E. P. Ippen, and F. X. Kaertner, Opt. Lett. **28,** 947 (2003).
5. R. K. Shelton, S. M. Foreman, L.-S. Ma, J. L. Hall, H. C. Kapteyn, M. M. Murnane, M. Notcutt, and J. Ye, Opt. Lett. **27,** 312 (2002).
6. A. Leitenstofer, C. Fürst, and A. Laubereau, Opt. Lett. **20,** 916 (1995).
7. Z. Wei, Y. Kobayashi, Z. Zhang, and K. Torizuka, Opt. Lett. **26,** 1806 (2001).
8. Z. Wei, Y. Kobayashi, and K. Torizuka, Opt. Lett. **27,** 2121 (2002).
9. M. Betz, F. Sotier, F. Tauser, S. Trumm, A. Laubereau, and A. Leitenstorfer, Opt. Lett. **29,** 639 (2004).
10. M. Guina, N. Xiang, A. Vainionpää, O. G. Okhotnikov, T. Sajavaara, and J. Keinonen, Opt. Lett. **26,** 1809 (2001).

Appendix 6

Publication 6

M. Rusu, E. U. Rafailov, R. Herda, O. G. Okhotnikov, S. M. Saltiel, P. Battle, S. McNeil, A. B. Grudinin, and W. Sibbett, "Efficient generation of green and UV light in a single PP-KTP waveguide pumped by a compact all-fiber system," *Appl. Phys. Lett.* **88**, 121105 (1–3) (2006).

Efficient generation of green and UV light in a single PP-KTP waveguide pumped by a compact all-fiber system

M. Rusu[a)]
Optoelectronics Research Centre, Tampere University of Technology, P.O. Box 692, FIN-33101 Tampere, Finland

E. U. Rafailov[b)]
Division of Electronic Engineering and Physics, University of Dundee, Dundee, DD1 4HN, United Kingdom

R. Herda and O. G. Okhotnikov
Optoelectronics Research Centre, Tampere University of Technology, P.O. Box 692, FIN-33101 Tampere, Finland

S. M. Saltiel
Faculty of Physics, University of Sofia, 5 J. Bourchier Boulevard, BG-1164, Sofia, Bulgaria

P. Battle and S. McNeil
AdvR Incorporation, 2311 S. 7th Avenue, Building No. 1, Bozeman, Montana 59715

A. B. Grudinin
Fianium Limited, 20 Compass Point, Ensign Way, Southampton, SO31 4RA, United Kingdom

W. Sibbett
School of Physics and Astronomy, University of St. Andrews, St. Andrews, KY16 9SS, United Kingdom

(Received 2 December 2005; accepted 30 January 2006; published online 20 March 2006)

We present simultaneous efficient second- (SHG) and third-harmonic generation (THG) in a single periodically-poled KTP waveguided crystal pumped by a compact femtosecond Yb-based laser in a condition of exactly phase-matched frequency doubling and nonphase-matched sum-frequency mixing processes. Internal conversion efficiency as high as 33% for SHG (532 nm) and ~2% for the cascaded THG (355 nm) is reported. We believe this to be a clear experimental demonstration that strong third-harmonic can be generated in frequency doubling crystals through a nonphase-matched sum-frequency mixing process. © *2006 American Institute of Physics*.
[DOI: 10.1063/1.2187396]

Sources of ultrashort pulses in the visible and UV spectral regions are important for a wide range of applications in ultrafast science and technology. Recent progress in biophotonics research such as microscopy, optical micromanipulation, and biomedical imaging continues to strengthen the need for compact, low-cost, visible, and UV sources that offer portability and practicality. Such laser-based sources have clear advantages over near-infrared lasers in allowing for stronger beam focusing, enhanced resolution in multidimensional imaging techniques[1] and high-resolution spectroscopy.[2] By using ultrashort-pulse lasers in preference to continuous-wave sources, it is possible to investigate ultrafast biological processes,[3] increase the resolution in microscopy,[4,5] and amplify weak signals in nonlinear and multiphoton techniques.[6–8] Imaging and display technology also draw useful benefits from ultrashort visible pulses, in breakthrough applications such as red/green/blue laser displays.[9] To date, frequency multiplication in nonlinear optical crystals has been the most efficient way to generate coherent visible and UV light. By employing small, robust crystals with periodically-poled structures to improve wavelength conversion efficiency[10,11] it has been possible to make frequency conversion the preferred candidate for out-of-the-lab visible and UV pulsed sources. The advent of fiber lasers provided a reliable and small footprint laser source[12] for use in a large selection of applications, including frequency conversion. When combined in a single configuration, a fiber laser and a suitable periodically poled crystal represent a practical and efficient source option for industrial use. In this paper, we report a periodically-poled KTP (PPKTP) crystal having a predesigned waveguide structure to implement a compact pulsed source for simultaneous generation of visible and UV light. A brief theoretical analysis is included to confirm that efficient frequency doublers can simultaneously yield efficient third harmonic. Several ways to improve the current performance are also suggested.

The PPKTP frequency-doubling crystal used in our work was fabricated by an ion-exchange and chemical poling technique.[13] This 12 mm long crystal was designed to provide optimized second-harmonic generation of 1065 nm incident radiation, at a temperature of 60 °C. The crystal is placed on a thermoelectric cooler/heater within a control loop that enabled the crystal temperature to be maintained to an accuracy of better than 0.1 °C. The pump light was focused in the crystal waveguide (cross-sectional area of 4 μm × 7 μm) without any special requirement concerning the Rayleigh range of the beam. To ensure maximum flexibility in operational wavelength, each of the embedded waveguides has been poled with a slightly different period ranging from 8.22 μm–8.72 μm. The duty factor D was 0.6. Therefore, tuning for the optimal conversion wavelength could be achieved either by tuning the temperature of the

[a)]Electronic mail: matei.rusu@tut.fi
[b)]Electronic mail: e.u.rafailov@dundee.ac.uk

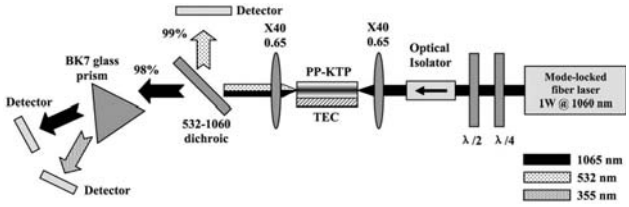

FIG. 1. Simplified layout of the experimental setup.

crystal or by changing the waveguide employed in second-harmonic generation (SHG).

The experimental setup for frequency doubling is shown in Fig. 1. The pump laser was built around a master oscillator-power amplifier (MOPA) architecture. The master source was a compact fiber laser mode-locked by a semiconductor saturable absorber mirror and its output signal power was boosted in a large mode area double-clad fiber amplifier pumped by a stack of 920 nm diode lasers. Driven at full power, the MOPA system could produce up to 1 W of average power with linearly polarized 3 ps pulses, at a repetition rate of 100 MHz. Figure 2(a) shows the optical spectrum of the laser operating at full power. A typical intensity autocorrelation trace is also provided as an inset. Self-phase modulation features are obvious in the spectrum, and any further increase in the average power was restricted by the onset of Raman effects.

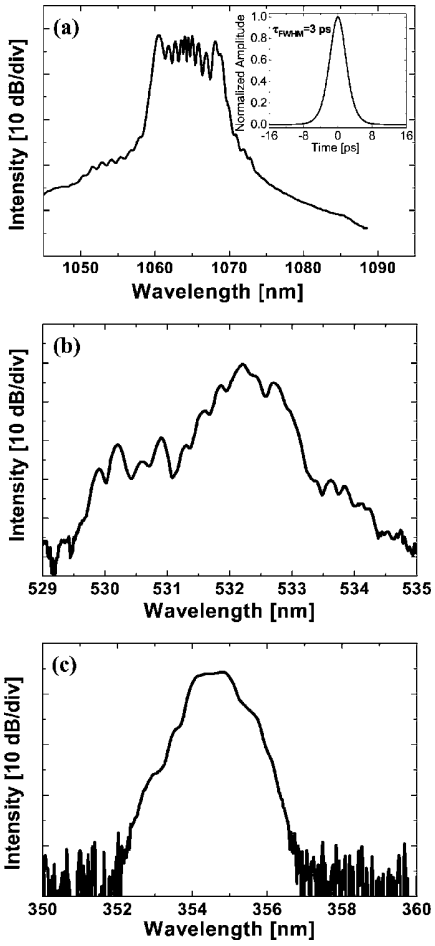

FIG. 2. (a) Optical spectrum of the fundamental radiation, inset shows the corresponding intensity autocorrelation trace ($\tau_{\mathrm{FWHM}} \sim 3$ ps); (b) Optical spectrum of the SH radiation. (c) Optical spectrum of the TH radiation.

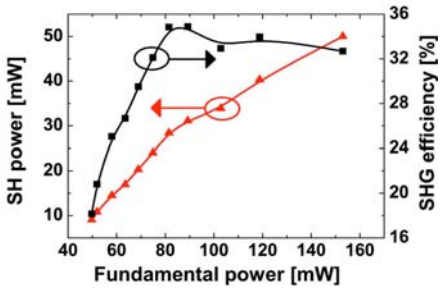

FIG. 3. (Color online) Generated SH average power and the internal efficiency of the PPKTP waveguide crystal as functions of the average power of the fundamental radiation.

When the laser beam was focused into the waveguide of the nonlinear crystal, intense nonlinear interactions give rise to a strong second-harmonic (SH) output that was collected by a microscope objective (Newport 40X) placed at the output of the crystal. To accurately measure its characteristics, the SH radiation was separated from the residual fundamental light by means of a dichroic mirror exhibiting 99% reflectivity at 532 nm, 98% transmission at 1060 nm, and ~95% transmission at 355 nm. Subsequent separation of the third-harmonic light from the fundamental was accomplished using a BK7—glass prism placed in the beam path.

The maximum measured second harmonic power was about 50 mW. Following collimation and separation from residual fundamental pump light and higher order harmonics, the SH signal was fed to a spectrometer and optical power meter. Figure 2(b) is a reproduction of the SHG optical spectrum. The conversion efficiency curve is plotted in Fig. 3. The saturation effects arising from strong two-photon absorption (TPA) (Ref. 14) and THG are evident in this plot. We measured a maximum SHG efficiency of 33%, where the main limiting factors in conversion efficiency are attributed to the limited spectral acceptance bandwidth of the nonlinear crystal and TPA.

The residual light transmitted through the dichroic mirror was directed through a BK7 glass prism that provides spectral dispersion. It was thus possible to separate the third harmonic beam component from the fundamental and to direct it to the input port of an optical spectrum analyzer. This produced the spectrum shown in Fig. 2(c), which exhibits a profile close to that of the second-harmonic signal. The bandwidth of the third-harmonic radiation is 1 nm which matches the input acceptance bandwidth of the nonlinear crystal. It is worth noting that, for the particular wavelength of the generated third-harmonic radiation, the transparency of the BK7 glass prism in Fig. 1 varies strongly with wavelength. However, owing to the narrow spectrum of the third-harmonic radiation, we do not expect this unwanted feature to cause any significant distortion in the measured spectral shape in Fig. 2(c).

Notably, the second- and third-harmonic radiations are generated *simultaneously* by nonlinear interactions that arise in the crystal. The power of the third-harmonic radiation was 3 mW, implying a conversion efficiency of 2%. Generation of third-harmonic radiation is attributed to a series of $\chi^{(2)}:\chi^{(2)}$ nonlinear cascaded processes (Ref. 15)—in our case the process of phase-matched SH generation followed by nonphase-matched sum frequency mixing (SFM) between the depleted fundamental and the strong SH light generated in the same waveguide.

To understand the mechanism of the generated TH signal, we introduce the quantity $M_{\mathrm{coh},m}=\pi/\Delta k_{2,m}$ ($\Delta k_{2,m}=k_3-k_2-k_1-2\pi m/\Lambda$) that we call quasi phase-matched (QPM) *coherence length* in analogy to the well known coherence length in volume nonlinear crystals. Using the Sellmeier equation formulation reported in literature,[16] we calculated the QPM coherence length for the processes of SFM in the PPKTP crystal for the relevant period of 8.8 μm that corresponds to first order QPM matching for the SHG process. We found that for $\lambda_{\mathrm{fund}}=1.065$ μm the SFM processes have QPM coherence lengths that correspond to different QPM orders of the SFM process equal to: $M_{\mathrm{coh},m}=\{1.5;2.3;4.7;71.0;4.2\}$ μm for $m=1-5$. For other m the QPM coherence length is even smaller. Thus one can expect rather efficient SFM processes and efficient generation of the TH signal with fourth-order QPM matching ($M_{\mathrm{coh},4}=71$ μm). The system of equations that describes the cascaded THG in single quadratic media with the plane wave and slow varying envelope approximations was taken from previous publications.[15] With the assumptions of exact phase matching for the SHG process, nondepletion of the fundamental wave due to SHG and THG, and nondepletion of SH wave due to THG, the system is simplified to:

$$\frac{dA_2}{dz}=-i\sigma_1 A_1^2;\quad \frac{dA_3}{dz}=-iA_1A_2\sum_{m(m\neq 0)}\sigma_{3,m}\exp(i\Delta k_{2,m}z), \tag{1}$$

where $\sigma_1=2\pi d_{\mathrm{eff},1}/\lambda_1 n_1 g_1$; $\sigma_{3,m}=2\pi d_{\mathrm{eff},3m}/\lambda_3 n_3 g_3$; with $d_{\mathrm{eff},1}=d_{zzz}2/\pi\sin(\pi D)$, $d_{\mathrm{eff},3m}=d_{zzz}2/m\pi\sin(m\pi D)$, and g_j—are the overlapping integrals. The duty factor D of the QPM structure used in our experiment is $D=0.6$, and therefore even order QPM matching is possible. The simplified solution of Eq. (1) for the squared third-harmonic amplitude when the small oscillating terms are neglected (except the term with $m=4$) gives

$$|A_3|^2\approx\left(\frac{1}{\pi}\sigma_1\sigma_3|A_1|^3LM_{\mathrm{coh},4}\right)^2. \tag{2}$$

From Eq. (2), it is evident that despite the fact that the second step (SFM) is nonphase matched, the total cascaded process of THG behaves in the manner of a phase-matched third-order process. This means we do not expect periodic modulation of the efficiency of THG on the length of the media. TH intensity grows quadratically with nonlinear media length and has cubic dependence on the input intensity $I_3\propto I_1^3$. The longer the QPM coherence length $M_{\mathrm{coh},m}$ of the SFM process, the more efficient the THG becomes. Estimates derived from Eq. (2), assuming $g_1=g_2=0.5$, show that with similar conditions experienced in this work, one can expect a THG efficiency of around 2.7% at an input power of 150 mW. It should be noted that the calculated efficiency does not take into account the absorption at $\lambda_{3\omega}=0.355$ μm.[16] The exact value of the overlap integrals g_1, g_2 is unknown and the effect of group velocities mismatch has also been neglected in our analysis. We consider the measured experimental efficiency to be consistent with this estimation. We thus demonstrated that efficient TH signal can be obtained under the condition of an initial phase-matched SHG process with a subsequent nonphase-matched SFM process. This is in contrast to some previously published conclusions[17,18] that efficient THG with phase matched SH process in single quadratic crystal is not possible. However, in several other publications, theoretical models have been derived that are in agreement with our work (citations in Ref. 15), but they do not include experimental demonstrations of efficient THG as reported here. Previously reported THG efficiencies in experiments of this type in bulk KTP and KDP were less than 10^{-7} and thus impractical.[17,19]

In conclusion, we demonstrated simultaneous second- and third-harmonic generation in a PPKTP waveguided crystal in a condition of exactly phase matched frequency doubling and nonphase-matched sum-frequency mixing processes. The pump laser source was a compact, all fiber, high power mode-locked system, that provided a good quality beam and hence efficient light coupling into the crystal. The waveguide structure of the crystal allowed us to use simple, low focal length collimating optics. This system is a possible candidate for providing the portable visible and UV light sources of the near future. It is worth noting that current system performance could be improved by employing a narrow spectrum laser source achievable, for instance, by using a large mode area fiber amplifier to defeat nonlinear processes in the current fiber amplifier. Moreover, the crystal acceptance bandwidth can be improved by using an aperiodically poled crystal with synthesized grating profile optimized for the available laser source.

The authors wish to acknowledge the support of the U.K. Engineering and Physical Sciences Research Council, Bulgarian Science Found (Grant No. 1201/2002), European Union FP6 project URANUS and AdvR, Inc. in Bozeman, Montana.

[1] P. N. Prasad, in *Introduction to Biophotonics* (Wiley, Hoboken, New Jersey, 2003), p. 203.
[2] H. Schnitzler, U. Frohlich, T. K. W. Boley, A. E. M. Clemen, J. Mlynek, A. Peters, and S. Schiller, Appl. Opt. **41**, 7000 (2002).
[3] R. S. Knox, J. Photochem. Photobiol., A **49**, 81 (1999).
[4] W. Rudolph, P. Dorn, X. Liu, N. Vretenar, and R. Stock, Appl. Surf. Sci. **208**, 327 (2003).
[5] S. W. Hell, P. E. Hanninen, J. Salo, A. Kuusisto, E. Soini, T. Wilson, and J. B. Tan, Opt. Commun. **113**, 144 (1994).
[6] B. Agate, C. T. A. Brown, W. Sibbett, and K. Dholakia, Opt. Express **12**, 3011 (2004).
[7] P. J. Campagnola, M. D. Wei, A. Lewis, and L. M. Loew, Biophys. J. **77**, 3341 (1999).
[8] E. Bordenave, E. Abraham, G. Jonusauskas, J. Oberle, and C. Rulliere, Opt. Express **10**, 35 (2002).
[9] Q. Ye, L. Shah, J. Eichenholz, D. Hammons, R. Peale, M. Richardson, A. Chin, and B. H. T. Chai, Opt. Commun. **164**, 33 (1999).
[10] E. U. Rafailov, D. J. L. Birkin, W. Sibbett, P. Battle, T. Fry, and D. Mohatt, Opt. Lett. **26**, 1961 (2001).
[11] A. A. Lagatsky, E. U. Rafailov, A. R. Sarmani, C. T. A. Brown, W. Sibbett, L. Ming, and P. G. R. Smith, Opt. Lett. **30**, 1144 (2005).
[12] O. G. Okhotnikov, L. Gomes, N. Xiang, T. Jouhti, and A. B. Grudinin, Opt. Lett. **28**, 1522 (2003).
[13] G. W. Arnold, G. De Marchi, F. Gonella, P. Mazzoldi, A. Quaranta, G. Battaglin, M. Catalano, F. Garrido, and R. F. Haglund Jr., Nucl. Instrum. Methods Phys. Res. B **116**, 507 (1996).
[14] B. Agate, E. U. Rafailov, W. Sibbett, S. M. Saltiel, P. Battle, T. Fry, and D. Mohatt, Opt. Lett. **28**, 1963 (2003).
[15] S. M. Saltiel, A. A. Sukhorukov, and Y. S. Kivshar, in *Progress in Optics* 47, edited by E. Wolf (Elsevier, North–Holland, New York, 2005), Chap. 1, p. 1.
[16] B. Boulanger, M. M. Fejer, R. Blachman, and P. F. Bordui, Appl. Phys. Lett. **65**, 2401 (1994).
[17] Y. Takagi and S. Muraki, J. Lumin. **87**, 865 (2000).
[18] P. Qiu and A. Penzkofer, Appl. Phys. B **45**, 225 (1988).
[19] S. A. Akhmanov, L. B. Meisner, S. T. Parinov, S. M. Saltiel, and V. G. Tunkin, Zh. Eksp. Teor. Fiz. **73**, 1710 (1977) (in Russian) [English translation: JETP Lett. **46**, 898 (1977)].

Appendix 7

Publication 7

M. Rusu and O. G. Okhotnikov, "All-fiber picosecond laser source based on nonlinear spectral compression," *Appl. Phys. Lett.* **89**, 091118 (1–3) (2006).

All-fiber picosecond laser source based on nonlinear spectral compression

M. Rusu[a] and O. G. Okhotnikov
Optoelectronics Research Centre, Tampere University of Technology, P.O. Box 692, 33101 Tampere, Finland

(Received 12 April 2006; accepted 19 July 2006; published online 31 August 2006)

The authors report the realization of an all-fiber system emitting high-quality ultrashort powerful light pulses at 1060 nm. The oscillator-amplifier system is intended for compact visible light generation via frequency conversion. Optical nonlinearity in a fiber amplifier is employed to compress the spectrum of pulses negatively prechirped in a hollow core photonic bandgap fiber. Second-harmonic generation in a periodically poled crystal is demonstrated. © *2006 American Institute of Physics*. [DOI: 10.1063/1.2339954]

Recent progress in biophotonics research such as microscopy, optical micromanipulation, and biomedical imaging strengthens the need for compact, low-cost, ultrashort pulse sources of visible light with enhanced portability and practicality. Visible wavelengths, which are difficult to generate directly from diode-pumped lasers, are routinely produced by pairing a short pulse infrared oscillator with a nonlinear optical system via frequency conversion. By employing nonlinear crystals with periodically poled structure to improve the conversion efficiency,[1] it has been possible to make this technique a strong candidate for out-of-the-laboratory visible pulsed sources. Remarkable conversion efficiencies of up to 40% with 225-fs-long visible light pulses have been reported by groups employing bulk solid state mode-locked lasers as sources of ultrashort infrared pulses[2] and periodically poled $LiTaO_3$ crystals. Owing to their small footprint, maintenance-free operation, and relaxed thermal requirements, fiber lasers and amplifiers are regarded as a very promising solution for compact sources of ultrashort pulses.[3,4] With the advent of semiconductor saturable absorber mirrors (SESAMs), ultrashort pulse fiber lasers in both low-[5] and high-power[6] versions started challenging fields of science traditionally occupied by bulk laser systems. Combining the mature, well-established fiber laser technology with periodically poled crystals, efficient and compact sources of ultrashort visible pulses became possible.

Periodically poled crystal engineering is subject to conflicting requirements. Long crystals are generally needed to ensure sufficient interaction length between the laser light and nonlinear medium. At the same time, long periodically poled crystals exhibit low operation bandwidth which seriously limits the amount of pump power usable in the conversion process. The main limitation in nonlinear conversion efficiency when using a fiber laser as pump source is the spectral broadening experienced by high power ultrashort pulses propagating in a fiber, owing to optical nonlinearity such as self-phase modulation and Raman effects. A trade-off between the nonlinear crystal length and its bandwidth must thus be enforced. Employing aperiodically poled crystals would alleviate these requirements due to increased acceptance bandwidth for a given interaction length,[7] as well as reduced temperature sensitivity.[8] However, there is a large amount of interest in employing conventional periodically poled crystals in frequency conversion schemes, owing to their ease of design and widespread commercial availability. It is then obvious that nearly transform-limited pulses having minimal bandwidth for a given pulse width are preferred for frequency conversion. Chirped pulse amplification (CPA) architecture,[9] where pulses are stretched, amplified, and then temporally compressed, is widely used to produce high-energy ultrashort pulses. Despite notable performance, CPA technique fails to control the pulse spectrum. The reported high peak powers are typically achieved at the expense of large spectral width, making CPA incompatible with long periodically poled crystals. A promising solution can be achieved by employing nonlinear effects to directly control the spectral width of the laser source.[10] The method exploits self-phase modulation in fiber amplifiers to effectively compress the spectrum of a negatively chirped input pulse. After generation, the pulse undergoes negative chirping in a medium with anomalous dispersion, followed by optical amplification. The positive chirp imposed on the pulse by self-phase modulation (SPM) in the amplifying fiber can compensate the original negative chirp of the pulse, leading to a redistribution of the spectral components of the pulse towards the central wavelength of the spectrum. Spectral compression ratio up to factor of 21 has been previously reported for high power systems.[11,12] The systems employed in prior work rely upon massive bulk diffraction gratings to provide negative dispersion. Power amplification is performed by double clad systems with heavy pumping techniques.

In this letter we demonstrate an all-fiber system employing nonlinear spectral compression resulting in nearly transform-limited pulses suitable for efficient frequency conversion. The system uses core-pumped amplifier technology, being suitable for compact integration. A frequency doubling experiment is performed to illustrate the performance of the pulsed source.

The optical setup of the system is given in Fig. 1. A linear cavity Yb-doped fiber laser mode locked by a SESAM and operating at 1040 nm is used as the master pulse source. The repetition rate of the fiber laser is 55 MHz. An optical isolator is spliced at the output of the laser to prevent back reflections from the stretcher-amplifier chain. Operated at full pump power, the master laser produces 7 mW of average optical power. The optical spectrum and autocorrelation trace of the laser pulses are given in Fig. 2(a). Owing to the isolator pigtails the pulses exhibit certain positive chirp, as in-

[a]Electronic mail: matei.rusu@tut.fi

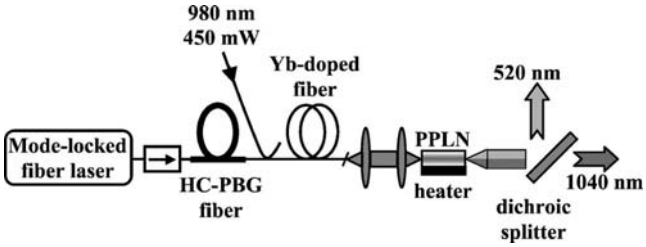

FIG. 1. Optical layout of the ultrashort visible pulse source. PPLN: periodically poled lithium niobate crystal. HC-PBG fiber: hollow-core photonic band gap fiber.

dicated by the large time-bandwidth product. The master oscillator pulses are launched into a 5-m-long span of hollow-core photonic band gap (HC-PBG) fiber (HC 1060, Blaze Photonics) with anomalous dispersion of 100 ps/nm/km at 1040 nm. The light is launched into and collected from the HC-PBG fiber by butt coupling with standard single-mode fiber. Careful alignment and fixing of the standard and HC-PBG fibers resulted in an environmentally stable, low-loss mechanical splice. The Fresnel back reflection from the solid-core/air-core interface in the splice is blocked by the optical isolator at the output of the laser. The autocorrelation trace and optical spectrum of the pulse at the output of the HC-PBG fiber are shown in Fig. 2(b). Owing to low nonlinearity of the air-core fiber, the spectrum of the pulses is nearly unchanged. The negatively chirped pulses are then launched into a core-pumped ytterbium fiber amplifier. A

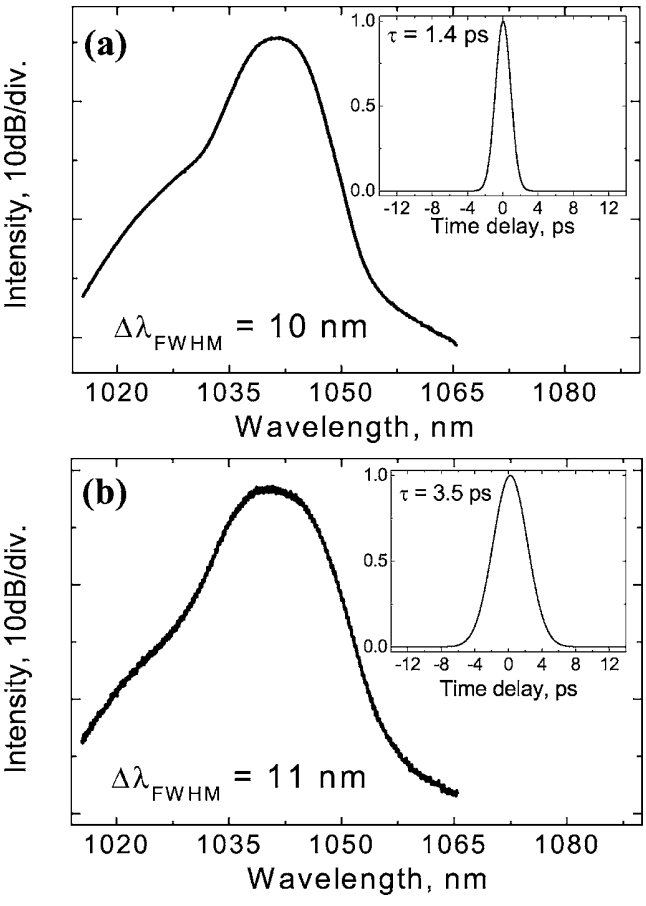

FIG. 2. Optical spectrum and autocorrelation trace of the pulses before (a) and after (b) HC-PBG fiber.

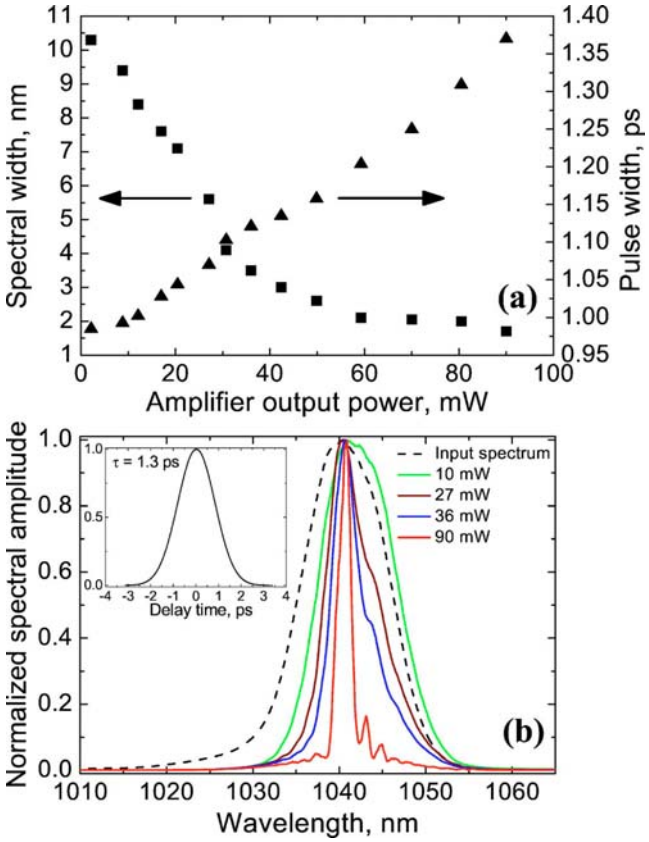

FIG. 3. (Color online) Pulse duration and spectral width evolution with amplifier output power. (a) Optical spectrum of output pulses for different amplifier powers, with autocorrelation trace of the pulse with the smallest spectral bandwidth shown as inset (b).

450 mW grating stabilized single-mode laser diode pumps the amplifier through a fused dichroic coupler. The total length of the optical amplifier is 4 m including the fiber coupler, active fiber, and input and output pigtails. The angle-cleaved output end of the amplifier delivers the spectrum-compressed pulses. An optical spectrum analyzer, optical power meter, and intensity autocorrelator were used to characterize the system.

The pump power of the amplifier seeded with negatively chirped pulses was gradually increased up to the maximum available value while monitoring the spectrum of the output pulses. For each setting of the amplifier power, the optical spectrum, autocorrelation trace, and average power were measured. Figure 3(a) shows the evolution of the spectrum and pulse width with amplifier power. As the amplifier power increases, the spectrum bandwidth of the output pulses decreases from the initial value of 10.3 nm down to a minimum value of 1.6 nm. At full pump power, the amplifier delivers 90 mW of average power in 1.3 ps pulses, yielding a peak power of 1.25 kW. This value can be regarded as good achievement for a simple core-pumped system using just two single-mode pump diodes. The time-bandwidth product of the output pulses decreases accordingly from 3.16 at low amplifier power to 0.58 at full power. The nearly transform-limited pulses stand proof to the high quality of spectral compression in the single-mode, core-pumped amplifier. Figure 3(b) presents spectra collected at the output of the amplifier for different power settings. The input pulse spectrum is shown with dashed line. The inset reveals the autocorrela-

tion trace of the pulse with the smallest bandwidth. The redshift of the spectrum, seen at low output power, is due to mismatch between the amplifier gain peak and input pulse spectrum.[11] At higher output powers, the spectra are centered near the peak wavelength of the input spectrum of 1040 nm. The special features of the compressed spectra (slight asymmetry and oscillations) are attributed to the relatively large third-order dispersion of the HC-PBG fiber stretcher.[10] The output pulse width increases with amplifier power, as shown in Fig. 3(a), since narrow spectral bandwidth eventually starts to limit pulse compression in the amplifying fiber. It is worth noting, however, that the duration of the pulse with the highest spectral compression is shorter than the pulse width of the master oscillator, shown in Fig. 2(a). In order to obtain high spectral compression at full amplifier power, the amount of negative prechirping in HC-PBG fiber should be exactly balanced by SPM developed in the amplifier. For instance, too long amplifying fiber may cause the spectrum to broaden again, after going through a minimum width value. This is obviously a nonoptimal behavior, as the pulse with the smallest optical bandwidth would not correspond to the highest output power from the amplifier. For the system depicted in Fig. 1, the amplifier fiber length and doping level were chosen properly to precisely balance the initial prechirping.

The amplifier output was coupled to a 10-mm-long periodically poled lithium niobate (PPLN) crystal optimized for operation at 1040 nm. The acceptance bandwidth of the crystal was 0.5 nm. The crystal was placed inside an electrical oven with a temperature control accuracy of 0.1 °C, heated at an optimal operation temperature of the crystal of 120 °C. Collimated light from the fiber amplifier was focused onto the PPLN crystal by means of a 35 mm biconvex lens. A half-wave plate was used for polarization control. Due to reflections from the uncoated optical facets, a maximum of 80 mW of infrared light could be launched into the PPLN crystal. The visible light at the crystal output was separated from unconverted fundamental infrared radiation by a dichroic mirror exhibiting 95% reflectivity for the second-harmonic light and 98% transmission at fundamental wavelength. At full amplifier power, we measured 12 mW of light at 520 nm, corresponding to an overall conversion efficiency of 15%. The spectrum of the second-harmonic radiation is given in Fig. 4. Its full width at half maximum of 0.5 nm matches the acceptance bandwidth of the crystal. Performing spectral integration in Fig. 3(b), we inferred the amount of power contained in the crystal acceptance bandwidth to be about 18 mW, yielding an effective second-harmonic efficiency of 66%. We deem the result reasonable for a core-pumped system employing only two single-mode pigtailed pump lasers.

In conclusion, we demonstrated an all-fiber laser source which exploits prechirping in anomalous dispersion photonic band gap fiber and subsequent nonlinear spectral compression in an optical amplifier to provide nearly transform-limited picosecond pulses. The source is suitable for efficient second-harmonic generation. This concept using photonic band gap fiber for negative chirping allows for low-loss all-fiber setups that may use low-noise and economic core-pumped amplifier solutions, resulting in remarkable frequency conversion efficiency at moderate power levels, comparable with the efficiency obtained from high power systems. With further technical improvements, the device could constitute a practical portable source delivering ultrashort visible pulses.

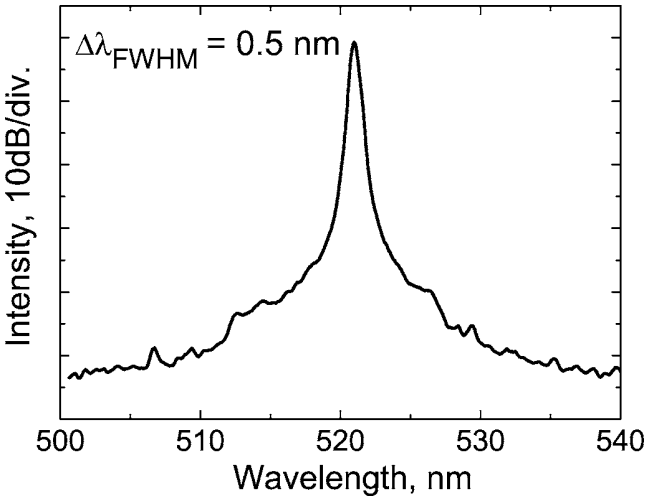

FIG. 4. Optical spectrum of the second-harmonic green light.

This work was financially supported by EU-FP6 project URANUS. The authors thank Stratophase Ltd. for supplying the PPLN crystal.

[1] E. U. Rafailov, D. J. L. Birkin, W. Sibbett, P. Battle, T. Fry, and D. Mohatt, Opt. Lett. **26**, 1961 (2001).
[2] A. A. Lagatsky, E. U. Rafailov, A. R. Sarmani, C. T. A. Brown, W. Sibbett, L. Ming, and P. G. R. Smith, Opt. Lett. **30**, 1144 (2005).
[3] F. Ö. Ilday, J. R. Buckley, H. Lim, F. W. Wise, and W. G. Clark, Opt. Lett. **28**, 1365 (2003).
[4] L. Goldberg, R. P. Koplow, and D. A. V. Kliner, Opt. Lett. **24**, 673 (1999).
[5] O. G. Okhotnikov, L. A. Gomes, N. Xiang, T. Jouhti, and A. B. Grudinin, Opt. Lett. **28**, 1522 (2003).
[6] A. Malinowski, A. Piper, J. H. V. Price, K. Furusawa, Y. Jeong, J. Nilsson, and D. J. Richardson, Opt. Lett. **29**, 2073 (2004).
[7] D. J. L. Birkin, E. U. Rafailov, G. S. Sokolovskii, W. Sibbett, G. W. Ross, P. G. R. Smith, and D. C. Hanna, Appl. Phys. Lett. **78**, 3172 (2001).
[8] B. Agate, E. U. Rafailov, W. Sibbett, S. M. Saltiel, K. Koynov, M. Tiihonen, W. Shunhua, F. Laurell, P. Battle, T. Fry, T. Roberts, and E. Noonan, IEEE J. Sel. Top. Quantum Electron. **10**, 1268 (2004).
[9] P. Maine, D. Strickland, P. Bado, M. Pessot, and G. Mourou, IEEE J. Quantum Electron. **24**, 398 (1988).
[10] M. Oberthaler and R. A. Höpfel, Appl. Phys. Lett. **63**, 1017 (1993).
[11] J. Limpert, T. Gabler, A. Liem, H. Zellmer, and A. Tünnermann, Appl. Phys. B: Lasers Opt. **74**, 191 (2002).
[12] J. Limpert, N. Deguil-Robin, I. Manek-Hýnninger, F. Salin, T. Schreiber, A. Liem, F. Rýser, H. Zellmer, A. Týnnermann, A. Courjaud, C. Hýnninger, and E. Mottay, Opt. Lett. **30**, 714 (2005).

Appendix 8

Publication 8

M. Rusu, A. B. Grudinin, O. G. Okhotnikov, "Slicing the supercontinuum radiation generated in photonic crystal fiber using an all-fiber chirped-pulse amplification system," *Opt. Express* **13**, 6390–6400 (2005).

Slicing the supercontinuum radiation generated in photonic crystal fiber using an all-fiber chirped-pulse amplification system

M. Rusu, A. B. Grudinin[*] and O. G. Okhotnikov

Optoelectronics Research Centre, Tampere University of Technology,
P.O. Box 692, FIN-33101, Tampere, Finland
[*]Fianium Ltd., UK
matei.a.rusu@orc.tut.fi

Abstract: We report on an experimental study of supercontinuum broadening in photonic crystal fiber performed by measuring the temporal behavior of spectrally-sliced radiation in different propagation regimes. The study confirms the soliton fission theory by observing the red-shifted fundamental solitons and blue-shifted nonsolitonic radiation.

OCIS codes: (140.3510) Lasers, fibers; (140.4050) Mode-locked lasers; (190.4370) Nonlinear optics, fibers; (190.4380) Nonlinear optics; (320.7160) Ultrafast technology

References

1. O. G. Okhotnikov, L. Gomes, N. Xiang, T. Jouhti, and A. B. Grudinin, "Mode-locked ytterbium fiber laser tunable in the 980-1070 -nm spectral range," Opt. Lett. **28**, 1522 (2003).
2. O. G. Okhotnikov, T. Jouhti, J. Konttinen, S. Karirinne and M. Pessa, "1.5- μm monolithic GaInNAs semiconductor saturable-absorber mode locking of an erbium fiber laser," Opt. Lett. **28**, 364 (2003).
3. M. Rusu, S. Karirinne, M. Guina, A. B. Grudinin, and O. G. Okhotnikov, "Femtosecond neodymium-doped fiber laser operating in the 894-909 nm spectral range," IEEE Photonics Technol. Lett. **16**, 1029 (2004).
4. Fianium Ltd., *Femtopower FP1060* product datasheet, http://www.fianium.com
5. A. B. Rulkov, M. Y. Vyatkin, S. V. Popov, J. R. Taylor, and V. P. Gapontsev, "High brightness all-fiber generation in 525-1800 nm range with picosecond Yb pumping," Opt. Express **13**, 377-381 (2005), http://www.opticsexpress.org/abstract.cfm?URI=OPEX-13-2-377
6. K. Sakamaki, M. Nakao, M. Naganuma, and M. Izutsu, "Soliton Induced Supercontinuum Generation in Photonic Crystal Fiber," IEEE J. Quantum Electron. **10**, 876-883 (2004).
7. S. Coen, A. H. L. Chau, R. Leonhardt, J. D. Harvey, J. C. Knight, W. J. Wadsworth, and P. St. J. Russell, "Supercontinuum generation by stimulated Raman scattering and parametric four-wave mixing in photonic crystal fibers," J. Opt. Soc. Am. B **19**, 753-764 (2002).
8. J. M. Dudley, L. Provino, N. Grossard, H. Maillotte, R. S. Windeler, B. J. Eggleton, and S. Coen, "Supercontinuum generation in air-silica microstructured fibers with nanosecond and femtosecond pulse pumping," J. Opt. Soc. Am. B **19**, 765-771 (2002).
9. A. V. Husakou and J. Herrmann, "Supercontinuum Generation of Higher-Order Solitons by Fission in Photonic Crystal Fibers," Phys. Rev. Lett. **87**, 203901(1)-203901(4) (2001).
10. N. I. Nikolov, T. Sorensen, O. Bang, and A. Bjarklev, "Improving efficiency of supercontinuum generation in photonic crystal fibers by direct degenerate four-wave mixing," J. Opt. Soc. Am. B **20**, 2329-2337 (2003).
11. J. Herrmann, U. Griebner, N. Zhavoronkov, A. Housakou, D. Nickel, J. C. Knight, W. J. Wadsworth, P. St. J. Russell, and G. Korn, "Experimental Evidence for Supercontinuum Generation by Fission of Higher-Order Solitons in Photonic Fibers," Phys. Rev. Lett. **88**, 173901 1-4 (2002).
12. T. Schreiber, J. Limpert, H. Zellmer, A. Tünnermann and K. P. Hansen, "High average power supercontinuum generation in photonic crystal fibers," Opt. Commun. **228**, 71-78 (2003).
13. J. M. Dudley, X. Gu, L. Xu, M. Kimmel, E. Zeek, P. O'Shea, R. Trebino, S. Coen, and R. S. Windeler, "Cross-correlation frequency resolved optical gating analysis of broadband continuum generation in photonic crystal fiber: simulations and experiments," Opt. Express **10**, 1215-1221 (2002), http://www.opticsexpress.org/abstract.cfm?URI=OPEX-10-21-1215
14. K. M. Hilligsoe, H. N. Paulsen, J. Thogersen, S. R. Keiding, and J. J. Larsen, "Initial steps of supercontinuum generation in photonic crystal fibers," J. Opt. Soc. Am. B **20**, 1887-1893 (2003).
15. I. Zeylikovich, V. Kartazaev, and R. R. Alfanov, "Spectral, temporal, and coherence properties of supercontinuum generation in microstructure fiber," J. Opt. Soc. Am. B **22**, 1453-1460 (2005).

#7753 - $15.00 USD Received 8 June 2005; revised 4 August 2005; accepted 5 August 2005

16. T. Hori, N. Nishizawa, T. Goto, and M. Yoshida, "Experimental and numerical analysis of widely broadened supercontinuum generation in highly nonlinear dispersion-shifted fiber with a femtosecond pulse," J. Opt. Soc. Am. B **21**, 1969-1980 (2004).
17. J. M. Dudley and S. Coen, "Numerical Simulations and Coherence Properties of Supercontinuum Generation in Photonic Crystal and Tapered Optics Fibers," IEEE Sel. Top. Quantum Electron. **8**, 651-659 (2002).
18. K. Mori, H. Takara, and S. Kawanishi, "Analysis and design of supercontinuum pulse generation in single-mode optical fiber," J. Opt. Soc. Am. B **18**, 1780-1792 (2001).

1. Introduction

Supercontinuum radiation in photonic crystal fibers (PCF) has recently found exciting applications in metrology, fundamental research and medical sciences. Intensive efforts have been put into optimizing supercontinuum (SC) radiation parameters, such as spectral width, flatness and brightness, as well as developing compact all-fiber sources of ultra broadband radiation with low power consumption. Recent progress in passively mode-locked fiber lasers producing picosecond and femtosecond optical pulses stimulated the research on generation techniques and underlying mechanisms of spectral broadening in PCF. The semiconductor saturable absorber mirror (SESAM) technology has contributed greatly to the abovementioned achievements in mode-locked fiber laser. The main features of fiber-based devices – high efficiency, reliability and small footprint – make them strong competitors to the ultrafast solid-state lasers. The broad fluorescence spectrum of fiber gain media has been successfully used in tunable and ultrashort pulse sources. Recently, pulse sources operating in a wavelength range from 895 to 1560 nm were reported with neodymium, ytterbium and erbium doped fibers [1-3]. Moreover, SESAM-based mode-locked fiber lasers have reached unprecedented levels of output power and stability [4], which renders them almost ideal candidates for compact sources of supercontinuum radiation. Combined with advanced nonlinear media such as photonic crystal fibers, mode-locked fiber lasers led to significant achievements in SC generation [5]. The underlying phenomena of such a large spectral broadening are still amongst the most interesting areas in supercontinuum research. Previous studies show that self-phase modulation (SPM) alone can not produce the large spectral broadening observed at low powers in highly nonlinear photonic crystal fibers [6-8]. Moreover, detailed characterization of the supercontinuum shows that the formation of ultra-broadband spectra cannot arise solely from an interplay between SPM and four-wave mixing (FWM). Recent theories describe supercontinuum radiation as an effect of a much more complex process of soliton fission [9], assisted by SPM and FWM [10]. Further theoretical and experimental work provided evidence of soliton fission during supercontinuum generation [11-13]. It should be emphasized, however, that self-phase modulation and four-wave mixing play a substantial role in the formation and evolution of supercontinuum radiation [10], as the two phenomena act cooperatively with soliton fission to provide significant broadening of the initial pump laser spectrum [14]. Particularly, the final shape of the supercontinuum radiation spectrum is determined by a set of cascaded phenomena (SPM, FWM, soliton fission), whose contribution to the supercontinuum generation process is weighed by several system parameters, like input pulse power and duration, fiber group velocity dispersion (GVD), and fiber nonlinearity.

Temporal evolution of optical pulses within the supercontinuum spectrum gives an essential knowledge for understanding the supercontinuum formation from a relatively narrow-bandwidth pump radiation and constitutes a valuable starting point for optimizing the parameters of nonlinear media used in practical supercontinuum generators. Prior research on spectro-temporal shape of supercontinuum pulses was carried out using complex interferometric systems [15-16] and provided useful information concerning supercontinuum radiation coherence and temporal evolution. An experimental investigation of temporal shape of supercontinuum pulses in normal and anomalous dispersion regimes of the nonlinear medium is meaningful, as it clearly identifies the nature of light pulses within the

#7753 - $15.00 USD Received 8 June 2005; revised 4 August 2005; accepted 5 August 2005

supercontinuum radiation, confirming that soliton fission assisted by SPM and FWM is the basis of supercontinuum broadening in PCF. In this paper, we demonstrate a simple scheme to characterize the temporal evolution of supercontinuum light pulses. The experimental setup employs a broadband optical filter to slice various spectral regions of a supercontinuum and a SHG autocorrelator to perform subsequent temporal shape analysis. Evidence of soliton fission-driven supercontinuum is found, along with traces of the phenomena that initiate spectral broadening.

2. Experimental setup

The setup used in the experiment is shown in Fig. 1.

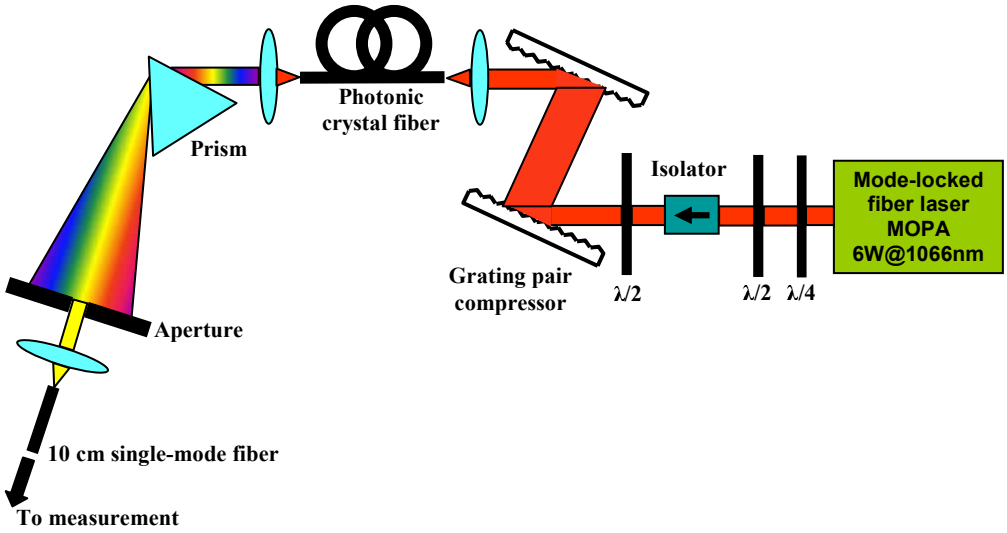

Fig. 1. Supercontinuum slicing setup with fiber MOPA pump source. MOPA: master oscillator and power amplifier

The laser source is an ytterbium (Yb) fiber-laser, mode-locked by a semiconductor saturable absorber mirror (SESAM) followed by a large mode-area (LMA) Yb-double clad fiber amplifier to boost the power. The master oscillator – power amplifier (MOPA) system produced up to 6 W of average power with 3 ps pulses at a repetition rate of 100 MHz. Figure 2 reveals the spectral characteristic of the laser output at full power and the corresponding autocorrelation trace. For optimal supercontinuum generation, the wavelength of the pump laser was set to 1066 nm, close to the zero-dispersion wavelength of the nonlinear fiber.

#7753 - $15.00 USD Received 8 June 2005; revised 4 August 2005; accepted 5 August 2005

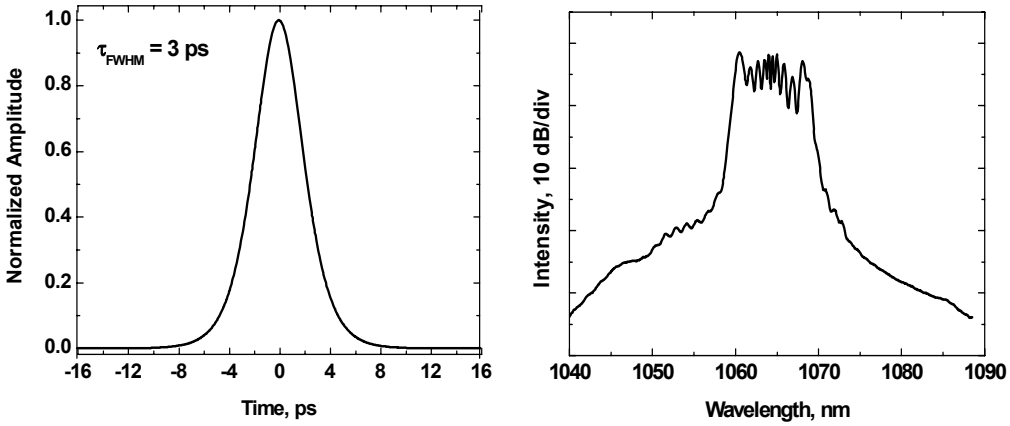

Fig. 2. Intensity autocorrelation and spectrum of the fiber source taken at full power.

Owing to nonlinearities in the amplifier fiber, the output pulses were up-chirped, which allowed for subsequent pulse compression in a diffractive grating pair exhibiting negative dispersion. The pulses emerging from the laser source are passed through a set of quarter- and half-wave plates which provide polarization corrections to the beam. A free-space optical isolator was employed to avoid back-reflections to the high-power amplifier which may adversely influence the system output power and spectrum. An additional half-wave plate aligns the polarization state of the light emerging from the isolator to ensure low-loss transmission through the grating pair pulse compressor. The grating pair removes the spectral chirp, resulting in the temporal compression of the pulse. Optimized group velocity dispersion of the grating pair yields a pulse width of 430 fs. This arrangement is known as chirped-pulse amplification (CPA) technique. The de-chirped pulse width and spectrum are shown in Fig. 3. Owing to very low nonlinearity, the grating pair compressor introduces only a minor distortion to the pulse spectrum.

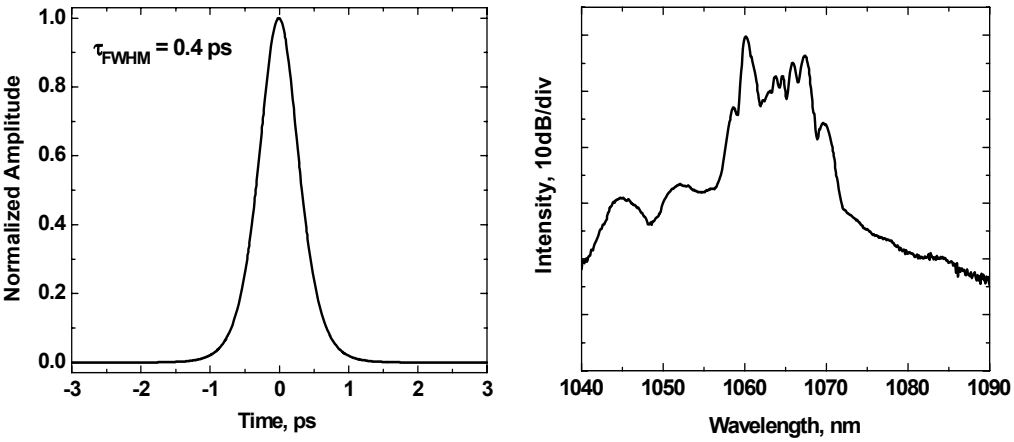

Fig. 3. Compressed pulse autocorrelation and spectrum.

#7753 - $15.00 USD Received 8 June 2005; revised 4 August 2005; accepted 5 August 2005

The average power after the grating compressor was 2.4 W. When driven close to maximum power, the laser output beam becomes randomly polarized, which creates additional losses in the grating compressor and optical isolator.

3. Experimental results

Firstly, the compressed pulses in Fig. 3 are coupled into a 15 m span of highly nonlinear fiber (Crystal Fibre NL-5.0-1065) with the zero dispersion wavelength around 1065 nm, and dispersion characteristic shown as inset in Fig. 4. The fiber transmission efficiency was 50% (accounting for lens coupling and fiber transmission losses), resulting in an average power of 1.2 W at the output of the fiber. Strong nonlinear interactions in the fiber led to the formation of broad supercontinuum radiation, presented in Fig. 4.

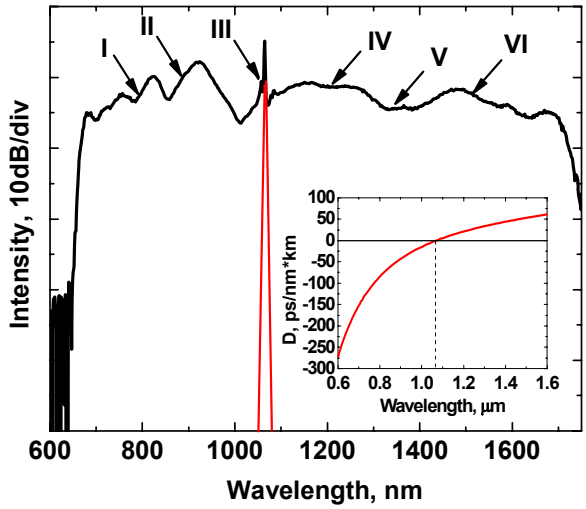

Fig. 4. Supercontinuum spectrum obtained with the setup shown in Fig. 1. Input laser spectrum at 1.06 μm is plotted with a red line. The inset shows the PCF dispersion map.

The supercontinuum generation was then investigated using pulses taken directly from the output of the power amplifier without subsequent compression in the grating pair compressor. The SC and pump spectra are illustrated in Fig. 5. Comparison of the supercontinuum spectra obtained with and without pulse compression reveals that the use of compressed pulses yielded only a minor improvement in the spectral bandwidth.

In the current system configuration, the uncompressed pulses energy was 40 nJ and their peak power was 13 kW. Following compression in the grating pair, laser pulses energy dropped to 24 nJ (as a result of losses in the compressor), whereas the peak power increased to 60 kW. Despite notable difference in the pulse characteristics, the compressed and uncompressed pulse trains produced nearly identical supercontinuum spectra. One reason behind this feature is the behavior of the pulse during the initial steps of supercontinuum generation. As shown further in the paper, upon entering the supercontinuum fiber, the pump pulse undergoes significant temporal compression attributed to an interplay between GVD and SPM [17].

#7753 - $15.00 USD Received 8 June 2005; revised 4 August 2005; accepted 5 August 2005

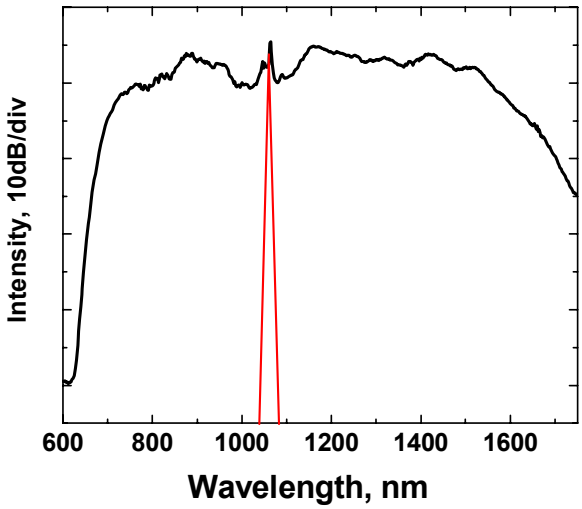

Fig. 5. Supercontinuum spectrum when uncompressed pulses are coupled into PCF (15 m of NL-5.0-1065 fiber). Input average power is 4 W, and output power is 1W. Input laser spectrum is plotted with red line.

The broad pulses with high energy are efficiently compressed inside the nonlinear fiber and reach peak power level comparable to the power of the pulses pre-compressed in the grating pair, thus leading to a comparable supercontinuum spectrum. Furthermore, assuming that the peak power is high enough, a long pulse would be converted inside the nonlinear fiber to a high order soliton, which in turn splits into a large number of fundamental solitons, resulting in a large amount of blue-shifted non-solitonic radiation emitted upon fission [9]. Owing to their relatively large peak power, the long uncompressed pulses generate large number of fundamental solitons and, consequently, a broad supercontinuum spectrum. These observations lead to a generic design guideline for supercontinuum generator sources: one should employ a source producing relatively broad pulses with high peak power. This will lead to high order solitons available for fission, and simultaneously stimulate peak power driven processes (SPM, Raman shifting, self-steepening, etc.). Therefore, practical designs should attempt a trade-off between pulse width and peak power to achieve optimal spectrum width.

To analyze temporal shape of supercontinuum pulses at different wavelengths, we performed spectrum slicing by means of a prism, as shown in Fig. 1. The prism was mounted on a motorized stage which can be precisely rotated, thus directing various wavelength components into the filtering aperture. By rotating the prism, the entire supercontinuum spectrum can be scanned. The selected spectral component is monitored with an optical spectrum analyzer, while an intensity autocorrelation trace is simultaneously taken for each selected part of the spectrum. The bandwidth of the spectral filter varied between 20 and 70 nm. To inspect the effects involved in the formation of supercontinuum, several sub-bands within the supercontinuum spectrum have been investigated. The central wavelengths of the explored sub-bands are marked in Fig. 4. The measurements of the spectrally-sliced pulses in normal and anomalous dispersion regimes confirm the soliton character of the pulses in anomalous dispersion regime and the stretched pulse character of the pulses sliced from the blue-shifted part of the spectrum, as predicted by the soliton fission theory [9]. Figure 6 shows the autocorrelations and spectra of the pulses sliced from the short-wavelength part of the supercontinuum spectrum with normal dispersion regime of propagation (indicated as I and II on Fig. 4). The peculiar shape of the autocorrelation trace is due to the non-solitonic

#7753 - $15.00 USD Received 8 June 2005; revised 4 August 2005; accepted 5 August 2005

properties of these pulses. Since the pulses propagate in normal dispersion regime, they undergo significant broadening and overlapping leading to autocorrelation features seen in Fig. 6. The autocorrelations and optical spectra in Fig. 6(b) and 6(d) are obtained directly after the output aperture shown in Fig. 1. The spectral width of the filter was set to avoid the pulse duration being influenced by excessive spectral filtering.

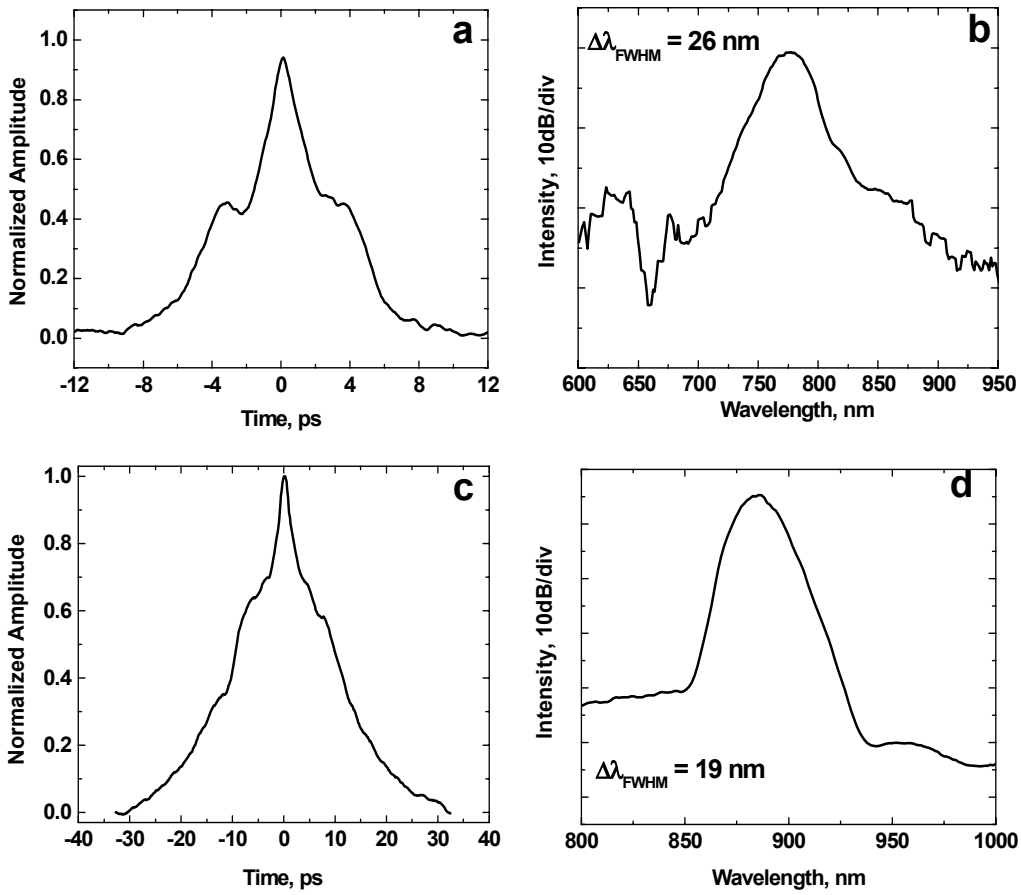

Fig. 6. Autocorrelations and spectra of the SC pulses in normal dispersion region, at 770 nm (a and b) and 880 nm (c and d).

Optical spectra and autocorrelation traces of the pulses sliced from the supercontinuum spectrum near the zero-dispersion wavelength of the nonlinear fiber are presented in Fig. 7. The spectral feature at 1065 nm originating from the residual pump is evident in the spectrum as a sharp peak (Fig. 7(b)).

#7753 - $15.00 USD Received 8 June 2005; revised 4 August 2005; accepted 5 August 2005

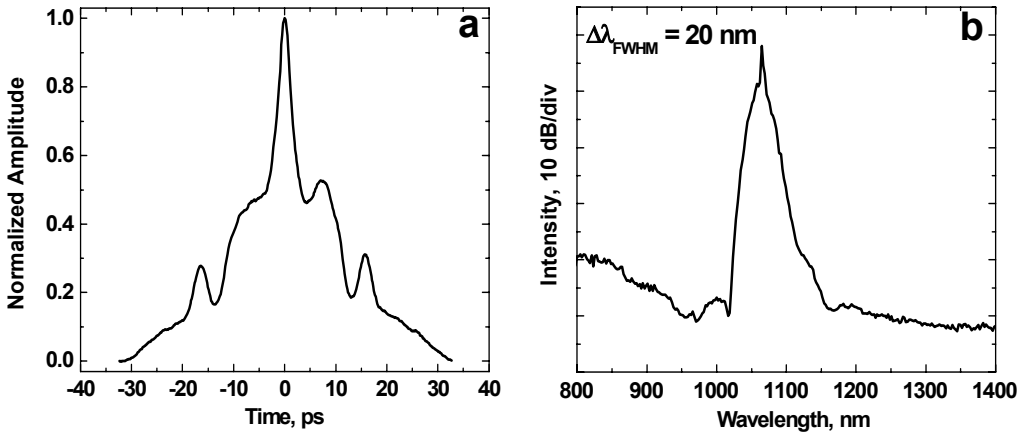

Fig. 7. Autocorrelation and spectrum of pulse sliced near zero dispersion wavelength (1065 nm)

The autocorrelation of the pump pulse shows apparent pulse breakup, which is in agreement with the theory [17]. It is worth noting that the pulse presented in Fig. 7 can be primarily regarded as a residual pump pulse left unconverted into supercontinuum radiation after propagation through the nonlinear fiber. The spike seen in the autocorrelation reveals the pulse width of 140 fs indicating that before Raman shifting, the input pulse undergoes significant compression, as described in [18]. This peak feature is ~3 times shorter than the initial input pulse shown in Fig. 3.

#7753 - $15.00 USD Received 8 June 2005; revised 4 August 2005; accepted 5 August 2005

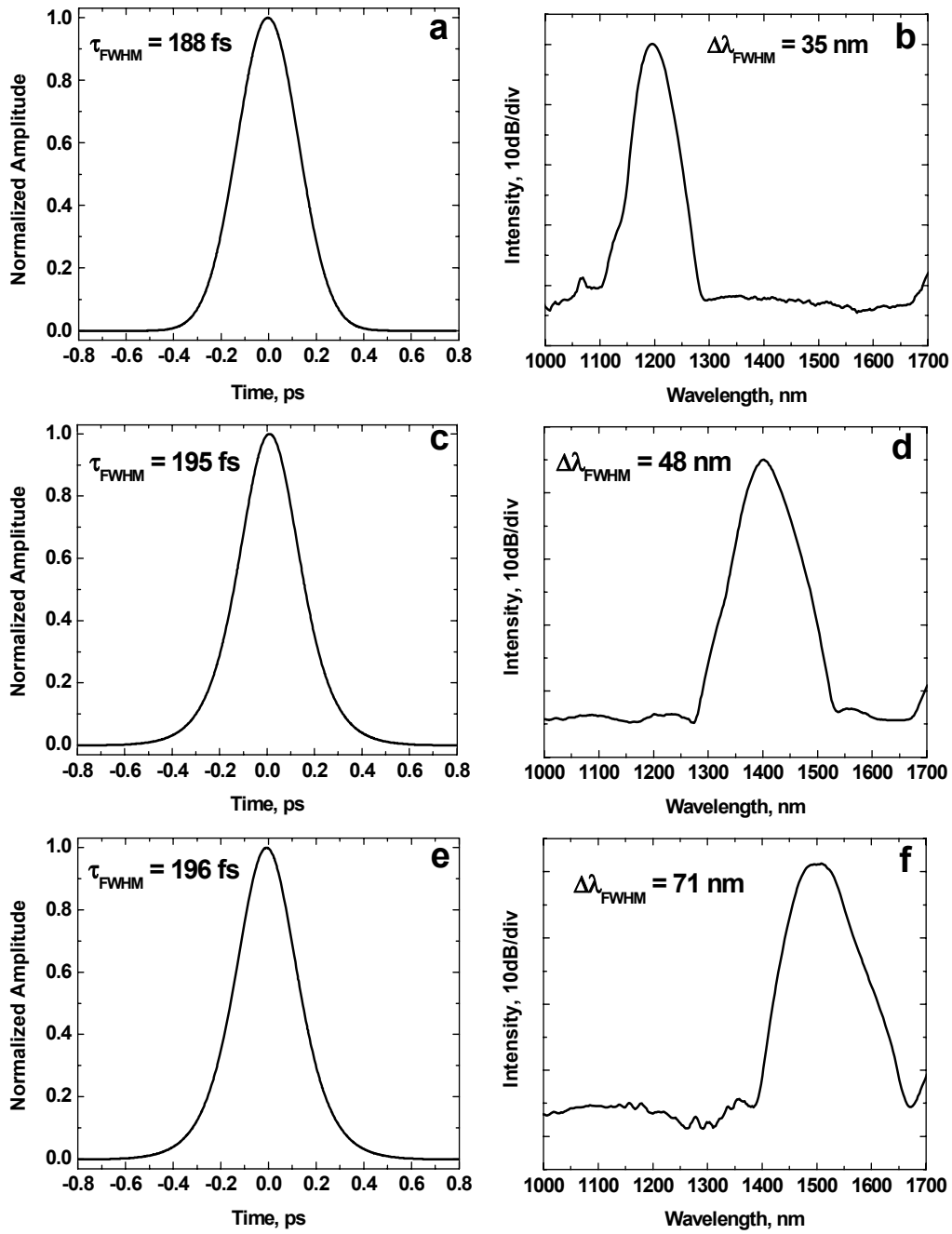

Fig. 8. Autocorrelation and spectra of pulses in anomalous dispersion regime: 1200 nm (a, b), 1400 nm (c, d), and 1500 nm (e, f).

The characteristics of the pulses in anomalous dispersion regime are shown in Figs. 8(a)-(f). The smooth, clean autocorrelations of the pulses in this regime indicate that they are steady-state solitons in agreement with the theoretical conclusions made in [9]. The soliton pulses are much shorter than the blue-shifted pulses, as inferred from Fig. 6. The sharp rise at the right

#7753 - $15.00 USD Received 8 June 2005; revised 4 August 2005; accepted 5 August 2005

end of the spectra in Fig. 8 is a spectrum analyzer artifact. All pulse widths have been derived assuming a $sech^2$ pulse shape. Despite the smooth, symmetric shape of the autocorrelation traces in Fig. 8, the calculated time-bandwidth product of the measured pulses exceeds the transform-limited value for fundamental solitons. This feature is likely due to the filtering procedure that provided spectra exceeding the bandwidth of the fundamental soliton. Another interesting feature derived from Fig. 8 is that the soliton pulses in the spectral range between 1200 and 1500 nm have practically the same width despite a 3-fold change of the nonlinear fiber dispersion in the mentioned wavelength range. This could be explained by the fact that spectral shift towards longer wavelengths requires pulses with higher energy. Therefore, it is expected that long-wavelength solitons have higher energies and, consequently, shorter durations. This phenomenon is balanced by the dispersion profile of the PCF and results in similar durations of the fundamental solitons observed at different wavelengths.

The temporal stability of the pulses sliced from the supercontinuum spectrum was studied for different dispersion regimes of the photonic crystal fiber. The situation shown in Fig. 9 has been observed for any scheme of supercontinuum generation discussed above.

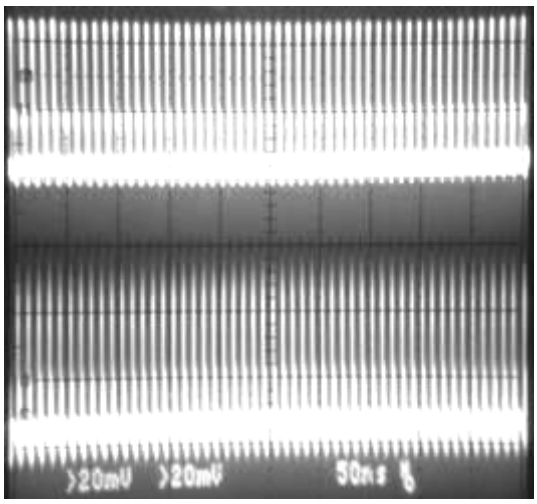

Fig. 9. Oscilloscope traces showing pulse train for soliton propagation regime (top) and normal dispersion regime (bottom).

The pulses sliced from the supercontinuum in the soliton regime can be clearly displayed on an analog scope (top trace in Fig. 9). On the contrary, the pulse train sliced at normal dispersion regime, i.e. nonsolitonic radiation, exhibits significant noise visible on the output pulses. The noise appears as large pulse-to-pulse amplitude variation.

4. Conclusions

We have investigated the temporal shape of different frequency components inside supercontinuum radiation. The measurements confirm the higher-order soliton fission theory. Upon launching into the fiber, the pump pulse first experiences significant compression followed by pulse breakup. The breakup of higher-order solitons results in the formation of red-shifted fundamental solitons and blue-shifted nonsolitonic radiation. The fundamental solitons with different colors propagate down the fiber at different group velocities without observable shape distortion. Due to the presence of several solitons with various frequencies, multiple blue-shifted peaks are generated leading to the formation of blue-shifted continuum. The blue-shifted pulses are longer than the soliton pulses by almost an order of magnitude and experience further severe broadening during propagation. The results provide an insight into

#7753 - $15.00 USD Received 8 June 2005; revised 4 August 2005; accepted 5 August 2005

the fundamental mechanisms of supercontinuum generation and would be useful in designing supercontinuum sources.

Acknowledgments

The authors acknowledge the financial support of the Finnish Academy of Sciences through SUPERNAL and GEMINI projects and the EU FP-6 URANUS project.

#7753 - $15.00 USD Received 8 June 2005; revised 4 August 2005; accepted 5 August 2005

Appendix 9

Publication 9

M. Rusu, S. Kivistö, C. B. E. Gawith, and O. G. Okhotnikov, "Red-green-blue (RGB) light generator using tapered fiber pumped with a frequency-doubled Yb-fiber laser," *Opt. Express* **13**, 8547–8554 (2005).

Red-green-blue (RGB) light generator using tapered fiber pumped with a frequency-doubled Yb-fiber laser

M. Rusu, S. Kivistö

Optoelectronics Research Centre, Tampere University of Technology, Finland
matei.rusu@tut.fi

C. B. E. Gawith

Stratophase Ltd., UK
corin.gawith@stratophase.com

O. G. Okhotnikov

Optoelectronics Research Centre, Tampere University of Technology, Finland

Abstract: We report on successful realization of a picosecond visible-continuum source embedding a single mode fiber taper. The output of ytterbium mode-locked fiber laser was frequency doubled in a periodically-polled lithium niobate (PPLN) crystal to produce green pump light. Spectral brightness of the white light generated in the tapered fiber was improved by limiting the broadening just to the visible wavelengths. The influence of taper parameters, particularly the dispersion, on white light spectrum has been studied.

OCIS codes: (190.4370) Nonlinear optics, fibers; (190.2620) Frequency conversion; (140.3510) Lasers, fiber; (320.7090) Ultrafast lasers; (130.3730) Integrated optics: Lithium niobate

References and Links

1. R. R. Alfano and S. L. Shapiro, "Observation of self-phase modulation and small-scale filaments in crystals and glasses," Phys. Rev. Lett. **24**, 592-594 (1970).
2. S. A. Diddams, D. J. Jones, J. Ye, S. T. Cundiff, J. L. Hall, J. K. Ranka, R. S. Windeler, R. Holzwarth, T. Udem, and T. W. Hansch, "Direct link between microwave and optical frequencies with a 300 THz femtosecond laser comb," Phys. Rev. Lett. **84**, 5102–5105 (2000).
3. I. Hartl, X. D. Li, C. Chudoba, R. K. Ghanta, T. H. Ko, J. G. Fujimoto, J. K. Ranka, and R. S. Windeler, "Ultrahigh resolution optical coherence tomography using continuum generation in an air-silica microstructured optical fiber," Opt. Lett. **26**, 608–610 (2001).
4. M. Nisoli, S. De Silvestri, O. Svelto, R. Szipocs, K. Ferencz, Ch. Spielmann, S. Sartania, and F. Krausz, "Compression of high-energy laser pulses below 5 fs," Opt. Lett. **22**, 522–524 (1997).
5. H. Takara, T. Ohara, K. Mori, K. Sato, E. Yamada, Y. Inoue, T. Shibata, M. Abe, T. Morioka, and K.-I. Sato, "More than 1000 channel optical frequency chain generation from single supercontinuum source with 12.5 GHz channel spacing," Electron. Lett. **36**, 2089–2090 (2000).
6. C. Lin and R. H. Stolen, "New nanosecond continuum for excited-state spectroscopy," Appl. Phys. Lett. **28**, 216-218 (1976).
7. J. K. Ranka, R. S. Windeler, A. J. Stentz, "Visible continuum generation in air-silica microstructure optical fibers with anomalous dispersion at 800 nm," Opt. Lett. **25**, 25-27 (2000).
8. T. A. Birks, W. J. Wadsworth, P. S. J. Russell, "Supercontinuum generation in tapered fibers," Opt. Lett. **25**, 1415-1417 (2000).
9. A. V. Husakou and J. Herrmann, "Supercontinuum Generation of Higher-Order Solitons by Fission in Photonic Crystal Fibers," Phys. Rev. Lett. **87**, 203901 1-4 (2001).
10. A. Liu, M. A. Norsen, and R. D. Mead, "60-W green output by frequency doubling of a polarized Yb-doped fiber laser," Opt. Lett. **30**, 67-69 (2005).
11. J. M. Dudley, L. Provino, N. Grossard, and H. Maillotte, "Supercontinuum generation in air–silica microstructured fibers with nanosecond and femtosecond pulse pumping," J. Opt. Soc. Am. B **19**, 765-771 (2002).
12. S. G. Leon-Saval, T. A. Birks, W. J. Wadsworth, P. St. J. Russell, and M. W. Mason, "Supercontinuum generation in submicron fibre waveguides," Opt. Express **12**, 2864-2869 (2004), http://www.opticsexpress.org/abstract.cfm?URI=OPEX-12-13-2864

#8587 - $15.00 USD Received 25 August 2005; Revised 5 October 2005; Accepted 5 October 2005

13. Fianium Ltd., FemtoPower1060, http://www.fianium.com/products/femtop.htm
14. Stratophase Ltd. grating design software.
15. T. A. Birks and Y. W. Li, "The shape of fiber tapers," J. Lightwave Technol. **10**, 432-438 (1992).
16. J. D. love, "Spot size, adiabaticity and diffraction in tapered fibres," Electron. Lett. 23, 993-994 (1987).
17. G. P. Agrawal, "Fiber-Optic Communication Systems," 2nd edition, Wiley, (1997).
18. J. Herrmann, U. Griebner, N. Zhavoronkov, A. Housakou, D. Nickel, J. C. Knight, W. J. Wadsworth, P. St. J. Russell, and G. Korn, "Experimental evidence for supercontinuum generation by fission of higher-order solitons in photonic fibers," Phys. Rev. Lett. **88**, 173901 1-4 (2002).

1. Introduction

Supercontinuum radiation (SC) has received remarkable attention since its early demonstration [1]. Despite complex interplay of nonlinear effects involved in the spectral broadening, supercontinuum radiation has been soon recognized as a useful tool for metrology [2], life sciences [3], the generation of ultrashort pulses [4], optical telecommunications [5]. Owing to their impressive spectral brightness, the SC sources represent an attractive alternative to traditional broadband (incandescent or fluorescent) light sources. Since the first demonstration of broadband light generation in guided media [6], SC sources based on improved nonlinear converters have become much more than just a subject for academic research. With the advent of powerful laser sources, ultra-broadband supercontinua exploiting different nonlinear media including photonic crystal fibers (PCF) [7] and fiber tapers [8] have been demonstrated.

Many applications require high-brightness RGB light sources with little energy outside the visible range. Traditional broadband sources fail to comply with these requirements, since typical "white-light" spectrum extends either in ultra-violet (e.g. with fluorescent emitters) or infrared (e.g. with incandescent sources) range. A supercontinuum source producing only visible light is a challenging task, since most supercontinuum sources nowadays use mode-locked infrared solid-state or fiber lasers. Using infrared lasers as a pump source to generate a visible continuum tends to be inefficient because significant fraction of the pump power is transferred to the far infrared, as expected from the SC formation mechanism [9]. A large amount of the pump energy is lost thus decreasing an overall efficiency of the RGB white-light source.

The visible light sources based on nonlinear frequency conversion with the spectrum broadening limited to RGB range would efficiently convert the pump power into visible light, providing better spectral brightness and wall-plug efficiency than the sources based on infrared-pump supercontinua. Since SC radiation is generated nearly symmetrically around the pump wavelength, the rational solution for visible light generation is to employ a pump laser whose wavelength is situated in the middle of the visible range around 530 nm.

Continuous improvement in nonlinear crystals has made a frequency conversion in periodically-polled crystals a practical technique to produce visible light from infrared lasers. Particularly, ytterbium fiber mode-locked lasers operating around 1060 nm and used together with nonlinear crystals optimized for frequency-doubling are a very promising source of visible pump pulses at 530 nm [10].

Another crucial issue in supercontinuum generation is the dispersion characteristic of the nonlinear medium. To achieve an efficient pump conversion to SC, the pump wavelength should match the zero dispersion wavelength (ZDW) of the nonlinear medium. The visible SC generators would thus require nonlinear media with zero-dispersion at visible wavelengths. PCF and fiber tapers can be engineered to have a ZDW around 530 nm. Notable results in broadband supercontinuum generation within both PCF and fiber tapers pumped with green light have been reported [11-12]. However, the spectral brightness of visible radiation and conversion efficiency are still to be improved by further optimization of the SC generator.

Fiber lasers have strong potential for the systems, where long term stability and maintenance-free operation are required. Semiconductor saturable absorber mirror (SESAM) based mode-locked fiber lasers are well known for their excellent pulse quality, small footprint and unprecedented reliability [13]. Mode-locked fiber lasers can produce ultrashort

#8587 - $15.00 USD Received 25 August 2005; Revised 5 October 2005; Accepted 5 October 2005

pulses with high peak power representing nearly ideal pump source for supercontinuum generation.

In this paper, we report on a high brightness, all-visible supercontinuum source using pump signal from mode-locked ytterbium fiber laser frequency-doubled in a periodically-poled lithium niobate (PPLN) crystal. White light radiation is then generated in a purposely-designed tapered fiber. An attractive feature of the tapered fiber important for practical SC sources is that ZDW could be easily adjusted by controlling the pulling conditions. We investigate the effect of taper ZDW and input power on a spectral bandwidth and shape of visible continuum. The results of this study show the tolerances of taper parameters that allow for efficient spectral broadening.

2. Experimental setup

The experimental setup used for supercontinuum generation is shown in Fig. 1.

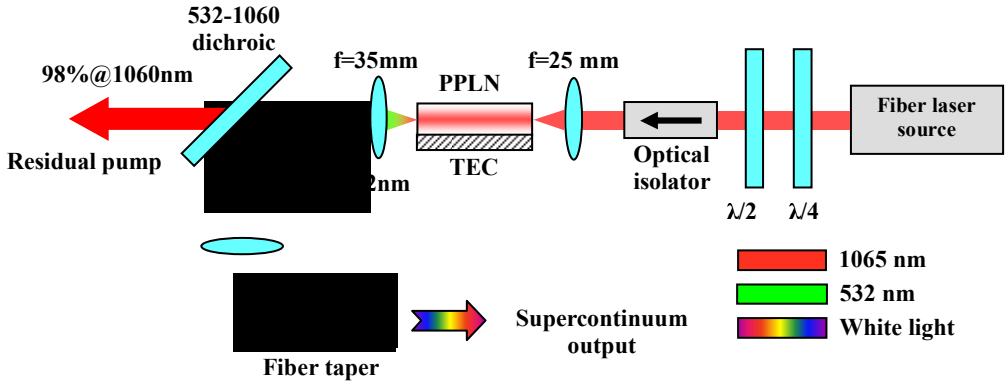

Fig. 1. Experimental setup for white light generation in tapered fibers: PPLN – periodically-poled lithium niobate; TEC – thermo-electric cooler.

The pump source is an Yb-doped fiber laser mode-locked by a SESAM. A double-clad Yb-fiber amplifier is used to boost the average power up to 2 W. The laser spectrum taken at full power with the center emission wavelength of 1064 nm is shown in Fig. 2(a). The pulse autocorrelation trace revealing a pump pulse width of 3 ps is shown as an inset. The pump laser beam passes through polarization correction waveplates and an optical isolator which eliminates back reflections preventing the changes in the power and spectrum of the system. Owing to random polarization of the pump beam, the polarization-dependent optical isolator limits the usable pump power to ~1 W.

#8587 - $15.00 USD Received 25 August 2005; Revised 5 October 2005; Accepted 5 October 2005

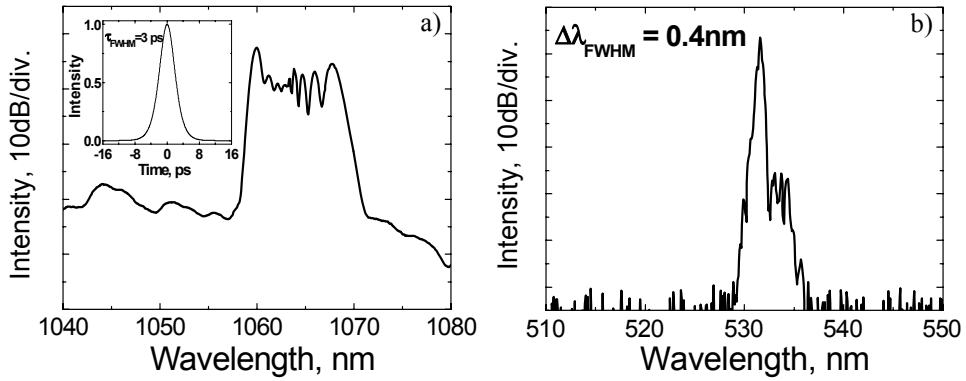

Fig. 2. Pump spectrum and autocorrelation shown as an inset (a) and corresponding spectrum of the second-harmonic (SH) radiation.

The nonlinear crystal used for frequency conversion was a 500 μm-long PPLN made by Stratophase Ltd. The PPLN grating structure was formed using standard photolithography. The domain inversion was performed in the z-axis at room temperature with a single high-voltage pulse of ~11 kV applied through liquid electrodes. A set of gratings with periods of 6.50, 6.54 and 6.58 μm was fabricated. In these experiments, best results have been obtained with 6.58-μm period grating operated at 160°C [14] which ensures optimum phase matching with our pump source with the wavelength centered at 1064 nm. The crystal was placed inside an electrical oven controlled by a digital feedback loop that allows to control the crystal temperature with a precision of 0.1°C. Additionally, high operating temperature eliminates any potential problems caused by the photorefractive effect. The pump light was focused onto the crystal using the lens with a focal length of 25 mm. At the highest pump power, we obtained ~120 mW of SH power, corresponding to a conversion efficiency of about 14%. The pump and SH radiation emerging from the crystal were combined using a lens with 35-mm focal distance and broadband antireflection coating. The SH light was then separated from residual pump radiation by a dichroic mirror exhibiting 99% reflectivity for the SH light and 98% transmission for the residual pump. The SH light was subsequently launched by a microscope objective into the pigtail of the fiber with a tapered segment. The maximum SH power coupled to the 8-μm core fiber pigtail was 80 mW. The spectrum of the SH light measured at full power is presented in Fig. 2(b). The spectral bandwidth of the SH radiation is 0.4 nm and it approximately matches the bandwidth of the PPLN crystal.

3. Fiber tapers

The fiber tapers studied in this experiment were fabricated using a home-made fiber tapering workstation. We use commercial SMF-28 fiber as primary material, because of its excellent diameter uniformity. During tapering, the fiber was heated by two hydrogen-oxygen burners equipped with separate gas flow controllers. The fiber through-put during tapering was monitored by launching a low power 532-nm signal into the input pigtail and reading the transmitted power continuously. The tapering rig is fully computer controlled, which enables us to build tapers with accurately adjusted length and diameter of the waist. To ensure low loss adiabatic tapers, we used a double-stage tapering strategy. First, the fiber is pulled under a fixed heated zone until the waist diameter reaches ~10 μm. Then the heated zone size increases linearly with progressive pulling of the fiber [15] until the target waist diameter is reached. To obtain consistent results, the computer program keeps the waist length constant for all tapers studied despite their waist diameter by controlling the amount of molten glass at the initial tapering stage. After pulling, the tapers are packaged in a plastic case and characterized. The taper waist diameter has been accurately measured using images taken by a high resolution CCD camera through a large magnification optical system (150X). Image

#8587 - $15.00 USD Received 25 August 2005; Revised 5 October 2005; Accepted 5 October 2005

analysis software was employed to determine the waist diameter with 0.05-μm accuracy. A typical bi-conical profile is presented in Fig. 3 showing a uniform waist with length of 19 cm for the taper with total length of 26 cm.

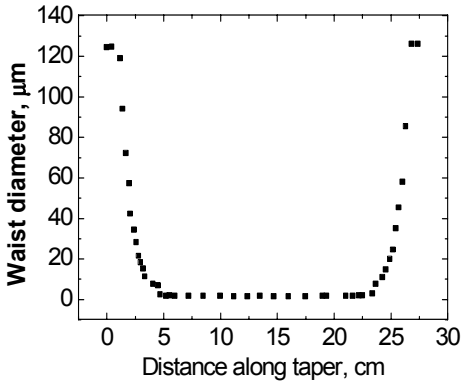

Fig. 3. Sample taper profile.

4. Experimental results

The potential of the tapered structures with different waist diameters to supercontinuum generation has been first examined by studying their chromatic dispersion at pump wavelength. It has been shown that the optical field during the propagation along the down-taper transition in a fiber detaches from the fiber core and penetrates into the cladding, becoming eventually guided by the glass-air interface [16]. The taper waist has been modeled with a circular strand of glass surrounded by air. This approximation is valid for structures used in SC experiments since tapering ratio exceeds 10^2 and therefore the fiber core becomes insignificantly small and cannot support the guided modes. Because our tapered transitions (conical sections of the structure) are short compared to the length of the waist, as seen from Fig. 3, we neglect the influence of the conical sections of the taper. The chromatic dispersion was evaluated by solving the propagation constant eigenvalue equation for a given waist diameter [17]. The chromatic dispersion at 531 nm for various diameters of the waist is given in Fig. 4.

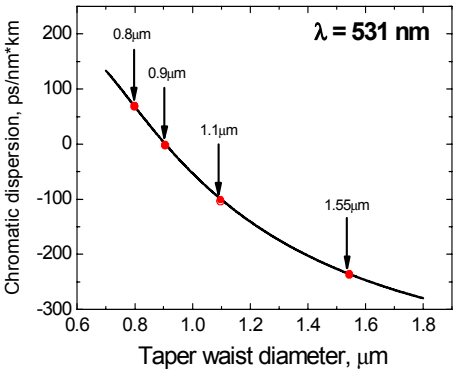

Fig. 4. Chromatic dispersion versus taper waist diameters for λ=531 nm. Waist diameters of tested tapers are indicated with arrows.

Figure 4 indicates that the optimum supercontinuum efficiency can be achieved with a 0.9-μm waist taper, whose zero dispersion wavelength matches the pump wavelength of 531 nm. The

#8587 - $15.00 USD Received 25 August 2005; Revised 5 October 2005; Accepted 5 October 2005

influence of taper parameters on SC efficiency was studied by varying the waist diameter. Particularly, it was confirmed that minor change in waist diameter (0.1 μm) affects drastically the SC efficiency. The dispersion characteristics of studied tapers are shown in Fig. 5.

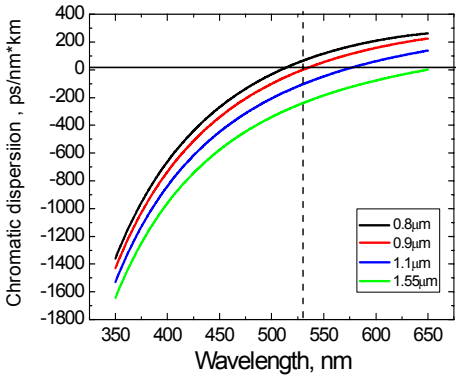

Fig. 5. Chromatic dispersion of tapered fibers with different parameters. The legend shows the taper waist diameters; the dashed line indicates the pump wavelength (531 nm).

With a fiber pulling workstation available for these experiments, the ZDWs of the tapers could be accurately adjusted during taper fabrication to match desired pump wavelength. All tapers used in this study have losses below 0.09 dB/cm at the pump wavelength.

After taper characterization, the output from PPLN crystal was coupled to the taper using objective lens. Strong nonlinear conversion to SC within the taper with the diameter of the waist of 0.9 μm providing optimal dispersion characteristics results in a radiation covering the entire visible wavelength range. The optical spectra of the visible continuum measured for different pump powers are shown in Fig. 6(a). Figure 6(b) illustrates the SC radiation after reflection from diffraction grating.

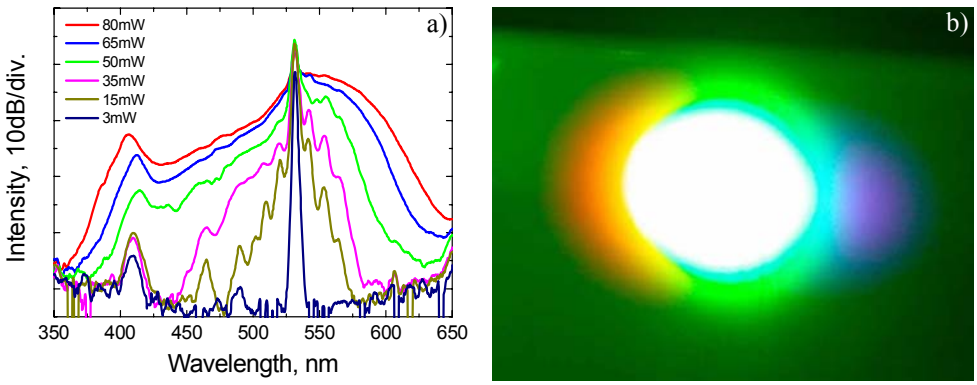

Fig. 6. Visible white light continuum at various input power levels (a) and supercontinuum spectrum photograph (b) for the taper with waist diameter of 0.9 μm.

From Fig. 6 it can be seen that the supercontinuum energy is limited to the visible wavelength range, without significant UV or IR components. At maximum pump power, the average power of supercontinuum radiation reaches ~55 mW corresponding to a spectral brightness of 0.17 mW/nm.

The effect of the ZDW on SC efficiency was then studied using tapers with different waist diameters. The SC spectra from the tapers measured at different input powers are presented in Fig. 7(a-c).

#8587 - $15.00 USD Received 25 August 2005; Revised 5 October 2005; Accepted 5 October 2005

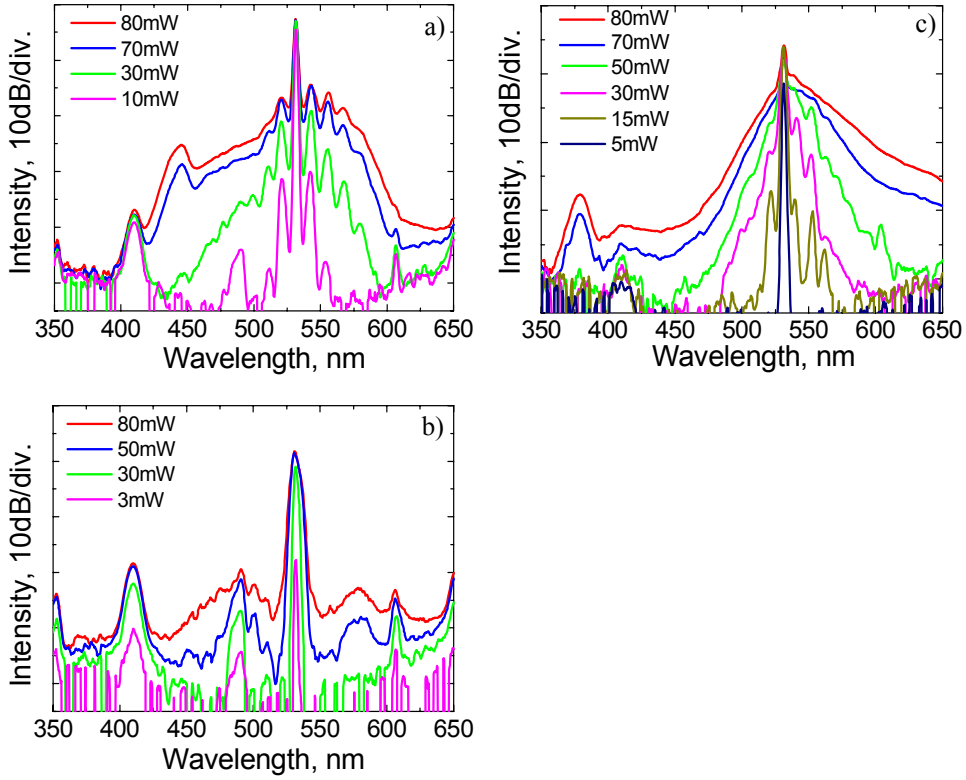

Fig. 7. Visible continua obtained in tapers with waist diameter of 1.1 μm (a), 1.55 μm (b), and 0.8 μm (c) with pump power as a parameter.

It can be seen that small variations in waist diameter result in a large change of the SC spectrum revealing an important role played by chromatic dispersion. The supercontinuum spectrum with improved bandwidth and flatness has been obtained from the taper with a zero dispersion wavelength closest to the pump wavelength. Increasing the taper waist diameter over the optimal value of 0.9 μm causes the pump pulse to propagate in normal dispersion regime which, combined with decreased nonlinearity due to larger waist cross-section, leads to lower supercontinuum generation efficiency, as seen from Fig. 7(a). Ultimately, a taper with a 1.55-μm diameter waist has too large normal dispersion and too low nonlinearity to generate significant spectral broadening, as seen in Fig. 7(b).

Using a taper with diameter only slightly smaller (~0.1 μm) than the optimal value leads to poor SC efficiency, as seen in Fig. 7(c). This effect can be understood from soliton fission theory of supercontinuum generation [9, 18]. As the taper waist diameter decreases, the pump pulse experiences higher anomalous dispersion. Consequently, the pump pulse is converted into a lower order soliton [9], despite a higher light density in the taper with decreased diameter of the waist. As a result, upon the breakup, the pump pulse generates lower number of fundamental solitons and hence the non-soliton blue-shifted radiation is also strongly reduced, as clearly seen from Fig. 7(c). In a contrary, the amount of red-shifted radiation increases as a result of enhanced Raman shifting and self-phase modulation owing to higher optical field intensity within the taper with the reduced waist diameter.

The results in Fig. 7 indicate that the tolerances for the taper waist required for efficient SC generation are very tight. A deviation of only 0.2 μm from the optimal waist diameter, that ensures the zero dispersion at the pump wavelength, can dramatically change the supercontinuum spectral shape. This conclusion is supported by the data shown in Fig. 4,

#8587 - $15.00 USD Received 25 August 2005; Revised 5 October 2005; Accepted 5 October 2005

which indicates that the large change in chromatic dispersion is expected even for small variations in the taper waist diameter.

5. Conclusion

We have demonstrated visible white-light generation using tapered fiber with engineered dispersion profile. Pump light was provided by a mode-locked ytterbium fiber laser frequency-doubled in a PPLN nonlinear crystal. An optimal taper diameter for supercontinuum generation was identified based on numerical simulations and measurements. The brightness of the source with the bandwidth covering entire visible spectral range is enhanced by limiting the spectral broadening in a tapered fiber to the visible wavelengths. The influence of taper parameters on the white light generation has been studied.

Acknowledgments

The authors would like to acknowledge the financial support of Finnish Academy through projects SUPERNAL and GEMINI and European Union project URANUS within framework EU-FP6.

#8587 - $15.00 USD Received 25 August 2005; Revised 5 October 2005; Accepted 5 October 2005

Tampereen teknillinen yliopisto
PL 527
33101 Tampere

Tampere University of Technology
P.O. Box 527
FIN-33101 Tampere, Finland